

**Structural Studies of Bacterial Multicomponent Monooxygenases:
Insights into Substrate Specificity, Diiron Center Tuning and
Component Interactions**

by

Matthew H. Sazinsky
B. S. Chemistry
Haverford College, 1999

SUBMITTED TO THE DEPARTMENT OF CHEMISTRY IN PARTIAL
FULFILLMENT OF THE REQUIREMENTS FOR THE DEGREE OF

DOCTOR OF PHILOSOPHY IN BIOLOGICAL CHEMISTRY
AT THE
MASSACHUSETTS INSTITUTE OF TECHNOLOGY

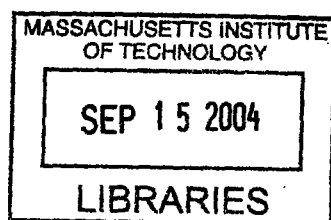
September 2004

© Massachusetts Institute of Technology, 2004
All rights reserved

Signature of Author: _____
Department of Chemistry
August 30, 2004

Certified By: _____
Stephen J. Lippard
Arthur Amos Noyes Professor of Chemistry
Thesis Supervisor

Accepted by: _____
Robert W. Field
Chairman, Departmental Committee on Graduate Studies



ARCHIVES

This doctoral thesis has been examined by a committee of the Department of Chemistry as follows:

Catherine L. Drennan
Committee Chair
Associate Professor of Chemistry

Stephen J. Lippard
Arthur Amos Noyes Professor of Chemistry
Thesis Supervisor

JoAnne Stubbe
Novartis Professor of Chemistry and Biology

Structural Studies of Bacterial Multicomponent Monooxygenases: Insights into
Substrate Specificity, Diiron Center Tuning and Component Interactions

by

Matthew H. Sazinsky

Submitted to the Department of Chemistry on August 30, 2004

In Partial Fulfillment of the Requirements for the Degree of

Doctor of Philosophy in Chemistry

Abstract

Bacterial multicomponent monooxygenases (BMMs) are capable of oxidizing a variety of hydrocarbon substrates at a non-heme carboxylate-bridged diiron center housed within a 200-250 kDa hydroxylase protein. Chapter 1 introduces the members of the BMM family as well as several related diiron proteins with functional relevance to BMMs. The structures of the individual components and the diiron centers are discussed in relation to their catalytic function and the tuning of the metal centers.

The structure of the toluene *o*-xylene monooxygenase hydroxylase (ToMOH) is presented in chapter 2. The dinuclear iron center is virtually identical to that in the methane monooxygenase hydroxylase (MMOH), yet several novel features, such as a 40 Å channel, may explain the differences in the substrate specificity between BMM subfamily members. A structural basis for

the regiospecificities of toluene monooxygenase and phenol hydroxylases is discussed

In Chapter 3 are described metal reconstitution studies of MMOH to probe the ligand geometries of the diiron center and the possible effects on the structure by the coupling protein, MMOB, and the orfY gene product, MMOD. The structures of Mn(II) and Co(II) reconstituted MMOH are identical to that of the diferrous protein. MMOB and MMOD make the addition and removal of iron from MMOH more difficult, suggesting that these proteins serve to block solvent and/or small molecule access to the active site by binding to the four-helix bundle housing the diiron center.

Product movement to and from the diiron centers of BMMs is essential for catalytic function. In chapter 4 the crystal structures of MMOH with several bound products are reported. The binding of these products alter the positioning of several side chains in the MMOH α -subunit cavities. The presence of 6-bromohexan-1-ol induces one of the active site helices to adopt a π conformation. Together, these findings suggest modes by which molecules may move through the MMOH cavities and how both substrates and MMOB may influence the structure of the active site pocket.

Thesis Supervisor: Stephen J. Lippard
Title: Arthur Amos Noyes Professor of Chemistry

To my parents, who have always provided me with the tools to succeed

Acknowledgements

The last five years have been one of the most interesting and challenging in my life. Like all graduate students who have survived the Ph.D. process, there were many good times and bad times, but more importantly there were a number of people who helped me along the way that I must thank for their support, intellectual insight, and occasional (but much needed) distractions from science. Without question, I owe my thesis advisor, Steve Lippard, a dept of gratitude for the excellent training I have received and the leeway he gave me during this time to explore many different avenues of research, especially when all of my main projects were not working. Steve's passion for science, broad interests and fearlessness toward research are truly remarkable. When am I finally ready to start my own career, I only hope that some of these qualities have rubbed off on me. I also pray that some of my many lab antics, like fabricating such wonderful literature survey titles as "Spectroscopic characterization of methane monooxygenase hydroxylase mutants from *M. trichosporium* OB3b," by Lipscomb et. al. have helped Steve to "lighten up" just a little bit of the years, but only time will tell.

I must also praise Steve's ability for assembling such a remarkable group of talented people with whom it has been a pleasure to work along side in lab. Most of what I learned about biochemistry I owe to the MMO subgroup. My initial crystallographic training began under the tutelage of Doug Whittington, who first introduced me to MMO and showed me the ins and outs of protein crystallography. Doug was an exceptional mentor and even after leaving MIT still fielded many of my crystallographic questions. In the absence of Doug, there were of course Dan Kopp, Maarten Merkx, George Gassner, Jens Müller, Edna Ambundo and Jessica Blazyk, the so called old-guard of MMO who were valuable resources over the years and have been a fun group with which to work. In the span of a graduate student lifetime, there is always turnover. During the years an entirely new generation of MMO personnel arrived, including Elisabeth Cadieux, Lisa Chatwood, Laurance Beauvais, Leslie Murray, Viviana Izzo, and Mike McCormick, whom I can honestly say have been some of the most colorful personalities I have yet to encounter. We have had some exciting times in the lab recently, thanks to our collaborations with Alberto Di Donato, for which I am very grateful. I know that I will truly miss this group of people, as well as my other labmates, Sungho Yoon, Yongwon Jung, Chris Chang, Carolyn Woodruff, and Dong Wang, when I finally move on to my post-doc.

During these five years I was fortunate to have several undergraduates assist me with my research. Sonya Tang, in particular, spent her entire undergraduate career working for me. Although there were few success on our ambitious projects, I admired her persistence and curiosity. I know she will be a fantastic MD/PhD student at Johns Hopkins. Also participating in my UROP army at one time or another were Shan Riku, Bret Boshco, Leo Drezhinin, Michelle Nyein, and Adam Silverman, who were all great students.

A lot of the research I've done could not have been performed without outside help. Therefore I must thank Cathy Drennan and her lab for their support throughout the years. Being the only protein crystallographer in the lab was not easy, but life would have been a thousand times more difficult if I could

not rely on Cathy, Tzanko Dukov, Fred Berkovitch, Eric Schreiter, Mike Sintchak, Hector Hernandez and Luke Higgins for their occasional assistance. Equally as important as Cathy's lab was that of the structural biology group at Wyeth Pharmaceuticals. I owe a lot of thanks to Will Somers for allowing me to intern one summer and to Joel Bard for his generous help in assisting me solve my first new protein structure and introducing me to the glorious world of automated crystallization.

In Steve's lab collaborations are an important fact of every day life and I have had numerous collaborators. Therefore, special thanks goes out Deanne Jackson Rudd from Keith Hodgson's lab for all of her XAS work and for making my numerous trips to SSRL so much more enjoyable (not that collecting diffraction data for 64 straight hours with little sleep isn't enjoyable). I thank Alberto Di Donato, Valaria Cafaro, and Ennio Notomista for a wonderful collaboration on ToMO and PH. This work has been source of real excitement for our labs, and I hope it will continue to be a fruitful for years to come. Gary Brudvig, Brian Hoffman, Roman Davydov, and Pierre Moenne-Loccoz have been fantastic collaborators and I am indebted to them for all of their spectroscopic work over the years.

Finally I'd like to thank my Haverford College professors Rob Scarrow, Jenni Punt, and Terry Newerth as well as Eileen Jaffe and Roland Dunbrack at Fox Chase Cancer Center for their support and the initial preparation they gave me make it this far.

To all of my friends and relatives, who have asked me time and time again when I'll be done and, who so often asked this question with a tone of voice made that MIT seem more like a jail than a graduate school, I can finally say "I'm done."

Table of Contents

Abstract	3
Dedication.....	5
Acknowledgements	6
Table of Contents.....	8
List of Tables.....	14
List of Schemes	16
List of Figures	17
Chapter One: Bacterial Multicomponent Monooxygenases.....	21
Environmental and Industrial Applications	23
Properties of Multicomponent Monooxygenases.....	25
The Hydroxylase Component of BMMs	26
The Global Fold	26
The Diiron Center.....	27
The Conserved Active Site Asparagine and Threonine	31
Hydrogen Bonding Networks.....	32
Substrate Access to the Diiron Center	33
The Reductase and Rieske Proteins	36
The Regulatory Protein.....	39
Structure of the Regulatory Protein	39
Function of the Effector Protein N-terminus.....	41
Affects of the Regulatory Protein on the Hydroxylase	42
The Big Picture: Component Interactions in sMMO	46

Reaction Cycle of Bacterial Multicomponent Monooxygenases	48
References	51

Chapter Two: Crystal Structure of the Toluene/*o*-Xylene

Monooxygenase Hydroxylase from *Pseudomonas stutzeri* OX1: Insight into Substrate Specificity, Substrate Channeling and Active Site

Tuning of Multicomponent Monooxygenases	75
Introduction	76
Experimental Procedures	78
Expression and Purification of ToMOH	78
Purification of ToMOD	79
Activity and Iron Assays	80
Crystallization and Data Collection	80
Structure Determination and Model Refinement	80
Results and Discussion	81
Global Fold and Topology of ToMOH	81
Electrostatic Surfaces of ToMOH and ToMOD	83
The Carboxylate-Bridged Diiron Center	83
Open Channel Access to the Diiron Active Site	87
Substrate Specificity of Four Component Alkene / Aromatic Monooxygenases	91
Acknowledgements	93
References	93
Footnotes	98

Chapter Three: Preparation and X-ray Structures of Metal-Free, Dicobalt, and Dimanganese Forms of Soluble Methane Monooxygenase	
Hydroxylase from <i>Methylococcus capsulatus</i> (Bath)	114
Introduction.....	115
Experimental.....	118
Materials and General Methods.....	118
Kinetics of Iron Release from MMOH _{red}	118
Preparation of Apo MMOH.....	119
Activity Assays.....	119
Kinetics of Iron Reconstitution of Apo MMOH.....	119
Isothermal Titration Calorimetry.....	120
Optical Spectroscopy of Co(II)-MMOH.....	120
CD Spectroscopy of Holo and Apo MMOH.....	121
Crystallization of Apo MMOH and its Mn(II) and Co(II) Derivatives.....	121
X-ray Diffraction Data Collection and Structure Refinement.....	121
Results.....	122
Generation of Apo MMOH.....	122
Reconstitution of Hydroxylase Activity.....	123
Isothermal Titration Calorimetry.....	124
UV-Vis Spectroscopic Study of Cobalt-Substituted MMOH.....	124
Global Folds of Apo, Mn(II), and Co(II) MMOH.....	126
Active Sites of Apo, Mn(II) and Co(II) MMOH.....	128
Discussion.....	130
Effects of MMOB and MMOD on Iron Binding to MMOH.....	130
Disorder within Helices E, F, and H.....	133

Helical Disorder and the MMOB/MMOD Binding Site	136
Structural Perturbations of the MMOH Dimetallic Center.....	137
Acknowledgments	138
References	139

Chapter Four: Product-Bound Structures of Soluble Methane

Monoxygenase Hydroxylase from *Methylococcus capsulatus* (Bath):

Protein Motion in the α-Subunit Cavities	161
Introduction.....	162
Experimental.....	165
Crystallization of MMOH and Small Molecule Soaks	165
Data Collection and Model Refinement	165
Results	166
Alcohol Binding to MMOH.....	166
Product Binding to Cavity 1	168
6-Bromoethanol Induced Structural Changes in Helix E	170
Connectivity Between the α -Subunit Cavities	172
Discussion	174
The MMOH Product-Bound State	174
Conformational Changes in Helix E	175
Cavity Gating and Molecule Movement Through MMOH.....	178
Why Cavities?	183
Acknowledgments	184
References	185

Appendix One: Characterization and Crystallization of the MMOH-MMOD Complex from <i>Methylococcus capsulatus</i> (Bath)	207
Introduction.....	208
Experimental.....	210
Protein Isolation and Purification	210
Construction and Purification of the MMOD Cys67Ser Mutant.....	211
Construction of the MMOD N-terminal Truncate.....	212
Creation of MMOD' and MMOD'-Cys67Ser	213
Proteolytic Digestion of MMOD	213
MALDI-MS of MMOD' Cys67Ser.....	214
UV-vis and Circular Dichroism Spectroscopy	215
Crystallization of the MMOH-MMOD Complex.....	215
Determination of Crystal Content by SDS-PAGE.....	215
Data Collection and Refinement	216
Mössbauer Spectroscopy	216
Results and Discussion	217
Prediction of the MMOD Structure.....	217
The Function of Cys-67	217
MMOB Induces Formation of an Oxo-Bridged Diiron(III) Center.....	218
Proteolysis and Mass Spectrometry of MMOD and MMOD Cys67Ser	220
Characterization of the MMOD Truncates.....	221
Crystallization of the MMOH-MMOD Complex.....	221
Conclusions.....	224
Acknowledgments	225
References	226

Biographical Note.....	244
Curriculum Vitae.....	245

List of Tables

Table 1.1.	Sequence Identity between the α -Subunits of the BMM Subfamilies	60
Table 1.2.	Bacterial Multicomponent Monooxygenase Sub-Families	61
Table 1.3.	Redox Potentials of sMMO.....	62
Table 2.1.	ToMOH Data Collection and Refinement Statistics.....	99
Table 2.2.	Comparison of BMM Active Site Pocket Residues.....	100
Table 2.3.	Reactivity and Product Distributions of TMOs and Mutant Isoforms	101
Table 3.1.	Data Collection and Refinement Statistics	144
Table 3.2.	MMOB and MMOD Binding Constants to Apo and Holo MMOH.....	145
Table 3.3.	Properties of Co(II)-Reconstituted Non-Heme Diiron Proteins....	146
Table 3.4.	Average B-factors for Selected Regions of the MMOH α -Subunits.....	147
Table 4.1.	Data Collection and Refinement Statistics	191
Table 4.2.	Halogenated Alcohol Binding Sites on MMOH.....	192
Table 4.3.	Cavity Connectivity and Side Chain Movements in Product Soaked MMOH Crystal Structures	193
Table 4.4.	Fe-Fe and Fe-O Bridge Ligand Bond Distances in Different Product-Bound Structures.....	194
Table 4.5.	Average B-factors for Selected Regions of the MMOH α -Subunits.....	195

Table A1.1	Relative Absorbance of the MMOH (μ -oxo)diiron(III) Species versus sMMO Activity	228
Table A1.2	LC-MS of MMOD and MMOD Cys67Ser	229
Table A1.3	MALDI-MS of Trypsin Digested MMOD' from the SDS-PAGE of MMOH-MMOD Crystals	230
Table A1.4	Data Collection and Processing Statistics of the MMOH- MMOD Crystals	231

List of Schemes

Scheme 3.1	sMMO catalytic cycle.....	148
------------	---------------------------	-----

List of Figures

Figure 1.1.	Operon Organization of BMMs	63
Figure 1.2.	Global Structures of MMOH and ToMOH	64
Figure 1.3.	Four-Helix Bundle Topology	65
Figure 1.4.	Dioxygen Utilizing Carboxylate-Bridged Diiron Centers	66
Figure 1.5.	Redox Dependant Conformational Changes in MMOH	67
Figure 1.6.	Hydrogen Bonding Network Behind the Diiron Centers.....	68
Figure 1.7.	Cavities and channels in α -Subunit of MMOH and ToMOH	69
Figure 1.8.	Structures of Reductase and Rieske Proteins.....	70
Figure 1.9	Electron transfer from MMOR to MMOH	71
Figure 1.10.	NMR Structures of the Regulatory Proteins	72
Figure 1.11	Docking model of the sMMO ternary complex.....	73
Figure 1.12.	Reaction Cycle of sMMO.....	74
Figure 2.1	Structure of ToMOH and Comparison to MMOH.....	102
Figure 2.2	Electrostatic Surfaces of ToMOH and ToMOD	103
Figure 2.3.	The Oxidized ToMOH and MMOH Diiron Centers	104
Figure 2.4.	Hydrogen bonding at or near the ToMOH and MMOH diiron centers	105
Figure 2.5.	Active Site structures of ToMOH and RNR-R2 Y208F with bound azide	106
Figure 2.6.	Difference UV-vis Spectrum of Azide Binding to ToMOH.....	107
Figure 2.7.	The ToMOH Substrate Channel.....	108
Figure 2.8.	Surface Representation of the ToMOH Substrate Channel	109
Figure 2.9.	Structures of ToMOH and MMOH α -Subunits Depicting	

	the Cavities and Channels with Bound Compounds.....	110
Figure 2.10.	F_o-F_c Simulated Annealing Omit Map of 4-Bromophenol Bound to the ToMOH Channel	111
Figure 2.11.	Entryways to the MMOH and ToMOH and MMOH Active Sites	112
Figure 2.12.	Stereoview of the ToMOH Active Site Pocket.....	113
Figure 3.1.	Kinetics of iron-release from MMOH_{red}	149
Figure 3.2.	Kinetics of formation of Active MMOH from apo MMOH and Fe^{2+}	150
Figure 3.3.	Effect of Iron Concentration on the Kinetics of Formation of Active MMOH.....	151
Figure 3.4.	Isothermal titration Calorimetry of MMOB and MMOD Binding to Holo and Aapo MMOH	152
Figure 3.5.	Optical Difference Spectra of Co(II) Reconstituted MMOH.....	153
Figure 3.6.	CD Spectra of Apo and Holo MMOH.....	154
Figure 3.7	B-factors of the Fe(II), Apo, Co(II), and Mn(II), α -Subunits	155
Figure 3.8	Stereoview of the Hydrogen Bonding Network Behind the Diiron Center in Apo MMOH.....	156
Figure 3.9	Structure of the Apo MMOH Active Site.....	157
Figure 3.10	Structures of the Apo, Mn(II) and Co(II) MMOH Active Sites	158
Figure 3.11	$ 2F_o - F_c $ Electron Density Maps Surrounding the Mn(II)- Soaked and Co(II)-Grown MMOH Active Sites	159
Figure 3.12	Superposition of the Apo, Mn(II), Co(II) MMOH Active Sites with Oxidized and Reduced MMOH	160
Figure 4.1	Hydrophobic Cavities in the MMOH α -Subunit.....	196

Figure 4.2	Stereoviews of Haloalcohol Binding Sites within MMOH.....	197
Figure 4.3	MMOH Active Sites with Bound Alcohols Products.....	198
Figure 4.4	Comparison of Side Chain Positions in the MMOH Active Site Cavities from Different Product Bound Structures.....	199
Figure 4.5	Stereoviews Comparing the 6-Bromohexan-1-ol Soaked and Oxidized MMOH Active Site Pockets	200
Figure 4.6	Structural Changes in Helix E of the Four-Helix Bundle	201
Figure 4.7	Structure of MMOH Soaked in 6-bromohexan-1-ol Following Chemical Reduction.....	202
Figure 4.8	Channel Formation in Product Bound MMOH.....	203
Figure 4.9	Movements in Leu-289 and Cavity Connectivity.....	204
Figure 4.10	The Affect of Asn-214 Conformation on Solvent Accessibility to the Diiron Center	205
Figure 4.11	Substrate Entrance and docking to ToMOH.....	206
Figure A1.1	sMMO oOperon from <i>Methylococcus capsulatus</i> (Bath)	232
Figure A1.2	Sequence Alignment of MMOD.....	233
Figure A1.3	Hypothetical 3D-Model of MMOD	234
Figure A1.4	Spectroscopic Characterization and Activity of MMOD C67S	235
Figure A1.5	UV-Vis Spectra of the MMOH-MMOB Complex.....	236
Figure A1.6	Mössbauer Spectra of ⁵⁷ Fe-MMOH with and without MMOB.....	237
Figure A1.7	LC-MS of Cys67Ser MMOD	238
Figure A1.8	MMOD' Binding to MMOH by UV-Vis.....	239
Figure A1.9	Inhibition of sMMO Activity by MMOD'	240
Figure A1.10	SDS-PAGE of the MMOH-MMOD High Salt Crystals.....	241
Figure A1.11	Crystals of the MMOH-MMOD' Cys67Ser Complex.....	242

Figure A1.12 Diffraction Pattern of the MMOH-MMOD'-C67S Crystals 243

Chapter 1

Non-Heme Diiron Bacterial Multicomponent Monooxygenases

Nature has evolved carboxylate-bridged diiron centers in proteins to perform a variety of functions. Included are iron storage in ferretin and bacterioferretin (1), O₂ transport in hemerythrin (2), radical generation in ribonucleotide reductase (3), peroxide scavenging in rubrerythrin (4), apoptosis regulation by the *chlamydia* associated death domain (CADD) (5), hydrocarbon desaturastion in stearyl-acyl carrier protein Δ^9 desaturase (6) and hydrocarbon oxidation in multicomponent monooxygenases (7-9). All of these metal centers are housed within a four-helix bundle, nature's preferred biological scaffold for generating a dimetallic center that utilizes O₂ or O₂-derived substrates. In the majority of those systems in which dioxygen activation chemistry is performed, four of the iron coordinating ligands are provided by two E(D)XXH motifs. The different functions and reactivities of these enzymes derive from the surrounding protein environment, which evolved to control the primary and secondary coordination spheres of the dimetallic center, introduce active site pockets and substrate channels, and create electron transfer pathways.

The bacterial multicomponent monooxygenase family of enzymes, BMMs, have a carboxylate-bridged dinuclear iron active site that hydroxylates a wide variety of hydrocarbon substrates including alkanes, alkenes, and aromatics. Six evolutionarily related subfamilies of BMMs have been characterized (Tables 1.1, 1.2) (7,8). These classes are methane monooxygenases (sMMOs), four component alkene/aromatic monooxygenases (TMOs), phenol hydroxylases (PHs), alkene monooxygenases (AMOs), hyperthermophilic toluene monooxygenases (SsoMMOs), and tetrahydrofuran monooxygenases (THMOs). Each of these subfamilies has evolved to act specifically on certain types of hydrocarbons to assist its host organism in survival. Members of the sMMO family are adept at

converting small alkanes to their respective alcohols, whereas TMOs, PHs, and SsoMOs specialize in the regiospecific hydroxylation of aromatics. Although sMMOs can hydroxylate over 50 different compounds including aromatics (10,11), most of the other family members cannot act on alkanes despite the fact that these enzymes are predicted by sequence homology and spectroscopy to have very similar diiron active sites. Propane monooxygenase (PMO), which is most similar to THMO, is the only non-sMMO sub-family member that hydroxylates alkanes (12).

Of the enzymes described above, only soluble methane monooxygenase is capable of activating the inert C–H bond of methane, which is one of the most difficult reactions to perform in nature. The differences in substrate specificity between the BMM subfamilies and the disparate activities of the related diiron proteins pose important questions with respect to the tuning dimetallic iron centers. Why are BMMs the only diiron enzymes that oxidize hydrocarbons and how do BMMs tune their active sites to hydroxylate different substrates? The substrate specificities and reactivities exhibited by the BMM sub-families may be attributed to subtle alterations in the iron coordination sphere and active site pocket residues, the nature of which is slowly becoming apparent. The fundamental properties that differentiate the other diiron proteins from each other remain to be clarified, however.

Environmental and Industrial Applications

Bacteria harboring multicomponent monooxygenases have the unique ability to utilize hydrocarbons as their sole source of carbon and energy (13,14).

The first committed step in the conversion of hydrocarbons to biomass is accomplished by these enzymes (eq.1). Because their hydroxylase components

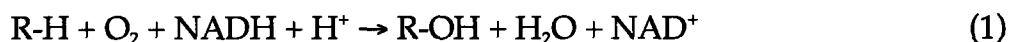


exhibit broad substrate specificity, BMMs have a substantial impact on the environment, for they contribute to the bioremediation of pollutants like trichloroethylene, chloroform, phenol, methyl ethers and petroleum spills and are responsible for keeping potent greenhouse gases like methane from reaching the atmosphere (13,15). The flexible nature of the BMM hydroxylase active sites that allows for such a wide range of substrate accommodation, endows these enzymes with their unique environmental cleansing capabilities. The bacteria and archaea containing BMMs inhabit almost any environment imaginable, some of which include polluted rivers and streams, arctic and ocean soil sediments, and thermal vents in the deep sea or near hot springs and volcanos. These bacteria, such as several *Pseudomonas* species which can survive in 50% toluene (v/v), have evolved incredible survival mechanisms and solvent tolerances, a quality that lends them to industrial application (16). Some BMM hydroxylations are highly regio- and enantiospecific. For instance, toluene 4-monooxygenase (T4MO) and toluene ortho-monooxygenase (TOM) produce *p*-cresol and *o*-cresol, respectively, in greater than 95% yield. Toluene 2-monooxygenase (T2MO), on the other hand, can epoxidize alternative substrates like 1-pentene and 1,3-butene to afford enantiospecific products in greater than 92% yield that can be used as feedstocks for the synthesis of chiral compounds (17-20). The availability of recombinant BMMs, such as the toluene monooxygenases and phenol hydroxylases (21,22), have allowed for the engineering of their active sites to accommodate and hydroxylate alternative

substrates with high selectivity and regiospecificity (20,23,24). Coupling these recombinant systems with a solvent tolerant host may facilitate the application and adaptation of these enzymes to industrial processes.

Properties of Multicomponent Monooxygenases

For catalysis, BMMs require a hydroxylase that contains a dinuclear iron center, a regulatory protein and a source of electrons. Although each of these systems utilizes similar components, the genetic makeup of the different BMM operons vary significantly in organization and content (Figure 1.1). In their most basic form, BMMs, such as the sMMO and PH subfamilies, require three protein components for activity. These components are a 220-250 kDa hydroxylase of the form of an $\alpha_2\beta_2\gamma_2$ heterodimer, a 10-16 kDa effector protein that couples electron transfer with hydrocarbon substrate activation, and a 38-40 kDa [2Fe-2S]- and FAD-containing reductase that shuttles electrons from NADH to the diiron center (25). The TMOs and the hyperthermophilic toluene monooxygenases (SsoMOs), such as the one from *Sulfolobus solfataricus* P2, require a 10 kDa Rieske protein as a fourth component to mediate electron transfer from the reductase to the diiron center (7,8). The α -subunit of the SsoMO hydroxylase is significantly different from the other family members and comprises two distinct peptide chains termed α_N and α_C . The α_N polypeptide has approximately 269 amino acids and relatively strong sequence homology to TMOs. The α_C polypeptide is 310 amino acids long, the first 54 of which are unique to this protein. The remainder of the sequence is homologous to the C-terminal portion of the TMO α -subunit. AMOs and THMOs are similar to the three component MMO and PH families

except that their hydroxylases do not have a γ -subunit (12,26,27). AMOs take the form of an $\alpha\beta$ monomer whereas the uncharacterized THMOs could be either $\alpha\beta$ monomers or dimers. The lack of a γ -subunit in these families, and the poor sequence conservation among those that do have one, suggest that this subunit is not critical to the function of the enzyme, but may be important in enzyme assembly. The operon for the PH system encodes for an additional protein of ~10 kDa, PHK (or DmpK), which is essential for assembly of the diiron center (Figure 1.1) (28). The sMMO system also encodes a protein of similar size, MMOD, having weak homology to PHK and which binds to the MMOH α -subunit, but its function has yet to be determined (29).

The identity between the different α -subunits from the different subfamilies ranges between 20-45% (Table 1.1.) Sequence analysis of these remarkably different enzyme systems suggest they may have evolved from a common ancestor (7,8). Given the conserved nature of the carboxylate-bridged diiron center among the all of the known four-helix bundle proteins, BMMs may represent one evolutionary branch of enzymes and proteins, the primordial relatives of which may include the R2 subunit of ribonucleotide reductase (RNR-R2), Δ^9 desaturase, rubrerythrin, ferritin, and CADD.

The Hydroxylase Component of BMMs

The Global Hydroxylase Fold

The X-ray crystal structures of the methane and toluene/*o*-xylene monooxygenase hydroxylase components have been solved. These enzymes are similar in global topology, which may be characteristic of other BMM family

members (Figure 1.2) (30,31). This component comprises two $\alpha\beta\gamma$ protomers that use protein-protein contacts between each of the α - and β - subunits to form the heterodimer. The interface between the protomers forms a large canyon in the middle of the protein, which is proposed to be the docking site for the reductase, Rieske, and regulatory protein components (30). The carboxylate-bridged diiron center is housed within a four-helix bundle assembled by helices B, C, E, and F of the α -subunit (Figure 1.3). Two of these helices, E and F, are on the hydroxylase surface and form a ridge of the canyon; the diiron center lies ~ 12 Å beneath the surface of the protein.

The α - and β - subunits are mostly all α -helical and the folds of both subunits are very similar, possibly owing to a gene duplication early in the evolutionary history of one of the subunits (8). The γ -subunits are the least conserved portion of the hydroxylase, varying greatly in docking position, structure, and sequence homology.

The Diiron Center

Among all known BMMs, a universally conserved set of glutamate and histidine ligands are responsible for forming the diiron center. Four of these ligands reside in two EXXH motifs on helices C and F. Sequence and spectroscopic comparisons between the different BMM families suggest that the structures of the dinuclear iron centers in these enzymes are essentially the same (7-9,32-34). In general, the core of the diiron unit is formed by two histidine residues, which coordinate to positions distal to the active site pocket, and a bridging carboxylate. This basic three-amino-acid structural motif is conserved among the related diiron proteins Δ^9 desaturase, ribonucleotide reductase,

rubrerythrin, ferretin, bacterioferretin, and CADD (Figure 1.4) (5,35). The remainder of the ligands in primary coordination sphere differ significantly from these proteins in identity and orientation. For MMOH and ToMOH, Fe1 is coordinated by a monodentate glutamate and a terminal water molecule, which hydrogen bonds to the dangling oxygen of the glutamate. Two monodentate carboxylates coordinate to Fe2. In the oxidized form of the protein, hydroxides and/or a H_3O_2^- anion occupy the bridging positions to complete the pseudooctahedral geometry of the iron atoms, which are separated by 3.0-3.1 Å (36-39). In different structures of MMOH and ToMOH, product alcohols and mono-anions like formate, acetate, and thioglycolate can occupy the bridging position facing the hydrophobic active site pocket (30,31,40,41). Only in the acetate bound structure, in which the data were collected at 4 °C, is the structure of the diiron center different. Here the Fe-Fe separation expands to 3.4 Å and both acetate O-atoms are bridging. By contrast, only one solvent derived O-atom bridges the irons at this position in the other oxidized forms of MMOH. The glutamate and histidine residues that coordinate to Fe2 are contributed by helices E and F, whereas the bridging carboxylate and the ligands coordinating to Fe1 come from helices B and C. For the homologous diiron active sites of RNR-R2, Δ^9 desaturase, bacterioferritin, and rubrerythrin, the flanking carboxylate ligands adopt different orientations and coordination modes, indicating one way by which these enzymes are differently tuned (Figure 1.4). In CADD there is a histidine where a glutamate ligand binds at Fe1 and an aspartate in place of the shifting glutamate coordinating at Fe2 (5). Since it is relatively unclear how CADD participates in apoptosis and what the substrates are for this enzyme, it is

difficult to imagine how this novel ligand configuration facilitates its specific catalytic activity. In one structure of class 1c RNR-R2 from *Clamylidia trachomatis*, the coordinating ligands and the geometric configuration at the diiron center appear are identical to those of MMOH_{ox} (42). Unlike MMOH, however, the dinuclear iron center in this enzyme is proposed to generate an Fe(III)Fe(IV) unit that fulfills the radical-forming function of the protein. Despite having nearly isostructural oxidized diiron(III) centers, the differences in catalytic function between MMOH and class Ic RNR-R2 emphasize the importance of the surrounding protein environment in controlling reactivity.

One feature that differs between most BMMs and their homologues is that the latter generally have oxo-bridged diiron(III) centers. The Fe–Fe distances in these proteins vary between 3.3–4.1 Å, compared to MMOH and ToMOH, which have Fe–Fe distances of 3.0–3.1 Å. Hydroxo-bridges are not universally characteristic of all BMMs, however. In the *Pseudomonas sp.* CF600 phenol hydroxylase ~85% of the diiron centers have oxo bridges (33). Single turnover at the metal center decreases both the relative population of oxo-bridged diiron(III) units and the activity of the enzyme. This result suggested that the hydroxo-bridged form of phenol hydroxylase, which comprises the other 15% of the dimetallic centers in the isolated enzyme, is inactive.

Upon reduction of MMOH to the diiron(II) form, the bridging hydroxides are displaced and Glu-243 undergoes a carboxylate-shift to occupy the bridging position cis to the histidine ligands while remaining chelated to Fe2 (Figure 1.4). The newly supplied active site pocket water molecule coordinates terminally to Fe1. As a result of these changes, the Fe–Fe distance increases to 3.3–3.4 Å and an open coordination site is formed on Fe2 facing the active site pocket. Based on

density functional theoretical calculations, it is hypothesized that this position is the primary location of O₂ activation by sMMO and perhaps all BMMs (43). Synthetic model studies of carboxylate-rich diiron compounds also reveal the necessity of such open positions for oxygenation chemistry to occur (44)

Glu-243 of MMOH is the only amino acid that appears to alter its coordination mode and positioning as MMOH cycles through the different redox states of the reaction cycle according to both structural and computational experiments (40,41,43,45,46). For RNR-R2 and rubrerythrin, more than one iron-coordinating carboxylate and histidine alter their conformations, in addition to the residue analogous to Glu-243 (Figure 1.4). Asp-84 and Glu-204 of RNR-R2 shift between monodentate and bidentate coordination modes to Fe1 and Fe2, respectively, whereas His-56 and Glu-97 of rubrerythrin alternate their coordination to Fe1, depending on the oxidation state of the enzyme. In contrast to these enzymes, the analogous ligands in MMOH and ToMOH are fixed in position by second-sphere hydrogen bonding interactions and geometric constraints. These restraints are required presumably to preserve conformational rigidity for these residues within the active site. The relative flexibility and positioning of the carboxylates in these different diiron proteins may be critical to tuning the activity of their respective dimetallic cores.

One interesting feature of the MMOH and ToMOH four-helix bundles is that helix E has a π -helical segment in a region of the protein that contributes a glutamate ligand to the diiron center as well as several residues to the active site pocket (Figure 1.3). This 10 amino acid π -helix in the middle of a mostly α -helical stretch also occurs in RNR-R2, Δ^9 desaturase, CADD and rubrerythrin; it

is absent in ferritin, bacterioferritin and hemerythrin. The differences in helical structure may be of functional significance, but there is currently no clear understanding of such. The enzymes harboring the π -helical segment have highly flexible iron ligands. The adjacent metal centers typically experience ligand conformational changes and variable Fe–Fe distances in the different oxidation states. These changes presumably occur throughout the catalytic cycle. Helix E of RNR-R2 from *Samonella typhimurium nrd*, for instance, undergoes conformational rearrangements upon reduction of the protein that allow for greater solvent access to the diiron center (47). For bacterioferretin, ferretin and hemerythrin, the all α -helical nature of the four-helix bundle may reflect greater rigidity.

The Conserved Active Site Asparagine and Threonine Residues

The iron-coordinating ligands are not the only residues that undergo redox-dependent conformational changes. Asn-214 of MMOH, a highly conserved residue on helix E, sits 4.0 Å above Glu-243 on the α -subunit surface in a gap formed at the interface of helices E and F. Reduction of the dinuclear iron center induces the Asn-214 side chain to shift inward, towards the diiron center, to occupy a space formerly occupied by the C β and C γ carbon atoms of Glu-243 (Figure 1.5) (40). Similar motions are observed in the oxidized and Mn²⁺ reconstituted forms of ToMOH (48). Thr-213 is also a highly conserved residue, the side chain of which adopts alternate rotameric conformations in the active site of MMOH. Although these changes do not always appear to be redox-dependent, in most of the oxidized structures of MMOH the threonine hydroxyl group points toward the back of the hydrophobic substrate pocket, whereas in

reduced MMOH, it points toward the diiron center. The crystal structures of oxidized and reduced MMOH also exhibit several different solvent configurations in the active site involving hydrogen bonding to the terminal water on Fe1, Glu-243, Asn-214, and Thr-213. Based on these observations it has been proposed that Thr-213 and Asn-214 may participate in proton transfer events (40). Cytochrome P-450 monooxygenases have a similarly positioned threonine residue hovering just above the heme cofactor in the active site. This threonine is essential for catalysis and proposed to assist in proton transfer to stabilize O₂ intermediates (49-51). Mutating the analogous threonine to either a serine, alanine or glycine in toluene 4-monooxygenase (T4MO) did not significantly affect the turnover rate or the coupling of NADH consumption to product formation (52). Although this threonine is present in all known BMM hydroxylases, these findings suggest it is not critical for catalysis. The exact functions of the universally conserved threonine and asparagine in BMMs are poorly understood and warrant future investigation.

Hydrogen Bonding Networks

The second and third coordination spheres of the diiron center may be essential to the function of the enzyme. As stated above, some residues in this region provide conformational constraints to modify the geometry of the diiron center. One hydrogen bonding network in particular extends ~12-13 Å from iron-coordinating histidines through the four-helix bundle to the hydroxylase surface in the canyon region at helix A (Figure 1.6). In all BMMs, the residues contributing to this network are absolutely conserved, implicating this region as being essential for either the folding of α -subunit and assembly of the diiron center or electron transfer (32). Similar networks occur in RNR-R2, Δ^9 desaturase,

rubrerythrin and bacterioferretin and involve similar residues. In RNR-R2 a conserved tryptophan in the pathway is required to formation of the Fe(III)Fe(IV) X intermediate and the tyrosyl radical (53,54). These findings demonstrate how the second and third coordination shells in a diiron enzyme can assist in catalytic function. Structural and biophysical investigations of electron transfer events within proteins indicate that the maximum distance between electron donor and acceptor partners is $\sim 14 \text{ \AA}$ (55,56). The FeS_4 core of rubrerythrin and the cytochrome of bacterioferretin are both within 14 \AA distance of their respective diiron centers, near a hydrogen bonding network similar to those in BMMs and RNR-R2 and positioned behind the iron-coordinating histidines. The ability to clone and express recombinant forms of PH and TMO make this network an intriguing target for future site-directed mutagenesis experiments.

Substrate Access to the Diiron Center

BMMs must orchestrate the movements of substrate and products for efficient catalysis. One way by which this task may be accomplished is through cavities and channels in the α -subunit, which control the passage of small molecules to and from the dinuclear iron center. The MMOH α -subunit contains five major hydrophobic cavities, three of which lead from the active site pocket to the protein surface (Figure 1.7) (38). Although cavities are also present in the β - and γ -subunits, none of these appear to form a path towards the diiron center. Cavity 1 defines as the diiron active site pocket in the four-helix bundle. Except for the iron-coordinating ligands and Thr-213, the remaining residues in this pocket are hydrophobic. Leu-110, Phe-188 and Thr-213 form the barrier between cavities 1 and 2 and mark the access point between the four-helix bundle and the

rest of the α -subunit. Cavities 2-5 contain mostly hydrophobic residues and lead toward the northern regions of the hydroxylase. In the different crystal forms of MMOH Leu-110, adopts alternate rotameric conformations (38). Based on these observations Leu-110 was hypothesized to gate small molecule access between cavities 1 and 2. Structures of MMOH solved with substrate mimics like xenon, dibromomethane, and iodoethane bound in cavities 2 and 3 provided evidence to support the hypothesis that substrates use these cavities for active site access (57). Recent product binding studies revealed that haloalcohols bind preferentially to cavities 1, 2 and 3, implying that these three serve as the principal route for both substrate entrance to and product egress from the diiron center (58). Some of these bound substrates perturb the residues gating cavities 1-3 to allow unimpeded access between all three hydrophobic pockets. The point at which this "pseudo-channel" gains access to the surface is unknown.

Unlike MMOH, ToMOH has a 35-40 Å long channel that follows a similar path through the hydroxylase α -subunit to the surface (31). The entrance to the ToMOH channel is well defined and resides at the edge of the canyon region in the northern part of the protein. Mutagenesis studies on phenol hydroxylase, in which a key residue predicted to block access to its diiron center was converted to a smaller alanine residue, allowed for enhanced reactivity toward larger aromatic substrates of this BMM subfamily member (20), thus implying that PHs use a similar channel for substrate entrance and product egress. These findings indicate that cavities and channels are universal features of BMMs, important for small molecule movement to and from the dimetallic center. The key to substrate preference for a given enzyme may be highly dependent upon the

morphology of the access channel and cavity gates. For instance, the natural substrate of sMMOs is a small gaseous molecule whereas for TMOs and PHs, it is a larger aromatic. For gaseous substrates, hydrophobic cavities may be essential for sequestering a molecule like methane whereas a hydrophobic channel may be better suited for the efficient movement of aromatic compounds to and from the diiron center. Although, sMMOs can hydroxylate aromatics, TMOs and PHs are far more efficient at performing this reaction, perhaps because of easier substrate access.

An alternate entrance to the diiron center may be directly through helices E and F of the four-helix bundle. Surface calculations from both the MMOH and ToMOH structures show that access to the MMOH surface is blocked by only a single residue, Asn-214 (202 ToMOH). As discussed previously, this Asn adopts different conformations in the oxidized and reduced forms of MMOH and ToMOH, presumably due to a structural link between this residue and the shifting carboxylate of Glu-243 (Glu-231 ToMOH). This amino acid is closest to the Asn and it alters its coordination mode in the different oxidation states of the hydroxylase (40). In the reduced form, the positional change in Asn-214 results in the formation of a large crevice on the surface of the protein between helices E and F that extends toward the active site and (41), in one protomer of MMOH_{red} , forms a pore connecting the surface to the diiron center (58). These redox-dependent changes suggest that the residue may control the passage of small species like the protein, CH_4 , CH_3OH , H_2O and O_2 to and from the active site. Curiously, the analogous residue in *Samonella typhimurium* RNR-R2, Y163, also undergoes redox-dependent movements to allow greater solvent access to the

diiron center (47), suggesting perhaps a shared mechanism to accomplish some as yet undefined task in these closely related enzymes.

The Reductase and Rieske Proteins

BMMs have evolved two types of systems to transfer electrons from NADH to the hydroxylase (7,8). One system involves just a 38-40 kDa reductase having both an N-terminal ferredoxin domain (R_{Fd}) and a C-terminal FAD-containing (R_{FAD}) domain. The other system, found in TMOs and SsoMOs, requires a 12 kDa Rieske protein to mediate electron transfer from the reductase to the hydroxylase. NMR structures of the individual R_{FAD} and R_{Fd} domains from sMMO *M. capsulatus* (Bath) are available (59,60), but the structure of the full length protein revealing the packing of the two domains to one another is not. The individual domains of the BMM reductases have strong sequence homology to other reductases found in nature and are members of the modular ferredoxin:NADP⁺ oxidoreductase (FNR) family (8,32,60,61). X-ray crystal structures have been solved of two full-length reductases, phthalate dioxygenase reductase (PDR) and benzoate 1,2-dioxygenase reductase (BenC) (Figure 1.8) (62). Both of these proteins have a different organization of their primary structure with respect to the positioning of ferredoxin and FAD domains in the amino acid sequence, but the relationship between the two domains in the tertiary structures of the proteins is remarkably similar. Since BenC has an N-terminal ferredoxin domain and C-terminal FAD domain, this protein is predicted to resemble more closely reductases from BMMs and therefore serves as the best current model for the structure of full-length MMOR.

A structure of the 12 kDa T4MO Rieske (T4MOC) protein has been solved recently by NMR spectroscopy (63,64). Although the coordinates have not been released, the structure is predicted to resemble the biphenyl dioxygenase system ferredoxin protein, which is 50% homologous (33% identical) to T4MOC (Figure 1.8) (65). Biochemical characterization of T4MOC and ToMOC reveal spectroscopic properties identical to those of other Rieske proteins (21,34).

Electron transfer kinetics in the sMMO systems have been investigated in detail by using stopped-flow optical spectroscopy (66-69). Briefly, after the binding of NADH to MMOR, the first electron transfer event produces the two-electron reduced FAD hydroquinone (FADH⁻) and NAD⁺ (Figure 1.9). Following the release of NAD⁺, a one-electron transfer step produces the flavin semiquinone (FADH[•]) and the reduced [2Fe-2S] intermediates. Two successive electron transfer steps ultimately yield the reduced hydroxylase. The reduction potentials of the MMOR cofactors are not affected by the hydroxylase or regulatory protein components (67), however, the coupling protein (MMOB) and the reductase components do alter the redox potentials of the hydroxylase (Table 1.3) (70-75). In general, the binding of MMOB decreases the potentials of the diiron center by ~ 100-200 mV, making it harder to reduce, whereas the docking of MMOR restores the potentials to the level observed before MMOB binding to MMOH to favor reduction. Recent biochemical analysis of the effects of MMOB and MMOR on intermolecular electron-transfer suggests that slow and fast pathways exist, depending upon the relative conformations of MMOH (69). The presence of MMOB favors the slow electron transfer pathway, whereas MMOH-MMOR complex formation in the absence of MMOB increases the population of

the hydroxylase in the fast electron-transfer conformation. The changes in the redox potentials induced by reductase binding indicate that this component may influence the structure of the hydroxylase or hydroxylase-effector protein complex. Despite alterations in the redox potentials of MMOH, MMOR does not influence the spectroscopic properties of the diiron site in the hydroxylase (9). Maximal steady-state activity and coupling *in vitro* is achieved with 0.5 equivalents of MMOR for every equivalent of MMOH (66). Although MMOR has a binding affinity for MMOH similar to that of MMOB and can dock to two possible sites on a single hydroxylase molecule, these findings indicate that MMOR binds transiently to the hydroxylase and that one reductase services multiple diiron centers. Similar observations have been made on the reconstituted toluene-4 and toluene/*o*-xylene monooxygenase systems (21,34).

The kinetics of electron transfer for the four-component monooxygenase systems have yet to be worked out. Although it is unknown why these families require an additional component, the Rieske protein may be necessary because the reduction potentials are different in the four-component alkane/aromatic monooxygenase subfamily. Alternatively, it has been postulated that the fourth component may be necessary to regulate NADH consumption by a host organism, since multiple reductase proteins in the same species could cross-react with different electron acceptors (8). This more complicated four-component system may therefore limit the wasteful consumption of NADH. Optimal steady state activity for the four-component T4MO and ToMO systems is achieved when two equivalents of the Rieske protein and substoichiometric amounts of the reductase are present for every hydroxylase (21,34).

The Regulatory Protein

Every known BMM requires a 10-16 kDa cofactorless regulatory protein for efficient catalysis (7,8,32). When this effector is complexed to the hydroxylase, the reactivity of the sMMO, PH, and T4MO diiron centers with hydrocarbons increases by 150-, 28-, 120-fold, respectively (33,76,77). The steady-state activity and the coupling of NADH consumption to substrate hydroxylation are most efficient when approximately one regulatory protein is present for each $\alpha\beta\gamma$ protomer (21,66,77,78). At lower regulatory protein:hydroxylase ratios, coupling efficiency decreases whereas, at higher ratios, the steady-state activity decreases. It has been demonstrated with the sMMO system from *Methylococcus capsulatus* (Bath) that the regulatory protein does not compete for the reductase binding sites, ruling out competitive inhibition as an explanation for the unknown decrease in activity at higher concentrations of the coupling protein (66). The large increase in activity when the regulatory protein and the hydroxylase are combined suggests that inactive and active forms of the hydroxylase exist in solution. Binding of the effector component thus shifts the relative population of hydroxylase molecules towards that active conformation of the enzyme. At present, only structural information is available for the inactive form of some BMM hydroxylases. The precise structural and chemical impact of the effector protein on the hydroxylase is essential for our understanding of BMM function and remains one of the biggest challenges facing research on these enzymes.

Structure of the Regulatory Protein

NMR structures of MMOB from *M. capsulatus* (Bath) and *M. trichosporium* (OB3b) have been determined, as well as those of the phenol hydroxylase P2

protein (DmpM) from *Pseudomonas sp.* CF600 and the toluene 4-monooxygenase (T4MOD) regulatory protein from *Pseudomonas medonica* KR1 (Figure 1.10) (79-83). In general, the coupling proteins are organized into a structured 80-95 amino acid core with flexible N- and C- terminal regions of variable length. The global folds of the four effector proteins differ slightly from each other despite having relatively good sequence similarity. The fold of *M. trichosporium* MMOB differs from that of *M. capsulatus* MMOB, having a more opened core due to the lack of helix-helix contacts which are present in the *M. capsulatus* structure. These structural differences are unexpected, considering that the sequence identity between the two is greater than 90%. The fold of T4MOD is more similar to that of *M. capsulatus* MMOB since it has these helix-helix contacts. DmpM adopts a different fold, more similar to that of *M. trichosporium* MMOB in which the protein core appears to have an open conformation. Secondary structure comparisons of the different NMR structures indicate that the global topology of the coupling protein from the different BMM families should be similar. The different tertiary folds observed in these NMR structures suggest that key constraints, required for a more accurate structure of the *M. trichosporium* MMOB and DmpM proteins, are missing. Such constraints for proteins that are inherently flexible are often difficult to obtain, however. The differences between these structures suggest that, under certain conditions the cores of the coupling proteins are relatively flexible. Preliminary reports of the X-ray structures of T4MOD indicate that the core of this protein can adopt at least three different conformations (84), thus lending further support to the possibility that the differences in the NMR structures are real. Flexibility in the

regulatory protein may allow it adopt different conformations when free in solution and bound to the hydroxylase.

Function of the Effector Protein N-terminus

The lengths of the N- and C-termini differ between the BMM effector proteins. Mutagenesis and proteolysis studies aimed at determining the functions of the termini have demonstrated that the BMMs systems use these segments differently. For sMMO proteins, the 35 amino acid N-terminus is critical to the function of the enzyme. Cleavage of the N-terminal region of MMOB from *M. capsulatus* (Bath) before residue 14 produces an inactive form of the protein, termed B', that binds to MMOH with slightly decreased affinity (70,85-87). It is incapable of altering the redox potentials of the hydroxylase diiron center, possibly because it cannot induce the necessary structural changes in MMOH (70). Reduced MMOH from *M. trichosporium* (OB3b) is unable to react with dioxygen when complexed to an MMOB deletion mutant (MMOB Δ 29) in which the first 29 amino acids are removed (80). The addition of the 29 amino acid N-terminal peptide to the complex between *M. trichosporium* (OB3b) MMOH and MMOB Δ 29 did not restore activity. CD and NMR spectroscopy confirmed that the deletion of this region does not alter the structure of the MMOB core. An *M. capsulatus* (Bath) MMOB deletion mutant lacking only the first five amino acids is active (88). By process of elimination, residues 6-13, which comprise the conserved amino acid sequence N₆AYXAGXX₁₃, may therefore be essential for the function of MMOB and for inducing the necessary structural changes in the hydroxylase. N-terminal residues closer to the core of MMOB are also important for catalytic function. Mutation of a conserved histidine at position 33 to an

alanine lead to a > 50-fold decrease in the formation rate of the diiron(III) peroxo intermediate (89). Given these findings, it is apparent that the MMOB N-terminus is absolutely critical to the catalytic function of sMMOs. The C-terminus of MMOB is less important for catalysis, despite having several conserved residues (88).

In contrast to MMOB, the regulatory proteins from the phenol hydroxylase and toluene monooxygenase enzyme systems do not require the N-terminal residues. For PHs, the N-terminus of the coupling protein is only 3-4 amino acids, most of which are not conserved (32). Deletion of the first 10 amino acids of the 16-amino acid T4MOD N-terminus affords an active protein with decreased affinity for the hydroxylase and which does not significantly affect the product distributions or the coupling of the enzyme system (90). Based on the apparent differences between the sMMO, PH, and TMO regulatory proteins, it is clear that each system has evolved different means by which to activate their respective hydroxylases.

Affects of the Regulatory Protein on the Hydroxylase

The regulatory protein has been investigated extensively to gain insight into the key structural and chemical changes this component induces near or at the diiron center of the hydroxylase to enhance the reactivity of the enzyme with dioxygen and hydrocarbons. These investigations revealed that the regulatory protein does not do just one thing to stimulate activity, but rather it induces multiple changes, which include altering the spectroscopic and redox properties of the hydroxylate diiron center and influencing the regiospecificity of the active site pocket. All of these different effects must somehow correspond to a set of

key structural changes induced by the binding of the regulatory protein to the hydroxylase.

X-ray absorption spectroscopy (XAS) is the most direct non-crystallographic method by which to determine whether the coupling protein induces gross structural changes in the diiron center in both its oxidized and reduced states. Early work on MMOH from *Methylococcus capsulatus* (Bath) and *Methylosinus trichosporium* (OB3b) revealed that MMOB has no remarkable affect on the XAS spectra or fitting parameters, indicating that this protein does not significantly perturb the iron environment in either the oxidized or reduced states of the protein (91,92). Recent advances in XAS methodology have allowed for the re-exploration of this question by using better model compounds and computational simulations (36,93). Oxidized and reduced MMOH from *M. capsulatus* (Bath) are now best fit by a single population of metal centers with Fe-Fe distances of 3.1 Å and 3.3 Å, respectively, a result that agrees better with the bulk of the crystallographic data on MMOH. The addition of the regulatory protein to reduced MMOH again does not change the structure of the diiron center, but, the Debye-Waller factors, which are a measure of thermal disorder for a fit atom, decrease. This finding indicates that binding of the regulatory protein to the hydroxylase serves to limit the flexibility or motion of the metal coordinating ligands.

Circular dichroism (CD) and magnetic circular dichroism (MCD) spectroscopic study of reduced MMOH from *Methyosinus trichosporium* (OB3b) indicates that the presence of MMOB alters the ligand field environment of only one of the Fe atoms (94). The other Fe atom is perturbed by substrates and inhibitors but only when MMOB is bound to the hydroxylase. Comparisons

between the different crystal structures of MMOH in its oxidized, mixed-valent and reduced states indicate that the position of Fe2 and its ligands vary the most from structure to structure, whereas Fe1 and its associated ligands do not move. Based on this analysis and the crystallographic B-factors, it is hypothesized that Fe2, the iron closest to the canyon surface, is most likely perturbed by MMOB, whereas Fe1 associates more readily with bound small molecules (40).

MMOH_{ox} has two high-spin Fe(III) ions that are antiferromagnetically coupled to form an EPR silent, diamagnetic diiron(III) center at 4.2 K. Cryoreduction of the diferric center by γ -irradiation at 77 K, which produces an EPR active mixed-valent Fe(III)Fe(II) dimetallic center with an $S=1/2$ spin state that maintains the structure of MMOH, has allowed for more detailed investigations of the physiologically relevant oxidized form of MMOH vis-a-vis that of the mixed-valent state, which is not a true intermediate based on our current understanding (95-97). EPR spectroscopy indicates MMOB has no effect on the oxidized diiron(III) cluster of MMOH, but, when MMOH_{ox} is complexed to products like methanol and phenol, MMOB does induce spectral changes (95). Products by themselves do not alter the EPR spectra of cryoreduced MMOH_{ox}. Moreover, MMOB favors DMSO and glycerol binding to MMOH_{ox}, whereas in its absence, the binding of these molecules is undetectable. For chemically reduced mixed-valent MMOH, MMOB can induce a spectral change in the $g = 1.84$ signal, indicating that it can alter the magnetic coupling of the Fe(III)Fe(II) metal center (76). It is unknown how MMOB may influence the structure of MMOH to induce these spectral changes or influence small molecule binding. The fully reduced Fe(II)Fe(II) MMOH has a characteristic $g = 16$ signal that is not altered significantly in the presence of MMOB, however (76,98-101).

Like MMOR, MMOB alters the redox potentials of the diiron center (Table 1.3) (70-75). Studies conducted on the *M. capsulatus* and *M. trichosporium* sMMO systems by using different experimental techniques have yielded potentials that vary considerably, making their interpretation very difficult. Qualitatively, it appears MMOB docking shifts the reduction potentials ~100-200 mV in the negative direction to disfavor electron transfer to the hydroxylase, whereas the addition of MMOR to the MMOH-MMOB complex moves the redox potentials in the opposite direction to restore the values to a level similar to or above that of MMOH alone. The changes in reduction potentials induced by different protein components indicate some unknown structural event occurs to influence the dinuclear iron center or its nearby environment.

The regulatory proteins from sMMO and T4MO also alter the substrate regiospecificities of the hydroxylase-catalyzed reactions (18,102). In the sMMO system without MMOB, primary alcohols and *m*-nitrophenol are the preferred products of alkane and nitrobenzene hydroxylation (102). The addition MMOB shifts the product ratios such that mostly secondary alcohols and *p*-nitrophenol are formed. The addition of 0.2 equivalents of MMOB per molecule of MMOH results in the same product distribution as adding 2 equivalents of MMOB, although the catalytic rates vary significantly. It was proposed that MMOB, like MMOR, has a historesis effect on MMOH, whereby the conformational changes induced by MMOB last long enough to produce the expected product ratio from the fully active system containing two MMOB molecules per MMOH. Similar changes in product regiospecificities are observed in the toluene 4-monooxygenase system where, upon the addition of T4MOD, the yield of *p*-cresol formation shifts from 69% to 96% (77). Mutagenesis studies on T4MOH in combination

with product analysis using toluene and alternative aromatic compounds as substrates indicate that the position of the universally conserved active site threonine, (T213 MMOH) is critical for influencing the distribution of products (52,77). The product ratio differences in the absence and presence of T4MOD indicate that the positioning of Thr-201, which resides on helix E of the four-helix bundle, is influenced directly by the regulatory protein. These findings are the first to suggest exactly where the regulatory protein may influence the structure of the hydroxylase.

The Big Picture: Component Interactions

The BMM hydroxylase component is a multi-subunit docking platform onto which the other essential protein components bind. Little information is available about the regulatory protein and reductase/Rieske protein docking sites on the hydroxylase. However, the available body of data are beginning to reveal where the likely binding positions for MMOR and MMOB are on the surface of MMOH. Each hydroxylase can accommodate up to two equivalents of the regulatory and reductase (or Rieske) components, although maximal activity is achieved with substoichiometric amounts of reductase (21,34,76,78). Isothermal titration calorimetry, gel filtration and chemical cross-linking experiments indicate that, in the sMMO system, MMOB and MMOR neither interact with each other when free in solution nor compete for the same binding site on MMOH (66,76). It is unknown whether the two proteins are in contact when they are actually docked onto MMOH.

Chemical cross-linking experiments indicate that the sMMO and PH regulatory proteins interact with the hydroxylase α -subunit (76,78). Changes in

the spectroscopic, redox, and regiospecificity properties of the hydroxylase suggest that the coupling protein binds in the vicinity of the diiron center, although long range structural perturbations cannot be ruled out. Saturation recovery EPR spectroscopy using spin-labeled MMOB, and more recent chemical cross-linking experiments in conjunction with mass spectrometry, place the MMOB binding site in the MMOH canyon region near helices E and F of the four-helix bundle (103,104). Several conserved residues on the MMOB surface experience NMR line broadening in the presence of MMOH. These include residues 22-26 in the N-terminus and E53, E94, L96, G97, F100, and D108 in the protein core, all of which define a face of the protein that may lie flush against the surface of the α -subunit (83). The line-broadened residues in the core of MMOH are conserved among the other BMM coupling proteins, implying that the regulatory proteins employ a similar binding face despite differences in the function of their N-termini.

Initial chemical-cross linking studies between MMOR and MMOH indicated that the reductase component binds to the β -subunit (76). More recently, cross-linking studies using just the MMOR ferredoxin domain suggest that the primary interaction is actually with the MMOH α -subunit (105). NMR line broadening experiments on the ferredoxin domain in the presence of MMOH indicate that the amino acids located on the face of the protein containing the [2Fe-2S] cluster pack against the hydroxylase surface (60). These regions, which center around the [2Fe-2S] cluster, include helices α_1 and α_2 (Figure 1.8). A synthetic peptide comprising residues 24-34 of helix α_1 was found previously to inhibit catalysis (38), a finding that is in agreement with the NMR

data. The current results imply that the underside of the ferredoxin domain lies flush against the hydroxylase surface. Comparisons to the homologous diiron proteins rubrerythrin and bacterioferretin, as well as to other proteins containing redox donor and acceptor cofactors, suggest that the [2Fe-2S] cluster should be within 14 Å of the diiron center when docked to MMOH (55,56,106,107). The application of theory to kinetic data for the intermolecular electron transfer events between MMOR and MMOH suggest that the [2Fe-2S] cluster lies approximately 11.0 Å from the dinuclear center of MMOH (69). Such a distance places the Fd domain on the α -subunit, possibly near the hydrogen bonding network that leads to the canyon surface (Figure 1.6a). Based on all of the findings described above, a hypothetical docking model of the MMOH-MMOB-MMOR complex is presented in Figure 1.11.

Reaction Cycle of Bacterial Multicomponent Monooxygenases

The most extensively studied BMM mechanism is that of sMMO from *Methylococcus capsulatus* (Bath) and *Methylosinus trichosporium* (OB3b). Although the other BMMs may use a slightly different mechanism and intermediates, we assume here they are similar to sMMO since their dimetallic centers are predicted or known to be nearly identical. The following reaction cycle is proposed, based on numerous structural, spectroscopic and computational studies.

The resting state of the enzyme is the oxidized diiron(III) form, MMOH_{ox} (30,38). Upon the binding of MMOB and MMOR, two electrons and two protons are transferred to the diiron center to generate the fully reduced Fe(II)Fe(II) dinuclear iron center, MMOH_{red} (37,40). The result of this process is a shift in the

Glu-243 carboxylate to occupy a bridging position between the irons and the formation of a bidentate chelating interaction with Fe₂, as described above.

The first spectroscopically observed intermediate upon introduction of O₂ is a diiron(III) peroxo species, MMOH_{peroxo} (108-110), which has been characterized by Mössbauer and UV-vis spectroscopy. It is predicted by DFT calculations to have a μ - η^2 : η^2 geometry with an Fe-Fe distance of ~ 3.6 Å, although resonance Raman spectroscopy has identified μ -1,2 peroxo diiron(III) intermediates in the homologous diiron centers of Δ^9 desaturase, a D84E mutant of RNR-R2, and ferretin (111-113). Stopped-flow kinetics on *M. trichosporium* sMMO in conjunction with EPR spectroscopy, monitoring the disappearance of the MMOH_{red} g 16 signal, indicate that at least one transient species must precede the peroxo intermediate (114). This O₂-binding intermediate has yet to be observed spectroscopically. DFT calculations suggest that two short lived intermediates, MMOH_{red}-primed and MMOH_{superoxo} may be required before O₂ coordination and generation of H_{peroxo} respectively (43).

As revealed by studies of substrates such as propylene or methyl vinyl ether, H_{peroxo} can epoxidize olefins (108,115). In the absence of such an electron rich substrate, H_{peroxo} converts to the di-(μ -oxo)-diiron(IV) intermediate Q, which is the species responsible for activating C-H bonds of hydrocarbons. This intermediate, which has been characterized by UV-vis, XAS, and Mössbauer spectroscopy, has an absorption maximum at 430 nm and a short Fe-Fe distance of 2.6 Å (108,114,116-118). The nature of C-H bond activation by Q has been the subject of much debate. Two mechanisms have been proposed, a concerted reaction in which one of the bridging O-atoms is inserted into a C-H bond and a

radical recoil/rebound reaction in which a hydrogen is abstracted from the substrate and the short-lived radical species recombines with the bridging OH (119). The final intermediate is the product bound state, $H_{product}$. Crystallographic studies in conjunction with EPR and ENDOR spectroscopy indicate that alcohol products bind to the bridging position between the iron atoms (41,95,120). This finding supports the proposal that C–H bond activation occurs at the bridging oxygen of intermediate Q, which faces the substrate cavity. It is unknown whether product leaves before the diiron center is reduced or if reduction induces product dissociation to restart the catalytic cycle. Based on theory, the former is energetically very favorable (45).

One of the biggest challenges to understanding the mechanism of hydrocarbon oxidation in BMMs is correlating the structure of the component complexes with the movements of the amino acids at the active site at each stage of the reaction cycle. The redox-dependent positional changes of Asn-214, the need for controlled movement of substrates and products into and out of the active site, and the component-induced conformational changes suggest that the hydroxylase structure, even beyond the diiron center, is in flux through out the catalytic cycle.

References

1. Corrondo, M. A. (2003) *EMBO J.* **22**, 1959-1968.
2. Stenkamp, R. E. (1994) *Chem. Rev.* **94**, 715-726.
3. Stubbe, J., and van der Donk, W. A. (1995) *Chem. Biol.* **2**, 793-801.
4. Kurtz, D. M. Jr. (2003) *Biochem. Biophys. Anaer. Bacteria*, 128-142.
5. Schwarzenbacher, R., Stenner-Liewen, F., Liewen, H., Robinson, H., Yuan, H., Bossy-Wetzell, E., Reed, J. C., and Liddington, R. C. (2004) *J. Biol. Chem.* **279**, 29320-29324.
6. Lindqvist, Y., Huang, W., Schneider, G., and Shanklin, J. (1996) *EMBO J.* **15**, 4081-4092.
7. Notomista, E., Lahm, A., Di Donato, A., and Tramontano, A. (2003) *J. Mol. Evol.* **56**, 435-445.
8. Leahy, J. G., Batchelor, P. J., and Morcomb, S. M. (2003) *FEMS Micro. Rev.* **27**, 449-479.
9. Merckx, M., Kopp, D. A., Sazinsky, M. H., Blazyk, J. L., Müller, J., and Lippard, S. J. (2001) *Angew. Chem. Int. Ed.* **40**, 2783-2807.
10. Green, J., and Dalton, H. (1989) *J. Biol. Chem.* **264**, 17698-17703.
11. Colby, J., Stirling, D. I., and Dalton, H. (1977) *Biochem. J.* **165**, 395-402.
12. Kotani, T., Yamamoto, T., Yurimoto, H., Sakai, Y., and Kato, N. (2003) *J. Bacteriol.* **185**, 7120.
13. Hanson, R. S., and Hanson, T. E. (1996) *Microbiol. Rev.* **60**, 439-471.
14. Widada, J., Nojiri, H., and Omori, T. (2002) *Appl. Microb. Biotech.* **60**, 45-59.
15. Little, C. D., Palumbo, A. V., Herbes, S. E., Lindstrom, M. E., Tyndall, R. I., and Gilmer, P. J. (1988) *Appl. Environ. Microb.* **54**, 951-956.
16. Sardesai, Y., and Bhosle, S. (2002) *Res. Microbiol.* **153**, 263-268.

17. Steffan, R. J., and McClay, K. R. (2000), patent no. WO 2000073425, US.
18. Pikus, J. D., Studts, J. M., McClay, K., Steffan, R. J., and Fox, B. G. (1997) *Biochemistry* **36**, 9283-9289.
19. McClay, K., Fox, B. G., and Steffan, R. J. (2000) *Appl. Environ. Microbiol.* **66**, 1877-1882.
20. Canada, K. A., Iwashita, A., Shim, H., and Wood, T. K. (2002) *J. Bacteriol.* **184**, 344-349.
21. Cafaro, V., Scognamiglio, R., Viggiani, A., Izzo, V., Passaro, I., Notomista, E., Dal Piaz, F., Amoresano, A., Casbarra, A., Pucci, P., and Di Donato, A. (2002) *Eur. J. Biochem.* **269**, 5689-5699.
22. Studts, J. M., Mitchell, K. H., Pikus, J. D., McClay, K., Steffan, R. J., and Fox, B. G. (2000) *Protein Expr. Purif.* **20**, 58-65.
23. Vardar, G., and Wood, T. K. (2004) *Appl. Environ. Microbiol.* **70**, 3253-3262.
24. Rui, L., Kwon, Y. M., Fishman, A., Reardon, K. F., and Wood, T. K. (2004) *Appl. Environ. Microbiol.* **70**, 3246-3252.
25. Leahy, J. G., Batchelor, P. J., and Morcomb, S. M. (2003) *FEMS Microbiol. Rev.* **27**, 449-479.
26. Gallagher, S. C., Cammack, R., and Dalton, H. (1997) *Eur. J. Biochem.* **247**, 635-641.
27. Gallagher, S. C., Cammack, R., and Dalton, H. (1999) *Biochem. J.* **339**, 79-85
28. Powlowski, J., Sealy, J., Shingler, V., and Cadieux, E. (1997) *J. Biol. Chem.* **272**, 945-951.
29. Merkx, M., and Lippard, S. J. (2001) *J. Biol. Chem.* **277**, 5858-5865.
30. Rosenzweig, A. C., Frederick, C. A., Lippard, S. J., and Nordlund, P. (1993) *Nature* **366**, 537-543.

31. Sazinsky, M. H., Bard, J., Di Donato, A., and Lippard, S. J. (2004) *J. Biol. Chem.* **279**, 30600-30610.
32. Coufal, D. E., Blazyk, J. L., Whittington, D. A., Wu, W. W., Rosenzweig, A. C., and Lippard, S. J. (2000) *Eur. J. Biochem.* **267**, 2174-2185.
33. Cadieux, E., Vrajmasu, V., Achim, C., Powlowski, J., and Münck, E. (2002) *Biochemistry* **41**, 10680-10691.
34. Pikus, J. D., Studts, J. M., Achim, C., Kauffmann, K. E., Münck, E., Steffan, R. J., McClay, K., and Fox, B. G. (1996) *Biochemistry* **35**, 9106-9119.
35. Kurtz, D. M. (1997) *J. Biol. Inorg. Chem.* **2**, 159-167.
36. Jackson Rudd, D., Sazinsky, M. H., Merckx, M., Lippard, S. J., Hedman, B., and Hodgson, K. O. (2004) *Inorg. Chem.* **43**, 4579-4589.
37. Rosenzweig, A. C., Nordlund, P., Takahara, P. M., Frederick, C. A., and Lippard, S. J. (1995) *Chem. Biol.* **2**, 409-418.
38. Rosenzweig, A. C., Brandstetter, H., Whittington, D. A., Nordlund, P., Lippard, S. J., and Frederick, C. A. (1997) *Proteins* **29**, 141-152.
39. Elango, N., Radhakrishnan, R., Froland, W. A., Wallar, B. J., Earhart, C. A., Lipscomb, J. D., and Ohlendorf, D. H. (1997) *Prot. Sci.* **6**, 556-568.
40. Whittington, D. A., and Lippard, S. J. (2001) *J. Am. Chem. Soc.* **123**, 827-838.
41. Whittington, D. A., Sazinsky, M. H., and Lippard, S. J. (2001) *J. Am. Chem. Soc.* **123**, 1794-1795.
42. Högbom, M., Stenmark, P., Voevodskaya, N., McClarty, G., Gräslund, A., and Nordlund, P. (2004) *Science* **305**, 245-248.
43. Gherman, B. F., Baik, M.-H., Lippard, S. J., and Friesner, R. A. (2004) *J. Am. Chem. Soc.* **126**, 2978-2990.
44. Yoon, S., Kelly, A. E., and Lippard, S. J. (2004), Submitted for publication

45. Dunietz, B. D., Beachy, M. D., Cao, Y., Whittington, D. A., Lippard, S. J., and Friesner, R. A. (2000) *J. Am Chem. Soc.* **122**, 2828-2839.
46. Gherman, B. J., Dunietz, B. D., Whittington, D. A., Lippard, S. J., and Friesner, R. A. (2001) *J. Am Chem. Soc.* **123**, 3836-3837.
47. Eriksson, M., Jordan, A., and Eklund, H. (1998) *Biochemistry* **37**, 13359-13369
48. McCormick, M. S., Sazinsky, M. H., and Lippard, S. J. Unpublished results.
49. Imai, M., Shimada, H., Watanabe, Y., Matsushima-Hibiya, Y., Makino, R., Koga, H., Horiuchi, T., and Ishimura, Y. (1989) *Proc. Natl. Acad. Sci. U.S.A.* **86**, 7823-7827.
50. Martinis, S. A., Atkins, W. A., Stayton, P. S., and Sligar, S. G. (1989) *J. Am Chem. Soc.* **111**, 9252-9253.
51. Yeom, H., Sligar, S. G., Li, H., Poulos, T. L., and Fulco, A. (1995) *Biochemistry* **34**, 14733-14740.
52. Pikus, J. D., Mitchell, K. H., Studts, J. M., McClay, K., Steffan, R. J., and Fox, B. G. (2000) *Biochemistry* **39**, 791-799.
53. Baldwin, J., Krebs, C., Ley, B. A., Edmondson, D. E., Huynh, B. H., and Bollinger, J. M., Jr. (2000) *J. Am. Chem. Soc.* **112**, 12195-12206.
54. Krebs, C., Chen, S., Baldwin, J., Ley, B. A., Patel, U., Edmondson, D. E., Huynh, B. H., and Bollinger, J. M., Jr. (2000) *J. Am. Chem. Soc.* **122**, 12207-12219.
55. Page, C. C., Moser, C. C., and Dutton, P. L. (2003) *Curr. Opin. Chem. Biol.* **7**, 551-556.

56. Page, C. C., Moser, C. C., Chen, X., and Dutton, P. L. (1999) *Nature* **402**, 47-52
57. Whittington, D. A., Rosenzweig, A. C., Frederick, C. A., and Lippard, S. J. (2001) *Biochemistry* **40**, 3476-3482
58. Sazinsky, M. H., and Lippard, S. J. Manuscript in preparation
59. Chatwood, L., Müller, J., Gross, J., Wagner, G., and Lippard, S. J. (2004) *Biochemistry*, **43**, in press.
60. Müller, J., Lugovskoy, A. A., Wagner, G., and Lippard, S. J. (2002) *Biochemistry* **41**, 42-51.
61. Blazyk, J. L., and Lippard, S. J. (2004) *J. Biol. Chem.* **2004**, 5630-5640.
62. Correll, C. C., Batie, C. J., Ballou, D. P., and Ludvig, M. L. (1992) *Science* **258**, 1604-1609.
63. Skjeldal, L., Peterson, F. C., Moe, L. A., Pikus, J. D., Doreleijers, J. F., Volkman, B. F., Westler, W. M., Markley, J. L., and Fox, B. G. Manuscript in preparation.
64. Wei, L., Moe, L. A., Skjeldal, L., Pikus, J. D., Jeremie, D., Markley, J. L., and Fox, B. G. (2001) *J. Biomolec. NMR* **21**, 73-74.
65. Colbert, C. L., Couture, M. M.-J., Eltis, L. D., and Bolin, J. T. (2000) *Structure* **8**, 1267-1278.
66. Gassner, G. T., and Lippard, S. J. (1999) *Biochemistry* **38**, 12768-12785
67. Kopp, D. A., Gassner, G. T., Blazyk, J. L., and Lippard, S. J. (2001) *Biochemistry* **40**, 14932-14941.
68. Blazyk, J. L., and Lippard, S. J. (2002) *Biochemistry* **41**, 15780-15794
69. Blazyk, J. L. (2003), Ph. D. thesis, Department of Chemistry, Massachusetts Institute of Technology.

70. Kazlauskaitė, J., Hill, H. A. O., Wilkins, P. C., and Dalton, H. (1996) *Eur. J. Biochem.* **241**, 552-556.
71. Liu, K. E., and Lippard, S. J. (1991) *J. Biol. Chem.* **266**, 12836-12839.
72. Liu, Y., Nesheim, J. C., Paulsen, K. E., Stankovich, M. T., and Lipscomb, J. D. (1997) *Biochemistry* **36**, 5223-5233.
73. Paulsen, K. E., Liu, Y., Fox, B. G., Lipscomb, J. D., Münck, E., and Stankovich, M. T. (1994) *Biochemistry* **33**, 713-722.
74. Woodland, M. P., Patil, D. S., Cammack, R., and Dalton, H. (1986) *Biochim. Biophys. Acta* **873**, 237-242.
75. Liu, K. E., and Lippard, S. J. (1995) *Adv. Inorg. Chem.* **42**, 263-289.
76. Fox, B. G., Liu, Y., Dege, J. E., and Lipscomb, J. D. (1991) *J. Biol. Chem.* **266**, 540-550.
77. Mitchell, K. H., Studts, J. M., and Fox, B. G. (2002) *Biochemistry* **41**, 3176-3188.
78. Cadieux, E., and Powlowski, J. (1999) *Biochemistry* **38**, 10714-10722.
79. Chang, S.-L., Wallar, B. J., Lipscomb, J. D., and Mayo, K. H. (1999) *Biochemistry* **38**, 5799-5812.
80. Chang, S., Wallar, B. J., Lipscomb, J. D., and Mayo, J. D. (2001) *Biochemistry* **40**, 9539-9551.
81. Hemmi, H., Studts, J. M., Chae, Y. K., Song, J., Markley, J. L., and Fox, B. G. (2001) *Biochemistry* **40**, 3512-3524.
82. Qian, H., Edlund, U., Powlowski, J., Shingler, V., and Sethson, I. (1997) *Biochemistry* **36**, 495-504.
83. Walters, K. J., Gassner, G. T., Lippard, S. J., and Wagner, G. (1999) *Proc. Natl. Acad. Sci. USA* **96**, 7877-7882.

84. Orville, A. M., Studts, J. M., Lountos, G. T., Mitchell, K. H., and Fox, B. G. (2003) *Acta Cryst. D* **D59**, 572-575.
85. Lloyd, J. S., Bhambra, A., Murrell, J. C., and Dalton, H. (1997) *Eur. J. Biochem.* **248**, 72-79.
86. Brandstetter, H., Whittington, D. A., Lippard, S. J., and Frederick, C. A. (1999) *Chem. Biol.* **6**, 441-449.
87. Chang, S.-L., Wallar, B. J., Lipscomb, J. D., and Mayo, K. H. (2001) *Biochemistry* **40**, 9539-9551.
88. Zhu, K., Sazinsky, M. H., Pozharski, E., MacArthur, R., Riku, S., Lippard, S. J., and Brudvig, G. W. Manuscript in preparation.
89. Wallar, B. J., and Lipscomb, J. D. (2001) *J. Am Chem. Soc.* **40**, 2220-2233.
90. Mitchell, K. H. (2002), Ph.D. thesis, Department of Biochemistry, University of Wisconsin-Madison, Madison.
91. Dewitt, J. G., Rosenzweig, A. C., Salifoglou, A., Hedman, B., Lippard, S. J., and Hodgson, K. O. (1995) *Inorg. Chem.* **34**, 2505-2515.
92. Shu, L., Lui, Y., Lipscomb, J. D., and Que, L. J. (1996) *J. Biol. Inorg. Chem.* **1**, 297-304.
93. Jackson Rudd, D., Sazinsky, M. H., Lippard, S. J., Hedman, B., and Hodgson, K. O. (2004) Manuscript in preparation.
94. Pulver, S. C., Froland, W. A., Lipscomb, J. D., and Solomon, E. I. (1997) *J. Am. Chem. Soc.* **119**, 387-395.
95. Davydov, R., Valentine, A. M., Komar-Panicucci, S., Hoffman, B. M., and Lippard, S. J. (1999) *Biochemistry* **38**, 4188-4197.
96. Davydov, R. M., Menage, S., Fontecave, M., Graslund, A., and Ehrenberg, A. (1997) *J. Biol. Inorg. Chem.* **2**, 242-255.

97. Davydov, R. M., Smieja, J., Dikanov, S. A., Zang, Y., Que, L., and Bowman, M. K. (1999) *J. Biol. Inorg. Chem.* **4**, 292-301.
98. Dewitt, J. G., Bentsen, J. G., Rosenzweig, A. C., Hedman, B., Green, J., Pilkington, S., Papaefthymiou, G. C., Dalton, H., Hodgson, K. O., and Lippard, S. J. (1991) *J. Am. Chem. Soc.* **113**, 9219-9235.
99. Fox, B. G., Surerus, K. K., Munck, E., and Lipscomb, J. D. (1988) *J. Biol. Chem.* **263**, 10553-10556.
100. Fox, B. G., Hendrich, M. P., Surerus, K. K., Andersson, K. K., Froland, W. A., Lipscomb, J. D., and Munck, E. (1993) *J. Am. Chem. Soc.* **115**, 3688-3701.
101. Hendrich, M. P., Munck, E., Fox, B. G., and Lipscomb, J. D. (1990) *J. Am. Chem. Soc.* **112**, 5861-5865.
102. Froland, W. A., Andersson, K. K., Lee, S. K., Liu, Y., and Lipscomb, J. D. (1992) *J. Biol. Chem.* **267**, 17588-17597.
103. MacArthur, R., Sazinsky, M. H., Kühne, H., Whittington, D. A., Lippard, S. J., and Brudvig, G. W. (2002) *J. Am. Chem. Soc.* **124**, 13392-13393.
104. Brazeau, B. J., Wallar, B. J., and Lipscomb, J. D. (2003) *Biochem. Biophys. Res. Comm.* **312**, 143-148.
105. Kopp, D. A., Berg, E. A., Costello, C. E., and Lippard, S. J. (2003) *J. Biol. Chem.* **2003**, 20939-20945.
106. deMare, F., Kurtz, D. M. J., and Nordlund, P. (1996) *Nat. Struct. Biol.* **3**, 539-546.
107. Frolow, F., Kalb, A. J., and Yariv, J. (1994) *Nat. Struct. Biol.* **1**, 453.
108. Valentine, A. M., Stahl, S. S., and Lippard, S. J. (1999) *J. Am. Chem. Soc.* **121**, 3876-3887.

109. Liu, K. E., Wang, D. L., Huynh, B. H., Edmondson, D. E., Salifoglou, A., and Lippard, S. J. (1994) *J. Am Chem. Soc.* **116**, 7465-7466.
110. Liu, K. E., Valentine, A. M., Qiu, D., Edmondson, D. E., Appelman, E. H., Spiro, T. G., and Lippard, S. J. (1995) *J. Am. Chem Soc.* **117**, 4997-4998.
111. Broadwater, J. A., Ai, J. Y., Loehr, T. M., Sanders-Loehr, J., and Fox, B. G. (1998) *Biochemistry* **37**, 14664-14671.
112. Moenne-Loccoz, P., Baldwin, J., Ley, B. A., Loehr, T. M., and Bollinger, J. M. (1998) *Biochemistry* **37**, 14659-14663.
113. Moenne-Loccoz, P., Krebs, C., Herlihy, K., Edmondson, D. E., Theil, E. C., Huynh, B. H., and Loehr, T. M. (1999) *Biochemistry* **38**, 5290-5295.
114. Lee, S.-K., Nesheim, J. C., and Lipscomb, J. D. (1993) *J. Biol. Chem.* **268**, 21569-21577.
115. Beauvais, L. G., and Lippard, S. J. Manuscript in preparation.
116. Liu, K. E., Valentine, A. M., Wang, D. L., Huynh, B. H., Edmondson, D. E., Salifoglou, A., and Lippard, S. J. (1995) *J. Am. Chem Soc.* **117**, 10174-10185
117. Lee, S. K., Fox, B. G., Froland, W. A., Lipscomb, J. D., and Münck, E. (1993) *J. Am Chem. Soc.* **115**, 6450-6451.
118. Shu, L. J., Nesheim, J. C., Kauffmann, K., Munck, E., Lipscomb, J. D., and Que, L. (1997) *Science* **275**, 515-518.
119. Baik, M.-H., Newcomb, M., Friesner, R. A., and Lippard, S. J. (2003) *Chem. Rev.* **103**, 2385-2420.
120. Smoukov, S. K., Kopp, D. A., Valentine, A. M., Davydov, R., Lippard, S. J., and Hoffman, B. M. (2002) *J. Am. Chem. Soc.* **124**, 2657-2663.

Table 1.1. Percent Sequence Identity Between α -Subunits of the BMM Subfamilies^a

	sMMOs	AMO	PH	TMO	SsoMO ^b	THMO
sMMOs	83.3 \pm 8.7	35.3 \pm 0.8	21.5 \pm 1.9	22.4 \pm 1.6	22.1 \pm 2.0	29.0 \pm 1.9
AMO		56.0 \pm 0.0	25.0 \pm 1.6	23.7 \pm 2.1	25.5 \pm 2.0	35.5 \pm 0.5
PH			71.8 \pm 10.9	26.8 \pm 2.1	29.2 \pm 6.8	23.6 \pm 1.0
TMO				58.4 \pm 14.0	43.5 \pm 4.4	22.2 \pm 1.0
SsoMO					100.0 \pm 0.0	40.0 \pm 0.0
THMO						100.0 \pm 0.0

a Adapted from Leahy et. al (8). Diagonal values are based on identity between members within a subfamily

b SsoMO identity was calculated by averaging the identity between the α N and α C domains.

Table 1.2. Bacterial Multicomponent Monooxygenase Sub-Families and Their Members

sMMO	TMO	PH	AMO	SsoMO	THMO
soluble methane monooxygenase (sMMO)	toluene 4-monooxygenase (T4MO)	phenol hydroxylase (PH)	alkene monooxygenase (AMO)	hyperthermophilic toluene monooxygenase (SsoMO)	tetrahydrofuran monooxygenase (THMO)
butane monooxygenase (BMO)	toluene/o-xylene monooxygenase (ToMO)	toluene o-monooxygenase (TOM)			propane monooxygenase (PMO)
	toluene 3-monooxygenase (T3MO)	dimethyl sulfide hydroxylase (DMSH)			
	four component phenol hydroxylase (PH4)	toluene/benzene 2-monooxygenase (T2MO)			
	four component alkene monooxygenase (AMO4)				
	isoprene monooxygenase (IMO)				

Table 1.3. Reduction Potentials of MMOH*

Protein Components	E₁^o (mV)	E₂^o (mv)	Reference
<i>M. capsulatus</i> (Bath)			
MMOH	+100 ± 15	-100 ± 15	(75)
MMOH·MMOB	+50 ± 15	-170 ± 15	(75)
MMOH	+48 ± 5	-135 ± 5	(71)
MMOH·MMOB·MMOR, propylene	<100 ± 25	~100 ± 25	(71)
MMOH	+248 ± 10	-142 ± 14	(70)
MMOH·MMOB	+219 ± 14	-189 ± 8	(70)
<i>M. trichosporium</i> OB3b			
MMOH	+76 ± 14	+21 ± 15	(73)
MMOH·MMOB	-52 ± 14	-115 ± 15	(73)
MMOH, methane	+72 ± 15	-33 ± 15	(72)
MMOH·MMOB, methane	-48 ± 15	-119 ± 15	(72)
MMOH·MMOB·MMOR, methane	+70 ± 15	+128 ± 15	(72)
MMOH·MMOR	+80 ± 15	+114 ± 15	(72)
MMOH·MMOB·MMOR	+76 ± 15	+125 ± 15	(72)

*Redox potentials reported here are vs. NHE, pH 7.0 and vary depending upon the experimental technique used.

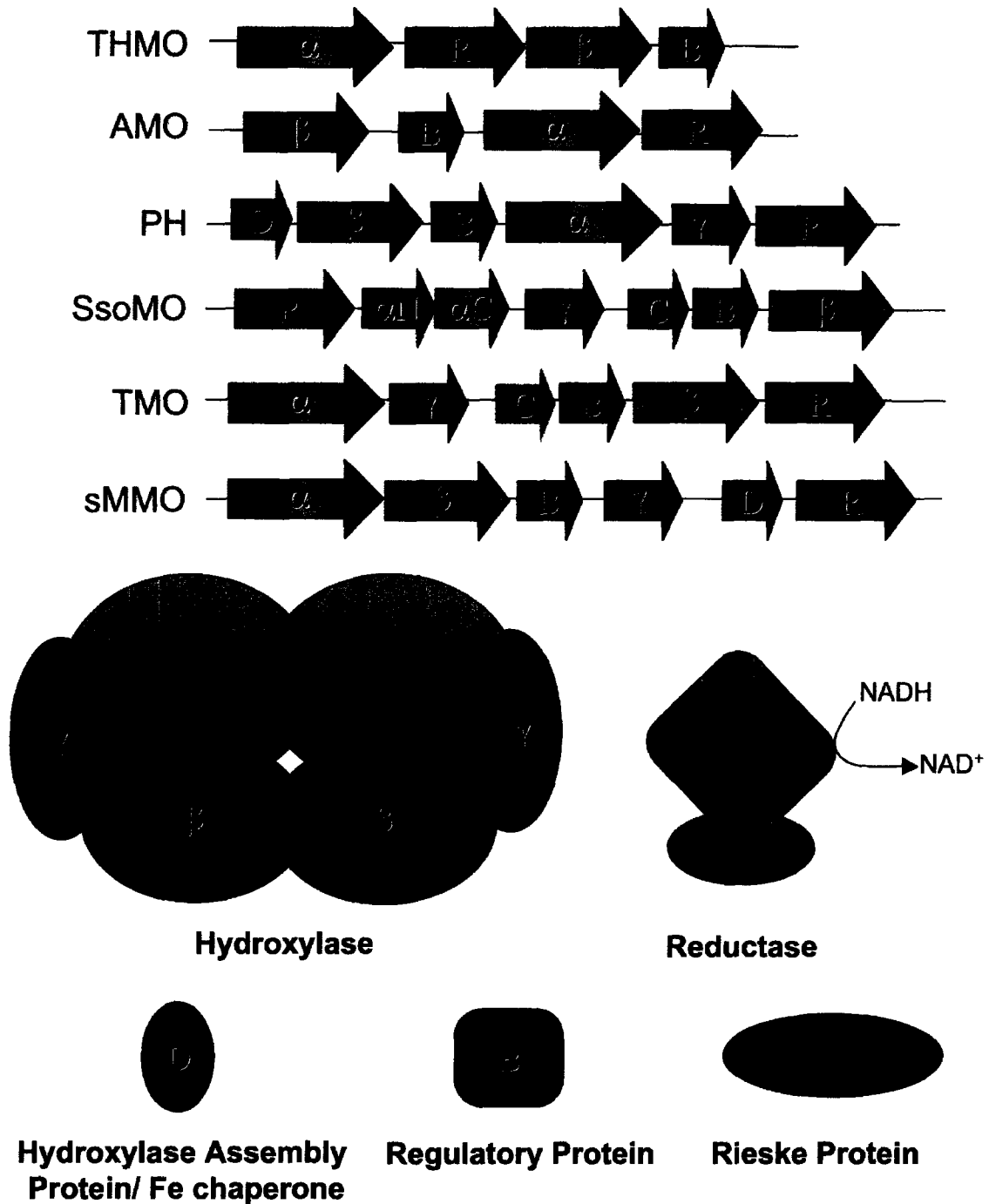


Figure 1.1. Operon organization of the bacterial multicomponent monooxygenase subfamilies. THMO, tetrahydrofuran monooxygenase; AMO, alkane monooxygenase; PH, phenol hydroxylase; SsoMO, hyperthermophilic monooxygenase; TMO, four-component alkene/aromatic monooxygenase; sMMO, soluble methane monooxygenase.

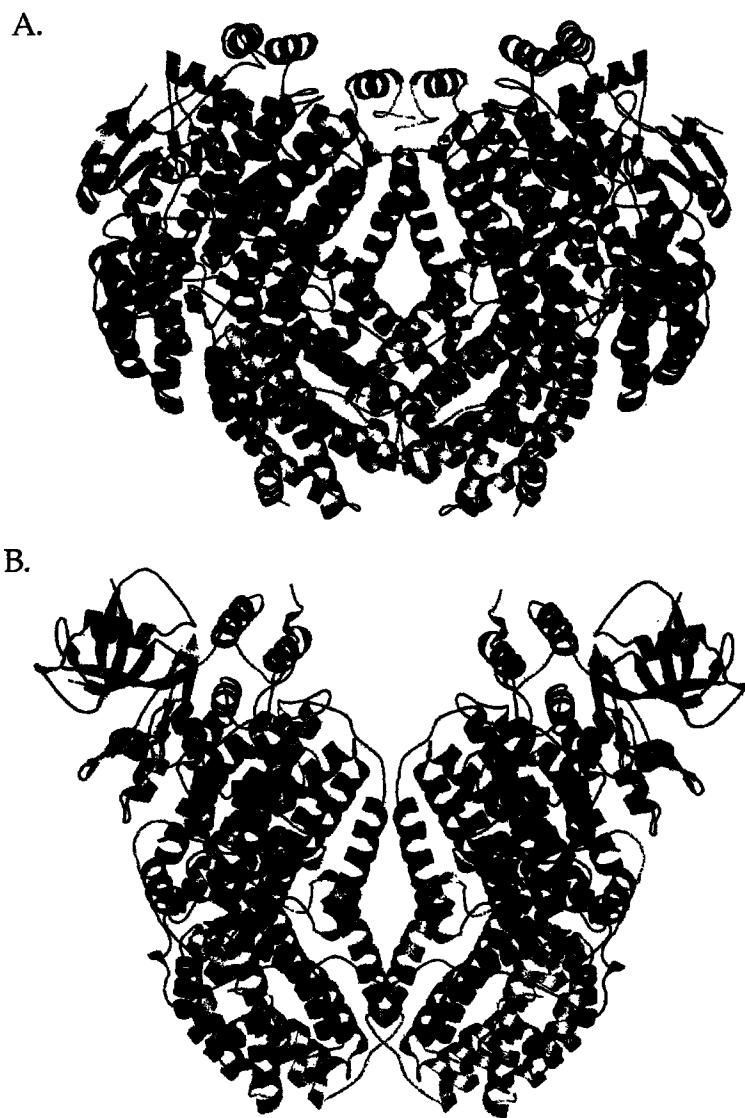


Figure 1.2. Structures of the (A) soluble methane monooxygenase and (B) toluene/*o*-xylene monooxygenase hydroxylase components. The $\alpha\beta$ subunits are colored blue, green, and purple respectively. The diiron centers are depicted as orange spheres.

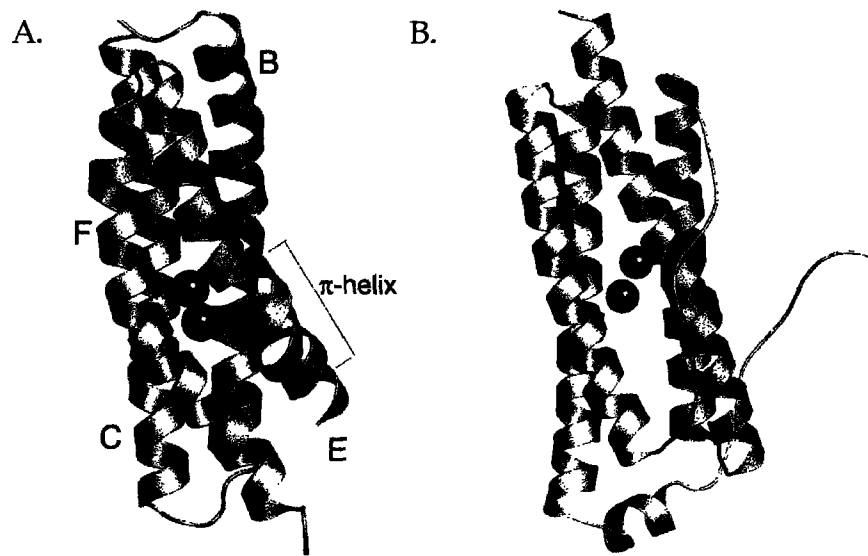


Figure 1.3. Four-helix bundles of (A) MMOH and (B) ferritin. Helices C, B, E, and F are labeled as is the π region of helix E.

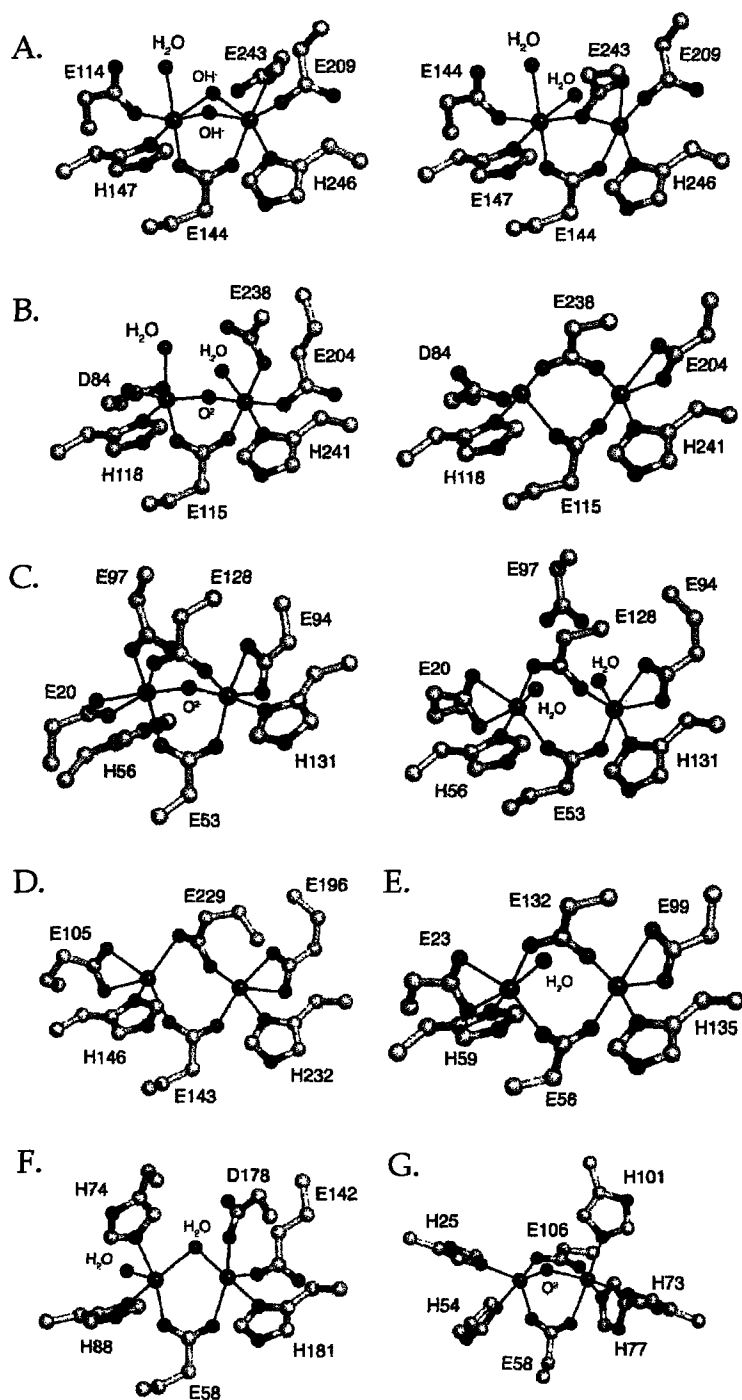


Figure 1.4. Dioxxygen-utilizing carboxylate-bridged diiron centers. (A) Oxidized (left) and reduced (right) MMOH, (B) oxidized (left) and reduced (right) RNR-R2, (C) oxidized (left) and reduced (right) rubrerythrin, (D) reduced stearyl-ACP Δ^9 desaturase, (E) reduced bacterioferritin, (F) Chlamydia associated death domain, (G) methemerythrin. The active site of Chlamydial RNR-R2 is identical to that of MMOH_{ox} although the bridging species is unknown. Also unknown is the true nature of the bridging species in the CADD active site.

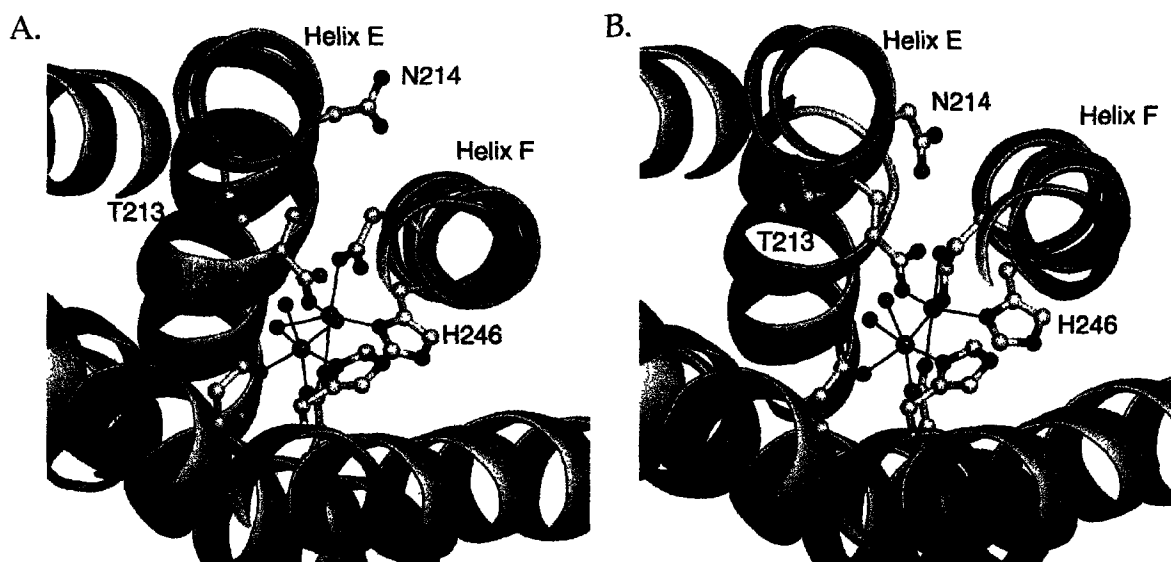


Figure 1.5. Redox-dependant conformational changes in the MMOH active site. (A) Oxidized MMOH and (B) reduced MMOH. Glu-243 resides underneath Asn-214. In most, but not all, reduced MMOH structures, the Thr-213 hydroxyl group points towards the diiron center, whereas in most oxidized MMOH structures, this hydroxyl group points toward the back of the hydrophobic active site cavity.

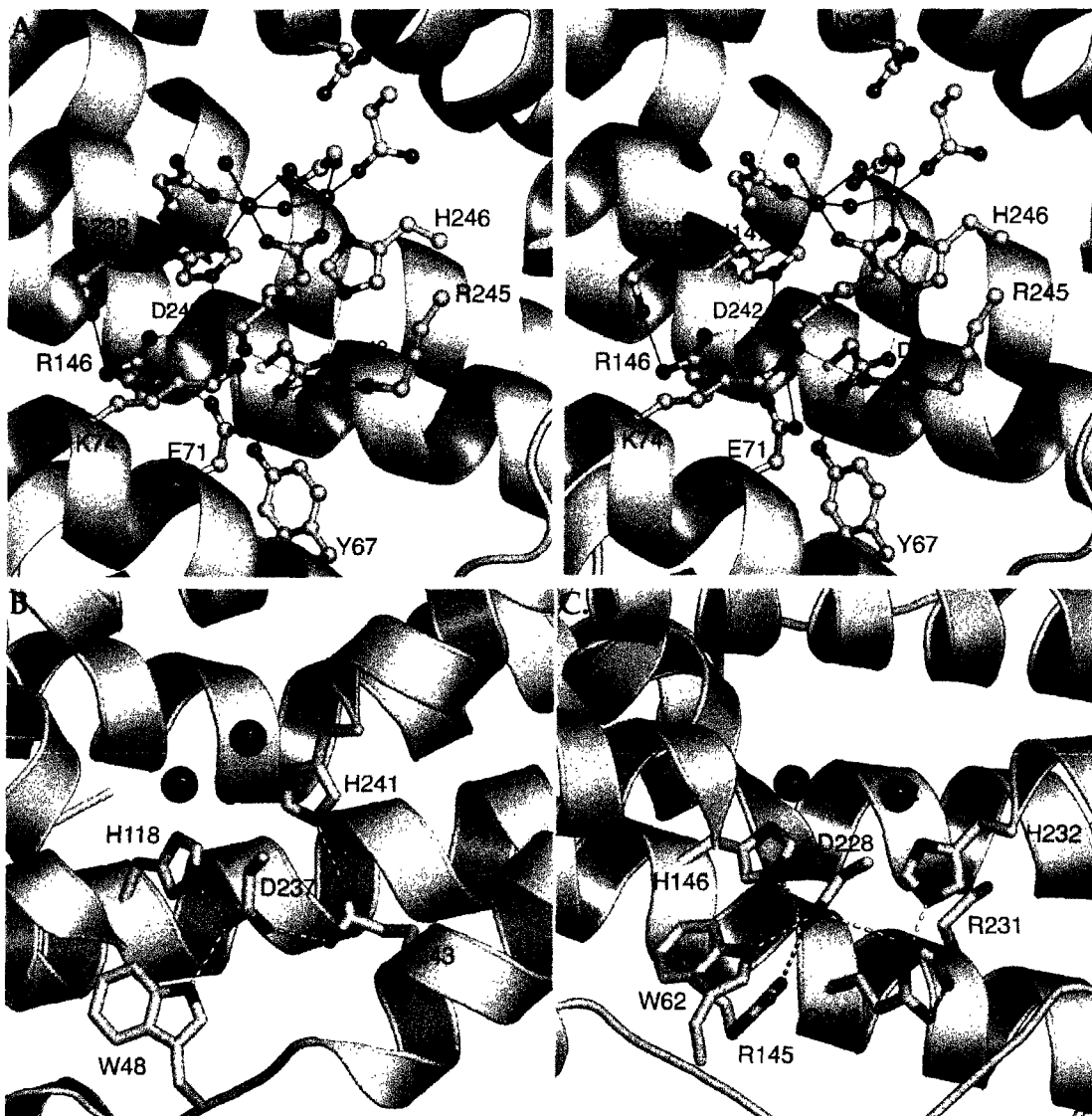


Figure 1.6. Hydrogen bonding network behind the diiron centers of (A) MMOH (in stereo) (B) RNR-R2, and (C) stearoyl-ACP Δ^9 desaturase.

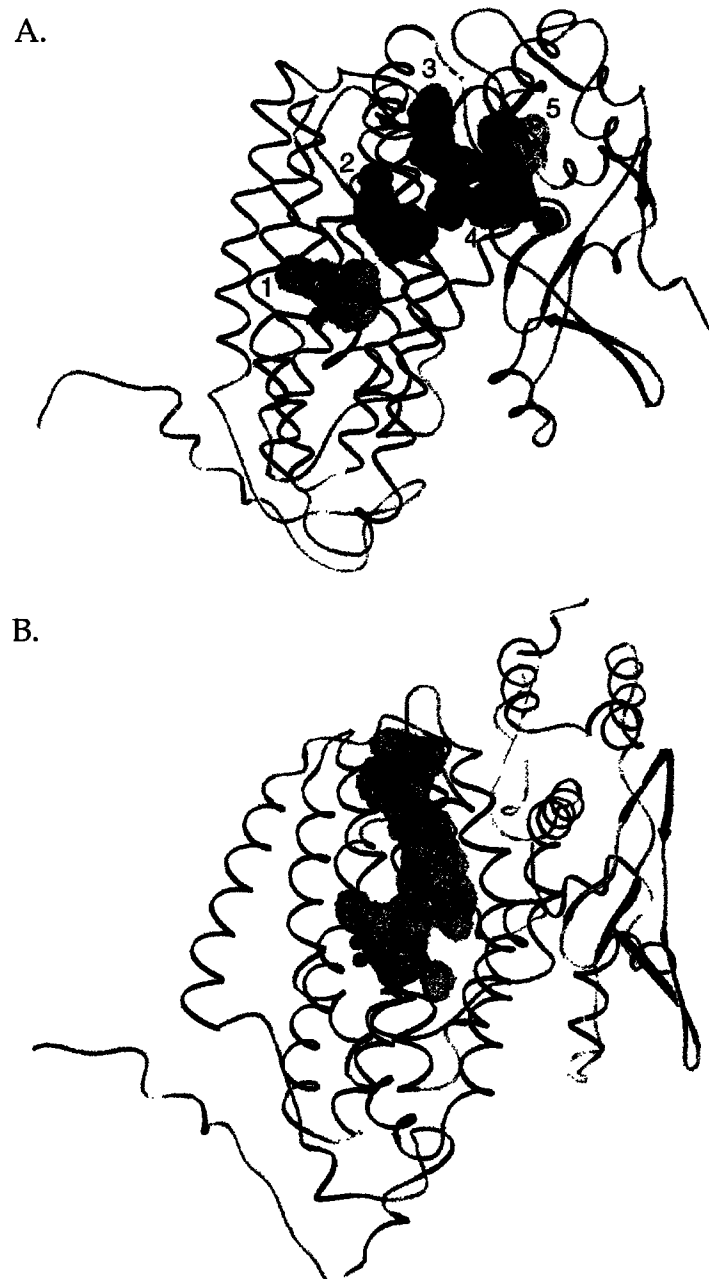


Figure 1.7. Cavities and channels in α -subunit of (A) MMOH and (B) ToMOH. The irons are depicted as yellow spheres and cavities 1-5 in MMOH are labeled accordingly. Cavities 3 and 4 (green) in MMOH are connected.

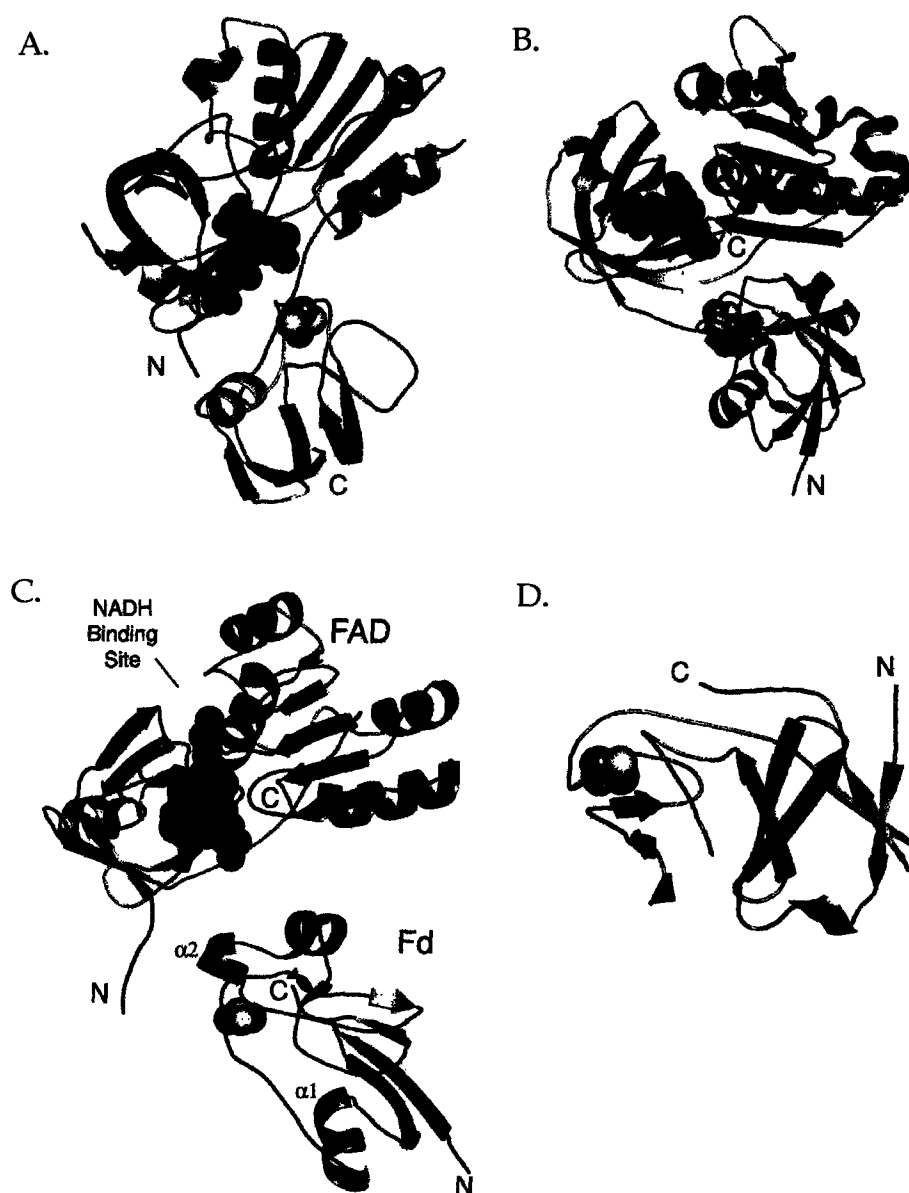


Figure 1.8. Structures of the (A) phthalate dioxygenase reductase, (B) benzoate 1,2-dioxygenase reductase, (C) MMOR flavin (FAD) and ferredoxin (Fd) domains, and (D) Rieske protein. FAD is depicted as red spheres and 2Fe-2S clusters are shown as yellow and orange spheres.

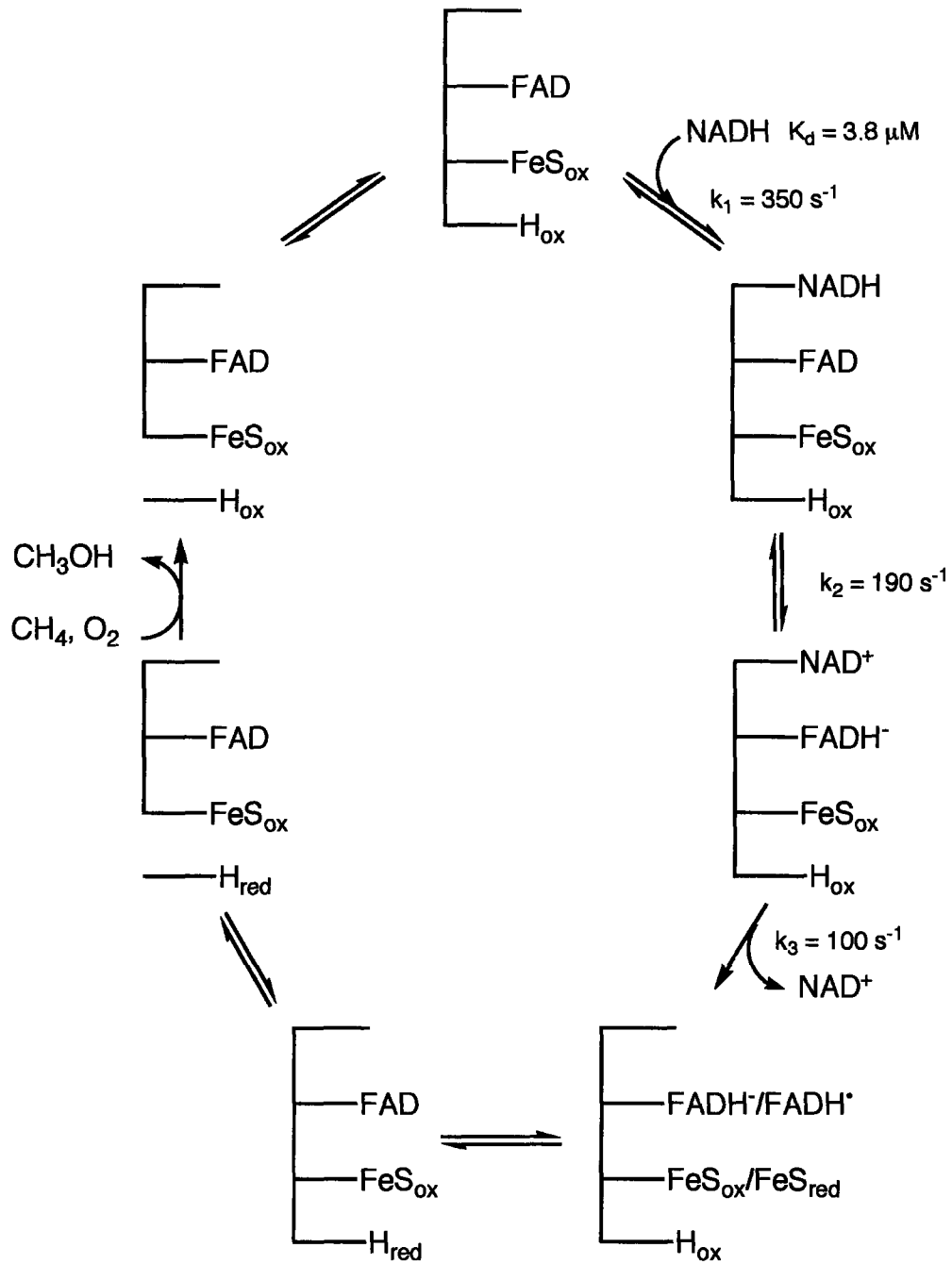


Figure 1.9. Electron transfer through MMOR to MMOH.

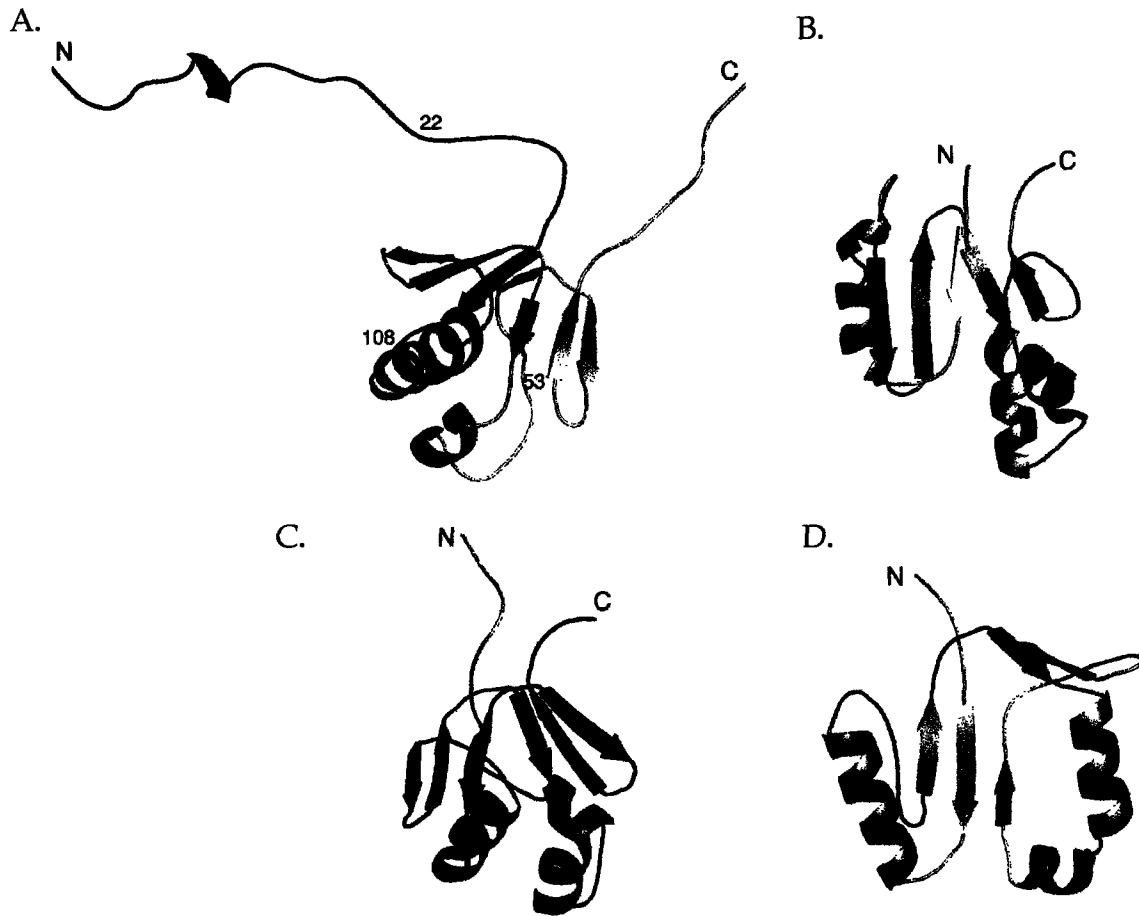


Figure 1.10. NMR structures of the regulatory proteins. (A) MMOB from *Methylococcus capsulatus* (Bath), (B) MMOB from *Methylosinus trichosporium* OB3b, (C) T4MOD from *Pseudomonas medonica* KR1, and (D) P2 from *Pseudomonas* sp. CF600.

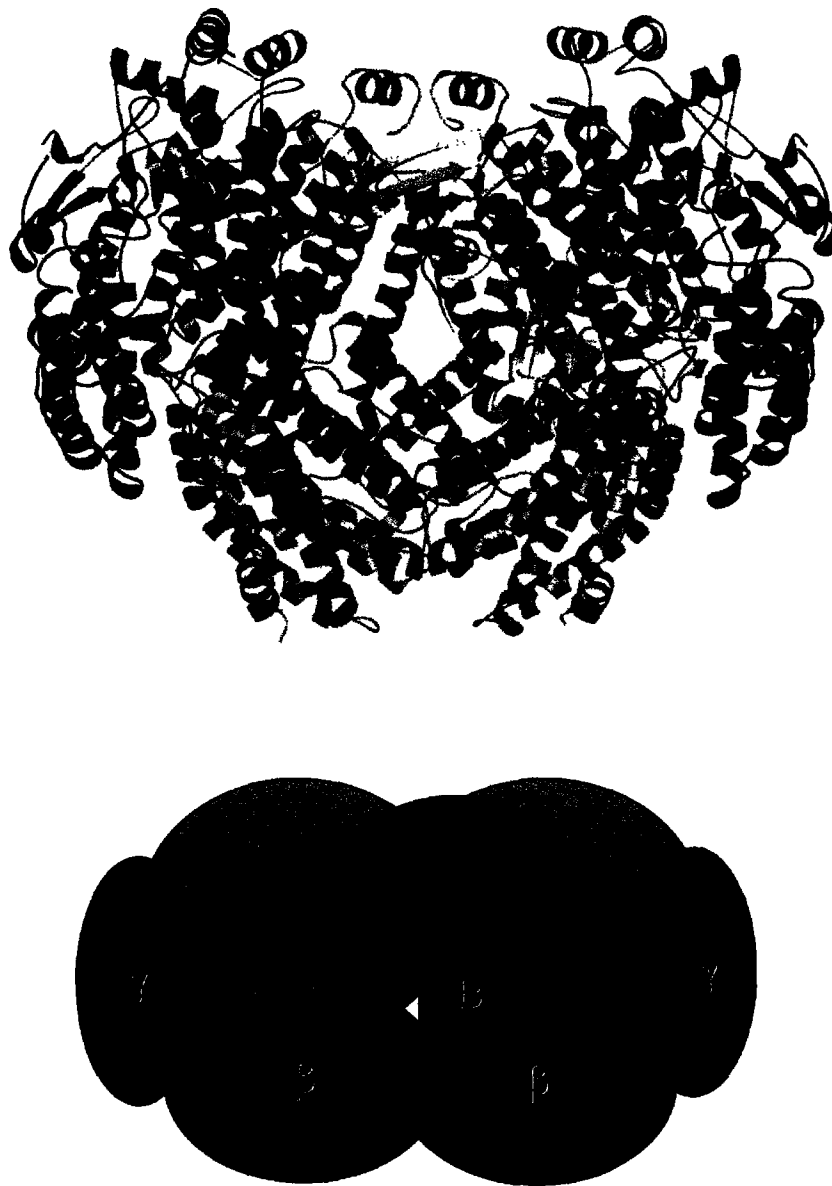


Figure 1.11. Docking model of the sMMO ternary complex depicted in ribbon (top) and cartoon (bottom) form. The diiron and [2Fe-2S] centers represented as orange spheres and yellow spheres, respectively (top). The positions of the components in the ribbon model are identical to those in the cartoon model.

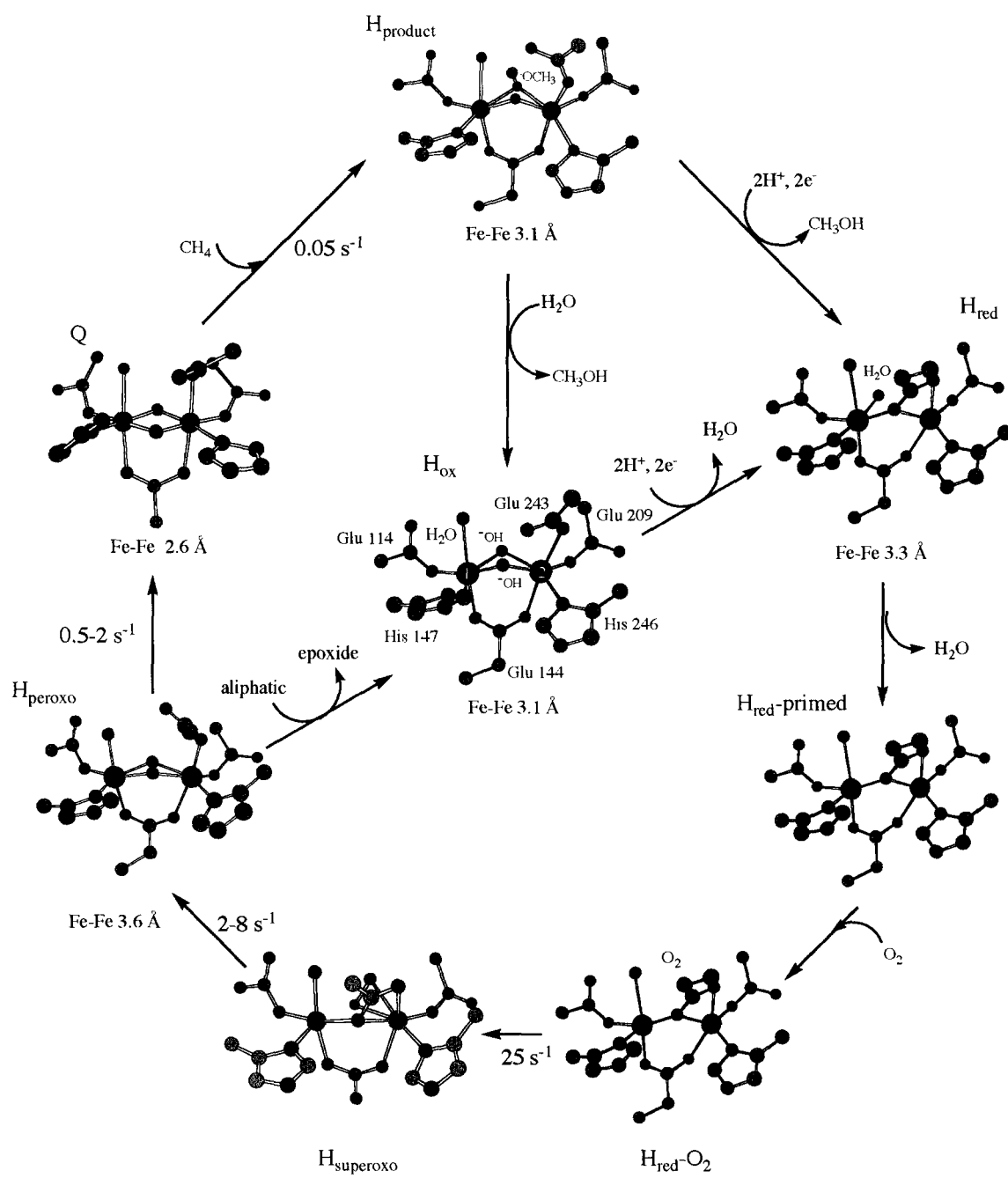


Figure 1.12. sMMO reaction cycle.

Chapter 2

Crystal Structure of the Toluene/*o*-Xylene Monooxygenase Hydroxylase from *Pseudomonas stutzeri* OX1: Insight into Substrate Specificity, Substrate Channeling and Active Site Tuning of Multicomponent Monooxygenases

Introduction

Bacterial multicomponent monooxygenases (BMMs)¹ comprise a family of carboxylate-bridged non-heme diiron enzymes capable of oxidizing a broad range of hydrocarbons including C₁-C₈ alkanes, alkenes, and aromatics (1,2). Four characterized subclasses of multicomponent monooxygenases have been defined (2,3). These are soluble methane monooxygenases (sMMOs), four component alkene/arene monooxygenases or toluene monooxygenases (TMOs), three component phenol hydroxylases (PHs), and $\alpha\beta$ alkene monooxygenases (AMOs), of which all are believed to have evolved from a common ancestor. Bacteria containing multicomponent monooxygenases are capable of using specific hydrocarbon substrates as their primary source of carbon and energy (1,2,4). The remarkable range of substrate specificity exhibited by these enzymes endows these bacteria with the ability to bioremediate environmentally harmful substances such as trichloroethylene and petroleum spills (5,6) and to regulate the global carbon cycle (4). BMMs can also perform regio- and stereospecific hydroxylations, making them useful for producing pure feedstocks for industrial synthesis (7). These enzyme systems, although highly homologous, have evolved different substrate specificities. Only soluble methane monooxygenase can activate the inert C-H bond of methane, which is one of the most difficult reactions to perform in nature (1), whereas the catalytic abilities of TMOs are limited to aromatics, alkenes, and some haloalkanes (2,5).

Substrate hydroxylation in BMMs occurs at a dioxygen-activated, carboxylate-bridged diiron center in the α -subunit of a ~220-250 kDa hydroxylase component that is an $(\alpha\beta\gamma)_2$ heterodimer or, in the case of one known AMO, an $\alpha\beta$ monomer (1-3,8,9). Sequence identity comparisons and spectroscopic studies suggest that the diiron centers

of the hydroxylase proteins from the different systems are structurally similar if not identical (1,10-13). Catalysis at this important dimetallic center proceeds more efficiently in the presence of a small, 10-16 kDa effector protein that alters the spectroscopic and redox properties of the diiron center and changes the regiospecificity of the reaction (1,14). Electrons are supplied by NADH via a reductase comprising either one or two protein components (1,2). The sMMO, PH, and AMO families utilize a 38-40 kDa reductase consisting of an N-terminal ferredoxin domain and a C-terminal FAD domain. The four component alkene/aromatic monooxygenase family requires a Rieske protein in addition to a reductase to facilitate electron transfer to the diiron center.

The methane monooxygenase hydroxylase (MMOH) is thus far the only member of the BMM family to have been structurally characterized (8,15). It is presently unknown and of great interest to determine how the hydroxylase components from the different enzyme systems tune the diiron active site and organize the substrate binding pocket to select for specific hydrocarbons. Understanding the factors responsible for controlling the regio- and stereospecificity of substrate hydroxylation is important for they will prove valuable in developing strategies for the bioremediation of xenobiotics and the synthesis of targeted compounds. Moreover, since fully active TMOs and PHs can be expressed recombinantly and purified from in *E. coli* whereas sMMO cannot, these enzyme systems are more useful, for environmental and synthetic applications, and they offer advantages for mechanistic investigations of the hydroxylation/oxidation chemistry (16-19).

Knowledge of the structure of the hydroxylase component from one or both of these systems has thus been highly desired for some time. In the present article we describe our work on the toluene/*o*-xylene monooxygenase hydroxylase (ToMOH)

from *Pseudomonas stutzeri* OX1. Toluene monooxygenases, which include monooxygenases from both the TMO and PH subclasses, have evolved to hydroxylate toluene specifically at the *ortho*, *meta* and *para* positions with high regiospecificity and to epoxidize alkenes with high stereospecificity (14,20). Other TMOs, such as the toluene/*o*-xylene monooxygenase (ToMO) from *Pseudomonas stutzeri* OX1, have relaxed toluene specificity (21), yet produce highly regiospecific products from alternate substrates like *o*-xylene, dimethylphenol, and *m*-cresol (22). The structure of a toluene monooxygenase hydroxylase offers the opportunity to understand how the enzyme tunes the reactivity of a carboxylate-bridged diiron center and adjusts the active site pocket to control product regiospecificity among the different TMOs and PHs. Here we report the structures of ToMOH in its oxidized, diiron(III) form as well as with bound 4-bromophenol and azide.

Experimental

Expression and Purification of ToMOH

ToMOH was expressed from the plasmid pET22BEA in BL21(DE3) *E. coli* cells (17). Cells were grown at 37 °C in 10 X 2 L baffled flasks containing 1 L of LB media. At an A_{600} of ~ 0.8 the temperature was lowered to 25 °C and ToMOH expression was induced immediately by adding IPTG to a final concentration of 25 μ M. At $t = 0, 1,$ and 2 h after induction, 1 mL of a 100 mM $\text{Fe}(\text{NH}_4)_2(\text{SO}_4)_2 \cdot 6\text{H}_2\text{O}$ solution was added to each flask. After 4 h, the cells were pelleted by centrifugation at 6000 rpm for 5 min, frozen in liquid nitrogen, and stored at -80 °C for further use.

Selenomethionine derivatized ToMOH was created by growing cells in LeMaster's media substituted with 90 mg/ L selenomethionine (23). The Se-Met ToMOH was expressed and stored as described above.

Purification of ToMOH was carried out essentially as described by Cafaro et al. (17). Thawed cells suspended in ~100 mL of cracking buffer were sonicated on ice using a 3/4 inch horn and six 1-min pulses with 1 min intervals between pulses to avoid excessive heating of the protein. The cracking solution contained buffer A (25 mM MOPS, pH 7.0, 50 mM NaCl, 10% glycerol, 2 mM cysteine, 200 μ M $\text{Fe}(\text{NH}_4)_2(\text{SO}_4)_2 \cdot 6\text{H}_2\text{O}$, 8 mM thioglycolate) plus Pefabloc, PMSF, 20 U of DNase and 5 mM MgSO_4 . Debris was removed from the supernatant by centrifugation at 35,000 rpm for 45 min. The supernatant was decanted, filtered through a 0.22 μ m membrane and then loaded onto a DEAE fast flow ion exchange column (26 mm x 40 cm) equilibrated in buffer A. The protein was eluted using a 50-400 mM NaCl gradient over 1200 mL. Fractions (14 mL) containing ToMOH were pooled, concentrated to less than 3 mL, and loaded onto an S300 size exclusion column (26 mm x 100 cm) preconditioned in 25 mM MOPS, pH 7.0, 100 mM NaCl, 10% glycerol. ToMOH fractions (10 mL) were pooled and loaded onto a phenylsepharose column (26 mm x 40 cm) equilibrated in 1.3 M NaCl, 25 mM MOPS, pH 7.0 and 10% glycerol. Before loading, NaCl was added to the ToMOH fractions from the S300 column to bring the final salt concentration to ~ 1.3 M. The protein was eluted from the column by using a salt gradient from 1.3-0.1 M NaCl over 1000 mL. The purest fractions were identified by SDS-PAGE, pooled, and used for crystallization and activity assays. The protein was stored at -80 °C. The average yield was 15 mg of pure protein per liter.

Purification of ToMOD

ToMOD was expressed from the plasmid pET22D(+)-*touD* in BL21(DE3) gold *E. coli* cells (24). Cells were grown in 8 X 1L baffled flasks in LB media at 37 °C until an OD at A_{600} of ~0.7 and then induced with 100 μ M IPTG at 30°C. After 3-4 h of

expression, the cells were harvested by centrifugation (5 min at 6000 rpm) and frozen at $-80\text{ }^{\circ}\text{C}$. Purification of ToMOD was carried out as described by Scognamiglio et al (24).

Activity and Iron Assays

Steady state activity assays were performed according to previously published procedures (17), and the iron content of the protein was assessed by the ferrozine assay (25). The activity and iron content were $1156 \pm 127\text{ nmol/min/mg}$ ($242 \pm 19\text{ min}^{-1}$) and $4.1 \pm 0.1\text{ Fe/dimer}$, respectively.

Crystallization and Data Collection

ToMOH was exchanged into buffer containing 10 mM MES, pH 7.1, and 10% glycerol by using a Millipore spin concentrator and then combined with ToMOD to create a $50\text{ }\mu\text{M}$ ToMOH and $100\text{ }\mu\text{M}$ ToMOD protein solution for crystallization. This solution was then mixed with an equal volume (2-4 μL) of a precipitant solution consisting of 100 mM HEPES, pH 7.5, 2.1-2.5 M $(\text{NH}_4)_2\text{SO}_4$, and 2-4 % PEG 400. Crystallization was achieved at $20\text{ }^{\circ}\text{C}$ by using the hanging drop vapor diffusion method. Crystals of ToMOH alone grew within 0.5-2 days. Well diffracting crystals of ToMOH could be grown under these conditions in the absence of ToMOD. Both the recombinant ToMOH and the Se-Met derivative crystallized under the same conditions. The Se-Met protein, however, diffracted better and was used for most of the studies. The cryogenic solution contained the precipitant solution plus 20-25% glycerol. The 4-bromophenol derivative was obtained by soaking crystals in 50 mM 4-bromophenol dissolved in crystallization buffer for 15 min. X-ray diffraction data were collected at ALS on BL 8.2.2. The HKL suite of programs were used to integrate and scale the data (26).

Structure Determination and Model Refinement

The heavy atom positions and experimental phases were determined in CNS (27) by SAD phasing on the selenium peak data using iterative cycles of manual peak picking from anomalous difference Fourier maps (Table 2.1). Solvent flattening using CNS improved the electron density map quality. The initial model was traced by Arp/wARP 6.0 (28). All refinement and manual rebuilding were performed with CNS and Xtalview (29). Rigid body refinement was carried out with CNS to generate initial models for the azide and bromophenol bound forms of ToMOH. The models were refined as described above.

The final model contained 901 amino acids out of 914 expected residues. The electron density for six residues on the α -subunit C-terminus, six residues on the β -subunit N-terminus, and one residue on the γ -subunit C-terminus were not observed. There were no other disordered regions in the structure and density for all surface side chains was available in the highest resolution structure. All of the modeled residues fell within the favorable regions on the Ramachandran plot.

Results and Discussion

Global Fold and Topology of ToMOH

ToMOH, crystallized from a solution containing the coupling protein (ToMOD), has a topology similar to that of MMOH (Figure 2.1a, b) with a crystallographically required C_2 symmetry axis separating the two $\alpha\beta\gamma$ protomers. The calculated r.m.s. deviations between the ToMOH and MMOH α - and β -subunits are 1.63 Å and 1.48 Å, respectively. The α -subunit fold differs most significantly at regions responsible for mediating interactions with the β - and γ -subunits (Figure 2.1c). The α -helices that comprise most of the α -subunits of ToMOH and MMOH, especially those that house

the diiron center and form the active site cavity, have almost identical structural topology. Similarly, the helical regions of the ToMOH and MMOH β -subunits are almost identical except for loops at the α/β interface (Figure 2.1c, d). As in MMOH, interactions between the $\alpha\beta\gamma$ protomers result in the formation of a canyon at the dimer interface. The canyon in ToMOH is slightly larger than that in MMOH, owing to a broader angle of interaction between the subunits at the α/β interface within the individual protomers. A consequence of this broad angle is a larger aperture across the C_2 axis in the center of the canyon (Figure 2.1a). The ToMOH dimer is stabilized mainly by interactions between the A helices of each α -subunit and a pair of helix-helix contacts between the β -subunits at the base of the protein, whereas MMOH utilizes four pairs of overlapping helices to stabilize the β - β subunit interactions. In MMOH but not ToMOH, the N-termini of the β -subunits extend across the α -subunits to form helix-helix interactions with each other at the northern end of the protein as depicted in Figure 2.1b.

The fold and location of the γ -subunit are strikingly different from that of MMOH (Figure 2.1e, f). In ToMOH, the γ -subunit binding sites reside at the northeastern and northwestern corners of the protein and exclusively contact the α -subunit. The secondary structure consists mostly of beta sheets and forms what may be described as mini- β -barrel, with a single helix enclosing the barrel fold. A 3D structure homology search using the EMBL-EBI SSM server reveals the γ -subunit to resemble the beta-Grasp fold of ubiquitin and the 2Fe-2S domains of ferredoxin (30). The γ -subunit is the least conserved protein component of the multicomponent monooxygenases, with less than 15% sequence similarity occurring for the methane, toluene and phenol families. No function has yet to be assigned to this subunit, although it may either

stabilize the protomer or assist in the formation of component complexes. Another possibility is that it may simply be a vestigial subunit with no function, since the AMO family apparently does not require a γ -subunit for function (9).

Electrostatic Surfaces of ToMOH and ToMOD

The electrostatic surfaces of ToMOH and a model of ToMOD built from the NMR structure of T4MOD (31) are presented in Figure 2.2. ToMOH is negatively charged except for positively charged patches in the canyon region of the molecule, which is the proposed docking site for the BMM regulatory protein (8,32,33). The surface of the ToMOD model is also negatively charged except for a patch on the top of the protein. Comparison to NMR line broadening studies on MMOB from *Methylococcus capsulatus* (Bath) (34) and biochemical characterization of MMOB mutants from *Methylosinus trichosporium* (OB3b) (35) suggest the negatively charged surfaces of ToMOD are the likely docking faces of the protein. If true, the electrostatic surfaces of ToMOH and the ToMOD model depict clearly the relative docking position of ToMOD in the canyon.

The Carboxylate-Bridged Diiron Center

The carboxylate-bridged diiron center is housed within a four-helix bundle in the α -subunit of ToMOH. Its structure resembles that predicted by sequence identity and spectroscopic comparisons to oxidized MMOH and the toluene 4-monooxygenase hydroxylase (T4MOH) to be a di(μ -hydroxo)- or μ -alkoxodiiron(III) center, except for a few notable, and possibly significant, differences (Figure 2.3a, b) (1,10,12). The Fe-Fe distance of 3.0 Å is identical to that of MMOH. The pseudooctahedral coordination geometry of Fe1 comprises Glu-104, His-137, one oxygen atom of the bridging carboxylate Glu-134, a terminal water molecule, a bridging hydroxide, and the oxygen atom of a monodentate bridging thioglycolate ion (see below). The terminal water

ligand hydrogen bonds to the dangling oxygen atoms of both Glu-104 and Glu-231, a feature that is observed in MMOH. Unlike MMOH, Glu-104 participates in a more intricate hydrogen bonding network involving Gln-141 and His-96, of which both are conserved among the members of the TMO subclass (Figure 2.4a, Table 2.2). In MMOH, the amino acid analogous to Gln-141 is Cys-151, of which the sulfur atom lies 4.5 Å from the carboxylate oxygen atom of Glu-114 (Figure 2.4b). This distance indicates that little or no interaction occurs between these residues. Since Cys-151 of MMOH and Gln-141 of ToMOH also align structurally with the radical-forming Tyr-122 residue of the R2 subunit of ribonucleotide reductase (RNR-R2), it has been speculated that the residue at this position in multicomponent monooxygenases may have an essential catalytic function (36). Mutagenesis studies on T4MO, in which Gln-141 was replaced with either a Cys, Val, Ala, or Phe, yielded active isoforms with unaltered regiospecificity towards toluene (Table 2.3). This result suggested that the residue at position 141 is not as essential for catalysis in the TMO subclass of enzymes (37-39). Replacing Gln-141 with Cys in T4MO did not afford an enzyme capable of oxidizing methane (37).

The coordination sphere of Fe₂ is formed by His-234, Glu-197, Glu-231, and oxygen atoms from the bridging carboxylate, thioglycolate and hydroxide ligands already identified. Surprisingly, His-234 coordinates to Fe₂ using its ε-nitrogen rather than the δ-nitrogen atom employed by His-137 for Fe₁ of ToMOH and both coordinating histidines of MMOH. ToMOH thus provides the first example of mixed δ- and ε-histidine coordination in the active site of a carboxylate-bridged diiron containing hydroxylase (Figure 2.3). It is unknown whether such a histidine ligand rotamer flip might influence the chemistry of the dimetallic center. The ε-nitrogen atoms of the iron-

coordinating histidine ligands in MMOH are part of an extensive hydrogen bonding network that extends from the four-helix bundle towards the surface of the protein formed by helix A in the canyon region (Figure 2.4d). Despite the rotamer flip, His-234 participates in a hydrogen bonding network that is identical to that of MMOH (Figure 2.4c). Such hydrogen bonding networks may function to pre-organize the active site for iron binding, facilitate electron transfer from the reductase to the diiron center, or both (10). A similar hydrogen bonding network in RNR-R2 delivers an electron from W48 to the diiron cluster during generation of the Fe(III)Fe(IV) intermediate X required for tyrosyl radical formation (40,41).

Some of the residues and solvent interactions in the Fe₂ second coordination sphere of ToMOH differ from those observed in MMOH. An ordered hydronium ion (H₃O⁺) mediates interactions between Glu-134, Glu-197, and Glu-111 in ToMOH (Figure 2.4a), whereas the amino group from the side chain of Gln-140 performs this role in MMOH (Figure 2.4b) (8). The hydronium ion assignment preserves charge neutrality and is supported by the out-of-plane displacement of the O-atom from the H-bond acceptor O-atoms in Glu-111, Glu-134 and Glu-197. Since Glu-111 of ToMOH and Gln-140 of MMOH do not align sequentially with one another, the proteins seemed to have evolved different strategies to preserve these interactions. Both Glu-111 and Gln-140 are part of localized hydrogen bonding networks linking these residues to amino acids on helix F, which forms part of the canyon region proposed for binding the coupling protein (32). Disruption of these hydrogen bonds due to binding of the coupling protein may allow this regulatory component to alter the chemical reactivity of the diiron center. These newly identified local hydrogen bonding networks in both the MMOH and ToMOH active sites highlight features not previously thought to be significant to the function of the enzyme.

The bridging ligands in the ToMOH active site are best fit as a hydroxide ion at the position cis to the coordinating histidines and a thioglycolate ion at the trans position that is accessible to solvent from the substrate-binding cavity. We tentatively assign the latter ligand as thioglycolate, a component in the purification buffer of the protein, based on the size and shape of its electron density (Figure 2.3c). Some residual difference density remains in the vicinity of the sulfur atom even after thioglycolate is modeled, suggesting possible partial oxidation to the sulfinate or perhaps positional disorder. Other buffer components such as DTT, sulfate ion, glycerol, ethylene glycol, and water, do not fit the density as well as thioglycolate and leave even more residual difference density. Nonetheless, it is clear that the species in this bridging position binds symmetrically to both iron atoms and must be a monoanion if the neutrality of the dimetallic center is to be preserved.

In the structure of oxidized ToMOH determined from crystals grown in the presence of 1.5 mM NaN_3 , but not ToMOD, the density at the bridging position is significantly altered (Figure 2.5). The new density is fit nicely by a monodentate, asymmetrically bound azide anion, a more strongly coordinating ligand than the thioglycolate anion. Because the buffers used in the purification of ToMOH and ToMOD were very similar, the absence of the thioglycolate feature cannot be attributed to the ToMOD buffer components. The identity of the electron density as azide is supported by the observation of a charge-transfer band at 450 nm in the UV-Vis spectrum of ToMOH following the addition of NaN_3 (Figure 2.6). A similar spectroscopic feature arises when azide is added to MMOH, stearyl-acyl carrier protein (ACP) Δ^9 desaturase, and rubrerythrin (42-44). The geometry of the asymmetrically bound azide ligand in ToMOH is similar to that of azide bound in the crystal structure of a reduced RNR-R2 Y208F mutant (Figure 2.5b) (45). Although

further spectroscopic evidence is desired to support the assignment of azide binding to iron in ToMOH, the above findings are consistent with previous structural and spectroscopic work.

In the catalytic cycle of MMOH, the first spectroscopically observable intermediate has been assigned as a μ -(peroxo)diiron(III) species (36). Although there is presently no evidence for such an assignment in ToMOH, we may surmise that it will exist. Protein and small molecule model compound crystal structures of the azido and/or peroxo bound forms of the hemerythrin diiron(III) and hemocyanin dicopper(II) metal centers demonstrate that azide-bound structures are good mimics for peroxide binding at metalloenzyme active sites and are capable of predicting the metal site at which O_2 is activated (46). The azido ToMOH structure suggests that O_2 may attack initially the Fe2 site to become activated. The observed 1,1-semibridging or bent end-on coordination of the bound azide ion suggests that a peroxide intermediate may adopt one of these two geometries before reacting with substrate or further rearranging to a di(μ -oxo)diiron(IV) Q-like intermediate. Density functional theory calculations detailing the reaction of O_2 with the diiron center in reduced MMOH predict initial attack at Fe2 for dioxygen activation, consistent with the above argument (47).

Open Channel Access to the Diiron Active Site

Within the ToMOH α -subunit lies a large channel of approximately 30-35 Å in length and 6-10 Å in width that connects the diiron center to the surface of the protein (Figure 2.7). Starting at the diiron center, the channel traverses the four-helix bundle between helices E and B, and extends toward the surface through a space created by the interface of helices D, E, B, G, and H (Figure 2.7b, 2.9e). At the surface of the protein, amino acid side chains create a fork in the channel, of which the arms lead to two

adjacent openings (Figure 2.7a, 2.8). These openings are located at the northern end of the molecule at the ridge of the canyon next to the C-terminal and N-terminal loops of helices E and H, respectively. The channel diameter of 6-10 Å is large enough to accommodate aromatic substrates or products as they move toward or away from the active site, respectively. Depending upon the crystal investigated, 3-4 ordered water molecules line the channel surface, which comprises both hydrophobic and hydrophilic residues (Figure 2.9a, 2.7b). Crystals soaked with the product analogue 4-bromophenol, chosen to facilitate identification of the hydroxyl group, contained 3 molecules in the channel (Figure 2.9b, 2.10). The 4-bromophenol molecules are positioned such that the hydroxyl moieties are directed towards the surface. Their orientations in the channel appear to be determined by a combination of both hydrogen bonding interactions between the bromophenol hydroxyl groups with the protein and by π -stacking interactions between the bromine atom, protein side chains and adjacent bromophenol phenyl rings. Although it is largely unknown whether the channel can direct the orientation of substrate molecules as they try to gain access to the active site pocket, or how such substrate steering might be accomplished, the positioning of the bromophenol molecules suggests that a mechanism of this kind exists. It is clear from these results that the channel is solvent accessible and large enough to accommodate ToMO substrates and products. We therefore propose this route as the major pathway for substrate entrance to and product egress from the diiron active site, perhaps through the separate openings. Whether or not O₂ reaches the active site principally by this or some other pathway is less obvious, since it is small enough to diffuse through the surface helices to reach the diiron center.

In the α -subunit of MMOH, protein side chains separating three major cavities prevent them from forming an analogous channel linking the diiron center with the surface of the protein (Figure 2.9c) (48). Previous structural studies of MMOH revealed that substrate analogues including xenon, iodoethane, and dibromoethane (48) as well as products like bromoethanol (49) can occupy these cavities (Figure 2.9f). Further analysis of these MMOH structures indicates that cavities 2 and 3 are linked in crystal form I MMOH and separated in crystal form II, demonstrating that residues within the core of the α -subunit can shift to gate substrate or product movement through the protein (Figure 2.9c, d). Comparison of the ToMOH channel with the MMOH cavities, with and without bound substrate analogues, reveals that the paths through the core of the α -subunit are very similar for the two proteins (Figure 2.7b, 2.9c, 2.9e, 2.9f). The only difference between the pathways is that the final MMOH cavity extends between helices D and G, reaching the surface on the other side of helix H. We suggest that they trace a universal route for molecular access to the diiron sites of other carboxylate-bridged diiron proteins of this class.

In MMOH, access to the hydrophobic cavity at the diiron center is blocked by Leu-110 and Phe-188, a feature previously termed the "leucine gate" (Figure 2.11b) (50). The small aperture between these residues suggested initially that only small substrates like methane would be capable of gaining access to the diiron center via this route. In the structures of two different MMOH crystal forms, Leu-110 adopts alternate rotameric conformations, revealing how larger substrates, like aromatics and C_2 - C_8 alkanes, might approach the active site. ToMOH has similar residues, Ile-100, Phe-176 and Phe-196, marking the entrance to the active site cavity, but the opening to the diiron center of this enzyme is much larger (Figure 2.11a). As a result, the iron atoms are directly accessible

to solvent and substrates from the channel. Among the different carboxylate-bridged diiron enzymes, O_2^- and H_2O_2 -derived intermediates have not yet been spectroscopically detected for TMOs, PHs, and rubrerythrin, proteins in which the diiron center is accessible, or predicted to be accessible, to bulk solvent. Stearoyl-ACP Δ^9 desaturase also has a large substrate channel similar to that of ToMOH that is very accessible to solvent. In the absence of the stearoyl-acyl carrier protein (ACP), however, intermediates are not observed in Δ^9 desaturase. We therefore suggest that the binding of the ACP allows for the accumulation of a spectroscopically observable μ -1,2-peroxodiiron(III) species (51,52), presumably because binding of the ACP blocks buffer access to the Δ^9 desaturase diiron center, which might quench this intermediate. Similarly, the high valent di(μ -oxo)diiron(IV) intermediate Q of MMOH and the Fe(III)Fe(IV) intermediate X of RNR-R2 are housed in relatively secluded hydrophobic environments. We further speculate that the failure to observe O_2^- or H_2O_2 -derived intermediates in TMO, PH, and rubrerythrin may be due to reactions with buffer components that can more readily access and react with these species in their active sites.

Mutagenesis experiments on T4MOH and toluene 2-monooxygenase (T2MO) targeting Ile-100 and Val-106, respectively, provide strong evidence to support the channel as the primary pathway for substrate entrance (37-39). Changing I100 to residues with larger side chains such as Arg and Trp inhibited toluene hydroxylation, presumably by blocking access to the active site cavity (Table 2.3). An I100Q mutant, in which Ile was replaced with a polar side chain of comparable size, was active, whereas the activity of an I100C mutation was compromised. The I100Q and I100C mutants indicate that the residue in this position need not be hydrophobic for TMOs to be

efficient catalysts and suggest that a small side chain is not beneficial, perhaps due to limited gating ability and greater exposure to solvent. A Val to Ala mutation of the analogous gate residue in T2MO from *Burkholderia capacia* G4, a member of the three-component PH family, resulted in enhanced ability to degrade naphthalene and three-ring fused aromatics including phenanthrene, fluorene and anthracene (53). In the light of the present structures, these findings strongly suggest that members of the PH subclass have a similar substrate channel. Furthermore, as the work on T2MO demonstrates, the ability to engineer TMOs and PHs to act on bigger aromatic substrates is most likely a consequence of modulating the dimensions of the channel.

Residues F176 and F196 at the active site also appear to be essential for activity (37,39). A F176A T4MO mutant could not oxidize toluene, TCE, or butadiene, whereas a F176L mutant was 100%, 25.5% and 38.4% as active toward these substrates, respectively, as compared to the wild type enzyme. The T4MO mutants F196Y and F196L were as active as the wild type protein, whereas F196I and F196G were less so. These results imply that the bulky side chains of F176 and F196 (Figure 2.11a) are important for controlling the activity of the enzyme, perhaps by limiting exposure of the iron centers to undesired solution components, or for guiding the bound substrate to the diiron center. Further work is required to clarify their roles.

Substrate Specificity of Four Component Alkene/Arene Monooxygenases

For TMOs the key to regiospecific hydroxylation is the topology of the active site pocket as defined by the residues that form its lining. The dimensions of the substrate channel may also be important. Although the coupling protein can affect the regiospecificity of the enzyme, it most likely functions in this manner by adding rigidity to the active site to enforce pre-programmed constraints in the enzyme, rather than by dictating specific regiochemistry (14).

The T4MO and T3MO enzymes, of which both require a glycine at residue 103 and a bulky hydrophobic amino acid at position 180, are highly para directing enzymes whereas PHs, which utilize a leucine and alanine at these positions, respectively, are strongly ortho directing (Table 2.2, 2.3). Mutagenesis work on T4MO has been carried out to probe how these active site residues affect the specificity of toluene monooxygenases (14,37,38). Substituting Gly 103 in T4MO with Leu increased the yield of *o*-cresol formation from 0.9% to 55.4%, confirming the importance of this amino acid in modulating the position of toluene ring hydroxylation (14). The size of the residue at position 103 can also affect the enantioselectivity of alkene epoxidation; the same G103L mutation increased the yield of (*S*)-butadiene epoxide from 67% to 90% (37). ToMOH, which differs significantly from the T4MO active site only at positions 103 and 180, has relaxed regiospecificity, as manifest by a product distribution of 36%, 19%, and 45% for *o*-, *m*- and *p*- cresol, respectively (22). Residue 103 in ToMOH is a Glu and points away from the active site such that its charged carboxylate group is buried (Figure 2.11a, 2.12). Only the α and β carbons face the substrate binding pocket. Since T4MO has no β carbon atom occupying this position, we propose that the relaxed regiospecificity of ToMO for toluene oxidation is partially due the β carbon atom from Glu at position 103 steering the toluene C2 position towards the diiron center, presumably through steric interactions with the methyl group of the substrate. The result of these interactions will force the phenyl ring to cant to the left or right.

It is unknown whether the amino acid differences at position 180, Met versus Ile, affect ToMO regiospecificity. Sequence comparison of the TMO and PH active sites suggest that smaller residues at positions 180 and 192 of T4MO, in addition to a larger residue at position 103, may be essential for the *ortho* hydroxylating regiospecificity of

PHs (Table 2.2). Having an Ala at position 180 and an Ile or Val at position 192 will create extra space in the active site cavity and possibly provide a niche for the toluene methyl group. As toluene approaches the active site through the cavity, the bulky residue at position 103 may steer the methyl group on the phenyl ring towards the Fe₂ side of the active site pocket where residues 180 and 192 reside. The result would be to expose the toluene C2 position to the diiron center with subsequent hydroxylation at the *ortho* position.

The above analysis suggests that it should be possible to design rationally BMM active sites to generate enzyme systems for specific industrial and environmental applications. Since structures are now available for both ToMOH and MMOH, two proteins having almost identical dimetallic centers, we are poised to address the question of why ToMOH cannot activate the inert C–H bond of methane. The present structure determination should also assist in the design of mutant forms of the protein in which intermediates in the dioxygen activation steps can be spectroscopically characterized, as in MMOH, and in revealing the factors responsible for hydroxylation specificity.

Acknowledgments

We thank Joel Bard (Wyeth Pharmaceuticals) for his help with solving the phases, Alberto di Donato and Valeria Cafaro (Universita' di Napoli Federico II) for supplying the ToMO plasmids and a sample of ToMOF, and Elisabeth Cadieux (MIT) for ToMOC.

References

1. Merkx, M., Kopp, D. A., Sazinsky, M. S., Blazyk, J. L., Müller, J. M., and Lippard, S. J. (2001) *Angew. Chem. Int. Ed.* **40**, 2782-2807.
2. Leahy, J. G., Batchelor, P. J., and Morcomb, S. M. (2003) *FEMS Micro. Rev.* **27**, 449-479.
3. Notomista, E., Lahm, A., Di Donato, A., and Tramontano, A. (2003) *J. Mol. Evol.* **56**, 435-445.
4. Hanson, R. S., and Hanson, T. E. (1996) *Microbiol. Rev.* **60**, 439-471.
5. Chauhan, S., Barbieri, P., and Wood, T. K. (1998) *Appl. Environ. Microbiol.* **64**, 3023-3024.
6. Sullivan, J. P., Dickinson, D., and Chase, H. A. (1998) *Crit. Rev. Microbiol.* **24**, 335-373.
7. Archelas, A., and Furstoss, R. (1997) *Annu. Rev. Microbiol.* **51**, 491-525.
8. Rosenzweig, A. C., Frederick, C. A., Lippard, S. J., and Nordlund, P. (1993) *Nature* **366**, 537-543.
9. Miura, A., and Dalton, H. (1995) *Biosci. Biotech. Biochem.* **59**, 853-859.
10. Coufal, D. E., Blazyk, J. L., Whittington, D. A., Wu, W. W., Rosenzweig, A. C., and Lippard, S. J. (2000) *Eur. J. Biochem.* **267**, 2174-2185.
11. Newman, L. M., and Wackett, L. P. (1995) *Biochemistry* **34**, 14066-14076.
12. Pikus, J. D., Studts, J. M., Achim, C., Kauffmann, K. E., Münck, E., Steffan, R. J., McClay, K., and Fox, B. G. (1996) *Biochemistry* **35**, 9106-9119.
13. Cadieux, E., Vrajmasu, V., Achim, C., Powlowski, J., and Münck, E. (2002) *Biochemistry* **41**, 10680-10691.
14. Mitchell, K. H., Studts, J. M., and Fox, B. G. (2002) *Biochemistry* **41**, 3176-3188.

15. Elango, N., Radhakrishnan, R., Froland, W. A., Wallar, B. J., Earhart, C. A., Lipscomb, J. D., and Ohlendorf, D. H. (1997) *Prot. Sci.* **6**, 556-568.
16. Lloyd, J. S., Finch, R., Dalton, H., and Murrell, J. C. (1999) *Microbiology* **145**, 461-470.
17. Cafaro, V., Scognamiglio, R., Viggiani, A., Izzo, V., Passaro, I., Notomista, E., Dal Piaz, F., Amoresano, A., Casbarra, A., Pucci, P., and Di Donato, A. (2002) *Eur. J. Biochem.* **269**, 5689-5699.
18. Studts, J. M., Mitchell, K. H., Pikus, J. D., McClay, K., Steffan, R. J., and Fox, B. G. (2000) *Protein Expr. Purif.* **20**, 58-65.
19. Divari, S., Valetti, F., Caposio, P., Pessione, E., Cavaletto, M., Griva, E., Gribaudo, G., Gilardi, G., and Giunta, C. (2003) *Eur. J. Biochem.* **270**, 2244-2253.
20. McClay, K., Fox, B. G., and Steffan, R. J. (2000) *Appl. Environ. Microbiol.* **66**, 1877-1882.
21. Bertoni, G., Bolognese, F., Galli, E., and Barbieri, P. (1996) *Appl. Environ. Microbiol.* **62**, 3704-3711.
22. Cafaro, V., and Di Donato, A. Unpublished results.
23. LeMaster, D. M., and Richards, F. M. (1985) *Biochemistry* **24**, 7263-7268
24. Scognamiglio, R., Notomista, E., Barbieri, P., Pucci, P., Dal Piaz, F., Tramontano, A., and Di Donato, A. (2001) *Prot. Sci.* **10**, 482-490.
25. Gibbs, C. R. (1976) *Anal. Chem.* **48**, 1197-1201.
26. Otwinowski, Z., and Minor, W. (1997) in *Methods Enzymol.* (Charles W. Carter, J., and Sweet, R. M., eds) Vol. 276, pp. 307-326, Academic Press, New York.
27. Brünger, A. T., Adams, P. D., Clore, G. M., Delano, W. L., Gros, P., Grosse-Kunstleve, R. W., Jiang, J.-S., Kuszewski, J., Nilges, N., Pannu, N. S., Read, R. J., Rice, L. M., Simonson, T., and Warren, G. L. (1998) *Acta Cryst. D* **54**, 905-921.

28. Lamzin, V. S., and Wilson, K. S. (1993) *Acta Crystallogr. D* **49**, 129-147.
29. McRee, D. E. (1999) *J. Struct. Biol.* **125**, 156-165.
30. Krissinel, E., and Henrick, K. (2003) in *Proceedings of the 5th International Conference on Molecular Structural Biology* (Kungl, A. J., and Kungl, P. J., eds), pp. 88, Vienna.
31. Hemmi, H., Studts, J. M., Chae, Y. K., Song, J., Markley, J. L., and Fox, B. G. (2001) *Biochemistry* **40**, 3512-3524.
32. MacArthur, R., Sazinsky, M. H., Kühne, H., Whittington, D. A., Lippard, S. J., and Brudvig, G. W. (2002) *J. Am. Chem. Soc.* **124**, 13392-13393.
33. Brazeau, B. J., Wallar, B. J., and Lipscomb, J. D. (2003) *Biochem. Biophys. Res. Comm.* **312**, 143-148.
34. Walters, K. J., Gassner, G. T., Lippard, S. J., and Wagner, G. (1999) *Proc. Nat. Acad. Sci. USA* **96**, 7877-7882.
35. Wallar, B. J., and Lipscomb, J. D. (2001) *Biochemistry* **40**, 2220-2233.
36. Feig, A. L., and Lippard, S. J. (1994) *Chem. Rev.* **94**, 759-805.
37. Steffan, R. J., and McClay, K. R. (2000), pp. patent no. WO 2000073425, US.
38. Pikus, J. D., Studts, J. M., McClay, K., Steffan, R. J., and Fox, B. G. (1997) *Biochemistry* **36**, 9283-9289.
39. Mitchell, K. H. (2002 Ph.D. dissertation) in *Department of Biochemistry*, University of Wisconsin-Madison, Madison.
40. Bollinger, J. M. J., Tong, W.-H., Ravi, N., Huynh, B.-H., Edmondson, D. E., and Stubbe, J. (1994) *J. Am. Chem. Soc.* **116**, 8042-8032.
41. Sahlin, M., Lassmann, G., Poetsch, S., Slaby, A., Sjoeborg, B.-M., and Graeslund, A. (1994) *J. Biol. Chem.* **269**, 11699-11702.

42. Gupta, N., Bonomi, F., Kurtz, D. M. J., Ravi, N., Wang, D. L., and Huynh, B. H. (1995) *Biochemistry* **34**, 3310-3318.
43. Atta, M., Fontecave, M., Wilkins, P. C., and Dalton, H. (1993) *Eur. J. Biochem.* **217**, 217-223.
44. Fox, B. G., Shanklin, J., Somerville, C., and Münck, E. (1993) *Proc. Natl. Acad. Sci. USA* **90**, 2486-2490.
45. Andersson, M. E., Högbom, M., Rinaldo-Matthis, A., Andersson, K. K., Sjöberg, B. M., and Nordlund, P. (1999) *J. Am. Chem. Soc.* **121**, 2346-2352.
46. Ai, J. Y., Broadwater, J. A., Loehr, T. M., Sanders-Loehr, J., and Fox, B. G. (1997) *J. Biol. Inorg. Chem.* **2**, 37-45.
47. Gherman, B. F., Baik, M.-H., Lippard, S. J., and Friesner, R. A. (2004) *J. Am. Chem. Soc.* **126**, 2978-2990.
48. Whittington, D. A., Rosenzweig, A. C., Frederick, C. A., and Lippard, S. J. (2001) *Biochemistry* **40**, 3476-3482.
49. Sazinsky, M. H., and Lippard, S. J. Manuscript in preparation.
50. Rosenzweig, A. C., Brandstetter, H., Whittington, D. A., Nordlund, P., Lippard, S. J., and Frederick, C. A. (1997) *Proteins* **29**, 141-152.
51. Broadwater, J. A., Achim, C., Münck, E., and Fox, B. G. (1999) *Biochemistry* **38**, 12197-12204.
52. Broadwater, J. A., Ai, J. Y., Loehr, T. M., Sanders-Loehr, J., and Fox, B. G. (1998) *Biochemistry* **37**, 14664-14671.
53. Canada, K. A., Iwashita, A., Shim, H., and Wood, T. K. (2002) *J. Bacteriol.* **184**, 344-349.
54. DeLano, W. L. (2002) <http://www.pymol.org> .
55. Guex, N., and Peitsch, M. C. (1997) *Electrophoresis* **18**, 2714-2723.

Footnotes

*This research was supported by the National Institute of Health Grants GM32134 (S. J. L.) and GM08334 (M.H.S.) and the Italian Ministry of University and Research ,PRIN/2000 and PRIN 2002 (A. D.)

The atomic coordinates and structure factors for the thioglycolate, azide and 4-bromophenol bound structures of ToMOH have been deposited under accession codes 1T0R, 1T0Q, and 1T0S, respectively, in the Protein Data Bank, Research Collaboratory for Structural Bioinformatics, Rutgers University, New Brunswick, NJ (<http://www.rcsb.org/>).

¹The abbreviations used are: BMM, bacterial multicomponent monooxygenase; sMMO, soluble methane monooxygenase; TMO, toluene monooxygenase; PH, phenol hydroxylase; AMO, alkene monooxygenase; MMOH, methane monooxygenase hydroxylase; ToMO, toluene /*o*-xylene monooxygenase; ToMOH, toluene /*o*-xylene monooxygenase hydroxylase; ToMOD, toluene /*o*-xylene monooxygenase effector protein; ToMOC, toluene /*o*-xylene monooxygenase Rieske protein; ToMOF, toluene /*o*-xylene monooxygenase reductase; T4MO, toluene 4-monooxygenase; T3MO, toluene 3-monooxygenase; T2MO, toluene 2-monooxygenase; RNR-R2, ribonucleotide reductase R2 subunit; ACP, acyl carrier protein; r.m.s, root mean square; LB, Luria Bertini; IPTG, isopropyl- β -D-thiogalactoside; MES, 4-morpholinoethanesulfonic acid; MOPS, 3-N-morpholinopropanesulfonic acid; PMSF, phenylmethylsulfonyl fluoride.

Table 2.1. Data collection, phase determination and refinement statistics

	Se-Met thioglycolate	Se-Met 4-Bromophenol	Se-Met Azide
Crystal growth conditions	+ToMOD	+ToMOD 50 mM bromophenol soak	-ToMOD 1.5 mM NaN ₃
Data collection			
Beamline	ALS 8.2.2	ALS 8.2.2	ALS 8.2.2
Wavelength (Å)	0.979	1.127	0.920
Space group	P3 ₁ 21	P3 ₁ 21	P3 ₁ 21
Unit cell dimensions (Å)	182.81x182.81x68.04	183.24x183.24x67.67	182.70x182.70x67.78
Resolution range (Å)	30-2.15	30-2.2	30-2.3
Total reflections	267,124	369,342	354,564
Unique reflections	69,535	66,417	58,500
Completeness (%) ^a	99.3 (93.6)	98.4 (86.4)	93.4 (91.7)
$I/\sigma(I)$	14.4 (8.6)	21.2 (4.1)	23.3 (5.1)
R_{sym} (%) ^b	3.2 (15.1)	9.9 (35.2)	10.0 (38.4)
Phasing			
Method	SAD	Molecular replacement	Molecular replacement
Number of sites/asymmetric unit	32		
Figure of merit	0.65		
Refinement			
R_{cryst} (%) ^c	19.9	23.6	21.8
R_{free} (%) ^d	22.5	27.3	26.7
Number of atoms			
Protein	7348	7365	7382
Water	250	287	418
r.m.s.d. bond length (Å)	0.0061	0.0068	0.0065
r.m.s.d. bond angle (°)	1.24	1.24	1.30
Average B-value (Å ²)	35.0	53.8	33.7

^aValues in parentheses are for the highest resolution shell. ^b $R_{\text{sym}} = \sum_i \sum_{hkl} |I_i(hkl) - \langle I(hkl) \rangle| / \sum_{hkl} \langle I(hkl) \rangle$, where $I_i(hkl)$ is the i^{th} measured diffraction intensity and $\langle I(hkl) \rangle$ is the mean of the intensity for the Miller index (hkl). ^c $R_{\text{cryst}} = \sum_{hkl} ||F_o(hkl)| - |F_c(hkl)|| / \sum_{hkl} |F_o(hkl)|$. ^d $R_{\text{free}} = R_{\text{cryst}}$ for a test set of reflections (5% in each case).

Table 2.2. Comparison of Active Site Pocket Residues from Four BMM Families

ToMO	H96	I100	E103	A107	A110	Q141	F176	M180	L192	F196	T201	F205
T4MO	H96	I100	G103	A107	G110	Q141	F176	I180	L192	F196	T201	F205
T3MO	H96	I100	G103	A107	A110	Q141	F176	F180	L192	F196	T201	F205
PH4	H96	I100	G103	A107	A110	Q141	F176	F180	L192	F196	T201	F205
AlkM	H96	I100	V103	A107	M110	D141	F176	M180	T192	L196	T201	F205
IsoM	H102	T106	V109	A113	M116	D147	F182	M186	T198	V202	T207	F211
PH3	F101	V105	L108	A112	G115	Q146	M180	A184	V196	F200	T205	F209
T2MO	F102	V106	L109	A113	G116	E147	F181	A185	V197	F201	T206	F210
DMS	F107	V111	L114	A117	G120	Q151	F185	A189	I201	F205	T210	F214
MMO	I106	L110	G113	A117	A120	C151	F188	F192	L204	G208	T213	I217
BMO	V103	L107	G109	A114	G117	T148	F185	F189	L201	G205	T210	I214
AMO	M87	L91	A94	A98	G101	L132	G167	F172	L184	A188	T193	L197

ToMO, toluene/o-xylene monooxygenase, *Pseudomonas stutzeri* OX1; T4MO, toluene 4-monooxygenase, *Pseudomonas mendocina* KR1; T3MO, toluene 3-monooxygenase, *Ralstonia pickettii* PKO1; PH4, four component phenol hydroxylase, *Ralstonia eutropha* JMP134; AlkM, alkene monooxygenase, *Xanthobacter sp.* Py2; IsoM, isoprene monooxygenase, *Rhodococcus sp.* AD45; PH3, three component phenol hydroxylase, *Pseudomonas sp.* CF600; T2MO, toluene 2-monooxygenase, *Burkholderia cepacia* JS150; DMSH, dimethyl sulfide hydroxylase, *Acinetobacter sp.* 20B; MMO, soluble methane monooxygenase, composite of all known strains; BMO, butane monooxygenase, *Pseudomonas butanovora*; AMO, $\alpha\beta$ alkene monooxygenase, *Gordonia rubripertinctus* B-276. All sequences were obtained from GenBank (<http://www.ncbi.nlm.nih.gov>)

Table 2.3. Reactivity and Product Distributions of TMOs and Mutant Isoforms

Protein/ Isoform	Active ^a	Toluene Degraded (mM)	TCE degraded (mM)	Butadiene degraded (mM)	% BME ^b R vs. S	Product Distribution (%)			
						Benzyl alcohol	<i>o</i> -cresol	<i>m</i> -cresol	<i>p</i> -cresol
ToMO ^c	Yes	-	-	-	-	-	36	19	45
T3MO (ref 34)	Yes	-	-	-	-	3.7	3.6	10.5	82.3
T2MO	Yes	-	-	-	-	n.d.	n.d.	n.d.	n.d.
T4MO	Yes	8.6 (0.03)	134 (8.8)	0.91	33 67 (1)	0.7	0.9	1.6	96.6
Q141F	Yes	-	-	-	-	0.9	1.2	3.5	94.3
Q141V	Yes	2.66 (0.59)	46 (6.4)	0.91 (0.12)	44 56 (1.6)	1.4	1.3	8.1	89.2
Q141C	Yes	7.03 (0.29)	147 (8.3)	1.2 (0.3)	37 63 (5)	6.0	4.0	5.0	85.0
Q141A	Yes	-	-	-	-	0.9	1.5	5.7	91.9
Q141S	No	-	-	-	-	-	-	-	-
Q141P	No	-	-	-	-	-	-	-	-
I100W	No	-	-	-	-	-	-	-	-
I100R	No	-	-	-	-	-	-	-	-
I100Q	Yes	-	-	-	-	0.6	1.2	0.2	97.9
I100C	Yes*	1.69 (0.4)	88(8.8)	0.17 (0.05)	60 40 (5)	-	-	-	-
F176L	Yes	2.2 (0.07)	150 (2.9)	0.35 (0.12)	40 60 (1)	-	-	-	-
F176A	No	-	-	-	-	-	-	-	-
F196Y	Yes	-	-	-	-	-	1.5	2.8	95.7
F196L	Yes	6.8 (0.09)	157 (10)	0.28(0)	37 63 (5)	2.1	-	0.8	97.1
F196I	Yes*	-	-	-	-	5.3	4.8	1.6	88.3
F196G	No	-	-	-	-	-	-	-	-
G103L	Yes	3.2(0.47)	0.0	1.2(0.04)	10 90 (3)	-	55.4	10.4	25.2
A107S	Yes	7.7(0.48)	139 (3.5)	1.9 (0.08)	16 84 (2)	-	-	-	-
A107G	Yes	-	-	-	-	1.1	59.2	5.6	34.0
G103L/ A107G	Yes*	-	-	-	-	-	89.0	-	11.0
I180F	Yes	-	-	-	42 58 (2)	1.9	0.2	1.2	96.7
L192M	Yes	4.2(0.69)	197(1.2)	-	27 73 (4)	-	-	-	-
F205I	Yes	-	-	-	28 72 (3)	1.0	3.5	14.5	81.0
T201S	Yes	8.7(.21)	138 (1.6)	1.1 (0.04)	58 42 (8)	1.2	1.5	1.4	95.4
T201A	Yes	-	-	-	-	1.3	2.9	1.6	94.2
T201C	Yes	-	-	-	-	1.1	4.5	0.1	94.3
T201F	Yes	-	-	-	-	11.5	41.9	-	46.6
T201X ^d	No	-	-	-	-	-	-	-	-

a. Activity determined by a wholecell colorimetric assay monitoring indol to indigo conversion. * Attenuated activity observed.

b. Butene monoepoxide product distribution for the R and S stereoisomers.

c. Cafaro, V., & Di Donato, A. (unpublished results)

d. X = C, D, H, I, L, M, N, P, Q, V, W, Y.

Results on T4MO and the T4MO mutants in columns 3-6 and 7-10 are from references (32) and (34), respectively.

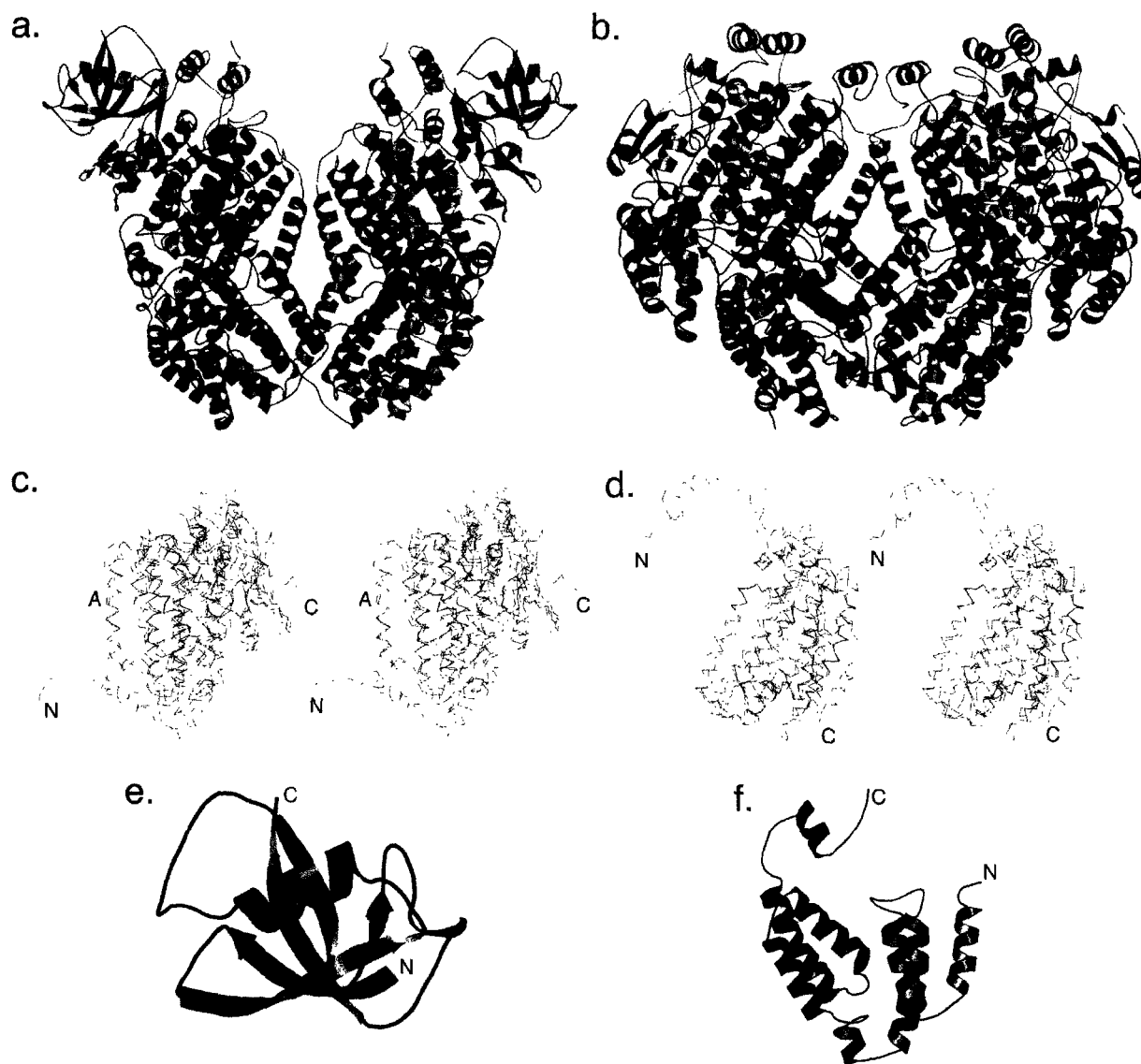


Figure 2.1. Structure of ToMOH and comparison to MMOH. Ribbon diagrams of the (a) ToMOH and (b) MMOH structures colored by polypeptide chain. The α -, β -, and γ -subunits are depicted in teal, purple, and blue, respectively. Superposition of the ToMOH (blue) and MMOH (purple) (c) α - and (d) β -subunit backbone trace in stereo. Letter A in (c) denotes the A-helix (see ref. 8 for full helix labeling scheme) (e) Ribbon diagram of the ToMOH γ -subunit. (f) Ribbon diagram of the MMOH γ -subunit. All graphics here and below were prepared by using PyMOL unless noted otherwise (54).

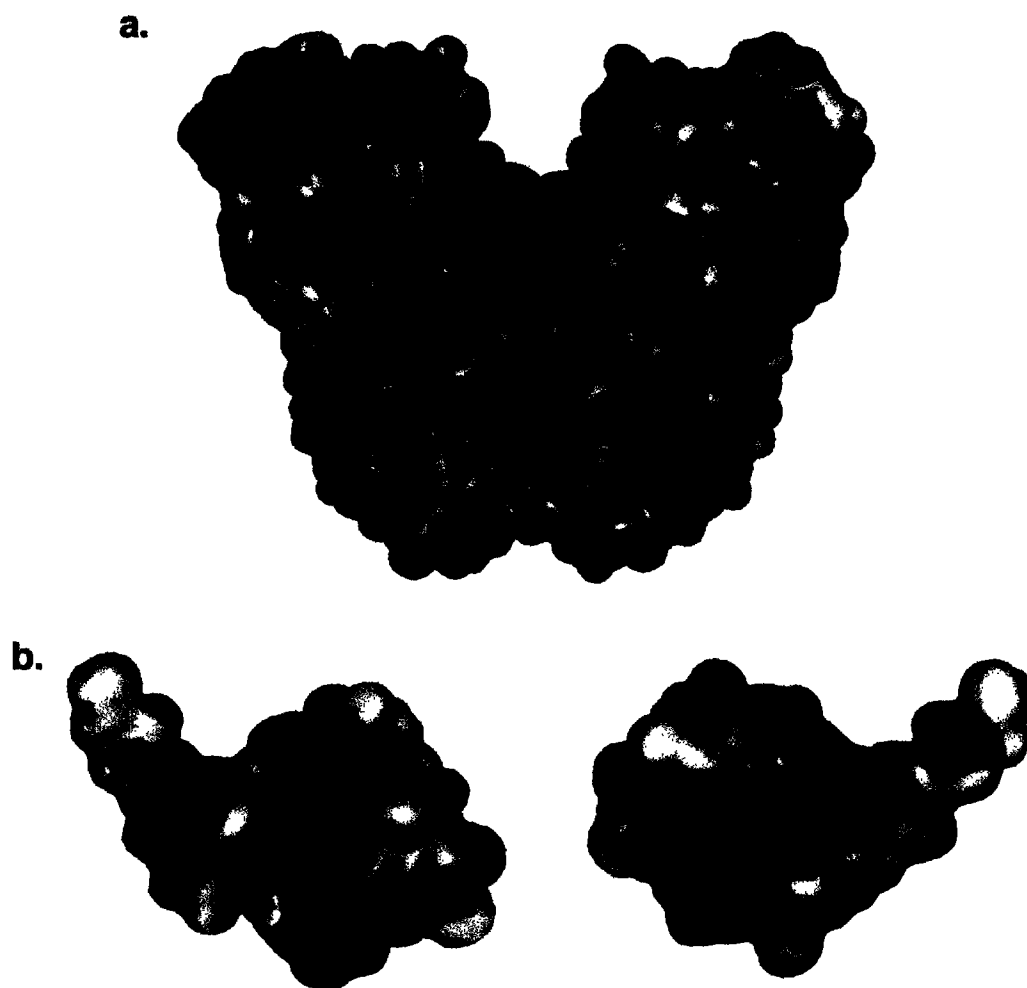


Figure 2.2. Electrostatic surfaces of (a) ToMOH and (b) a ToMOD model built from the coordinates of T4MOD (PDB: 1G10). Both faces of ToMOD are depicted. Red and blue patches represent negatively and positively charged regions. The figure was generated by using the program MOE (CCG Inc.).

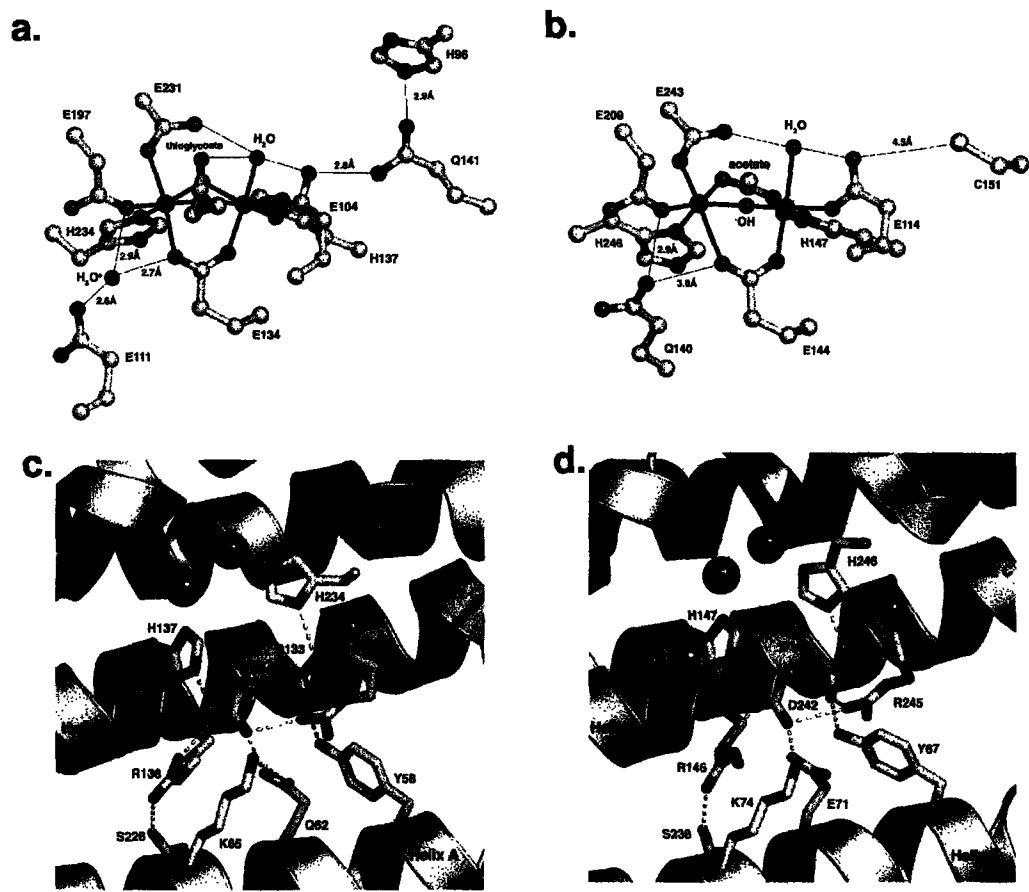


Figure 2.4. Hydrogen bonding at or near the ToMOH and MMOH diiron centers. Hydrogen bond interactions to the coordinated glutamate ligands of (a) ToMOH and (b) MMOH. Atoms are colored as in Figure 2.2a. (c) The conserved hydrogen bonding network behind the histidine ligands in ToMOH and (d) MMOH. Amino acid residues are depicted in stick form and are colored by atom type. Ribbons are colored in green and hydrogen bonds are presented as yellow dashes.

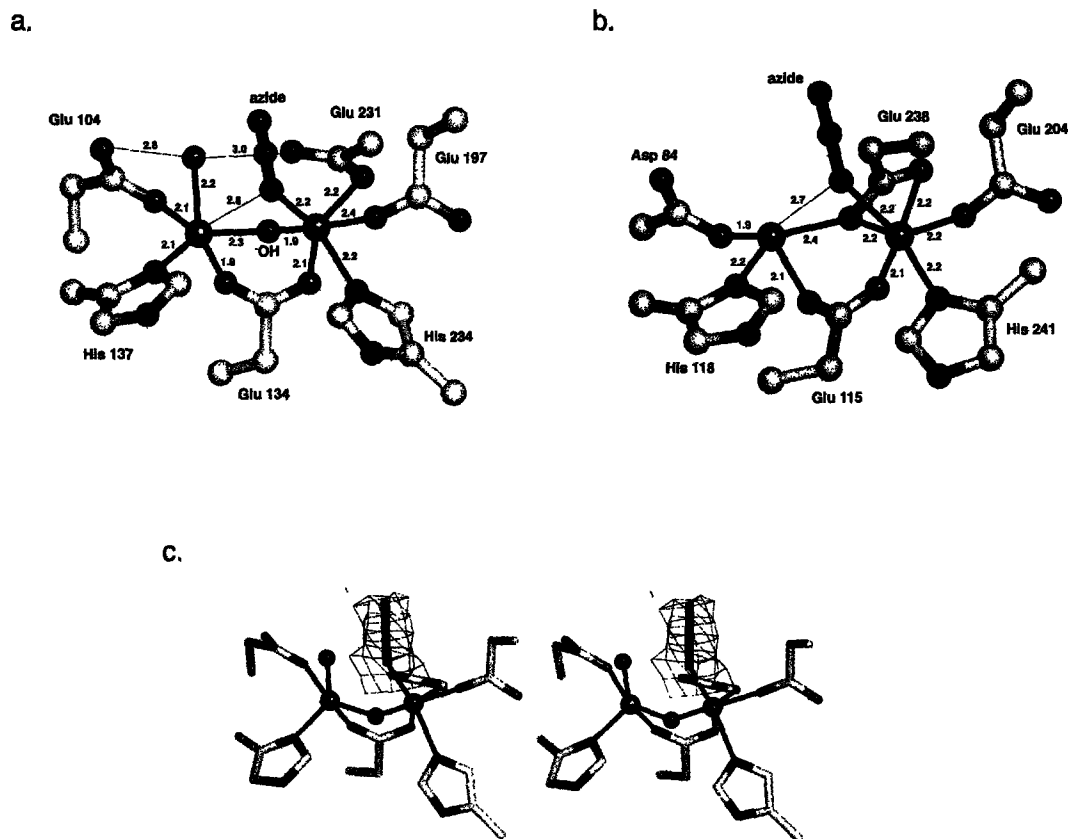


Figure 2.5. Active site structures of ToMOH and RNR-R2 Y208F with bound azide. (a) Active site of oxidized ToMOH with azide bound asymmetrically depicted as in Figure 2a. The Fe2-N-N bond angle is 147° in ToMOH and the Fe-Fe distance is 3.0 Å. (b) The active site of RNR-R2 Y208F, depicted as in Figure 2.2a, with azide bound asymmetrically. The Fe2-N-N bond angle is 130° and the iron atoms are 3.4 Å apart. (c) Stereoview of the azide ligand bound to ToMOH accompanied by a $|F_o| - |F_c|$ ssa-omit map contoured to 1.2 σ .

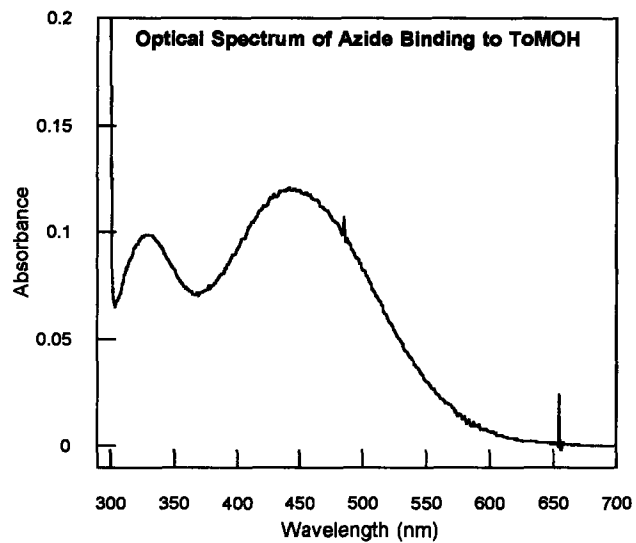


Figure 2.6. Difference UV-vis spectrum of azide binding to ToMOH. The optical spectra of protein solutions containing 30 μM ToMOH, 50 mM NaCl, 10% glycerol in 25 mM MOPS, pH 7.0, \pm 400 mM azide were recorded and subtracted from each other. Peak maxima occur at 335 and 450 nm.

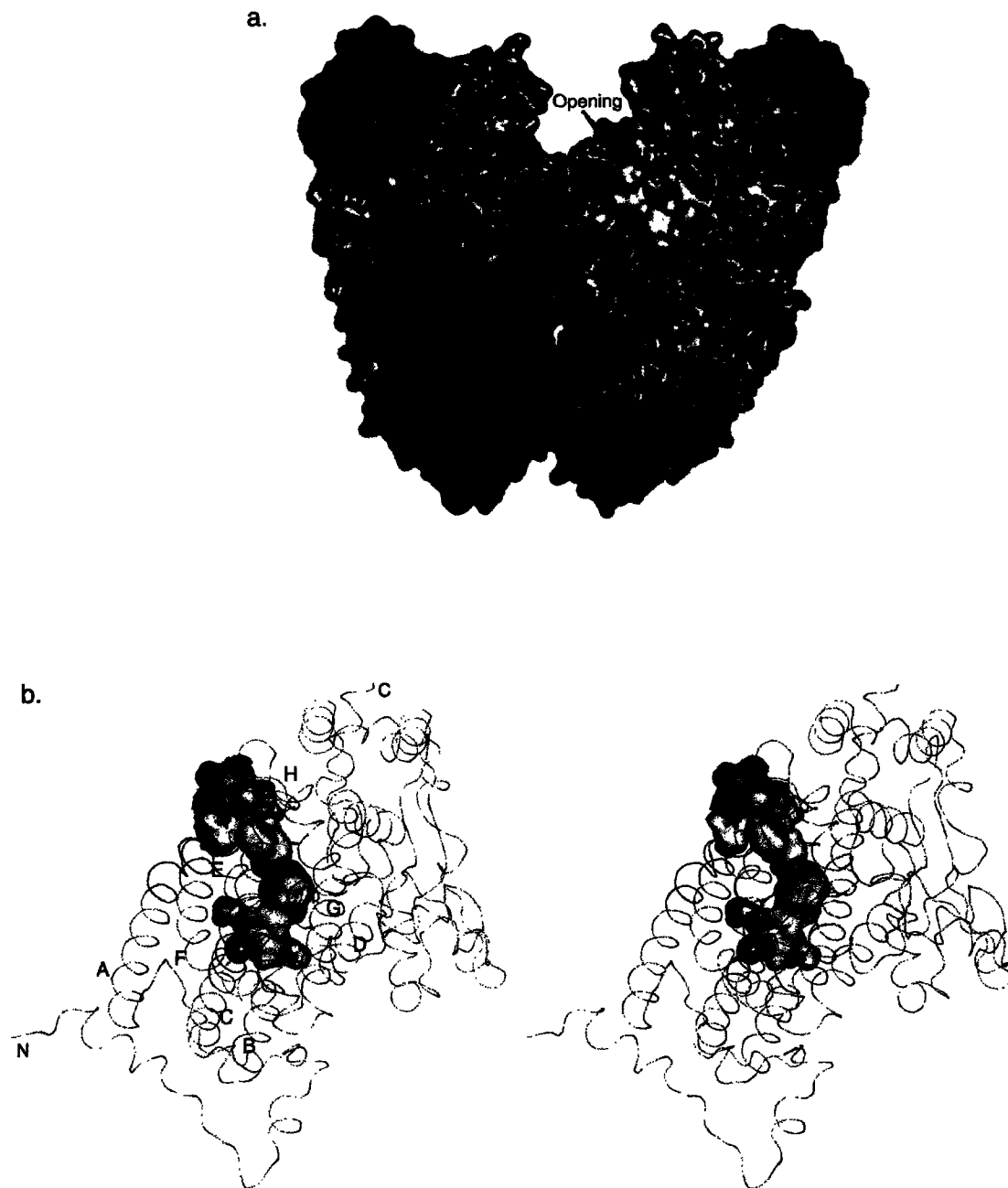


Figure 2.7. The ToMOH substrate channel. (a) Location of the ToMOH channel openings on the surface of the protein, in yellow. The subunits are colored as described in Figure 2.1a. (b) Surface representation of the ToMOH α -subunit channel in the colored by atom type in stereo. The diiron center is represented by orange spheres. The N- and C- termini and helices A-H are labeled.

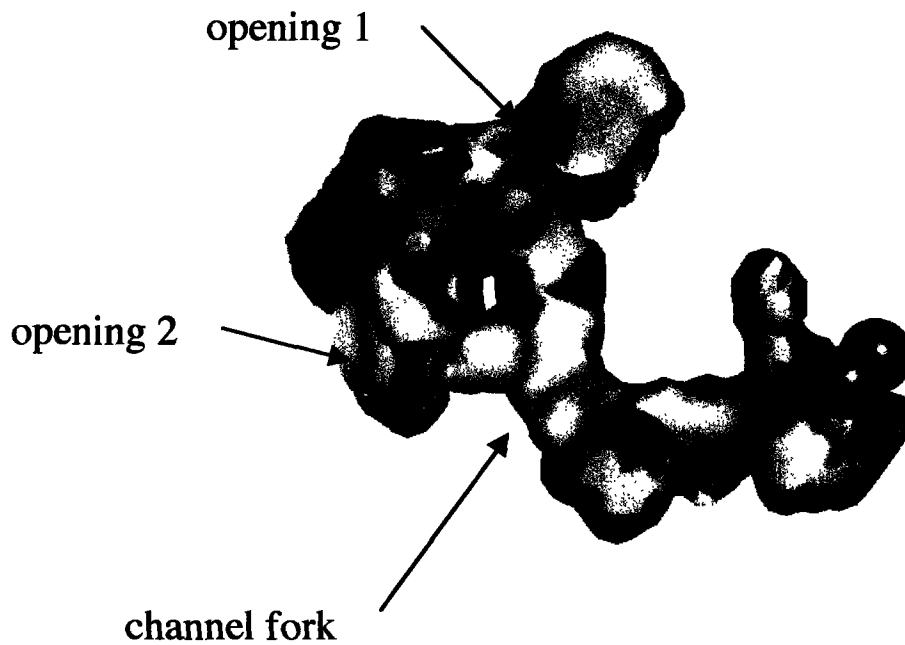


Figure 2.8. Surface representation of the ToMOH substrate channel. The channel is colored by atom type and the iron atoms are depicted as orange spheres. The two possible entrances to the channel are indicated as well as the point at which these entryways merge.

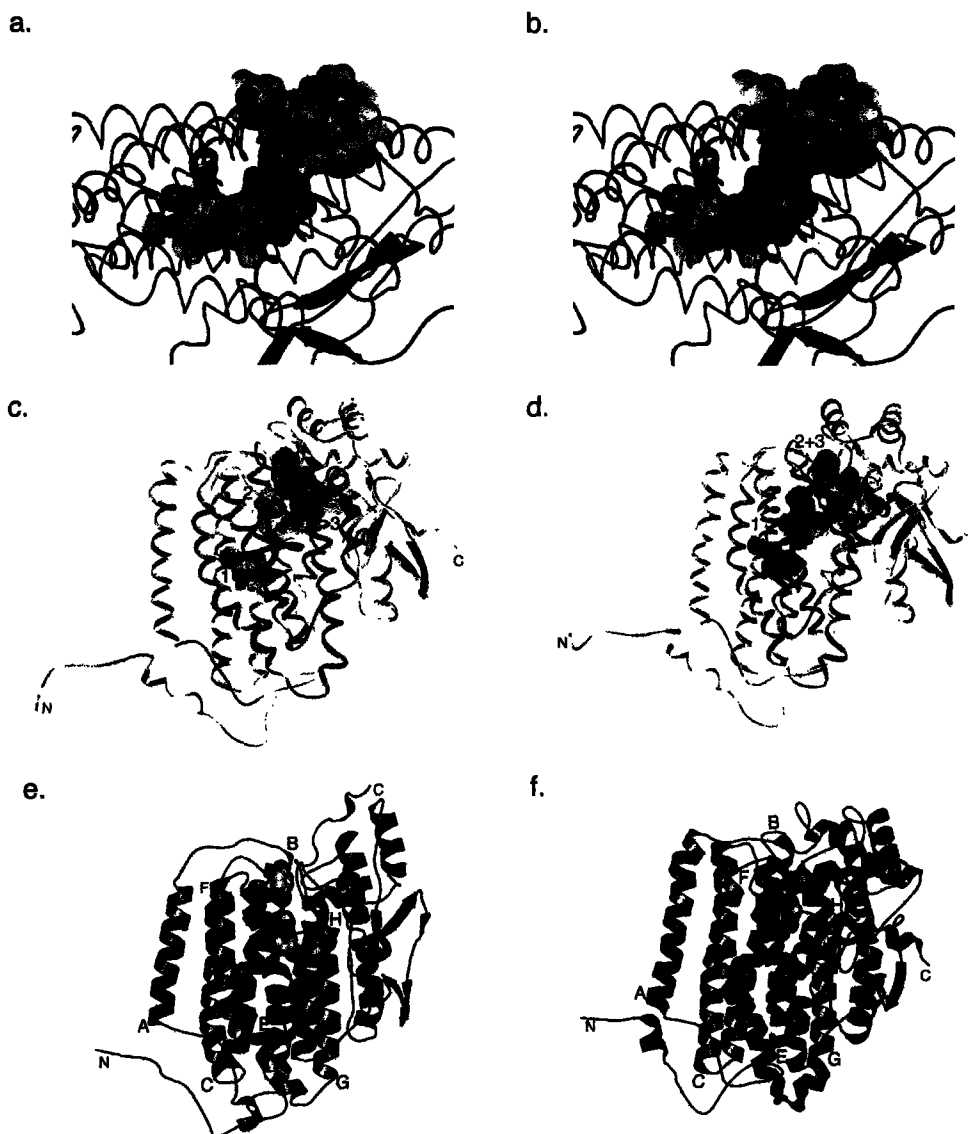


Figure 2.9. Structures of ToMOH and MMOH α -subunits depicting the cavities and channels with bound compounds. (a) Structure of the ToMOH α -subunit depicting water (red spheres) in the channel (gray surface) leading from the diiron center (orange spheres) to the protein surface. The ToMOH helices are depicted as purple ribbons. (b) Structure of the ToMOH α -subunit showing 4-bromophenol in the channel. Bromophenol is colored red and depicted in spacefilling form. The channel and protein are colored as in a. (c) Cavities in the α -subunit of form II MMOH (pdb code 1FZ1), depicted as solid blobs, are labeled 1-3 according to their proximity to the active site iron atoms (orange spheres). (d) Structure of the MMOH α -subunit from form I MMOH (pdb code 1MTY) demonstrating that cavities 2 and 3 can form a continuous channel to the entrance of the diiron center. (e) Ribbon structure of the TMOH α -subunit and (f) MMOH α -subunit with 4-bromophenol and dibromoethane bound, respectively. The small molecules are in spacefill and colored by atom type. The α -helices A-C and E-H are labeled. Helix D lies beneath helix G. Figures c and d were created by using Swiss-PDB Viewer (55).

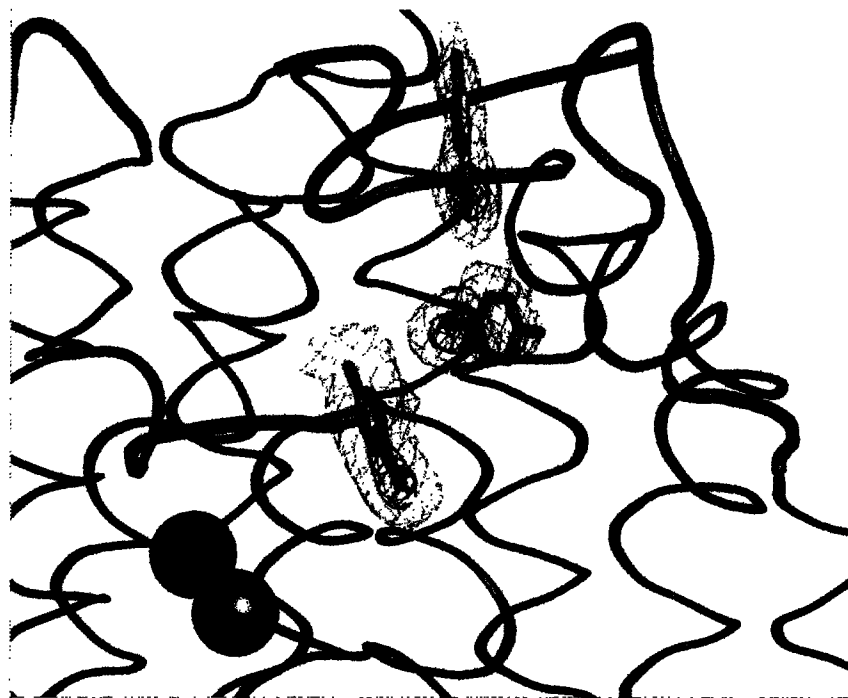


Figure 2.10. F_o-F_c sa-omit map of 4-bromophenol bound to the ToMOH channel. Bromophenol is colored by atom type, iron is represented by orange spheres, and the ToMOH α -sunit helix are shown as ribbons. The sa-omit map is contoured to 3σ (blue) and 7σ (red).

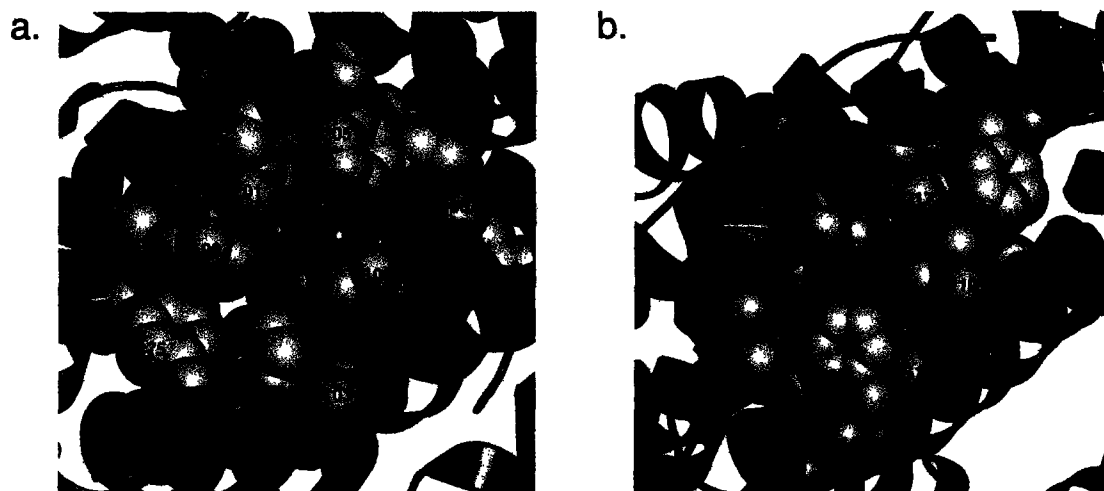


Figure 2.11. Entryways to the ToMOH and MMOH active sites. (a) Spacefilling representation of the ToMOH active site entrance as substrate would approach it through the channel. Access to the diiron center is formed by residues 100, 176 and 196. The diiron center is depicted as orange spheres whereas the rest of the atoms are colored by type. The α -subunit helices are colored blue. (b) Space-filling representation of the MMOH active site pocket depicting access to the diiron center as substrates would approach the leucine gate (residues F188 and L110) after passage through the MMOH α -subunit cavities. Atoms and ribbons are represented as in *a*.

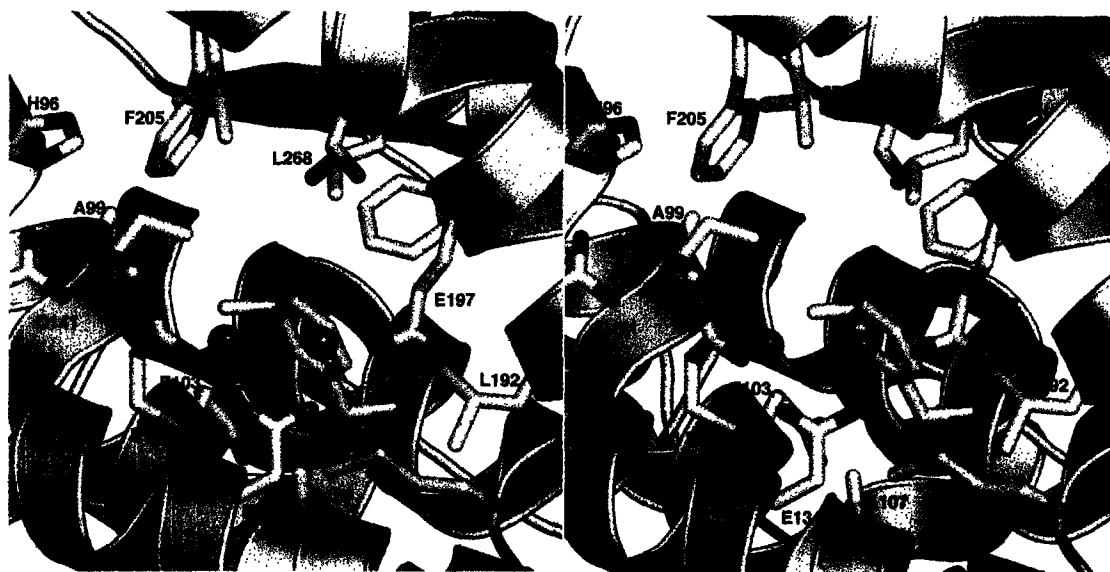


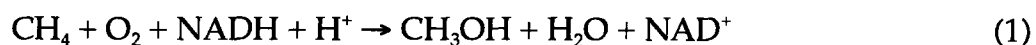
Figure 2.12. Stereoview of the ToMOH active site pocket from the other side of the diiron center. The iron atoms are depicted as orange spheres. Amino acid side chains forming the substrate pocket and iron ligands are colored by atom and are presented as sticks. The α -subunit helices are shown in green.

Chapter 3

**Preparation and X-ray Structures of Metal-Free, Dicobalt and Dimanganese Forms
of Soluble Methane Monooxygenase Hydroxylase from
Methylococcus capsulatus (Bath)**

Introduction

The hydroxylase protein (MMOH) of soluble methane monooxygenase (sMMO) from *Methylococcus capsulatus* (Bath) harbors a non-heme, carboxylate-bridged diiron center within a four-helix bundle that catalyzes the oxidation of methane to methanol (1). This reaction is the first in a metabolic pathway that enables methanotrophic bacteria to utilize methane as a sole source of energy and carbon (eq. 1). In addition to



MMOH, two other proteins, MMOR and MMOB, are required for catalysis. MMOR is a flavin- and ferredoxin-containing reductase that transfers electrons obtained from NADH via its ferredoxin domain to reduce the diiron center in MMOH to the Fe(II)Fe(II) oxidation state. At this oxidation level, MMOH can react with dioxygen to form several activated oxygen intermediates, but only in the presence of a 16-kDa cofactorless regulatory protein, MMOB. Two of these intermediates, a peroxo-bridged diiron(III) species (H_{peroxo}) and an oxo-bridged diiron(IV) complex (Q) have been studied extensively by using a variety of time-resolved spectroscopic techniques and density functional theoretical (DFT) calculations (1,2). As the diiron center proceeds through the different intermediates during the course of the reaction, the Fe–Fe distance and the positions of the bridging carboxylates change to accommodate different oxidation states, substrate binding, and substrate activation (Scheme 3.1). Recently, a fourth protein component within the soluble methane monooxygenase operon, MMOD, was identified in cells expressing sMMO and found to inhibit catalysis by binding to the MMOH α -subunit with an affinity similar to that of MMOB and MMOR (3). The function of the 11-kDa MMOD protein is still unclear, but it has been hypothesized to be involved in the folding of MMOH and assembly of the diiron center in vivo.

Several four-helix bundle containing non-heme diiron proteins, including MMOH, the R2 subunit of type I ribonucleotide reductase (RNR-R2), hemerythrin and bacterioferritin can be converted to their apo forms, from which various metal substituted derivatives have been prepared (4-11). Structural studies of the apo proteins have been useful in probing the contributions of divalent metal ions to the proper folding of the native forms (6,10,12,13). The X-ray structure of apo RNR-R2 from *E. coli*, for instance, has a global fold identical to that of the holo protein and an active site containing four buried negatively charged glutamate residues in close proximity to each other (6,14). This finding raised the question of how a polypeptide can fold into a globular domain with an interior comprising several charged carboxylate residues and how iron might be transferred efficiently to such a pre-organized buried active site. Unlike ribonucleotide reductase, the apo form of hemerythrin is less stable than its holo form, indicating that its dimetallic center contributes significantly to stabilizing the tertiary fold (10).

Structural and spectroscopic studies of the metal-reconstituted forms of the diiron proteins mentioned above have provided insight into their active site geometries and helped to identify alternate metal-ligand interactions that may be relevant to catalysis and function (4-11). Cobalt(II) and manganese(II) have been the most attractive candidates for replacing the native iron in these proteins. Both are similar to iron(II) in charge and ionic radius and have attractive optical (Co^{2+}) and magnetic (Co^{2+} and Mn^{2+} are EPR-active) properties that allow their binding geometries to be investigated. In addition, both can exist in different oxidation states. Stable peroxo- and superoxo-bridged dicobalt(III) centers are well known (15) and, if formed in the MMO active site, could provide valuable information regarding the structure of the H_{peroxo} intermediate. Stable high-valent dimanganese centers such as Mn(III)Mn(IV) and

Mn(IV)Mn(IV) have precedent in both synthetic analogues and metalloenzymes (16,17). If formed in manganese-reconstituted MMOH, they could provide a model for high-valent intermediates such as Q in sMMO and X in RNR-R2. Dimanganese(II) derivatives have been prepared of ribonucleotide reductase (4,8,18), hemerythrin (10,18), and methane monooxygenase (5). The X-ray structure reported for manganese-substituted *E. coli* RNR-R2 in the Mn(II)Mn(II) oxidation state proved to be a good mimic of the chemically and photo-reduced enzyme, whereas the mixed-valent Mn(II)Mn(III) structure identified a novel iron-ligand conformational change in one of the coordinated Glu ligands. Both structures contributed to a mechanistic understanding of O₂ activation and tyrosyl radical generation in RNR (4,8). Dicobalt(II) forms have also been reported for ribonucleotide reductase (7), hemerythrin (11) and bacterioferritin (9), allowing them to be characterized by optical spectroscopy. The structure of dicobalt(II)-reconstituted mouse RNR-R2 exhibited metal ligand conformations that were not previously observed in the active sites of these enzymes. The dicobalt(II) structure resembled more closely that of the reduced MMOH diiron center than reduced *E. coli* RNR-R2 (19). Neither the dimanganese(II) and the dicobalt(II) metal-substituted forms of RNR reacted with dioxygen (7,18). The dicobalt(II) complexes were also unreactive towards hydrogen peroxide.

We report here a new method for preparing apo MMOH from the native enzyme in nearly quantitative yield. The apo protein is stable and, upon addition of Fe(NH₄)₂(SO₄)·6H₂O, MMOH regains most of its native activity. The availability of apo MMOH allowed us to examine the effects of metallation in the presence of MMOB or MMOD and to prepare cobalt and manganese reconstituted forms of MMOH. The X-ray crystal structures of apo MMOH and derivatives with dinuclear Co(II) and dinuclear Mn(II) centers were determined. The results provide new insight into the

geometric flexibility of the carboxylate-bridged dimetallic centers and the contribution of the coordinated metal ions to the folding and stability of the four-helix bundle that houses them. These results also suggest possible effects of MMOB and MMOD on the hydroxylase protein.

Experimental

Materials and General Methods

MMOH was purified from *M. capsulatus* (Bath) as previously described (3,20). Purified MMOH contained 3.5-4.0 Fe/dimer and catalyzed the epoxidation of propylene with a rate of 0.35 s^{-1} (250 mU mg^{-1}) at $25 \text{ }^\circ\text{C}$. MMOB (21), MMOR (22), and MMOD (3) were obtained from recombinant expression systems in *E. coli* as described. Iron analysis was performed by using a ferrozine assay (23).

Kinetics of Iron Release from MMOH_{red}

A solution of $100 \text{ }\mu\text{M}$ MMOH in 25 mM MOPS, $\text{pH } 7.0$, 120 mM NaCl, $100 \text{ }\mu\text{M}$ methylviologen, and 5% (v/v) glycerol was made anaerobic by repeated vacuum/ N_2 cycles. Sodium dithionite was added to a final concentration of 5 mM and the solution was incubated for at least 30 min to allow full reduction of the MMOH diiron centers. A Thünberg cuvette filled with 1.8 mL 25 mM MOPS, $\text{pH } 7.0$, 120 mM NaCl, and 2 mM 1,10-phenanthroline was made anaerobic by repeated vacuum/ N_2 cycles and sodium dithionite was added to a final concentration of 5 mM . The cuvette was mounted in a HP8354 diode array spectrophotometer (Hewlett Packard) and the reaction was started by anaerobic addition of $200 \text{ }\mu\text{L}$ of the MMOH_{red}-containing solution to the cuvette (final concentration, $10 \text{ }\mu\text{M}$). The formation of $[\text{Fe}(o\text{-phen})_3]^{2+}$ was monitored at 510 nm ($\epsilon = 11,100 \text{ M}^{-1}\text{cm}^{-1}$) for 8-36 h at $25 \text{ }^\circ\text{C}$. Reactions in the presence of MMOD and MMOB

were performed in the same manner by adding 220 μM of either protein to the 100 μM MMOH solution prior to reduction by dithionite.

Preparation of Apo MMOH

A 2 mL solution of 0.2 mM MMOH, 4 mM 1,10-phenanthroline, 1 mM methylviologen in 25 mM MOPS pH 7.0, 120 mM NaCl, 5% glycerol was made anaerobic in a glass vial with a rubber septum by repeated vacuum/ N_2 cycles. A 20 μL aliquot of an anaerobic 400 mM sodium dithionite solution was added and the reaction was incubated at room temperature for 5 h. Apo MMOH was separated from these reagents and the $[\text{Fe}(o\text{-phen})_3]^{2+}$ complex by using an EconoPac 10DG (BioRad) disposable desalting column equilibrated with a buffer containing 25 mM MOPS, pH 7.0, 120 mM NaCl, and 5% glycerol. Fractions containing apo MMOH were identified by their absorption at 280 nm, pooled, concentrated, and stored at $-80\text{ }^\circ\text{C}$.

Activity Assays

The activity of sMMO was assayed by monitoring the formation of propylene oxide from propylene by gas chromatography or consumption of NADH ($\epsilon_{340} = 6220\text{ M}^{-1}\text{ cm}^{-1}$) by UV-vis spectroscopy essentially as described (3,24).

Kinetics of Iron Reconstitution of Apo MMOH

Iron reconstitution of apo MMOH was performed as described previously with the following changes (3). The reconstitution reaction was run under aerobic and anaerobic conditions; the latter employed a septum-sealed glass vial made anaerobic by repeated vacuum/nitrogen cycles. Apo MMOH (47.5 μM) was incubated with 0.5 mM $\text{Fe}(\text{NH}_4)_2(\text{SO}_4)_2 \cdot 6\text{H}_2\text{O}$ in 25 mM MOPS, pH 7.0, 120 mM NaCl, 2 mM DTT, and 5% (v/v) glycerol) at 25 $^\circ\text{C}$. At several time points after adding the iron solution, samples were taken and assayed for propylene activity by gas chromatography as described above.

The effect of the iron concentration on the kinetics of iron reconstitution was studied by anaerobic incubation of 35 μM apo MMOH with 1.48, 0.49, and 0.15 mM $\text{Fe}(\text{NH}_4)_2(\text{SO}_4)_2 \cdot 6\text{H}_2\text{O}$ in 25 mM MOPS, pH 7.0, 120 mM NaCl, 2 mM DTT, and 5% (v/v) glycerol, at 25 °C. Aliquots were taken at various time points over the course of several hours and the MMO activity was assayed at 25 °C by using propylene as a substrate and monitoring the concentrations of NADH at 340 nm.

Isothermal Titration Calorimetry

Calorimetric experiments were performed by using a VP-ITC titration calorimeter (Microcal). All protein samples were exchanged by dialysis at 4 °C into a buffer comprising 25 mM MOPS, pH 7.0, and 5% glycerol before use. Tris(2-carboxyethyl)phosphine (TCEP) (1 mM) was added to all buffers in which MMOD was present. The reaction cell contained 1.4 mL holo or apo MMOH at 15 μM concentration. The injection syringe was filled with 250 μM MMOD or 313 μM MMOB and was rotating at 310 rpm during the titration. The titration experiments consisted of 40 injections, each of 6 μL for a duration of 6 s with 420 s intervals between injections. The temperature during the titration was kept at 20 °C. The data were analyzed by using software provided by Microcal.

Optical Spectroscopy of Co(II)-MMOH

Apo MMOH was centrifuged at 14,000 g for 30 min immediately before addition of cobalt(II) chloride to remove small amounts of denatured protein that would otherwise make the observation of the very weak Co(II) d-d transitions difficult. A cuvette was filled with 450 μL of a 105 μM apo MMOH solution in 25 mM MOPS, pH 7.0, 120 mM NaCl, and 5% (v/v) glycerol, and the spectra were recorded. A small aliquot of a 10 mM $\text{CoCl}_2/0.1$ mM HCl stock solution was added and a second

spectrum was taken after re-equilibration. After correction for dilution, a difference spectrum was calculated by subtracting the apo MMOH spectrum from that of the Co-containing solution.

CD Spectroscopy of Holo and Apo MMOH

Samples of apo and holo MMOH for circular dichroism analysis contained 10 mM potassium phosphate, pH 7.0, and 0.1 μ M hydroxylase. Spectra were recorded on an Aviv CD spectrophotometer at 25 °C and were the average of 5 scans.

Crystallization of Apo MMOH and its Mn(II) and Co(II) Derivatives

Apo, Co(II)-, and Mn(II)-substituted MMOH were crystallized at 4 °C by using a method similar to those previously published with the following modifications (25). Well solutions contained 160 mM MOPS, pH 7.0, 350 mM CaCl_2 , 10 % (w/w) PEG 8000 and 0.015 % NaN_3 . Protein drops contained 3 μ L of 40 μ M apo MMOH in 25 mM MOPS, pH 7.0, 1.5 μ L of well solution, and 1.5 μ L of an MMOH microseed solution prepared in the mother liquor. Mn(II) and Co(II) reconstituted MMOH were created by crystallizing apo MMOH in the presence of 10-20 mM MnCl_2 or CoCl_2 or soaking apo MMOH crystals for 30 min in a cryo-solution comprising 160 mM MOPS, pH 7.0, 350 mM CaCl_2 , 10 % (w/w) PEG 8000, 25% (v/v) glycerol and 50 mM MnCl_2 or CoCl_2 . Crystals of apo MMOH did not grow well in the presence of MnCl_2 and therefore a structure of Mn(II)-grown MMOH was not determined.

X-ray Diffraction Data Collection and Structure Refinement

Data sets were collected at SSRL on beam lines 9-1 and 7-1. The program MOSFLM (26) was used to determine a collection strategy with knowledge of the space group ($P2_12_12_1$), and the unit cell (70 Å x 171 Å x 222 Å). Data sets were collected at 100 K with a 0.5° oscillation over a 100-120° rotation of the crystal. The HKL suite of

programs were used to index and scale the data (27). The scaling and refinement statistics for the apo, Co(II)-grown and Mn(II)-soaked apo MMOH structures are listed in Table 3.1.

The initial phases were determined by rigid body refinement in CNS (28) using a starting model in which the iron and the metal-coordinating ligands were removed. The protein models were built in XtalView (29) and refined by using CNS. PROCHECK was used to check the final model geometry and statistics (30). The atomic coordinates and structure factors for the apo, Mn(II), and Co(II) MMOH structures have been deposited in the Protein Data Bank, Research Collaboratory for Structural Bioinformatics, Rutgers University, New Brunswick, NJ (<http://www.rcsb.org/>).

Results

Generation of Apo MMOH

A previously reported method for the preparation of apo MMOH used 3,4-dihydroxybenzaldehyde to extract the ferric ions from the active sites of the resting enzyme (5). The ferric complex of this ligand remains bound to the protein and the addition of a second chelating agent, 8-hydroxyquinolinesulfonate, is required to prepare iron-depleted MMOH. In our hands this method did yield preparations with ~0.2 Fe/MMOH, but the procedure also resulted in the formation of a brown color that was not removed easily by anion exchange or size exclusion chromatography.

Extraction of iron from iron-binding proteins is often easier when the metal ion is reduced to Fe^{2+} , for which ligand exchange rates are more rapid compared to Fe^{3+} . To test whether this property also holds for MMOH, the enzyme was reduced by the addition of excess sodium dithionite and methylviologen. An aliquot was then transferred anaerobically to a cuvette containing the strong Fe^{2+} chelator 1,10-

phenanthroline, and the formation of the red/orange $[\text{Fe}(o\text{-phen})_3]^{2+}$ complex was monitored by optical spectroscopy at 510 nm ($\epsilon_{510\text{ nm}} = 11,100\text{ M}^{-1}\text{cm}^{-1}$). Figure 3.1 shows that formation of the tris(phenanthroline)iron(II) complex is complete after approximately 3 h at 25 °C. A fit of the absorbance at 510 nm using a single exponential gave a rate constant of 1.6 h^{-1} and the release of 3.8 Fe atoms perMMOH dimer. Excess reagents and the $[\text{Fe}(o\text{-phen})_3]^{2+}$ complex are easily separated from apo MMOH by using a desalting column. This new method gave colorless apo MMOH preparations with very little residual iron ($< 0.1\text{ Fe/MMOH dimer}$) in 80-90% yield.

Both MMOB and MMOD affect the structure of the MMOH diiron sites (3). It has been demonstrated previously that MMOB can block the reconstitution of active MMOH from apo MMOH and $\text{Fe}(\text{NH}_4)_2(\text{SO}_4)\cdot 6\text{H}_2\text{O}$, but it is unclear whether MMOD inhibits iron uptake since activity assays were the method by which iron reconstitution was monitored and MMOD inhibits hydroxylase activity (3). To determine whether MMOB and MMOD affect the stability of MMOH_{red} , the reaction of the latter with 1,10-phenanthroline was repeated in the presence of 2.2 mol-equivalents of MMOB or MMOD (Figure 3.1). The release of Fe^{2+} is severely inhibited by both proteins, the rate constants being 0.07 h^{-1} and 0.11 h^{-1} , respectively, for the two.

Reconstitution of Hydroxylase Activity

Previous studies reported variable success in reconstitution of catalytically active MMOH from apo MMOH and iron salts (5,31). Figure 3.2 reveals that simple addition of excess $\text{Fe}(\text{NH}_4)_2(\text{SO}_4)\cdot 6\text{H}_2\text{O}$ to apo MMOH, either anaerobically or aerobically, restores the formation of active enzyme to the same level as native MMOH within 2 h at 25 °C. The rate of reconstitution depends on the iron concentration (Figure 3.3). The observation that complete restoration of activity occurs upon incubation of apo MMOH with Fe^{2+} demonstrates that the apo protein is not irreversibly unfolded. Anaerobic

addition of $\text{Fe}(\text{NH}_4)_2(\text{SO}_4)_2 \cdot 6\text{H}_2\text{O}$ to apo MMOH also results in formation of the $g = 16$ signal typical of MMOH_{red} (1), providing additional evidence that the native diiron center has been restored (not shown) (32).

Isothermal Titration Calorimetry

Several different experimental techniques have been used to determine the binding constants of MMOB and MMOD to MMOH (3,24); however, no method has yet compared directly the relative affinities of these two proteins for apo and holo MMOH. Isothermal titration calorimetry (ITC) was therefore performed to measure the binding of MMOB and MMOD to the metallated and de-metallated forms of the hydroxylase. The normalized binding isotherms and calculated titration curves are presented in Figure 3.4. The data were best fit by using a cooperative binding model in which two molecules of MMOB or MMOD were assumed to bind to MMOH with affinities, K_{d1} and K_{d2} (eq 2). In these equations H represents MMOH and X either MMOB or MMOD.



The calculated dissociation constants are presented in Table 3.2. These results clearly indicate that MMOB has a stronger affinity for holo MMOH than MMOD and that the latter binds more tightly to apo MMOH than does MMOB. The MMOB and MMOD binding constants for apo and holo MMOH, as determined by ITC, are consistent with the values derived from previous work (3,24).

UV-Vis Spectroscopic Study of Cobalt-Substituted MMOH

The availability of an efficient method for preparing apo MMOH with low iron content and no contaminating chromophores allowed us to explore the coordination chemistry of the MMOH active site ligands. Two metal-substituted forms of MMOH containing dicobalt(II) and dimanganese(II) centers were prepared. The optical

spectroscopic bands of Co(II) contain valuable information about its coordination geometry (33). Octahedrally coordinated d^7 Co(II) complexes typically display visible absorption bands with extinction coefficients of $5\text{-}40\text{ M}^{-1}\text{cm}^{-1}$. Tetrahedral or pseudotetrahedral sites show much more intense d-d bands with extinction coefficients ranging from $200\text{-}800\text{ M}^{-1}\text{cm}^{-1}$, and 5-coordinate sites have intensities that are somewhere in between these values. For this reason, substitution with cobalt(II) is often used to probe the coordination properties of metal binding sites in proteins having spectroscopically silent metal ions such as Zn^{2+} (34). Figure 3.5 shows difference spectra obtained after subtraction of the spectrum of apo MMOH from that of the apo protein in the presence of 1, 2 and 4 mole-equivalents of CoCl_2 . The spectra exhibit maximal absorption at 520 nm with an extinction coefficient of $35\text{-}40\text{ M}^{-1}\text{cm}^{-1}$. Addition of excess CoCl_2 resulted in additional spectral changes with a similar shape but significantly lower extinction coefficient ($7\text{ M}^{-1}\text{cm}^{-1}$) that is typical of aquated Co(II). Prolonged standing of the Co-containing MMOH solution in air did not lead to any spectral changes, indicating that the metal ion is not readily oxidized to the Co(III) state by dioxygen. The extinction coefficient for the protein-bound Co(II) is in the middle of the range characteristic of hexacoordinate Co(II). Five-coordinate Co(II) often shows additional bands around 600 nm. Since these are absent in Co(II)-MMOH, the metal coordination in the enzyme appears to be distorted octahedral. The spectrum of $\text{Co}_2\text{-Hr}$ displays a maximum at 519 nm with a very similar extinction coefficient of $34\text{ M}^{-1}\text{cm}^{-1}$ (Table 3.3) (11). In addition it has bands at 650 nm and 850 nm, and a pentacoordinate Co(II) site was therefore assigned (11). Binding of Co(II) to bacterioferritin gives rise to a spectrum with maxima at 520, 555, 600, and 625 nm with extinction coefficients ranging from $75\text{-}155\text{ M}^{-1}\text{cm}^{-1}$. This spectrum was interpreted as arising from pentacoordinate or pseudotetrahedral Co(II) (9). The Co(II) form of ribonucleotide

reductase contains maxima at 515 and 550 nm with $\epsilon_{550\text{nm}} = 115 \text{ M}^{-1}\text{cm}^{-1}$ indicative of a pentacoordination (7).

Global Folds of Apo, Mn(II), and Co(II) MMOH

Apo MMOH crystals were grown by using conditions similar to that for the holo protein. The crystallization drops contained a substantial amount of heavy precipitate as compared to those observed for holo MMOH, which are typically free of aggregated protein. Crystals of apo MMOH diffracted on average to 2.3 Å versus 2.0 Å for the holo protein and were roughly half the size (0.25 x 0.1 x 0.1 mm vs. 0.5 x 0.3 x 0.08 mm). The addition of CoCl_2 to the crystallization solutions resulted in larger crystals, comparable in size to holo MMOH, which diffracted to 2.0-2.1 Å and had less precipitation. Well diffracting crystals did not grow in the presence of MnCl_2 . Instead, heavy precipitate was generated. The Mn(II) form of MMOH was generated by soaking apo crystals with MnCl_2 . Because of differences in the preparation of the Co(II) and Mn(II) MMOH crystals, the final structures will be referred to as Co(II)-grown and Mn(II)-soaked MMOH. The observations made during the crystallization of holo and apo enzyme suggest that the apo protein is prone to aggregation due to localized unfolding in the metal-coordinating four-helix bundle and that the addition of divalent metal ions like Co(II) may help refold the protein. The CD spectra of apo and holo MMOH are identical, indicating the overall structure of MMOH in solution is perturbed very little by removal of its iron (Figure 3.6).

The global structure of apo MMOH is similar to that of MMOH in both crystal forms I and II holo (25,35). Regions of the α -subunit, including portions of the diiron-containing four-helix bundle, however, are more disordered with higher average temperature factors (Table 3.4, Figure 3.7a, b). The electron density for residues 195-

206, 247-267, and 312-325, on helices E, F, and H, respectively, near the α/β -subunit interface is sparse and, for some residues, absent altogether. This result reflects disorder, as evidenced by higher average B-factors in these regions (68.3 \AA^2) compared to the same regions in reduced MMOH (38.3 \AA^2) and by the average B-factors for the α -subunits of holo (27.4 \AA^2) and apo MMOH (41.7 \AA^2). Except for the regions of helices E, F, and H mentioned above, the folds of the α , β , and γ subunits appear unperturbed by the lack of iron. The same regions that are disordered in apo MMOH are even more so in Mn(II)-soaked MMOH. The relative thermolability of these regions increases on average from 42.0 \AA^2 to 85.6 \AA^2 (Table 3.4, Figure 3.7d). The only difference occurs for residues near the metal-binding center, which are ordered due to the presence of Mn(II). In the Co(II)-grown structure, helices E, F, and H are perfectly ordered and electron density is available for all of their residues. This observation is consistent with lower average B-factors and smaller discrepancies between the B-factors of the α -subunit and the regions of interest on helices E, F, and H.

The "northern" end of the four-helix bundle is highly ordered in the apo, Mn(II), and Co(II) MMOH structures. This ordering may reflect stability provided by the hydrogen bonding network behind the active site histidines that extend $\sim 12\text{-}13 \text{ \AA}$ to the surface of the protein (21). In the apo and Mn(II) structures, electron density is available for all of these residues and their positions with respect to those in the MMOH_{red} and MMOH_{ox} structures are not perturbed (Figure 3.8). In the apo RNR-R2 structure, a similar network remains intact (6).

Active Sites of Apo, Mn(II) and Co(II) MMOH

In the structure of apo MMOH, the metal-coordinating ligands at the active site demonstrate more flexibility (Figure 3.9, 3.12a). Glu-209 and Glu-243, which form part of helices E and F, respectively, are partially disordered. The positions of Glu-114 and Glu-144 are similar to those observed in the holo protein with the exception of the Glu-114 carboxylate group, which has rotated by 90° with respect to its position in the holo protein to hydrogen bond to two water molecules modeled into the electron density between the four glutamates. The analogous residue in *E. coli* RNR-R2, D84, can adopt a conformation similar to that of Glu-114 in apo MMOH and coordinate to iron in both a bidentate chelating or monodentate fashion, depending upon the oxidation state and preparation of the enzyme (8,36,37). The alternate conformation of the Glu-114 carboxylate in the apo structure suggests that second shell coordination sphere constraints, originating from the protein to hold the carboxylate in place, are absent. Hydrogen bonding to the terminal water molecule on Fe1 in the oxidized and reduced forms of MMOH may dictate the typical monodentate coordination of Glu-114. Second coordination sphere water molecules, however, also interact with the glutamate and the terminal water molecule in the different oxidized and reduced structures of MMOH. In the oxidized form, positional variations and/or the absence of these waters from one structure to the next make them unlikely contributors to the stabilization of the Glu-114 geometry. In the reduced form, a water molecule consistently bridges the non-coordinating oxygen of Glu-114 and the amide backbone of Leu-110, but it is unknown whether this water has a significant impact on the conformation of this residue (25,35,38,39). Glu-144 of apo MMOH forms hydrogen bonds to both an active site water molecule and the amine moiety of Gln-140, the side chain of which has shifted slightly compared to its position in the holo protein. The remaining metal-coordinating ligands,

His-147 and His-246, are highly ordered. The His-246 side chain in apo MMOH shifts slightly towards the vacant Fe²⁺ binding, yet despite this shift is still within hydrogen bonding distance of Asn-242. The position of His-147 is unperturbed in the apo structure.

The two water molecules are modeled into the electron density at the Fe1 binding position in the active site. These waters are 2.4 Å from each other and 2.5-3.0 Å from the carboxylate and histidine ligands. However, they cannot neutralize the overall four negative charges contributed by the glutamates in this buried region of the protein nor do they account for all of the electron density in the area. Calcium, which is a major constituent of the MMOH crystallization buffer, could not be modeled successfully into this region. Attempts to do so at full occupancy resulted in unreasonable geometry and negative difference electron density artifacts. Given the overall disorder in the apo MMOH active site from both α -subunits, we cannot exclude the possibility this site may be at least partially occupied by an adventitious cation like sodium, the presence of which would help to neutralize the buried charge. A hydronium ion (H₃O⁺) or protonation of the histidines would also neutralize the charge. Between Glu-144 and Asn-140 there is a large feature of difference electron density. Again, because of disorder within the region, it is unknown what atoms account for this electron density. In the absence of any definitive proof, we tentatively assign this density to water but recognize fully that a satisfactory solution is not at hand.

The Mn(II)-reconstituted active sites in each of the two α -subunits have metal-ligand distances and geometry similar to those in the chemically reduced forms of MMOH (Figures 3.10c,d; 3.11). The Mn–Mn distances lie between 3.2-3.5 Å depending on the protomer, but otherwise the dimanganese and diiron forms of MMOH are

isostructural (Figure 3.2b). The active site of Co(II)-grown MMOH is also similar to that of the chemically reduced native protein and Mn(II) reconstituted MMOH except that the Co–Co distances are shorter, being 3.1 Å and 3.0 Å (Figures 3.10d,e; 3.11; 3.12c). The pseudooctahedral geometry observed for both cobalt ions in both protomers is in accord with electronic spectral data on the Co(II)-reconstituted enzyme. Comparison of the Mn(II), Co(II), and Fe(II) active sites reveals that Glu-209, Glu-243, and His-246 are the most flexible ligands, a feature that is perhaps required to accommodate the varying metal-metal distances (Figure 3.12b, c). It is also of interest to note that the position of metal 1 does not vary among these structures whereas that of metal 2 does. Similar observations were made previously by comparing the oxidized, mixed-valent, and reduced forms of MMOH (39). As a result of the movements of metal 2 and its coordinating residues, the water molecule between the metals that extends into the active site pocket can adopt bridging, semi-bridging, and terminal coordination modes. The varied positions of this water molecule may be important for opening a coordination site for the reaction of dioxygen with one of the iron atoms (38).

Discussion

Effects of MMOB and MMOD on Iron Binding to MMOH

We have developed a new method for generating apo MMOH and can quantitatively observe its formation by monitoring the absorbance at 510 nm of $[\text{Fe}(\text{o-phen})_3]^{2+}$ which accumulates during the process. The rate constant for iron release from the protein is 1.6 h^{-1} and the process is complete in just under 3 hours. MMOB and MMOD significantly alter the kinetics of Fe(II) release from MMOH, the rate constants being 0.07 h^{-1} and 0.11 h^{-1} , respectively. Removal of iron from the MMOB-MMOH and MMOD-MMOH complexes is estimated to take over 40 hours to complete. Previous

iron reconstitution studies monitoring enzyme activity as a function of time demonstrated that MMOB also slows the binding of Fe(II) to the active site (3). It is unknown at present whether MMOD alters the rate of iron uptake. From these results we learn that MMOB and MMOD both decrease the relative k_d values for iron release and that MMOB decreases the relative rate constant for iron uptake. The question that remains to be answered is, by what mechanism do these proteins exert such an affect on MMOH?

MMOB and MMOD both bind to the surface of the α -subunit of MMOH (3,40), affect the spectroscopic and redox properties of the MMOH diiron center (1), stimulate (MMOB) or inhibit (MMOD) hydroxylase activity, and in the case of MMOB alter the product regioselectivity (41). How these proteins alter the structure of MMOH has been an important unanswered question about this class of multicomponent enzymes because detailed structures of the MMOH-MMOB and MMOH-MMOD complexes are unknown. Recent saturation recovery EPR and chemical cross-linking data suggest that the MMOB binds somewhere on helices E and F, a result that is consistent with previous spectroscopic and biochemical findings (42-44). Moreover, biochemical investigations indicate that MMOB and MMOD compete with each other for the same binding site on MMOH (3).

In view of this minimal information about MMOB and MMOD docking, the present iron release data suggest that these proteins modulate the direct release of iron through the four-helix bundle by binding to the regions of helices E and F that are closest to the diiron center and physically disrupting conformational changes required for Fe(II) exit. It is unlikely that the metal ions will traverse the three hydrophobic cavities in the core of the MMOH α -subunit to escape into the solvent (45). There is

evidence to support a model whereby MMOB and MMOD binding rigidify residues on helices E and F, limiting protein breathing within this region required for Fe(II) extrusion to solvent. Studies of the sMMO and toluene 4-monooxygenase (T4MO) regiospecific hydroxylations reveal the their respective regulatory proteins can shift the product distributions of some substrates (41,46). If the regulatory protein from both enzyme systems binds to helices E and F, residues on these helices that help form the active site pocket, specifically Ile-217, Thr-213, Gly-208, Leu-204, Phe-192, and Phe-188 in MMOH, must move when the hydroxylase-regulatory protein complex is formed. Mutagenesis and product distribution studies involving Thr-201 from T4MO, analogous to Thr-213 of sMMO, using different aromatic substrates strongly suggest that the regulatory protein directly influences the position of this absolutely conserved active site of residue on helix E (47). Crystallographic studies of MMOH containing different bound product molecules demonstrate that residues 212-216 on helix E can undergo dramatic structural rearrangements and attest to the inherent flexibility of this region of the four-helix bundle (48). In the absence of the regulatory protein, the substrate binding cavity and helices E and F can be thought of as being in a relaxed state. When in the regulatory protein is present, this region may become less flexible, enforcing specific product formation. Such enhanced rigidity close to the diiron center may slow the rates of Fe(II) uptake and release by MMOH in the presence of MMOB. In addition to this mechanism, direct blocking of an exit pore may contribute to the kinetics of Fe(II) mobilization.

If the above interpretations are correct, the kinetic data on Fe(II) trafficking through MMOH in the presence of MMOB and MMOD also suggest that the binding of these proteins may limit solvent access to the diiron center. The crystal structure of the toluene/*o*-xylene monooxygenase hydroxylase (ToMOH), which has a diiron center

geometry identical to that in MMOH, suggests that differences in the reactivity of sMMO and ToMO are based on the greater access of hydrocarbon substrates to the diiron center of the latter (49). Thus the regulatory proteins in these different multicomponent monooxygenase enzyme systems may also serve to gate access to the active sites from solvent, in addition to altering product regiospecificity, by controlling substrate access and altering proton and electron transfer to the diiron centers. An MMOB quadruple mutant from *M. trichosporium* OB3b, in which its surface residues N107, S109, S110, and T111 were mutated to either an alanine or glycine, exhibited a 7-fold decrease in the rate of intermediate Q decay in the presence of methane and a 3-fold increase in Q reactivity toward the alternate substrates furan and nitrobenzene (50). Based on this finding, it was proposed that these mutations in MMOB, which essentially trim the topology of its surface, allow for increased solvent and substrate access to the MMOH active site. It was also proposed that the faster rate of Q decay for the MMOB quadruple mutant (0.12 s^{-1}) versus the wild type protein (0.039 s^{-1}) in the absence of substrate, in addition to the 7-fold decrease in the rate of methane hydroxylation, could be due to enhanced solvent access. This concept of solvent penetration/protection would assign to MMOB another subtle, yet possibly important, function in addition to those suggested previously.

Disorder within Helices E, F, and H

Comparisons between the apo, Mn(II)-soaked, and Co(II)-grown MMOH structures reveal that metal binding to the four-helix bundle is essential for the proper folding of helices E, F, and H. The differences in the ordering of these helices in the Mn(II)-soaked and Co(II)-grown structures are striking. Why does the addition of Mn(II) to apo MMOH crystals fail to reorder the four-helix bundle when this region of

the protein is not involved in crystal packing? One explanation may be that the apo MMOH crystals trap residues 195-206, 247-267, and 312-325 in a partially unfolded state, which upon addition of metal cannot refold properly. In contrast, solubilized apo MMOH may have a higher degree of freedom than the crystalline form and can therefore refold properly to a 'native-like' state before nucleation and crystal growth in the presence of metal ions. The observation that 80-90% of the sMMO hydroxylation activity is recovered by reconstituting apo MMOH with Fe(II) indicates that the apo protein is not irreversibly trapped in an unfolded state. The fact that Co(II)-grown MMOH crystals contain properly refolded hydroxylase is consistent with the return of activity in Fe(II) reconstituted MMOH.

The source of the disorder in helices E, F, and H is puzzling, for how does the absence of metal ions in the middle of four-helix bundle translate to heavily disordered regions more than 20 Å away in the α -subunit near the α/β interface? One force driving the destabilization of helices E and F could be the close proximity of the four potentially negatively charged carboxylates within a buried region of the protein. The repulsion of these charges, if uncompensated, may be the cause the disorder in Glu-209 and Glu-243 and result in an unwinding of their respective helices. No such effect was reported in the different crystal structures of apo ribonucleotide reductase, however (6,14). These proteins diffract to a similar resolution as apo MMOH and were crystallized at lower pH (6.0-6.5), near the pK_a of histidine, the protonation of which can partially compensate for the negative charges in the active site. MMOH crystallizes at pH 7.0, making charge compensation by protonated histidines less likely.

Alternatively, the disorder may be due to destabilization of the second and third metal coordination spheres. Comparison of the structures of MMOH and ToMOH reveals that the conformations of two Fe²⁺-coordinating glutamate residues in both

proteins is stabilized by hydrogen bonding to Gln-140 and Glu-111, respectively (49). Each of these residues also participates in a local hydrogen bonding network involving non-conserved amino acid side chains and structural water molecules, which lead from the diiron center toward the α/β interface region of the four-helix bundle. In MMOH, removal of iron may destabilize these interactions and disrupt the protein fold. At present, there is no direct obvious structural correlation between demetalation of the enzyme and the disorder in helices E, F, and H 20 Å away from the active site .

The northern end of the four-helix bundle is highly ordered in the apo and Mn(II) grown MMOH structures, presumably due to the hydrogen bonding network behind the diiron center that involves both coordinating histidines. A similar observation was made about the structure of apo RNR-R2 (6). Based on this finding it was hypothesized that the active site of RNR-R2 is pre-organized before iron is inserted. This network has subsequently been determined to be essential for delivering an electron from W48 to diiron center in order to help generate the Fe(III)Fe(IV) intermediate needed for the generation of the tyrosyl radical (51,52). By analogy, the hydrogen bonding network in MMOH, which is absolutely conserved in all known multicomponent monooxygenase families like phenol hydroxylases, toluene monooxygenases, and alkene monooxygenases (21), may be a part of the electron transfer pathway from the 2Fe-2S cluster in the reductase or Rieske protein to the diiron center of the hydroxylase. The proposed ~13 Å electron transfer distance from the diiron center to the surface is consistent with the observation that most redox partners in metalloproteins typically fall within this distance (53). This emerging principle for electron transfer distances holds true for rubredoxin and bacterioferritin of which both have electron donor metallo-cofactors ~14 Å behind the diiron center histidines that are incorporated into the fold of the protein (54,55). If our above hypothesis is correct, it

can be surmised that these types of monooxygenases have evolved highly specific and highly rigid pathways for efficient electron transfer.

Helical Disorder and the MMOB/MMOD Binding Site

Isothermal titration calorimetry studies indicate that MMOB has a 3.4-fold higher affinity for MMOH_{ox} over apo MMOH and that MMOD has a 5.5-fold higher affinity for apo MMOH over the native hydroxylase. Moreover, these values indicate that, if MMOB and MMOD were together in solution, MMOB would bind preferentially to MMOH_{ox} and MMOD would bind preferentially to apo MMOH. The differences in the binding affinities of MMOB and MMOD for oxidized and apo MMOH indicate that the apo protein surface must be slightly different than that of the holo enzyme. Cross-linking and saturation-recovery EPR studies place the MMOH-MMOB binding site on helices E and F of the α -subunit near the α/β -subunit interface (42-44). The predicted MMOB binding surface on MMOH coincides well with the disordered regions of helices E, F, and H in the apo and Mn(II)-soaked structures of MMOH. Furthermore, MMOB and MMOD are likely to compete for the same binding region on the surface of the MMOH α -subunit (3). Since helices E, F, and H exhibit the only structural differences in the apo and Mn(II) structures, and the affinities of MMOB and MMOD for MMOH change depending upon the metalation state, the disordered regions in MMOH may therefore be highlighting the locations of the MMOB and MMOD docking sites. Investigations into the properties underlying the principles of protein-protein recognition indicate that binding faces are generally solvent accessible and highly flexible (56-59). The disordered regions on MMOH exhibit both properties and their locations are consistent with biochemical and spectroscopic data placing MMOD and MMOB near the diiron center on this region of the four-helix bundle (42-44).

Structural Perturbations at the MMOH Dimetallic Center

One reason for solving both metalated and demetaled structures of MMOH was to probe the active site and nearby surface of the protein for various structural perturbations that may shed light on the possible affects of MMOB on the properties of MMOH. Spectroscopic studies of the MMOH-MMOB complex from *Methylococcus capsulatus* (Bath) and *Methylosinus trichosporium* OB3b indicate the affects of MMOB to be very subtle. Ligand field CD and MCD results for MMOH from *M. trichosporium* OB3b suggest that MMOB alters the coordination environment of only one of the two iron atoms in the reduced protein (60). XAS spectra comparing MMOH_{red} and $\text{MMOH}_{\text{red}}+\text{MMOB}$ are virtually identical, suggesting that MMOB exerts a very small structural effect on the diiron center geometry (61). From crystallographic work it was surmised that Fe2 is the site being most perturbed since it lies closer to the surface, changes positions in the oxidized, reduced and mixed-valent structures of MMOH, and coordinates to amino acid residues on helices E and F that are more flexible according to the B-factors from the different MMOH crystal structures and positional changes in the different oxidation states (25,35,39,62). The present Mn(II) and Co(II) structures provide further crystallographic evidence supporting variability in the coordinating ligands and metal positions on the "Fe2" side of the active site. These findings also suggest that, as MMOH cycles through the reduced, peroxo, Q, and oxidized intermediates, Glu-209, Glu-243, and His-246 are most likely to shift to accommodate the range of Fe-Fe distances, from 2.6-3.6 Å. One interesting feature in the MMOH_{red} , Mn(II), and Co(II) structures is that the water molecule between the metal ions in the substrate-binding active site pocket varies between bridging, semi-bridging, and terminal coordination modes. Such a change in coordination may well explain the observed MCD and XAS results. The movement of this water molecule may be important for opening a

coordination site where dioxygen can bind and react with one of the iron atoms (38). Presumably the Fe2 site is most reactive toward dioxygen since the bridging water seems to favor binding to Fe1 in most cases. This observation is also consistent with DFT calculations detailing the reactions of O₂ with MMOH_{red} (63).

Acknowledgements

We thank Dr. Maarten Merkx and Dr. Elisabeth Cadieux for their assistance with the iron reconstitution studies and ITC. We also thank Sonya Tang for her assistance in solving the apo MMOH structure.

References

1. Merkx, M., Kopp, D. A., Sazinsky, M. H., Blazyk, J. L., Müller, J., and Lippard, S. J. (2001) *Angew. Chem. Int. Ed.* **40**, 2783-2807.
2. Baik, M.-H., Newcomb, M., Friesner, R. A., and Lippard, S. J. (2003) *Chem. Rev.* **103**, 2385-2420.
3. Merkx, M., and Lippard, S. J. (2001) *J. Biol. Chem.* **277**, 5858-5865.
4. Atta, M., Nordlund, P., Åberg, A., Eklund, H., and Fontecave, M. (1992) *J. Biol. Chem.* **267**, 20682-20688.
5. Atta, M., Fontecave, M., Wilkins, P. C., and Dalton, H. (1993) *Eur. J. Biochem.* **217**, 217-223.
6. Åberg, A., Nordlund, P., and Eklund, H. (1993) *Nature* **361**, 276-278.
7. Elgren, T. E., Ming, L.-J., and Que, L., Jr. (1994) *Inorg. Chem.* **33**, 891-894.
8. Högbom, M., Andersson, M. E., and Nordlund, P. (2001) *J. Biol. Inorg. Chem.* **6**, 315-323.
9. Keech, A. M., Le Brun, N. E., Wilson, M. T., Andrews, S. C., Moore, G. R., and Thomson, A. J. (1997) *J. Biol. Chem.* **272**, 422-429.
10. Zhang, J., -H., and Kurtz, D. M., Jr. (1992) *Proc. Natl. Acad. Sci. USA* **89**, 7065-7069.
11. Zhang, J.-H., Kurtz, J. M., Jr., Maroney, M. J., and Whitehead, J. P. (1992) *Inorg. Chem.* **31**, 1359-1366.
12. Hill, B. R., Raleigh, D. P., Lombardi, A., and Degrado, W. F. (2000) *Acc. Chem. Res.* **33**, 745-754.
13. Maglio, O., Natri, F., Pavone, V., Lombardi, A., and Degrado, W. F. (2003) *Proc. Natl. Acad. Sci. USA* **100**, 3772-3777.

14. Andersson, M. E., Högbom, M., Rinaldo-Matthis, A., Blodig, W., Liang, Y., Person, B.-O., Sjöberg, B.-M., Su, X.-D., and Nordlund, P. (2004) *Biochemistry* **43**, 7966-7972.
15. Bernhardt, P. V., and Lawrance, G. A. (2004) *Comprehensive Coordination Chemistry II* **6**, 1-145.
16. Pecoraro, V. L., Gelasco, A., and Baldwin, M. J. (1995) *Advances in Chemistry Series* **246**, 265-301.
17. Pecoraro, V. L., Baldwin, M. J., and Gelasco, A. (1994) *Chem. Rev.* **94**, 807-826.
18. Stemmler, T. L., Sossong, T. M., Jr., Goldstein, J. I., Ash, D. E., Elgren, T. E., Kurtz, D. M., Jr., and Penner-Hahn, J. E. (1997) *Biochemistry* **36**, 9847-9858.
19. Strand, K. R., Karlsen, S., and Andersson, K. K. (2002) *J. Biol. Chem.* **277**, 34229-34238.
20. Willems, J.-P., Valentine, A. M., Gurbiel, R., Lippard, S. J., and Hoffman, B. M. (1998) *J. Am. Chem. Soc.* **120**, 9410-9416.
21. Coufal, D. E., Blazyk, J. L., Whittington, D. A., Wu, W. W., Rosenzweig, A. C., and Lippard, S. J. (2000) *Eur. J. Biochem.* **267**, 2174-2185.
22. Kopp, D. A., Gassner, G. T., Blazyk, J. L., and Lippard, S. J. (2001) *Biochemistry* **40**, 14932-14941.
23. Gibbs, C. R. (1976) *Anal. Chem.* **48**, 1197-1201.
24. Gassner, G. T., and Lippard, S. J. (1999) *Biochemistry* **38**, 12768-12785.
25. Rosenzweig, A. C., Brandstetter, H., Whittington, D. A., Nordlund, P., Lippard, S. J., and Frederick, C. A. (1997) *Proteins* **29**, 141-152.
26. Leslie, A. G. W. (1992) *Joint CCP4+ESF-EAMCB Newsletter on Protein Crystallography* **26**.
27. Otwinowski, Z., and Minor, W. (1997) *Methods Enzymol.* **276**, 307-326.

28. Brünger, A. T., Adams, P. D., Clore, G. M., Delano, W. L., Gros, P., Grosse-Kunstleve, R. W., Jiang, J.-S., Kuszewski, J., Nilges, N., Pannu, N. S., Read, R. J., Rice, L. M., Simonson, T., and Warren, G. L. (1998) *Acta Cryst. D* **54**, 905-921.
29. McRee, D. E. (1999) *J. Struct. Biol.* **125**, 156-165.
30. Laskowski, R. A., MacArthur, M. W., Moss, D. S., and Thornton, J. M. (1993) *J. Appl. Cryst.* **26**, 283-291.
31. Green, J., and Dalton, H. (1988) *J. Biol. Chem.* **263**, 17561-17565.
32. Merkx, M., Bautista, J., and Lippard, S. J. (2001) Unpublished results .
33. Banci, L., Bencini, A., Benelli, C., Gattechi, D., and Zanchini, C. (1982) *Struct. Bonding* **52**, 37-86.
34. Maret, W., and Vallee, B. L. (1993) *Methods Enzymol.* **226**, 52-71.
35. Rosenzweig, A. C., Frederick, C. A., Lippard, S. J., and Nordlund, P. (1993) *Nature* **366**, 537-543.
36. Logan, D. T., Su, X.-D., Åberg, A., Regnström, K., Hajdu, J., Eklund, H., and Nordlund, P. (1996) *Structure* **4**, 1053-1064.
37. Nordlund, P., Sjöberg, B.-M., and Eklund, H. (1990) *Nature* **345**, 593-598.
38. Rosenzweig, A. C., Nordlund, P., Takahara, P. M., Frederick, C. A., and Lippard, S. J. (1995) *Chem. Biol.* **2**, 409-418.
39. Whittington, D. A., and Lippard, S. J. (2001) *J. Am. Chem. Soc.* **123**, 827-838.
40. Fox, B. G., Liu, Y., Dege, J. E., and Lipscomb, J. D. (1991) *J. Biol. Chem.* **266**, 540-550.
41. Froland, W. A., Andersson, K. K., Lee, S. K., Liu, Y., and Lipscomb, J. D. (1992) *J. Biol. Chem.* **267**, 17588-17597.
42. Brazeau, B. J., Wallar, B. J., and Lipscomb, J. D. (2003) *Biochem. Biophys. Res. Comm.* **312**, 143-148.

43. MacArthur, R., Sazinsky, M. H., Kühne, H., Whittington, D. A., Lippard, S. J., and Brudvig, G. W. (2002) *J. Am. Chem. Soc.* **124**, 13392-13393.
44. Zhu, K., Sazinsky, M. H., Pozharski, E., MacArthur, R., Riku, S., Lippard, S. J., and Brudvig, G. W. (2004) Manuscript in preparation.
45. Whittington, D. A., Rosenzweig, A. C., Frederick, C. A., and Lippard, S. J. (2001) *Biochemistry* **40**, 3476-3482.
46. Pikus, J. D., Studts, J. M., McClay, K., Steffan, R. J., and Fox, B. G. (1997) *Biochemistry* **36**, 9283-9289.
47. Mitchell, K. H., Studts, J. M., and Fox, B. G. (2002) *Biochemistry* **41**, 3176-3188.
48. Sazinsky, M. H., and Lippard, S. J. (2004) Manuscript in preparation.
49. Sazinsky, M. H., Bard, J., Di Donato, A., and Lippard, S. J. (2004) *J. Biol. Chem.* **279**, 30600-30610.
50. Wallar, B. J., and Lipscomb, J. D. (2001) *J. Am. Chem. Soc.* **123**, 2220-2233.
51. Baldwin, J., Krebs, C., Ley, B. A., Edmondson, D. E., Huynh, B. H., and Bollinger, J. M., Jr. (2000) *J. Am. Chem. Soc.* **122**, 12195-12206.
52. Krebs, C., Chen, S., Baldwin, J., Ley, B. A., Patel, U., Edmondson, D. E., Huynh, B. H., and Bollinger, J. M., Jr. (2000) *J. Am. Chem. Soc.* **122**, 12207-12219.
53. Page, C. C., Moser, C. C., and Dutton, P. L. (2003) *Curr. Opin. Chem. Biol.* **7**, 551-556.
54. deMare, F., Kurtz, D. M. J., and Nordlund, P. (1996) *Nat. Struct. Biol.* **3**, 539-546.
55. Frolow, F., Kalb, A. J., and Yariv, J. (1994) *Nat. Struct. Biol.* **1**, 453-460.
56. Sundberg, E. J., and Mariuzza, R. A. (2000) *Structure* **8**, R137-142.
57. Lo Conte, L., Chothia, C., and Janin, J. (1999) *J. Mol. Biol.* **285**, 2177-2198.
58. Jones, S., and Thornton, J. M. (1996) *Proc. Natl. Acad. Sci. USA* **93**, 13-20.

59. DeLano, W. L., Ultsch, M. H., de Vos, A. M., and Wells, J. A. (2000) *Science* **287**, 1279-1283.
60. Pulver, S. C., Froland, W. A., Lipscomb, J. D., and Solomon, E. I. (1997) *J. Am. Chem. Soc.* **119**, 387-395.
61. Dewitt, J. G., Rosenzweig, A. C., Salifoglou, A., Hedman, B., Lippard, S. J., and Hodgson, K. O. (1995) *Inorg. Chem.* **34**, 2505-2515.
62. Elango, N., Radhakrishnan, R., Froland, W. A., Wallar, B. J., Earhart, C. A., Lipscomb, J. D., and Ohlendorf, D. H. (1997) *Prot. Sci.* **6**, 556-568.
63. Gherman, B. F., Baik, M.-H., Lippard, S. J., and Friesner, R. A. (2004) *J. Am. Chem. Soc.* **126**, 2978-2990.
64. DeLano, W. L. (2002) DeLano Scientific LLC, San Carlos, CA, USA.

Table 3.1. Data Collection and Refinement Statistics.

	Apo MMOH	Mn(II)-MMOH	Co(II)-MMOH
Crystal growth conditions		MnCl ₂ soaked apo MMOH	CoCl ₂ grown apo MMOH
<i>Data collection</i>			
Beamline	SSRL 9-1	SSRL 7-1	SSRL 7-1
Wavelength (Å)	1.00	1.08	1.08
Space group, Z	P2 ₁ 2 ₁ 2 ₁ , 4	P2 ₁ 2 ₁ 2 ₁ , 4	P2 ₁ 2 ₁ 2 ₁ , 4
Protomers per asymmetric unit	2	2	2
Unit cell dimensions (Å)			
<i>a</i>	70.35	70.92	71.44
<i>b</i>	171.62	171.67	171.84
<i>c</i>	221.01	220.27	220.93
Resolution range (Å)	30-2.1	30-2.3	30-2.1
Total reflections	607,337	289,572	584,441
Unique reflections	156,085	117,119	159,323
Completeness (%) ^a	92.2 (88.3)	91.7 (90.7)	97.7 (90.4)
<i>I</i> / σ (<i>I</i>)	13.6 (3.1)	11.3 (2.8)	12.2 (2.9)
<i>R</i> _{sym} (%) ^b	6.9 (43.5)	5.8 (29.5)	5.7 (38.8)
<i>Refinement</i>			
<i>R</i> _{cryst} (%) ^c	22.3	21.1	21.4
<i>R</i> _{free} (%) ^d	26.5	25.9	24.5
Number of atoms			
Protein	17312	17317	17325
Water	795	1116	847
r.m.s.d. bond length (Å)	0.0061	0.0060	0.0061
r.m.s.d. bond angle (Deg)	1.194	1.161	1.18
Average B-value (Å ²)	40.0	42.6	37.7

^aValues in parentheses are for the highest resolution shell. ^b $R_{\text{sym}} = \sum_i \sum_{hkl} |I_i(hkl) - \langle I(hkl) \rangle| / \sum_{hkl} \langle I(hkl) \rangle$, where $I_i(hkl)$ is the i^{th} measured diffraction intensity and $\langle I(hkl) \rangle$ is the mean of the intensity for the Miller index (hkl). ^c $R_{\text{cryst}} = \sum_{hkl} ||F_o(hkl)| - |F_c(hkl)|| / \sum_{hkl} |F_o(hkl)|$. ^d $R_{\text{free}} = R_{\text{cryst}}$ for a test set of reflections (5% in each case).

Table 3.2. MMOB and MMOD Binding Constants to Apo and Holo MMOH

Sample	K_{d1} (μM)	K_{d2} (μM)
Apo MMOH + MMOB	0.21 ± 0.027	69 ± 57
Apo MMOH + MMOD	0.027 ± 0.0043	0.29 ± 0.032
Holo MMOH + MMOB	0.062 ± 0.013	0.70 ± 0.035
Holo MMOH + MMOD	0.15 ± 0.045	0.63 ± 0.16

Table 3.3. Properties of Co(II)-Reconstituted Non-Heme Diiron Proteins

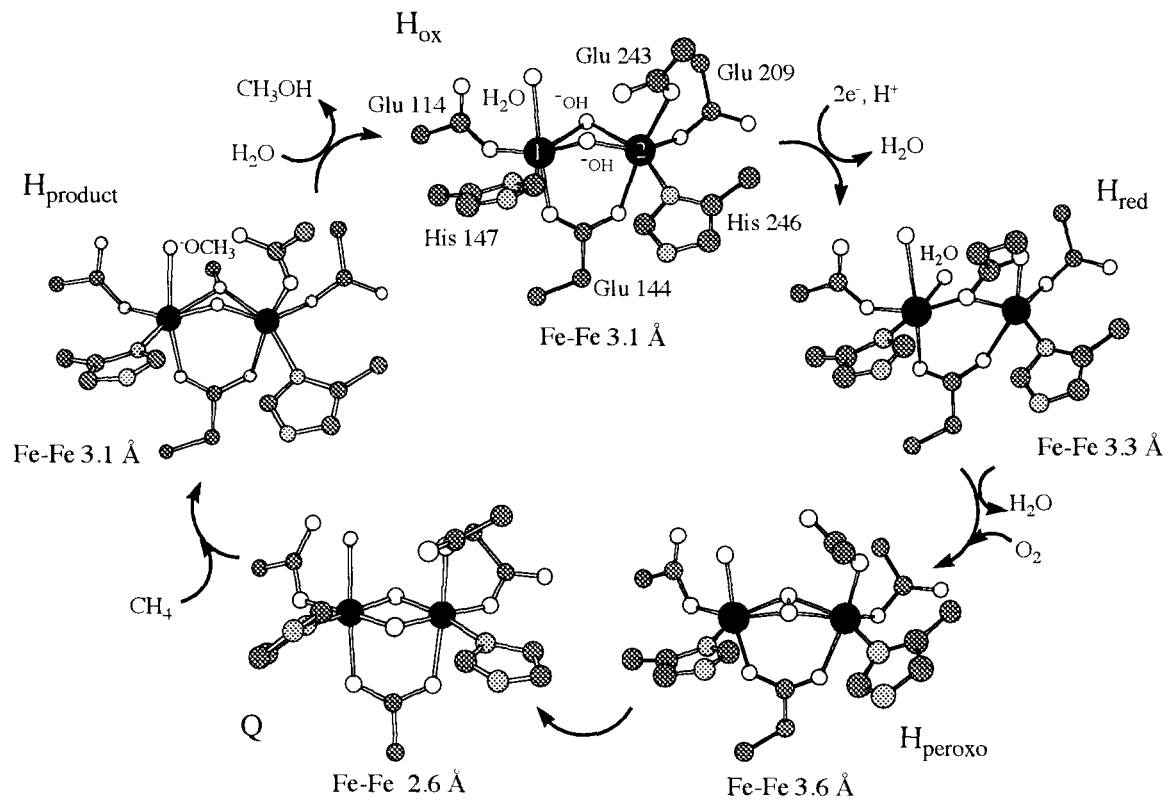
	λ_{max} (nm)	ϵ ($\text{M}^{-1} \text{cm}^{-1}$)	Predicted Geometry ^a	Reference
methane monooxygenase	520	35-40	distorted octahedral	this work
hemerythrin	519 650 850	34	pentacoordinate	(11)
bacterioferritin	520 555 600 625	75-155	pentacoordinate/ pseudotetrahedral	(9)
ribonucleotide reductase R2 protein	515 550	115	pentacoordinate	(7)

a. The predicted geometries are based on spectroscopic studies of structurally characterized small molecules

Table 3.4. Average B-factors for Selected Regions of the MMOH α -Subunits*

Residues	H _{red}	Apo	Co(II)- grown	Mn(II)- soaked
α -subunit	28.0	41.7	37.1	42.8
(18-527)	26.8	41.8	37.5	44.5
195-206	25.8	60.9	39.2	72.0
(helix E)	27.2	57.4	43.0	71.0
247-267	38.9	70.4	49.0	90.6
(helix F)	41.1	68.9	53.5	91.8
312-325	51.4	79.8	63.5	106.3
(helix H)	45.2	72.1	58.7	83.4
Average helices E,F,H	38.3	68.3	51.5	85.6
(avg. EFH)	+10.9	+26.5	+14.2	+42.0
- (avg. α -subunit)				

* Units are in Å^2 . The average B-values for each protomer in the $\alpha_2\beta_2\gamma_2$ dimer are presented. The pdb file 1FYZ was used to calculate the average B-factors for form-II MMOH_{red}.



Scheme 3.1. sMMO catalytic cycle.

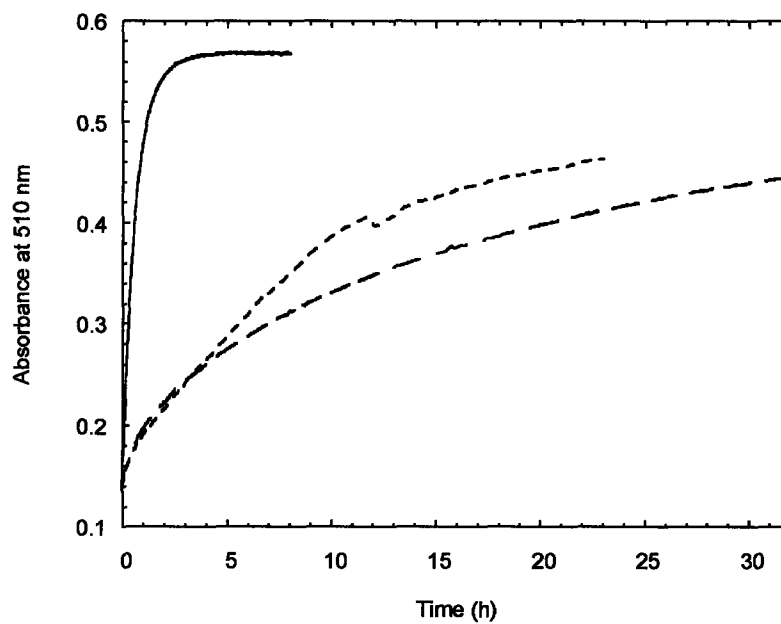


Figure 3.1. Kinetics of iron-release from MMOH_{red} in the presence of 1,10-phenanthroline as monitored by the formation of $[\text{Fe}(o\text{-phen})_3]^{2+}$ at 510 nm. The reaction was carried out anaerobically as described in the text in the presence or absence of 22 μM MMOD or 22 μM MMOB. Solid line, MMOH_{red} only; short dashed line, MMOH_{red} + MMOD; long dashed line, MMOH_{red} + MMOB.

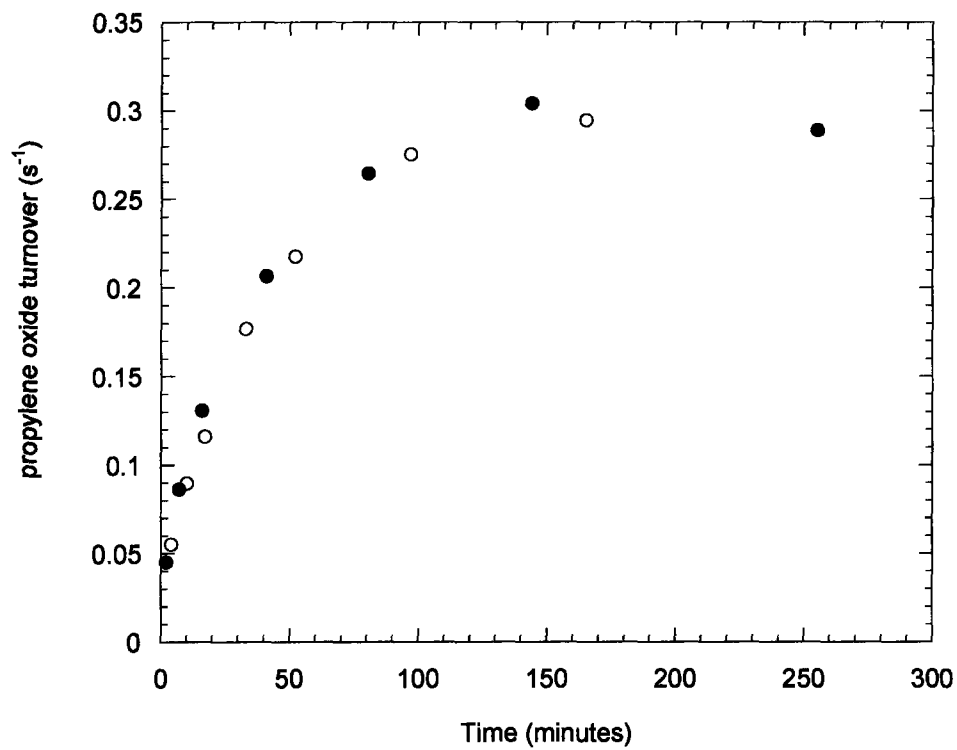


Figure 3.2. Kinetics of formation of active MMOH from apo MMOH and Fe²⁺ at 25 °C under anaerobic (°) and aerobic conditions (•). MMOH activity assays are monitoring the formation of propylene oxide by using gas chromatography as described in the text.

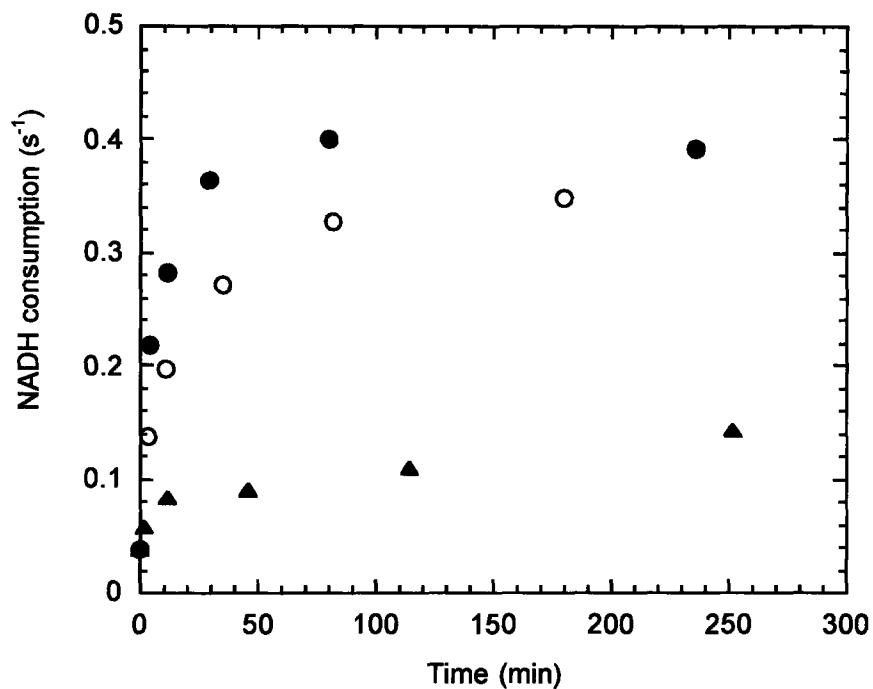


Figure 3.3. Effect of iron concentration on the kinetics of formation of active MMOH from the apo protein and Fe^{2+} . Apo MMOH ($35 \mu\text{M}$) was incubated with 1.48 (●), 0.49 (°), and 0.15 mM (▲) $\text{Fe}(\text{NH}_4)_2(\text{SO}_4)_2 \cdot 6\text{H}_2\text{O}$ in 25 mM MOPS, pH 7.0, 120 mM NaCl, 2 mM DTT, and 5% (v/v) glycerol, at 25°C under anaerobic conditions. MMO activity was assayed at 25°C by using propylene as a substrate and monitoring the NADH concentrations at 340 nm as described in the experimental methods.

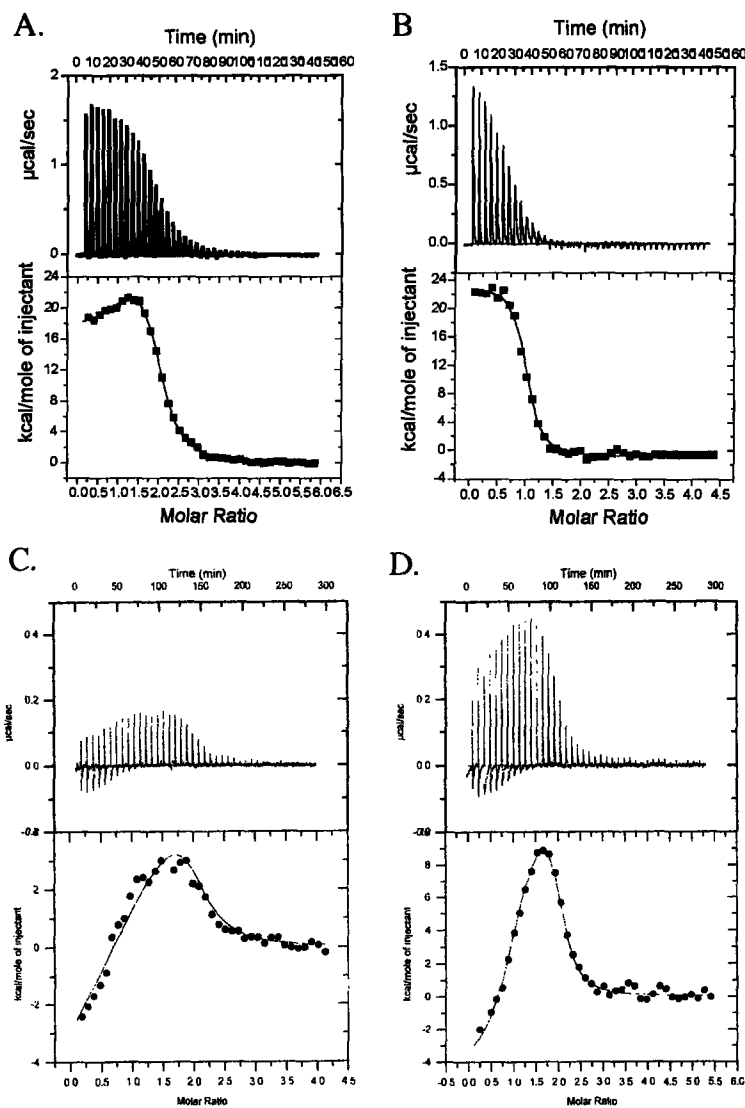


Figure 3.4. Isothermal titration calorimetry of MMOB and MMOD binding to holo and apo MMOH. MMOB was titrated to holo (A) and apo (B) MMOH as described in the text. The titrations of MMOD to holo and apo MMOH are depicted in C and D, respectively. The integrated data are also shown with fits to a sequential binding equation where $n = 2$. The binding constants are listed in Table 3.2.

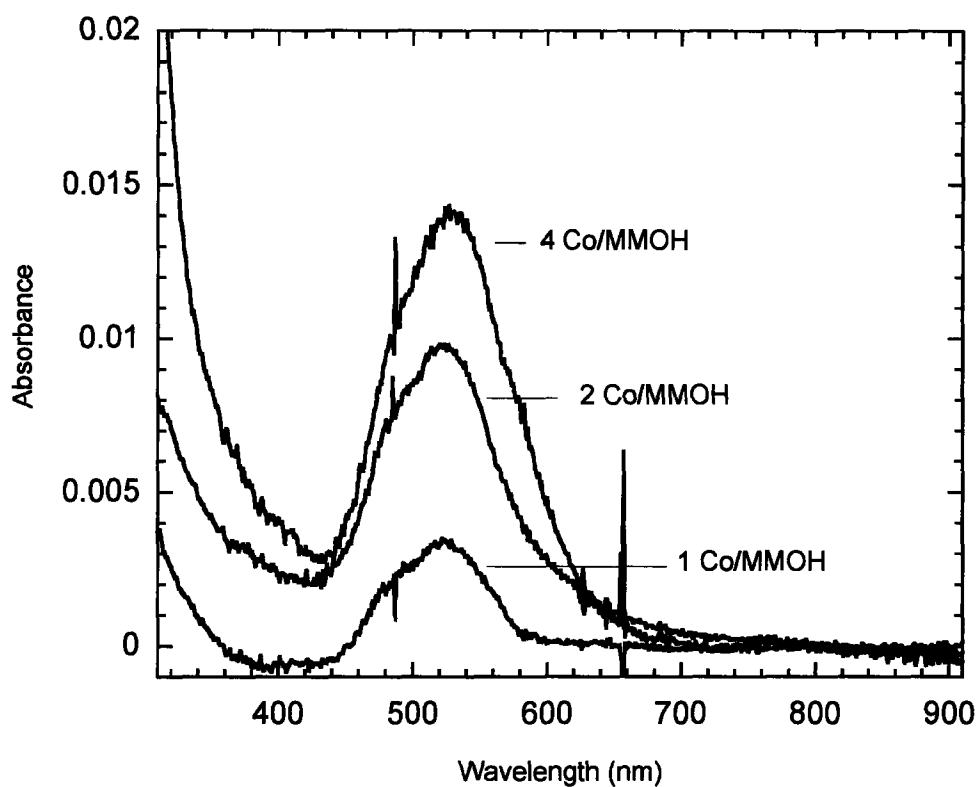


Figure 3.5. Optical difference spectra obtained by subtracting the spectrum of apo MMOH (105 μM) from that of apo MMOH in the presence of 1, 2, and 4 mol-equiv of CoCl₂. Conditions are given within the text.

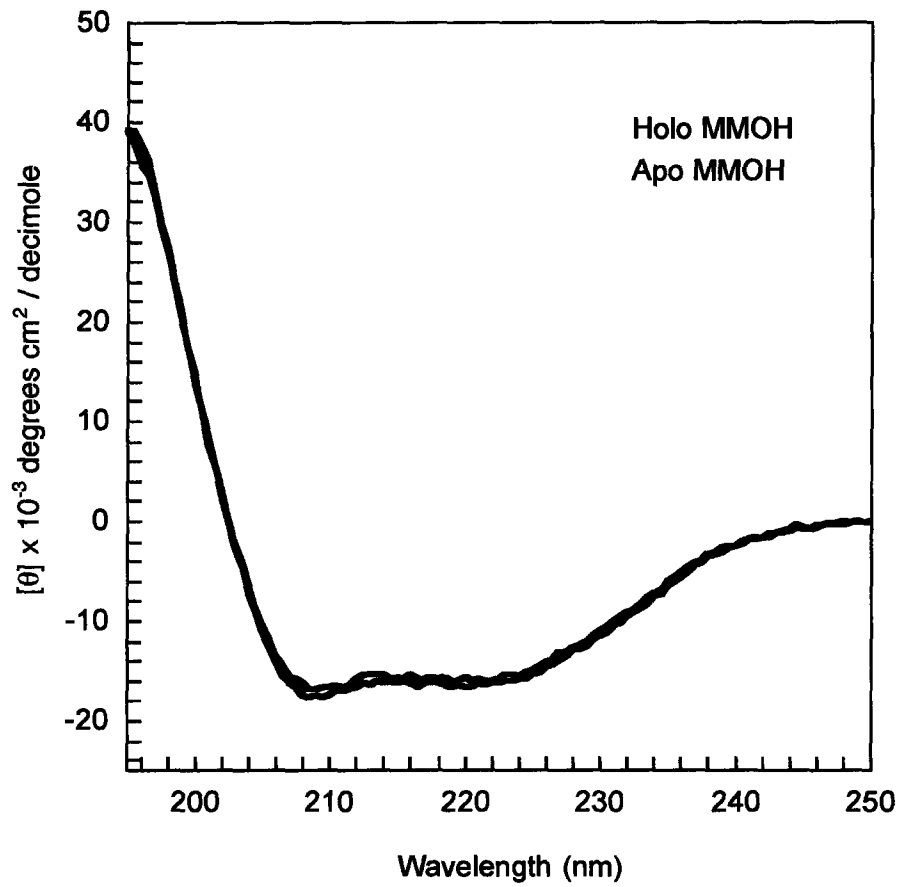


Figure 3.6. CD spectra of 0.1 μM holo (red) and apo (black) MMOH in 10 mM potassium phosphate, pH 7.0 at 25 $^{\circ}\text{C}$.

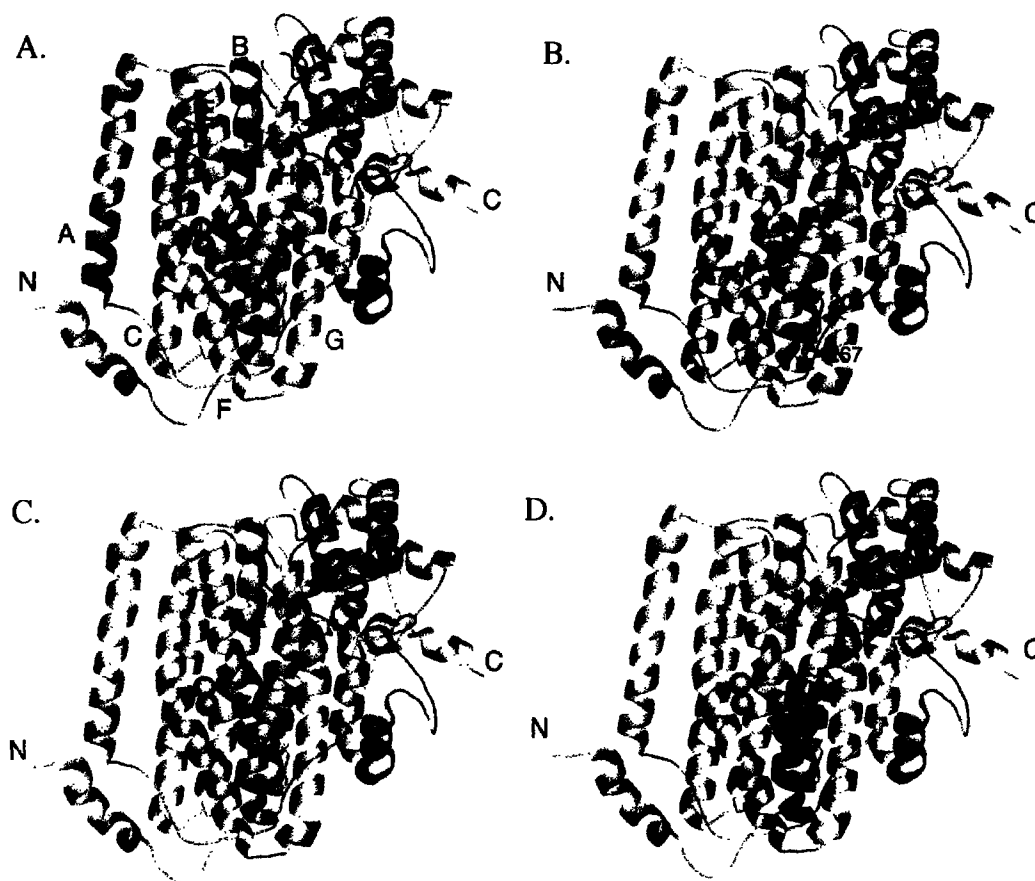


Figure 3.7. Structures of an α -subunit from each of the (A) Fe(II) (B) apo (C) Co(II)-grown and (D) Mn(II)-soaked forms of MMOH colored by their B-factors. Blue and red shading represent low to high B-factors, respectively. Blue represents low disorder where as red represents high thermal disorder. The α -helices (A-H) and metal ion positions (1 and 2) are labeled in (A) and are the same in all panels. The positions of residues marking the start or end of regions with poor electron density, as defined in Table 3.4, are presented in (B). The pdb file 1FYZ was used to generate figure 3.7a. All figures using protein coordinates were generated by using PyMOL (64).

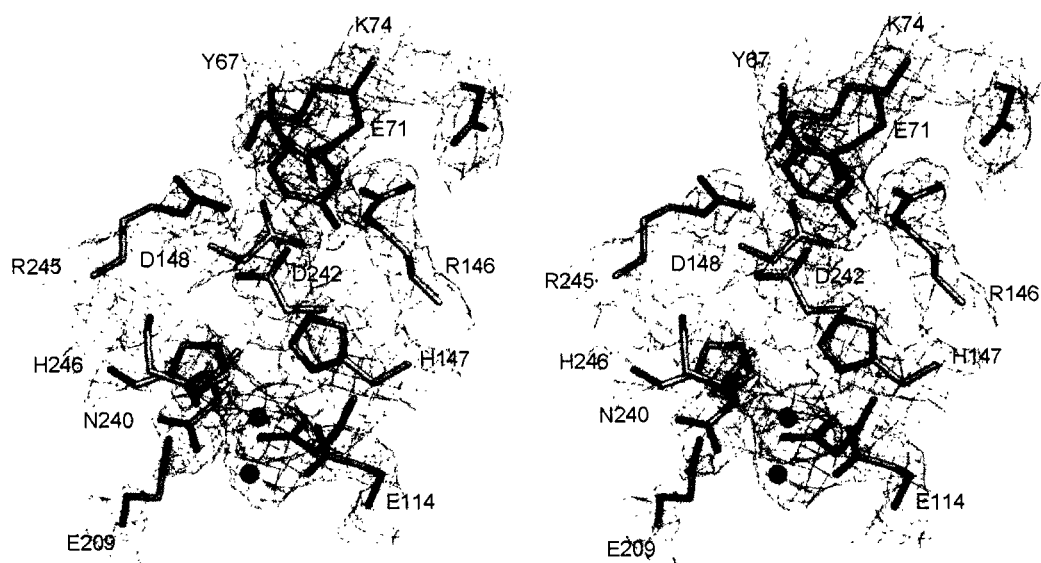


Figure 3.8. Stereoview of the hydrogen bonding network behind the diiron center in apo MMOH. The $2|F_o| - |F_c|$ map is depicted with contours to 1.0σ . Hydrogen bonding networks for the Mn(II)-soaked and Co(II)-grown MMOH structures are identical to those within the holo and apo enzymes (not shown). Water molecules are depicted as red spheres.

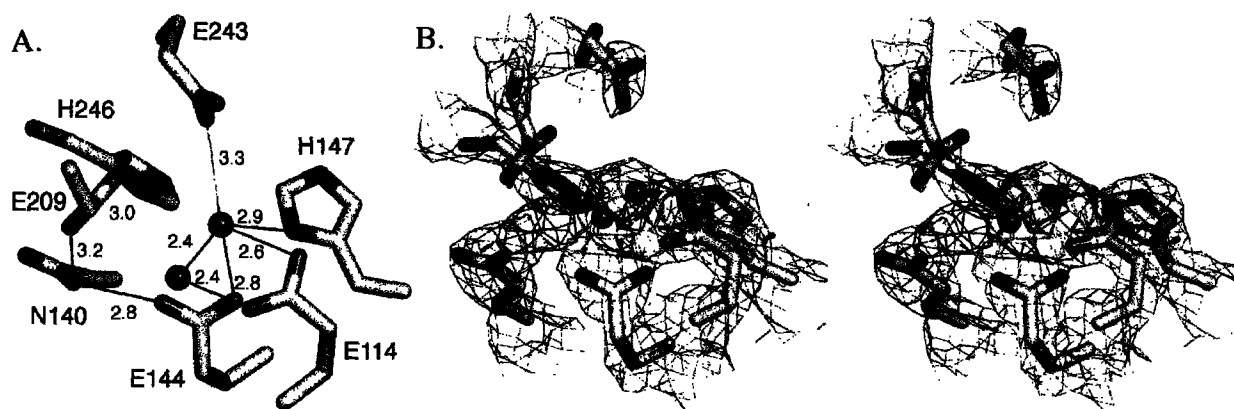


Figure 3.9. (A) Structure of the apo MMOH active site depicting hydrogen bonding patterns (black lines) and distances. Weak hydrogen bonds are depicted as green lines. (B) Stereoview of the apo active site from protomer 1. The $2|F_o| - |F_c|$ electron density map (green) is contoured to 1σ and the $|F_o| - |F_c|$ map (pink) is contoured 3σ . Red spheres represent water molecules. The structure of the apo site from the second protomer is more disordered than the first, and therefore more difficult to model (not shown).

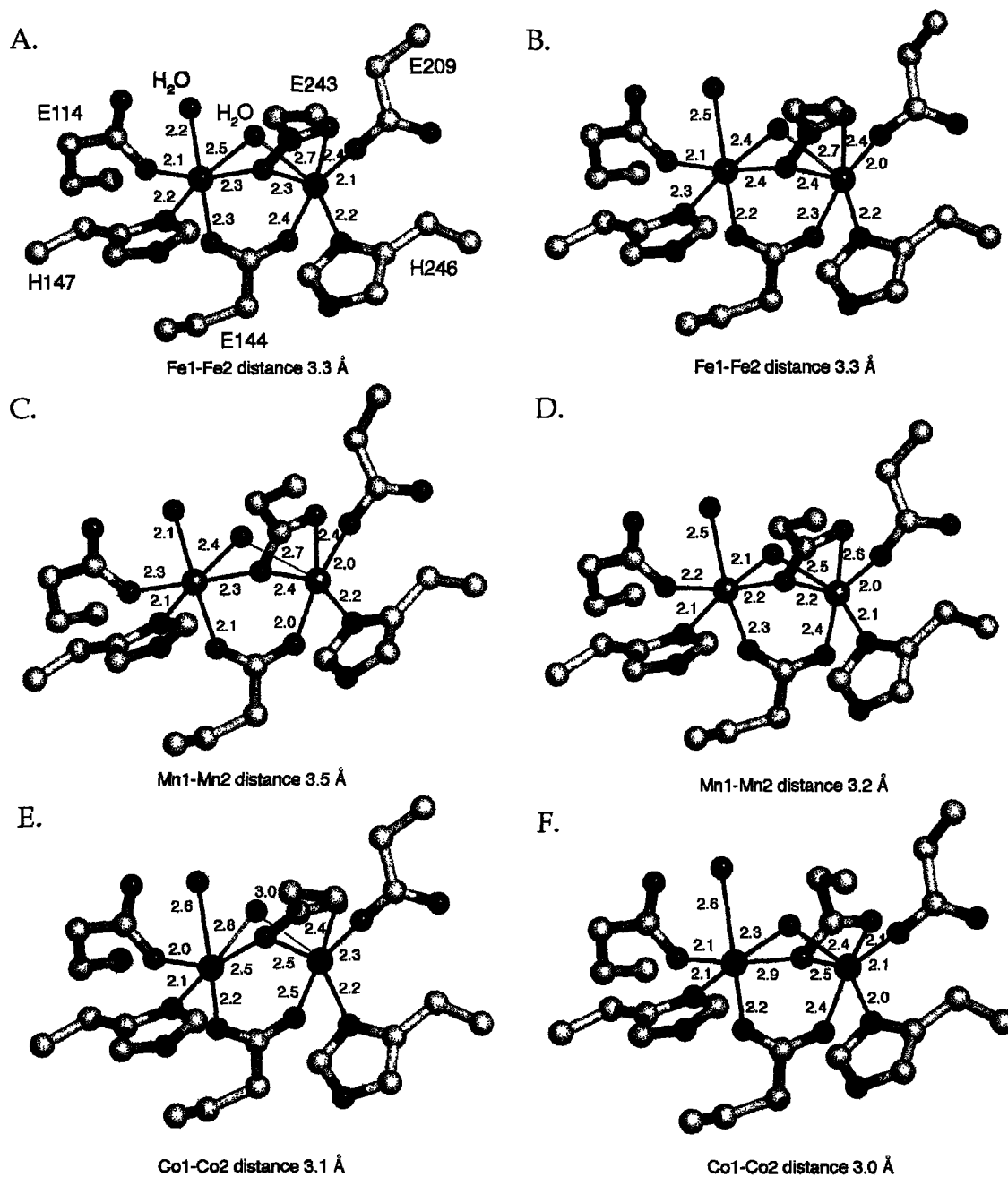


Figure 3.10. Structures of the MMOH active sites. (A) MMOH_{red} protomer 1. (B) MMOH_{red} protomer 2. (C) Mn(II) protomer 1. (D) Mn(II) protomer 2. (E) Co(II) protomer 1. (F) Co(II) protomer 2. Panels B-F are labeled as in A. Electron density contour plots for the Co(II) and Mn(II) active sites are depicted in Figure 3.9.

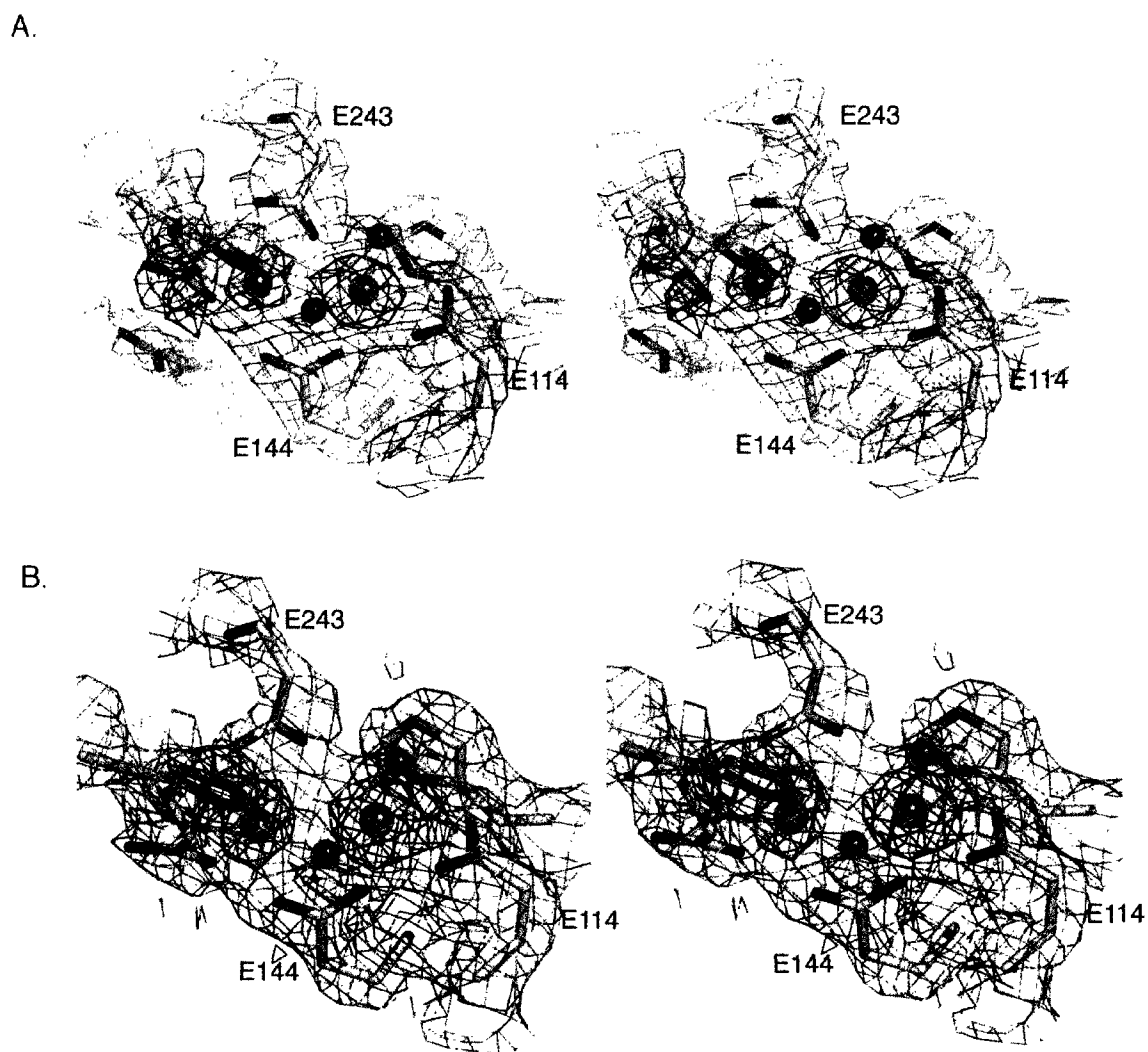


Figure 3.11. $2|F_o| - |F_c|$ electron density maps surrounding the (A) Mn(II)-soaked and (B) Co(II)-grown MMOH active sites in stereo. Maps are contoured to 1.0 σ (green) and 5 σ (purple). Metal atoms and water molecules are depicted as purple and red spheres, respectively.

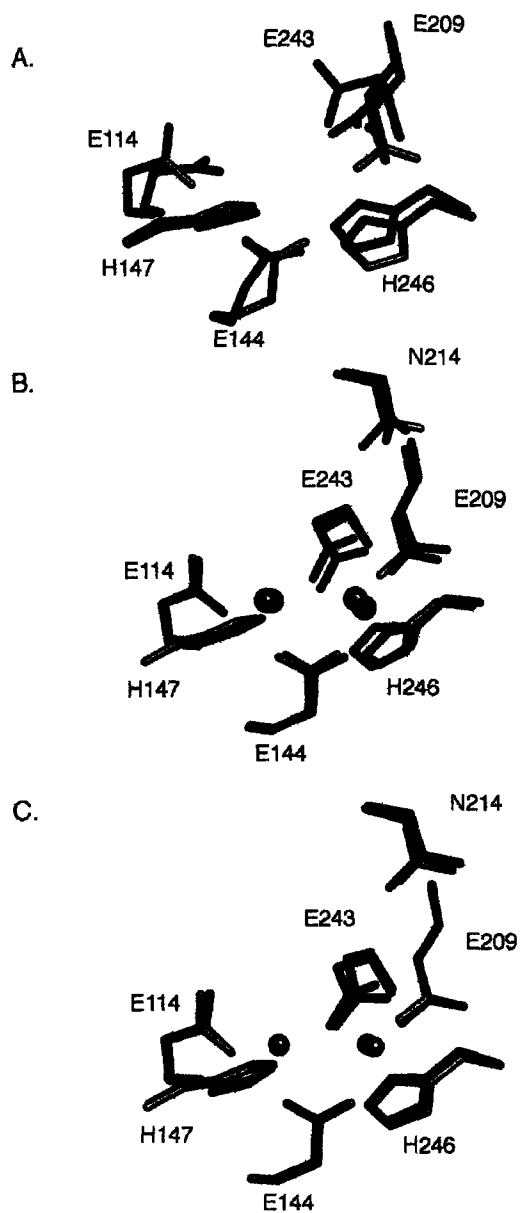


Figure 3.12. Superposition of the apo, Mn(II), and Co(II) forms of MMOH (red) with the native MMOH active sites (blue). (A) Apo versus oxidized MMOH (pdb 1FZ1). (B) Mn(II) versus reduced MMOH (pdb 1FYZ). (C) Co(II) versus reduced MMOH. Each superposition was generated by matching the appropriate α -subunits.

Chapter 4

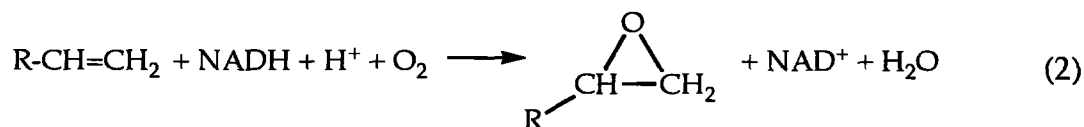
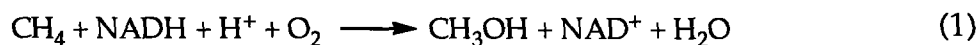
**Product-Bound Structures of the Soluble Methane Monooxygenase
Hydroxylase from *Methylococcus capsulatus* (Bath): Protein Motion
in the α -Subunit**

Introduction

Microorganisms play a significant role in bioremediation as demonstrated by their ability both to cleanse environments contaminated with such xenobiotics as oil spills, haloalkanes, and aromatics and to use these hydrocarbon substrates as a source of carbon and energy (1-3). Non-heme diiron bacterial multicomponent monooxygenases (BMMs) (4,5), including the soluble methane monooxygenase, four-component alkene/aromatic monooxygenase, phenol hydroxylase and alkene monooxygenase subfamilies, are in part responsible for the chemically challenging transformations performed by the microorganisms harboring these enzymes. Only members of the soluble methane monooxygenase (sMMO) subfamily, methane, butane, and related monooxygenases, can hydroxylate alkanes. This unique property has garnered much attention among those interested in C-H bond activation chemistry and in bioengineering these enzymes for synthetic and environmental applications.

Soluble methane monooxygenase is a three component enzyme system comprising a 251 kDa hydroxylase of the form $\alpha_2\beta_2\gamma_2$ (MMOH), a 16 kDa cofactorless protein (MMOB) that couples electron transfer with dioxygen activation, and a 38 kDa [2Fe-2S]- and FAD-containing reductase (MMOR) (6). At a carboxylate-bridged diiron center housed within a four-helix bundle in each of the MMOH α -subunits, both diiron(III) peroxo and high-valent di(μ -oxo)-diiron(IV) intermediates convert hydrocarbon substrates either to alcohols or epoxides (eqs 1 and 2) (6-8). For these reactions to take place, several substrates, including the hydrocarbon, O_2 , $2e^-$ and H^+ , must access the diiron center when the MMOR and MMOB components are bound to the hydroxylase (9). For

efficient activity, the enzyme must precisely time these interactions as well as facilitate the extrusion of products from the active site through non-interfering



pathways. To account for the differences in polarity between the hydrophobic and polar substrates and products, it has been proposed that sMMO may invoke different routes through MMOH for their entry and exit (10).

Several hydrophobic cavities in the MMOH α -subunit have been identified, of which three extend from the active site pocket, cavity 1, through the core of the protein to the surface (Figure 4.1) (10,11). In two different crystal forms of MMOH, Leu-110, which sits at the interface between cavities 1 and 2, adopts alternate rotamer conformations and was therefore proposed to gate substrate passage between these two cavities (11,12). Subsequently, it was demonstrated that small halogenated alkanes and xenon can bind in cavities 2 and 3 (10), reinforcing the hypothesis that they delineate an essential pathway for substrate entrance into the diiron center other than direct diffusion through the the four-helix bundle in which the active site is held. Further evidence in support of the postulated hydrocarbon route was the discovery, in the toluene/*o*-xylene monooxygenase hydroxylase (ToMOH), of a 35-40 Å long channel that traces a path identical to that of the MMOH cavities (13). This finding suggested that all multicomponent monooxygenases deliver substrates and extrude products along this pathway.

The remarkable bioremediating capabilities of some methanotrophs derive from their ability to hydroxylate, and thereby consume, a variety of different substrates, which include branched, cyclic, aromatic, and linear hydrocarbons of up to C8 in length (14-16). Given the size of some of these substrates, it is difficult to imagine how an enzyme that is designed for processing small substrates like CH₄ and O₂ can accommodate molecules as large as octane, methylcubane, and *trans*-1-methyl-2-phenylcyclopropane in the same manner (14,17-19). For sMMO to act on these alternative substrates, its active site must be relatively flexible, yet specific enough to guide and orient them towards the diiron center for hydroxylation. If these larger substrates diffuse through the cavities to gain access to the active site, significant rearrangement of key residue side chains must occur.

In the present work, we determined several crystal structures of MMOH with bound aromatic and halogenated alcohols of C2-C8 in length in order to investigate how the enzyme accommodates so many different hydrocarbon compounds and to track the likely route of product passage from the diiron center. Different haloalcohols were introduced into MMOH crystals the halogen atom facilitating identification of the hydroxyl group in the electron density maps. These molecules bind in cavities 1-3 of MMOH, alter the conformations of key residues separating the three cavities, and in one case induce novel secondary structure rearrangements in helix E, a component of the four-helix bundle that contributes several key amino acids to the active site pocket. These findings reveal how sMMO can accommodate can large substrates and strongly suggests that substrates as well as products can move through MMOH along the same path. The unprecedented folding rearrangements in helix E also reveal one

way in which MMOB could induce structural changes in MMOH to influence its reactivity.

Experimental

Crystallization of MMOH and Small Molecule Soaks

MMOH was purified as described previously (20,21). Ferrozine assays confirmed the presence of 3.8 ± 0.1 Fe/MMOH and propylene oxidation, followed by measuring NADH consumption, confirmed the activity of the enzyme to be $\sim 250\text{-}300$ nmol min⁻¹ mg⁻¹ (50-60 s⁻¹) (9). Form II crystals were obtained at 4 °C by using the sitting drop vapor diffusion method under conditions similar to those described previously (11,22). Briefly, well solutions contained 160 mM MOPS, pH 7.0, 350 mM CaCl₂, 10% PEG 8000 (w/w), and 0.015% NaN₃. Crystallization drops were formed by combining 3 μL of a 50 μM MMOH solution in 25 mM MOPS, pH 7.0 with 1.5 μL of well solution and 1.5 μL of an MMOH microseed stock solution (50 mM MOPS, pH 7.0, 220 mM CaCl₂, 10% (w/w) PEG 8000, and 25% (v/v) glycerol). The cryo-solution for crystal freezing contained the well solution plus 25% glycerol. Small molecules were soaked into MMOH crystals by bathing them in a cryo-solution containing various haloalcohols. Soaking times and small molecule concentrations depended upon crystal stability and are listed in Table 4.1.

Data Collection and Model Refinement.

Data sets were collected at SSRL on beam lines 7-1, 9-1, and 11-1 at 100 K with 0.5° oscillations over a 100-120° rotation of the crystal about the φ axis. The program MOSFLM (23) was used to determine a collection strategy and the HKL suite of programs was used to index and scale the data (24). Molecular

replacements and refinement were performed by using CNS and XtalView (25,26). The final crystal and model statistics are presented in Table 4.1. The different product bound hydroxylase structures closely resembled those described previously (10-12). The MMOH α -subunit cavities were calculated by using a 1.4 Å radius water probe in Swiss-PDB Viewer (35)

Results

Alcohol Binding to MMOH

Several ω -haloalcohols were soaked into crystals of MMOH. The halogen atom differentiates the alcohol group from the methyl group at the opposited end of the linear hydrocarbon chain in the electron density maps. The various locations of each of the soaked halogenated molecules are described in Table 4.2 and depicted in Figure 4.2.

At the active site (cavity 1), 2-bromoethan-1-ol, 3-chloropropan-1-ol, 3-bromo-3-buten-1-ol and 6-bromohexan-1-ol bind to a position bridging the two iron atoms (Figure 4.3, Table 4.3). For 6-bromohexan-1-ol, electron density is available for only the bromine atom and the first few carbons after the alcohol moiety. 8-Bromooctan-1-ol and the aromatic alcohols were not located in this cavity. Lower occupancies, higher B-values and weaker electron density are observed, in general, as the size of the bound alcohol in cavity 1 increases (Table 4.2).

All of the non-aromatic haloalcohols bind to cavities 2 and 3 with the exception of 8-bromooctan-1-ol, which spans these cavities in one protomer and binds to only cavity 3 in the other. Electron density for 8-bromooctan-1-ol is

available primarily for the bromine atoms and the first few attached carbon atoms. Density for the remainder of the chain is absent, possibly reflecting positional disorder. In contrast, the electron density is present for almost all of the 2-bromoethan-1-ol, 3-chloropropan-1-ol, 3-bromo-3-buten-1-ol, and 6-bromohexan-1-ol atoms in cavities 2 and 3.

Aromatic compounds such as benzene and nitrobenzene are sMMO substrates and their product alcohols, phenol and *p*-nitrophenol, bind to the diiron center as demonstrated by UV-vis and EPR spectroscopic investigations (27-30). It was therefore unexpected that, in the structures of MMOH crystals soaked in phenol, 4-fluorophenol, and 4-bromophenol, electron density for these molecules was detected only in cavity 3. *p*-Nitrophenol also binds to cavity 3 and none other (data not shown). The different aromatics were used to examine the effects of variable polarity and pK_a of the -OH group on binding to the active site, but this approach was not fruitful. These phenolic compounds are smaller than 6-bromohexan-1-ol and 8-bromooctan-1-ol and their substrate precursors (e.g., benzene) are more reactive with MMOH (62 mU/mg) than either hexane or octane (9-40 mU/mg) (14). This observation indicates that the crystals of MMOH in the absence of bound MMOB may not be flexible enough to accommodate more rigid compounds bearing an aromatic ring.

The halogenated alcohols also bind to several regions on the surface of MMOH. Included are the α/β and β/β subunit interfaces, N-terminal portions of the β -subunit, and the α -subunit near the α/γ interface. Figure 4.2 and Tables 4.2 and 4.3 report where these different molecules bind, which in general tend to be hydrophobic crevices and niches on the surface of the protein. None of the

bound surface alcohols is positioned within a reasonable distance from a potential cavity opening.

Product Binding to Cavity 1

In each of the 2-bromoethan-1-ol, 3-chloropropan-1-ol, 3-bromo-3-buten-1-ol, and 6-bromohexan-1-ol structures, the hydroxyl group of the alcohol displaces the bridging OH^- or H_3O_2^- ion facing the hydrophobic pocket in cavity 1 and binds to the diiron center in either a bridging, or in some protomers, a semi-bridging fashion (Figure 4.3). On average the distances from Fe1 and Fe2 to the alcohol oxygen atom are each $\sim 2.3 \text{ \AA}$ (Table 4.4). Methoxy- and ethoxy-bridged high-spin diiron(III) centers typically have bridging Fe–O bond distances between 1.9–2.1 \AA , according to results for model complexes deposited in the Cambridge Structural Database. In the methanol-bound structure of MMOH these distances were each 2.1 \AA (31). The longer bond distances observed for the various product-soaked structures suggest that the alcohol rather than the alkoxide species may be coordinated to the diiron(III) center, but the resolution of the structures is not significantly high to allow for a definitive assignment. The coordination sphere around the irons is relatively unperturbed and identical to that of oxidized MMOH and its methanol and ethanol bound forms (31).

In all cases, the bound halogenated alcohols extend from the diiron center bridging position towards the back of cavity 1 either near Leu-110 and Phe-188, which serve as the gates to cavity 2, or Phe-192, Gly-208, and Leu-204, which form a niche on the Fe2 side of the active site pocket. In some cases, depending upon the length of the product analogue, the chlorine and bromine atoms are positioned over the aromatic rings of either Phe-188 or Phe-192. The chlorine atom of 3-chloropropan-1-ol is disordered, binding to both of the sites mentioned

above, as evidenced by the forked electron density in one of the two active sites (Figure 4.3). The bromine atom of 6-bromohexan-1-ol is situated at the roof of the active site cavity and occupies the position of Thr-213 in MMOH_{ox}, which has moved because of structural rearrangements that occur in helix E (see below) (Figures 4.5 and 4.6). The presence of these small alcohols in cavity 1 perturbs the rotameric conformations of Ile-217, Leu-110, Phe-188, and Thr-213 (Figure 4.4). Leu-110 adopts different conformations in the two different crystal forms of MMOH (11). The presence of the haloalcohol substrates in crystal form II induces this residue to adopt a conformation similar to that observed in form I MMOH crystals. The phenyl ring of Phe-188, which comprises part of the "leucine gate," shifts to the left or right in the different MMOH structures, seemingly in concert with positional changes in Leu-110. Thr-213 exhibits two rotameric conformations in the product-soaked structures. In the 2-bromoethan-1-ol and 8-bromooctan-1-ol structures, the threonine hydroxyl group points towards the diiron center, whereas in the remaining bound product structures, including those with methanol and ethanol, the Thr-213 methyl group points towards the diiron center. These two different conformations have been observed previously in crystal structures of oxidized and reduced MMOH (11,12,32,33). In some product-soaked structures, such as the one with bound 2-bromoethan-1-ol, a methyl group on the Ile-217 side chain adopts a different orientation to point towards the diiron center rather than towards Leu-110. Presumably, these conformational changes are intended to accommodate better the bound products. The alternate rotameric conformations of these residues are responsible for increasing the access between cavities 1 and 2 (see below) (Figure 4.4).

6-Bromohexan-1-ol Induced Structural Changes in Helix E

Helix E is part of the four-helix bundle housing the diiron active site and forms one of the ridges of the canyon on the surface of MMOH. In all previously determined crystal structures of the enzyme, residues 202-211 of helix E adopt a π secondary structure, whereas the rest of its residues adopt an α -helical fold (10-12,31-34). At the active site, there are three universally conserved residues, Glu-209, Thr-213, and Asn-214 on helix E. Glu-209 coordinates to the diiron center, Thr-213 forms the roof of the active site cavity and Asn-214 positions itself at the interface between the cavity and the surface above the iron-coordinating residue Glu-243. In the 6-bromohexan-1-ol bound structure, this helix, in both α -subunits of the MMOH dimer, undergoes a dramatic rearrangement in secondary structure (Figures 4.5 and 4.6). In this altered form of MMOH, residues 212-216 (FTNPL) adopt a π -helix configuration. As a result, Thr-213 shifts to occupy the former position of Asn-214, Asn-214 shifts to occupy the former position of Pro-215, Pro-215 moves to occupy a space between its former position and that of Leu-216, and Leu-216 moves further into the active site pocket towards the leucine gate (Figures 4.5 and 4.6). At residue 217 the peptide backbone and side chain positions resume the more typical α -helical fold. As a result of these rearrangements in MMOH, both the universally conserved Thr-213 and Asn-214 residues now lie mainly on the hydroxylase surface and the volume of cavity 1, as calculated by Swiss-PDB Viewer, increases from $\sim 250 \text{ \AA}^3$ to $\sim 330 \text{ \AA}^3$. This volume change is primarily a result of shifting Thr-213 out, and sliding Leu-216 in, to the active site pocket. In the altered structure, Leu-216 sits $\sim 5 \text{ \AA}$ behind the former position of Thr-213 and replaces it

as one of the residues that gates access between cavities 1 and 2. Despite the alterations in this region of the protein, the structure of the diiron center is not perturbed. Moreover, the changes within this helix do not open a pore between it and helix F of the four-helix bundle to allow direct access to the surface from the diiron center or the active site pocket. As mentioned previously, the bromine atom of 6-bromohexan-1-ol localizes to the position formerly occupied by Thr-213. It appears likely that the binding of this large product analogue to the active site cavity, and perhaps displacement of the Thr-213 side chain, induces the structural rearrangements in helix E.

X-ray data to 2.5 Å were also obtained for an MMOH crystal first soaked in 6-bromohexan-1-ol and then chemically reduced with dithionite and methylviologen. The electron density for most of the protein is sufficiently strong to fit to a model. In both protomers the electron density in the active site is weak and, for residues 205-215, missing altogether (Figure 4.7). Although an exact structure of this important region cannot be determined at this time, several key observations which are relevant to the current work can be made by inspection of the electron density maps and overall B-factors of the structure (Table 4.5). Strong difference electron density is not observed for the bromine atom of 6-bromohexan-1-ol in the active site, indicating that reduction of the diiron center results in 6-bromohexan-1-ol leaving this region. Cavities 2 and 3, however, are occupied by this molecule since strong electron density corresponding to bromine is clearly evident (Figure 4.7). The absence of electron density for residues 205-215 of helix E reflects positional disorder and suggests that extrusion of 6-bromohexan-1-ol from the active site induces yet another structural reorganization in this region. Previous studies on chemically reduced

MMOH crystals have not induced a disorder of this magnitude near the active site cavity (32,33).

Connectivity Between the α -Subunit Cavities

In the different product-soaked structures, the amino acid side chains separating the different cavities shift to allow access from one cavity to the next (Figure 4.8 and Table 4.3). The side chains of Leu-110, Phe-188 and Thr-213 separate cavities 1 and 2 whereas those of Phe-109, Val-285, Leu-289, and Tyr-291 separate cavities 2 and 3. In all of the haloalkane soaked structures, cavities 2 and 3 are connected owing to a shift in the position of Leu-289 (Table 4.4, Figure 4.8). This residue adopts an alternate rotameric conformation in the 8-bromooctan-1-ol bound structure as a result of the product analogue traversing the cavity gate. Comparisons between the other alcohol soaked structures with that of oxidized MMOH reveal that Leu-289 shifts slightly only in its side chain and backbone to allow greater access between cavities 2 and 3 (Figure 4.9). The differences in the position of the Leu-289 side chain may be insignificant with respect to the connectivity between cavities 2 and 3. The distinction between these two cavities may therefore not be definitive and can vary depending on the programs used to calculate solvent accessibility. The other residues in cavity 2 adopting alternate rotameric conformations are Met-184, Phe-282 and Leu-286. Comparisons between the oxidized, 8-bromooctan-1-ol, 6-bromohexan-1-ol, and 2-bromoethan-1-ol bound structures indicate that positional changes in Phe-282 and Leu-286 are essential for MMOH to accommodate the different soaked product analogues (Figure 4.8).

Side chain movements in Leu-110, Phe-188, and Thr-213 of the 2-bromoethan-1-ol and 8-bromooctan-1-ol structures allow for access between

cavities 1 and 2 (Figures 4.4 and 4.8). These movements, in addition to those in cavities 2 and 3, produce a ~ 40 Å channel leading from the diiron center to cavity 3. This result is the first "channel-like" occurrence in an MMOH structure. In the other product-soaked structures, which do not exhibit connectivity between cavities 1 and 2, Leu-110 and Phe-188 undergo similar positional shifts as those observed in the 2-bromoethan-1-ol and 8-bromooctan-1-ol structures. Thr-213, however, is positioned so that its hydroxyl group points towards the gates to block access between cavities 1 and 2. In the open gate configuration, the threonine hydroxyl group points towards the diiron center (Figure 4.4). In the reduced structures of MMOH, in which the Thr-213 hydroxyl group is usually pointing toward the diiron center, Leu-110 and Phe-188 do not alter their positions to allow connectivity between the active site and cavity 2 (32,33). The change in the side chain orientation of Thr-213, as well as the structural adjustments in Leu-110 and Phe-188, are therefore key to opening access between cavities 1 and 2. The rotameric changes in Ile-217 have no effect.

Because of these findings, cavities were calculated for the different crystal structures of MMOH in its different oxidation and small molecule bound states to track previously unassigned changes in the α -subunit. The three cavities in the oxidized, mixed valent, methanol, ethanol, iodoethanol, dibromomethane, and xenon bound forms differ little from one another. The structure of reduced MMOH from form I crystals exhibits slight movements in Leu-289, allowing access between cavities 2 and 3, as reported previously (13). In reduced form II MMOH crystals, cavities 2 and 3 are connected, and cavity 1 is continuous with the MMOH surface in one protomer, indicating that molecular rearrangements have occurred to give the active site pocket direct access to solvent in the reduced

state of the protein. Further analysis reveals that movement in conserved Asn-214 results in the formation of a small pore between helices E and F of the four-helix bundle that leads from the surface to the diiron center (Figure 4.10). In previous reduced structures it was noticed that the movement of Asn-214 forms a deep crevice in the four-helix bundle (36). This pore is 3.5-3.7 Å in diameter at the opening and 1.8-2.0 Å in diameter at its narrowest point. In the oxidized form of MMOH, Asn-214 shifts to close the pathway. These structural differences suggest that Asn-214 may control the entrance of small substrates like O₂, H₃O⁺, or possibly even CH₄, which have van der Waals radii of 1.52-2.15 Å, respectively, in their narrowest dimension. The presence of MMOB or protein breathing may help to widen pore diameter to facilitate the movement of these molecules into the active site.

Cavity 3, which is further removed, is formed by helices B, D, G and capped by several loops connecting the α-subunit helices. In each of the product-soaked structures, no detectable side chain movements occur here. In no structure is the surface of this cavity contiguous with the surface of the protein.

Discussion

The MMOH Product-Bound State

The binding of halogenated alcohols to the bridging position of the diiron center extends previous crystallographic results demonstrating that methanol and ethanol bind to the oxidized diiron center by displacing the bridging ligand faces the active site pocket (31). The geometry of the remaining iron-ligating atoms is unperturbed. These findings confirm EPR (29) and ENDOR (37) studies demonstrating that alcohols bind to the diiron(III) active site. As proposed

previously, the alcohol bound structures represent the final state of the enzyme, H_{product} after alkane hydroxylation by Q and suggest C–H bond activation by this intermediate occurs here. (31). Density functional theory (DFT) calculations of Q reactivity with substrate are in agreement with this proposal (38).

Conformational Changes in Helix E

Helix E is part of the α -subunit four-helix bundle that lies on the surface of MMOH near the canyon and contains within it three absolutely conserved residues, Glu-209, Thr-213, and Asn-214. In all known crystal structures of MMOH and ToMOH, residues 202-211 (190-199 ToMOH) adopt a π -helical secondary structure (10-13,31-34). The binding of 6-bromohexan-1-ol to MMOH induces reorganization of the π -helix to extend it to residues 212-216, which otherwise adopt an α -helical fold. Despite these changes, the structure of the diiron center remains unaffected. The unexpected geometric rearrangements in helix E are unprecedented in bacterial multicomponent monooxygenases and may have important functional implications.

One obvious consequence of the changes in helix E is that MMOH can accommodate larger molecules. The calculated volumes for cavity 1 in MMOH_{ox} and the 6-bromohexan-1-ol bound structure are $\sim 250 \text{ \AA}^3$ and 330 \AA^3 , respectively, indicating clearly that the changes provide extra space for larger substrates and products like 6-bromohexan-1-ol. It is noteworthy, moreover, that MMOH undergoes a structural rearrangement that requires significant reorganizational energy to accommodate 6-bromohexan-1-ol binding, rather than simply excluding this product analogue from the active site, similar to what is observed for the aromatic alcohols that bind only in cavity 3. On the other hand, the α - to

π -helical transition in residues 212-216 may be a thermodynamically downhill process, once the threshold energy for such reorganization is reached. If movement in this helix is critical to accommodate a large substrate, however, why would an enzyme that hydroxylates CH_4 design into its fold such a reorganization mechanism unless it has another associated function?

The structural changes may represent an as yet unidentified effect of MMOB on the structure of MMOH. Previously, when we considered how MMOB might induce structural changes in the hydroxylase, we assumed that the effects would occur at the protein surface and translate to the diiron center. The binding of such a large substrate to the MMOH active site may have triggered the reverse process to provide a glimpse of the MMOB altered hydroxylase structure. Only the structure of the MMOH-MMOB complex will confirm whether an α - to π -helix change in the four-helix bundle is induced by the effector protein. Several lines of evidence, however, support the notion that the changes in helix E are physiologically relevant.

The coupling proteins in both the soluble methane monooxygenase and toluene 4-monooxygenase systems affect product regiospecificity (39-41) and bind to helices E and F of the hydroxylase α -subunits (42-44). To alter substrate regiospecificity, the coupling protein must in some way modulate the structure of the hydroxylase active site pocket to influence the formation of one product outcome over another. Mutagenesis and product distribution studies of toluene 4-monooxygenase, in which conserved Thr-201 (213 in MMOH) is changed to alanine, suggest that the coupling protein alters the structure of the hydroxylase within the vicinity of this residue (40). The rearrangements observed here for

residues 212-216 on helix E of MMOH provide the first direct structural evidence supporting the hypothesis that this region of the protein can adopt more than one configuration. Furthermore, these structural changes in helix E may be responsible for the altered substrate regio- and stereospecificities in the presence of the regulatory protein, and reflect coupling protein induced changes in the hydroxylase active site pocket. It is also important to note that the structural rearrangements in helix E do not perturb the geometry of the diiron center, a result that is highly consistent with numerous XAS, EPR, Mössbauer experiments on oxidized MMOH in the presence of MMOB (21,29,45-49).

Reduction of the 6-bromohexan-1-ol soaked MMOH crystals induces disordering of residues 205-215 and loss of the alcohol from the active site cavity. The disorder suggests the occurrence of another conformation change. Although the nature of this change is unknown, it appears that helix E can adopt more than one structure and may do so throughout the sMMO reaction cycle.

MMOH is not the only diiron enzyme in which helix conformational changes are observed. Helix E of class I ribonucleotide reductase (RNR-R2), like MMOH, adopts a π -helical fold in a region of the protein adjacent to its diiron center (50-52). The structure of this helix in class Ib RNR-R2s, which occur in such species as *Salmonella typhimurium* and *Mycobacterium tuberculosis*, exhibits redox dependent conformational changes. Residues Phe-162 and Tyr-163, the structural analogues of Thr-213 and Asn-214 in MMOH, are repositioned to allow the reduced diiron(II) center greater access to solvent and O₂ from the surface of the enzyme (51,52). These changes are not observed, however, in the structurally characterized class Ia RNR-R2 proteins from mouse and *E. coli* (53-55). Never the less, BMM hydroxylases are highly homologous to regions of the

class I RNR-R2, in both the structure of the dimetallic center and topology of the four-helix bundle. The conserved topology in helix E and the observed conformational changes in both the BMM and class 1b RNR-R2 enzymes imply that these helical movements may represent a universal mechanism for function among the four-helix bundle proteins housing dimetallic centers.

Inter-Cavity Gates and Molecule Movement Through MMOH

The structures of MMOH with different bound alcohols shed some light on how a small molecule might move in and out of cavity 1 at the diiron center. Previously, MMOH structures with bound substrate analogues in cavities 2 and 3 (10), and the identification of different rotameric conformations in Leu-110 (11), led to the hypothesis that the three hydrophobic α -subunit cavities may be the route for substrate entrance to the diiron center. The different product-soaked structures presented here suggest that the cavities can be used as a means of product egress as well as substrate entrance. The alternate rotameric conformations observed for those residues that form barriers between cavities 1, 2 and 3 reveal for the first time how side chain movements can affect connectivity between the active site pocket and cavities 2 and 3 in the hydrophobic core of MMOH. In one product-soaked structure, 8-bromooctan-1-ol traverses the gate between cavities 2 and 3, outlining clearly the likely movement from one cavity to the next. Conformational changes in Thr-213, Ile-110, Phe-188, and Leu-289 are therefore likely to occur throughout the catalytic cycle to allow substrate and product passage to and from the active site.

The presence of the halogenated molecules in cavities 1-3 indicates that, in the crystalline state, MMOH is flexible enough to accommodate such product analogues. The structural changes in helix E, the cavity gates and amino acid

residues Leu-286 and Phe-282 in cavity 2 indicate how substrate accommodation may be achieved. In the active site cavity 1, lower occupancies, higher B-values and weaker electron density are the consequences of the increased size of the bound alcohol, possibly reflecting greater difficulty in substrate accommodation and diffusion through the α -subunit. These observations about product binding reflect the trends in alkane reactivity with the diiron center reported previously (14), where methane is the most active substrate, octane the least reactive, and the reactivities of ethane through heptane falling sequentially in between. In contrast to the haloalcohols, rigid products like aromatic alcohols bind only to cavity 3, despite the fact that some of them, like phenol, bind to the diiron center in the absence of MMOB, as revealed spectroscopically (30). One explanation may be that MMOH is too rigid in its crystalline state to permit passage of these compounds to the active site cavity. We conclude that additional structural changes, yet to be observed, must occur to allow these products access to the diiron center.

It is interesting to note that the aromatic products and 8-bromooctan-1-ol appear only in cavity 3. This result suggests that a region of the protein near cavity 3, which comprises mostly loops connecting the different α -helices, may be the initial point of entry for substrates and the final point of exit for products. The observation that all of the bound alcohols generally exhibit higher occupancy, lower B-values, and stronger electron density in cavity 3 than in cavities 1 or 2, lends further support to this proposal. The trend in the B-values is also highly consistent with data from the dibromomethane and iodoethane soaked crystals (10).

One question that has not been addressed is how MMOB may effect the movement of molecules to and from the diiron center. MMOB alters the sMMO product distributions (41), enhances CH₄ and O₂ reactivity with the diiron protein (45,56), binds somewhere near helices E and F of the α -subunit four-helix bundle (42-44), and perturbs the spectroscopic properties of the oxidized diiron(III) center when substrates like methanol and phenol are bound (29). Recent mutagenesis studies of ToMOH indicate that the residue analogous to Asn-214, Asn-202, is essential for binding of its coupling protein (57). This finding, in conjunction with cross-linking and saturation recovery EPR data placing MMOB within this region, requires that some part of MMOB be positioned on helix E above the diiron center. Metal reconstitution studies indicate that MMOB limits both the entry and exit of Fe²⁺ to cavity 1, possibly by decreasing α -subunit side chain fluctuations and providing a greater barrier for solvent access (22). Steady state and stopped-flow kinetic studies of an MMOB quadruple mutant containing smaller amino acids at the predicted MMOH-MMOB interface allow enhanced reactivity of larger substrates like furan and nitrobenzene with the diiron center (58). Methane, however, exhibits decreased reactivity, which was attributed to quenching of the oxygenated iron intermediate by solvent. This conclusion is consistent with the solvent barrier hypothesis put forward to explain the slow rates of Fe²⁺ uptake and removal from MMOH in the presence of MMOB (22). Moreover, deuterium isotope effects for C₂H₆ versus C₂D₆ hydroxylation are observed only when the sMMO system is reconstituted with the MMOB-Quad mutant, implying that the rate-limiting step of substrate diffusion for the reactivity ethane with MMOH can be

altered by MMOH-MMOB interactions (59). These findings were interpreted to indicate that MMOB gates substrate access to the diiron center, presumably through the four-helix bundle, by a molecular sieving effect. The crystallographic results presented here suggest the contrary, because of the apparent entrance of small molecules into the active pocket is through the MMOH α -subunit cavities rather than through the four-helix bundle. So how does one rationalize the current biochemical and structural data?

Perhaps two modes of substrate entrance into cavity 1 exist. Preferred gaseous substrates like CH_4 and O_2 may enter through the four-helix bundle, whereas the less preferred larger substrates may enter through cavity 3 and then diffuse through cavity 2 to the α -subunit to cavity 1. Product egress for all alcohols would be through cavities 1-3. The redox-dependent conformational changes of Asn-214, and the resulting pore granting solvent access to the diiron center due to these changes, imply that small molecule entrance via this route may be possible. Interaction of MMOB with Asn-214 could be the trigger for O_2 gating (56), possibly by inducing conformational shifts to make the overall diameter of the pore more acceptable for O_2 and CH_4 entrance into the active site, in addition to changing the properties of the dinuclear iron center.

ToMOH has an identical Asn residue that undergoes redox dependent conformational changes, exactly mimicking those found in MMOH (13,60). However, the presumed pathway for both toluene entrance and cresol egress is through a 40 Å channel that follows the same path through the α -subunit as delineated by the cavities in MMOH. For two enzymes with the nearly identical diiron centers and supposedly similar mechanisms of dioxygen activation and

hydrocarbon oxidation, ToMO is 20 times more reactive toward aromatics than sMMO (13,14), perhaps reflecting better substrate access. Since the regulatory protein enhances O₂ reactivity in the ToMO system, as it does for sMMO, the most logical explanation that preserves a common mechanism for the two enzyme systems is that the four-helix bundle opening is a point of entry for small gaseous substrates. The present crystallographic data suggest that the cavities in MMOH represent the exclusive route of product exit. This question of how small molecules move through BMMs may be clarified by detailed mutagenesis studies on the hydroxylase component and by obtaining a crystal structure of the hydroxylase-regulatory protein complex.

Although the present results provide better insight into how products and substrates may enter and exit the buried active site of sMMO, it is unknown how the enzyme coordinates their movements throughout the reaction cycle. Is substrate reactivity with the diiron center a case of free diffusion or are other structural events happening to control the passage of small molecules and prevent excessive solvent access to make catalysis more efficient? For instance, methanol is not only the product of the sMMO reaction, but it is also a highly reactive substrate (14,61). The same holds true for aromatic monooxygenases, which can perform up to three successive hydroxylations of a single aromatic compound (62). It seems likely that some phenomena controlling product and substrate movement must occur to prevent the enzyme from wastefully consuming energy in the host organism. The different conformations of Thr-213 and Asn-214 in the oxidized and reduced states of MMOH suggest that redox correlated movements may allow access to the diiron center access from the α -subunit cavities and the surface of the protein throughout the sMMO reaction

cycle, thus providing perhaps a mean by which the enzyme can control the passage of small molecules to and from the active site.

Why Cavities?

Together, the structures of MMOH with bound substrate and product analogues outline a clear pathway by which some small molecules may move through the α -subunit. The "open cavity" or "channel-like" conformation observed in the 2-bromoethan-1-ol and 6-bromohexan-1-ol structures is remarkably similar to that of the channel in toluene monooxygenases, which gives the diiron center in these BMMs unimpeded access to the protein surface (13). The major structural difference between the sMMO and TMO hydroxylase components is the greater solvent access in the latter. It has been hypothesized (13) that solvent access may be responsible for the differential methane reactivity in the sMMO and TMO systems. For an aromatic hydroxylating protein, methane may be too small a substrate to block solvent access from the channel. In contrast, aromatic compounds, when docked into the ToMO active site pocket, can reliably function in this manner (Figure 4.11), thereby keeping the active oxygen intermediates from being quenched by buffer components. For sMMO, the cavity gates may similarly function to block solvent access to the interior of the protein (Figure 4.4b) and to facilitate reactivity of methane with the dioxygen-activated diiron center. If true, the presence of cavities in sMMO may be absolutely essential to its function.

Several studies of dioxygen-utilizing iron proteins have demonstrated the importance of protecting a redox active metal center from solvent as a means of preserving the activity of the protein. Myohemerythrin and hemerythrin are members of the carboxylate-bridged diiron center family of proteins that

function to transport dioxygen in marine invertebrates. Mutagenesis studies on a conserved leucine residue that was proposed previously to gate O₂ entrance into the hydrophobic active site indicate that the size and shape of this residue are required to gate solvent access to the diiron center and limit autooxidation (63,64). Similarly, the dioxygen-coordinating face of the heme moiety in hemoglobin and myohemoglobin is buried within the interior of the protein. Solvent access to this center inactivates the protein by oxidation of the heme to the ferric state (65). The principle of solvent exclusion, although not a new one in bioinorganic chemistry, may not have received proper consideration in our understanding of BMMs. Protection of the diiron center may be achieved in two ways. As demonstrated by stopped-flow studies on sMMO from *M. trichosporium* (OB3b) using the MMOB-Quad mutant (58) and by metal reconstitution studies of MMOH from *M. capsulatus* (Bath) (22), binding of the effector protein is one method by which the enzyme system limits solvent and substrate access to the diiron center directly through the four-helix bundle. The use of cavities and channels in the hydroxylase α -subunit is the other manner in which solvent movement may be controlled. For sMMO and ToMO, the principle of solvent exclusion may be the key to the differences in substrate reactivity between the two enzymes and their families.

Acknowledgments

We thank Lisa Chatwood, Yongwon Jung, Dan Kopp, Mike McCormick and Adam Silverman for assistance with data collection and processing.

References

1. Hanson, R. S., and Hanson, T. E. (1996) *Microbiol. Rev.* **60**, 439-471.
2. Sullivan, J. P., Dickinson, D., and Chase, H. A. (1998) *Crit. Rev. Microbiol.* **24**, 335-373.
3. Pieper, D. H., and Reineke, W. (2000) *Curr. Opin. Biotech.* **11**, 262-270.
4. Leahy, J. G., Batchelor, P. J., and Morcomb, S. M. (2003) *FEMS Microbiol. Rev.* **27**, 449-479.
5. Notomista, E., Lahm, A., Di Donato, A., and Tramontano, A. (2003) *J. Mol. Evol.* **56**, 435-445.
6. Merkx, M., Kopp, D. A., Sazinsky, M. S., Blazyk, J. L., Müller, J. M., and Lippard, S. J. (2001) *Angew. Chem. Int. Ed.* **40**, 2783-2807.
7. Beauvais, L. G., and Lippard, S. J. (2004) Manuscript in preparation.
8. Valentine, A. M., Stahl, S. S., and Lippard, S. J. (1999) *J. Am. Chem. Soc.* **121**, 3876-3887.
9. Gassner, G. T., and Lippard, S. J. (1999) *Biochemistry* **38**, 12768-12785.
10. Whittington, D. A., Rosenzweig, A. C., Frederick, C. A., and Lippard, S. J. (2001) *Biochemistry* **40**, 3476-3482.
11. Rosenzweig, A. C., Brandstetter, H., Whittington, D. A., Nordlund, P., Lippard, S. J., and Frederick, C. A. (1997) *Proteins* **29**, 141-152.
12. Rosenzweig, A. C., Frederick, C. A., Lippard, S. J., and Nordlund, P. (1993) *Nature* **366**, 537-543.
13. Sazinsky, M. H., Bard, J., Di Donato, A., and Lippard, S. J. (2004) *J. Biol. Chem.* **279**, 30600-30610.
14. Colby, J., Stirling, D. I., and Dalton, H. (1977) *Biochem. J.* **165**, 395-402.

15. Dalton, H. (1980) *Adv. Appl. Microbiol.* **26**, 71-87.
16. Green, J., and Dalton, H. (1989) *J. Biol. Chem.* **264**, 17698-17703.
17. Choi, S.-Y., Eaton, P. E., Kopp, D. A., Lippard, S. J., Newcomb, M., and Shen, R. (1999) *J. Am. Chem. Soc.* **121**, 12198-12199.
18. Valentine, A. M., LeTadic-Biadatti, M. H., Toy, P. H., Newcomb, M., and Lippard, S. J. (1999) *J. Biol. Chem.* **274**, 10771-10776.
19. Liu, K. E., Johnson, C. C., Newcomb, M., and Lippard, S. J. (1993) *J. Am. Chem Soc.* **115**, 939-947.
20. Fox, B. G., Froland, W. A., Dege, J. E., and Lipscomb, J. D. (1989) *J. Biol. Chem.* **264**, 10023-10033.
21. Willems, J. P., Valentine, A. M., Gurbiel, R., Lippard, S. J., and Hoffman, B. M. (1998) *J. Am. Chem. Soc.* **120**, 9410-9416.
22. Sazinsky, M. H., Merkx, M., Cadieux, E., Tang, S., and Lippard, S. J. (2004) Manuscript in preparation.
23. Leslie, A. G. W. (1992) *Joint CCP4+ESF-EAMCB Newsletter on Protein Crystallography* **26**.
24. Otwinowski, Z., and Minor, W. (1997) in *Methods Enzymol.* (Charles W. Carter, J., and Sweet, R. M., eds) Vol. 276, pp. 307-326, Academic Press, New York.
25. Brünger, A. T., Adams, P. D., Clore, G. M., Delano, W. L., Gros, P., Grosse-Kunstleve, R. W., Jiang, J.-S., Kuszewski, J., Nilges, N., Pannu, N. S., Read, R. J., Rice, L. M., Simonson, T., and Warren, G. L. (1998) *Acta Cryst D* **54**, 905-921.
26. McRee, D. E. (1999) *J. Struct. Biol.* **125**, 156-165.

27. Andersson, K. K., Froland, W. A., Lee, S.-K., and Lipscomb, J. D. (1991) *New J.Chem.* **15**, 411-415.
28. Liu, K. E., Valentine, A. M., Wang, D. L., Huynh, B. H., Edmondson, D. E., Salifoglou, A., and Lippard, S. J. (1995) *J. Am. Chem Soc.* **117**, 10174-10185.
29. Davydov, R., Valentine, A. M., Komar-Panicucci, S., Hoffman, B. M., and Lippard, S. J. (1999) *Biochemistry* **38**, 4188-4197.
30. Andersson, K. K., Elgren, T. E., Que, L., and Lipscomb, J. D. (1992) *J. Am. Chem. Soc.* **114**, 8711-8713.
31. Whittington, D. A., Sazinsky, M. H., and Lippard, S. J. (2001) *J. Am. Chem. Soc.* **123**, 1794-1795.
32. Rosenzweig, A. C., Nordlund, P., Takahara, P. M., Frederick, C. A., and Lippard, S. J. (1995) *Chem. Biol.* **2**, 409-418.
33. Whittington, D. A., and Lippard, S. J. (2001) *J. Am. Chem Soc.* **123**, 827-838
34. Elango, N., Radhakrishnan, R., Froland, W. A., Wallar, B. J., Earhart, C. A., Lipscomb, J. D., and Ohlendorf, D. H. (1997) *Prot. Sci.* **6**, 556-568.
35. Guex, N., and Peitsch, M. C. (1997) *Electrophoresis* **18**, 2714-2723.
36. Whittington, D. A., and Lippard, S. J. (1998) *ACS Symposium Series* **692**, 334-347.
37. Smoukov, S. K., Kopp, D. A., Valentine, A. M., Davydov, R., Lippard, S. J., and Hoffman, B. M. (2002) *J. Am. Chem. Soc.* **124**, 2657-2663.
38. Gherman, B. J., Dunitz, B. D., Whittington, D. A., Lippard, S. J., and Friesner, R. A. (2001) *J. Am Chem. Soc.* **123**, 3836-3837.
39. Pikus, J. D., Studts, J. M., McClay, K., Steffan, R. J., and Fox, B. G. (1997) *Biochemistry* **36**, 9283-9289.

40. Mitchell, K. H., Studts, J. M., and Fox, B. G. (2002) *Biochemistry* **41**, 3176-3188.
41. Froland, W. A., Andersson, K. K., Lee, S. K., Liu, Y., and Lipscomb, J. D. (1992) *J. Biol. Chem.* **267**, 17588-17597.
42. Zhu, K., Sazinsky, M. H., Pozharski, E., MacArthur, R., Riku, S., Lippard, S. J., and Brudvig, G. W. (2004) Manuscript in preparation.
43. MacArthur, R., Sazinsky, M. H., Kühne, H., Whittington, D. A., Lippard, S. J., and Brudvig, G. W. (2002) *J. Am. Chem. Soc.* **124**, 13392-13393
44. Brazeau, B. J., Wallar, B. J., and Lipscomb, J. D. (2003) *Biochem. Biophys. Res. Comm.* **312**, 143-148.
45. Fox, B. G., Liu, Y., Dege, J. E., and Lipscomb, J. D. (1991) *J. Biol. Chem.* **266**, 540-550.
46. Fox, B. G., Hendrich, M. P., Surerus, K. K., Andersson, K. K., Froland, W. A., Lipscomb, J. D., and Münck, E. (1993) *J. Am. Chem. Soc.* **115**, 3688-3701.
47. Dewitt, J. G., Rosenzweig, A. C., Salifoglou, A., Hedman, B., Lippard, S. J., and Hodgson, K. O. (1995) *Inorg. Chem.* **34**, 2505-2515.
48. Dewitt, J. G., Bentsen, J. G., Rosenzweig, A. C., Hedman, B., Green, J., Pilkington, S., Papaefthymiou, G. C., Dalton, H., Hodgson, K. O., and Lippard, S. J. (1991) *J. Am. Chem. Soc.* **113**, 9219-9235.
49. Shu, L. J., Liu, Y., Lipscomb, J. D., and Que, L. (1996) *J. Biol. Inorg. Chem.* **1**, 297-304.
50. Nordlund, P., and Eklund, H. (1995) *Curr. Opin. Struct. Biol.* **5**, 758-766
51. Eriksson, M., Jordan, A., and Eklund, H. (1998) *Biochemistry* **37**, 13359-13369.

52. Uppsten, M., Davis, J., Rubin, H., and Uhlin, U. (2004) *FEBS Lett.* **569**, 117-122.
53. Atta, M., Nordlund, P., Aberg, A., Eklund, H., and Fontecave, M. (1992) *J. Biol. Chem.* **267**, 20682-20688
54. Logan, D. T., Su, X. D., Åberg, A., Regnström, K., Hajdu, J., Eklund, H., and Nordlund, P. (1996) *Structure* **4**, 1053-1064.
55. Strand, K. R., Karlsen, S., and Andersson, K. K. (2002) *J. Biol. Chem.* **277**, 34229-34238.
56. Liu, Y., Nesheim, J. C., Lee, S. K., and Lipscomb, J. D. (1995) *J. Biol. Chem.* **270**, 24662-24665.
57. Cadieux, E., McCormick, M. S., Sazinsky, M. H., and Lippard, S. J. (2004) Manuscript in preparation.
58. Wallar, B. J., and Lipscomb, J. D. (2001) *Biochemistry* **40**, 2220-2233.
59. Brazeau, B. J., Wallar, B. J., and Lipscomb, J. D. (2001) *J. Am. Chem. Soc.* **123**, 10421-10422.
60. McCormick, M. S., Sazinsky, M. H., and Lippard, S. J. (2004) Unpublished results.
61. Ambundo, E. A., Friesner, R. A., and Lippard, S. J. (2002) *J. Am. Chem. Soc.* **124**, 8770-8771.
62. Cafaro, V., Izzo, V., Scognamiglio, R., Notomista, E., Capasso, P., Casbarra, A., Pucci, P., and Di Donato, A. (2004) *Appl. Env. Microb.* **70**, 2211-2219.
63. Farmer, C. S., Kurtz, D. M., Jr., Phillips, R. S., Ai, J., and Sanders-Loehr, J. (2000) *J. Biol. Chem.* **275**, 17043-17050.

64. Raner, G. M., Martins, L. J., and Ellis, W. R., Jr. (1997) *Biochemistry* 36, 7037-7043.
65. Stryer, L. (1995) *Biochemistry*, 4th Ed., W. H. Freeman and Company, New York.

Table 4.1. Data Collection and Refinement Statistics

	2-Br-ethan-1-ol		3-Cl-propan-1-ol		3-Br-3-buten-1-ol		6-Br-hexan-1-ol		8-Br-octan-1-ol		phenol		4-F-phenol		4-Br-phenol		6-Br-hexan-1-ol reduced		
	20	100 mM	20	10 mM	15	15	15	10 mM	10 mM	10 mM	10 mM	10 mM	60 mM	60 mM	10 mM	60 mM	60 mM	60	
Soaking time (min)	20		10		15	15	15		15	15	15	15	60	60	60	60	60	60	
Soaking concentration	100 mM		10 mM		saturating	saturating	saturating		saturating	saturating	saturating	saturating	10 mM	10 mM	10 mM	10 mM	10 mM	saturating	
Data collection																			
Beamline	SSRL 7-1		SSRL 11-1		SSRL 11-1	SSRL 11-1	SSRL 11-1	SSRL 11-1	SSRL 11-1	SSRL 11-1	SSRL 11-1	SSRL 11-1	SSRL 9-1	SSRL 9-1	SSRL 9-1	SSRL 9-1	SSRL 9-1	SSRL 9-1	
Wavelength (Å)	1.08		1.00		1.00	1.00	1.00	1.00	1.00	1.00	1.00	1.00	0.979	0.979	0.979	0.979	0.979	0.979	
Space group	P2 ₁ 2 ₁ 2 ₁		P2 ₁ 2 ₁ 2 ₁		P2 ₁ 2 ₁ 2 ₁	P2 ₁ 2 ₁ 2 ₁	P2 ₁ 2 ₁ 2 ₁	P2 ₁ 2 ₁ 2 ₁	P2 ₁ 2 ₁ 2 ₁	P2 ₁ 2 ₁ 2 ₁	P2 ₁ 2 ₁ 2 ₁	P2 ₁ 2 ₁ 2 ₁	P2 ₁ 2 ₁ 2 ₁	P2 ₁ 2 ₁ 2 ₁	P2 ₁ 2 ₁ 2 ₁	P2 ₁ 2 ₁ 2 ₁	P2 ₁ 2 ₁ 2 ₁	P2 ₁ 2 ₁ 2 ₁	
Unit cell dimensions (Å)																			
<i>a</i>	71.28		70.47		70.63	70.63	70.41	70.41	70.41	70.41	70.41	70.41	71.18	71.18	71.18	71.18	71.18	71.05	
<i>b</i>	171.53		171.93		171.86	171.86	171.08	171.08	171.08	171.08	171.08	171.55	171.55	171.55	171.55	171.55	171.55	171.60	
<i>c</i>	221.424		220.50		220.62	220.62	220.62	220.62	220.62	220.62	220.62	221.09	221.09	221.09	221.09	221.09	221.09	220.41	
Resolution range (Å)	30-1.95		30-2.4		30-1.8	30-1.8	30-2.0	30-2.0	30-2.0	30-2.0	30-2.0	30-1.96	30-2.3	30-2.3	30-2.3	30-2.3	30-2.3	30-2.5	
Total reflections	798,442		403,659		842,480	842,480	674,046	674,046	674,046	674,046	674,046	787,803	462,856	462,856	458,493	458,493	458,493	506,562	
Unique reflections	197,561		102,181		244,201	244,201	176,340	176,340	176,340	176,340	176,340	193,972	119,593	119,593	119,660	119,660	119,660	92,629	
Completeness (%) ^a	99.8 (98.2)		99.4 (97.7)		98.3 (93.8)	98.3 (93.8)	97.3 (83.7)	97.3 (83.7)	97.3 (83.7)	97.3 (83.7)	97.3 (83.7)	99.7 (99.4)	99.3 (99.8)	99.3 (99.8)	98.3 (98.2)	98.3 (98.2)	98.3 (98.2)	98.2 (86.9)	
<i>I</i> / σ (<i>I</i>)	13.1 (2.7)		15.1 (3.2)		16.8 (2.8)	16.8 (2.8)	16.2 (4.1)	16.2 (4.1)	16.2 (4.1)	16.2 (4.1)	16.2 (4.1)	12.8 (3.2)	17.6 (4.2)	17.6 (4.2)	16.6 (4.1)	16.6 (4.1)	16.6 (4.1)	14.7 (3.3)	
<i>R</i> _{sym} (%) ^b	8.2 (46.1)		7.9 (34.6)		9.0 (32.6)	9.0 (32.6)	7.4 (26.2)	7.4 (26.2)	7.4 (26.2)	7.4 (26.2)	7.4 (26.2)	7.4 (40.4)	9.0 (38.1)	9.0 (38.1)	9.0 (36.8)	9.0 (36.8)	9.0 (36.8)	5.8 (46.4)	
Refinement																			
<i>R</i> _{cryst} (%) ^c	19.9		20.9		22.7	22.7	20.6	20.6	20.6	20.6	20.6	22.5	21.7	21.7	22.1	22.1	22.1	23.5	
<i>R</i> _{free} (%) ^d	23.1		23.6		25.8	25.8	23.5	23.5	23.5	23.5	23.5	25.3	25.3	25.3	26.5	26.5	26.5	28.4	
Number of atoms	18640		18269		18366	18366	18290	18290	18290	18290	18290	17787	17927	17927	17926	17926	17926	17344	
Protein	17317		17317		17324	17324	17320	17320	17320	17320	17320	17317	17327	17327	17327	17327	17327	17231	
Water	1169		892		988	988	954	954	954	954	954	448	580	580	579	579	579	95	
r.m.s.d. bond length (Å)	0.0055		0.0066		0.0058	0.0058	0.0055	0.0055	0.0055	0.0055	0.0055	0.0058	0.0064	0.0064	0.0068	0.0068	0.0079		
r.m.s.d. bond angle (°)	1.16		1.30		1.17	1.17	1.19	1.19	1.19	1.19	1.19	1.20	1.20	1.20	1.23	1.23	1.30		
Average B-value (Å ²)	26.5		30.3		36.2	36.2	37.1	37.1	37.1	37.1	37.1	25.1	41.3	41.3	40.9	40.9	66.4		
PDB ID	xxxx		xxxx		xxxx	xxxx	xxxx	xxxx	xxxx	xxxx	xxxx	xxxx	xxxx	xxxx	xxxx	xxxx	xxxx	xxxx	xxxx

^aValues in parentheses are for the highest resolution shell. ^b $R_{\text{sym}} = \sum_{hkl} |I(hkl) - \langle I(hkl) \rangle| / \sum_{hkl} I(hkl)$, where $\langle I(hkl) \rangle$ is the h^{th} measured diffraction intensity and $\langle I(hkl) \rangle$ is the mean of the intensity for the Miller index (hkl). ^c $R_{\text{cryst}} = \sum_{hkl} |F_o(hkl) - |F_c(hkl)|| / \sum_{hkl} |F_o(hkl)|$. ^d $R_{\text{free}} = R_{\text{cryst}}$ for a test set of reflections (5% in each case).

Table 4.2. Halogenated Alcohol Binding Sites on MMOH

Compound	Location	Occupancy	B-value (\AA^2)	Compound	Location	Occupancy	B-value (\AA^2)	
2-Br-ethan-1-ol	$\alpha 1$, cavity 1	0.87	42.9	3-Cl-propan-1-ol	$\alpha 1$, cavity 1	1.00	36.3	
	$\alpha 1$, cavity 2	0.92	44.0		$\alpha 1$, cavity 2	1.00	41.8	
	$\alpha 1$, cavity 3	0.75	57.8		$\alpha 1$, cavity 3	1.00	15.9	
	$\alpha 2$, cavity 1	0.85	44.0		$\alpha 2$, cavity 1	1.00	43.3	
	$\alpha 2$, cavity 2	0.90	43.7		$\alpha 2$, cavity 2	1.00	20.1	
	$\alpha 2$, cavity 3	0.94	41.7		$\alpha 2$, cavity 3	1.00	6.0	
	$\alpha 1/\beta 1$ interface	0.88	33.1	3-Br-3-butenol	$\alpha 1$, cavity 1	0.83	85.8	
	$\beta 1$, inner	0.83	56.4		$\alpha 1$, cavity 2	0.77	96.1	
	$\beta 2$, inner	0.76	62.9		$\alpha 1$, cavity 3	0.93	79.0	
	$\alpha 2/\beta 2$ interface	0.89	36.8		$\alpha 2$, cavity 1	0.65	99.7	
	$\beta 1$, inner	0.83	54.3		$\alpha 2$, cavity 2	0.76	97.3	
6-Br-hexan-1-ol	$\alpha 1$, cavity 1	0.78	66.0	$\alpha 2$, cavity 3	1.00	70.0		
	$\alpha 1$, cavity 2	0.75	66.1	$\alpha 1/\beta 2$ interface	1.00	74.9		
	$\alpha 1$, cavity 3	0.75	50.4	$\alpha 2/\beta 1$ interface	0.90	82.6		
	$\alpha 2$, cavity 1	0.87	67.1	$\alpha 1$, surface	0.55	79.5		
	$\alpha 2$, cavity 2	1.00	51.1	$\alpha 2$ on $\gamma 2$ side	0.64	91.8		
	$\alpha 2$, cavity 3	0.72	47.5	8-Br-octan-1-ol	$\alpha 1$, cavity 3	0.84	46.5	
	$\alpha 1/\beta 2$ interface	0.62	82.9		$\alpha 1$, cavity 2+3	0.80	61.6	
	$\alpha 2/\beta 1$ interface	0.58	70.6		$\alpha 1$ on $\gamma 1$ side	0.83	81.4	
	$\alpha 2$, surface	0.51	81.6		$\alpha 2$ on $\gamma 2$ side	0.87	64.0	
	$\alpha 1/\beta 1$ N-term	0.87	74.7		4-Br-phenol	$\alpha 1$, cavity 3	0.93	58.3
	$\alpha 2/\beta 2$ N-term	0.77	76.5			$\alpha 2$, cavity 3	0.91	64.1
	$\alpha 1$ on $\gamma 1$ side	0.82	81.4					
	$\alpha 2$ on $\gamma 2$ side	0.77	69.5					

* $\alpha 1$, $\alpha 2$, $\beta 1$, $\beta 2$, $\gamma 1$, $\gamma 2$ refer to the subunits of protomers 1 and 2. Occupancies are presented for just the bromine and chlorine atoms. These values are subject to change upon further refinement of the MMOH structures.

Table 4.3. Cavity Connectivity and Side Chain Movements in Product-soaked MMOH Crystal Structures

Alcohol	Cavity 1	Cavity 2	Cavity 3	Protomer 1	Cavity Connectivity	Protomer 2	Cavity Connectivity	α -subunit Backbone Perturbations	Cavity Side Chains with Altered Positions ^a
2-bromoethan-1-ol	✓	✓	✓	1+2+3	1+2+3	1+2+3			Cav1: L110, F188, T213, I217 Cav2: L289, M184
3-chloropropan-1-ol	✓	✓	✓	2+3	2+3	2+3			Cav1: L110, F188 Cav2: L289, M184
3-bromo-3-buten-1-ol	✓	✓	✓	2+3	2+3	2+3			Cav1: L110, F188 Cav2: L289, M184
6-bromohexan-1-ol	✓	✓	✓	2+3	2+3	2+3	residues 212-216		Cav1: L110, F188, I217, F212-L216 Cav2: F282, L286, L289, M184
8-bromooctan-1-ol	✓	✓ ^b	✓	1+2+3	2+3	2+3			Cav1: L110, F188, T213 Cav2: L289, M184
4-fluorophenol		✓	✓	none	none	none			Cav1: L110 Cav2: M184
4-bromophenol		✓	✓	none	none	none			Cav1: L110, T213 Cav2: M184
Phenol		✓	✓	none	none	none			Cav1: L110 Cav2: M184

^a Based on comparison to MMOH_{ox} crystal form II α -subunits.^b Designates product that spans cavities 2 and 3.

Table 4.4. Fe-Fe and Fe-O Bridge Ligand Bond Distances in Different Product-Bound Structures^a

	H ^{ox} (PDB:1MHY)	methanol (PDB:1FZ6)	ethanol (PDB:1FZ7)	2-Br-ethan-1-ol	3-Cl-propan-1-ol	3-Br-buten-3-ol	6-Br-hexan-1-ol
Fe1-Fe2	3.0	3.0	3.2	3.1 3.2	3.2 3.1	3.2 3.0	3.1 3.1
Fe1-ROH	2.1 (OH)	2.1	2.2	2.4 2.2	2.3 2.1	2.3 2.1	2.3 2.2
Fe2-ROH	2.2	2.1	2.6	2.4 2.4	2.3 2.5	2.1 2.0	2.3 2.3
Fe1-OH	1.7	1.9	2.1	1.9 2.0	2.0 1.9	2.2 2.3	2.2 2.2
Fe2-OH	2.0	1.9	1.8	1.8 2.0	1.9 1.8	2.0 2.1	1.9 1.8

^a All distances are in Å. Distances from both protomers are listed from those active sites in which an alcohol was bound. Values are reported for coordinate published in the protein data base (PDB) or from this work.

Table 4.5. Average B-factors for Selected Regions of the MMOH α -Subunits*

Residues	Reduced MMOH (2.1 Å)	Reduced 6-Br-hexan-1-ol Soaked MMOH (2.6 Å)	Oxidized 6-Br-hexan-1-ol Soaked MMOH (1.8 Å)	3-Br-3-buten-1-ol Soaked MMOH _{ox} (2.4 Å)
a-subunit	28.0 26.8	68.8 68.8	32.8 36.7	38.2 40.3
β -subunit	30.0 40.5	50.2 73.2	28.3 44.8	30.1 48.8
γ -subunit	26.1 48.3	54.2 54.3	30.7 54.5	33.1 60.2
195-225 (helix E)	25.8 27.2	79.8 78.6	32.4 33.8	43.7 42.8
230-260 (helix F)	38.9 41.1	93.5 94.2	31.4 34.9	37.9 47.6
205-215 (helix E)	39.9 40.3	88.6 90.3	41.0 39.0	60.0 55.3

* Units are in Å². The average B-values for each protomer in the $\alpha_2\beta_2\gamma_2$ dimer are presented. The pdb file 1FYZ was used to calculate the average B-factors for form-II MMOH_{red}.

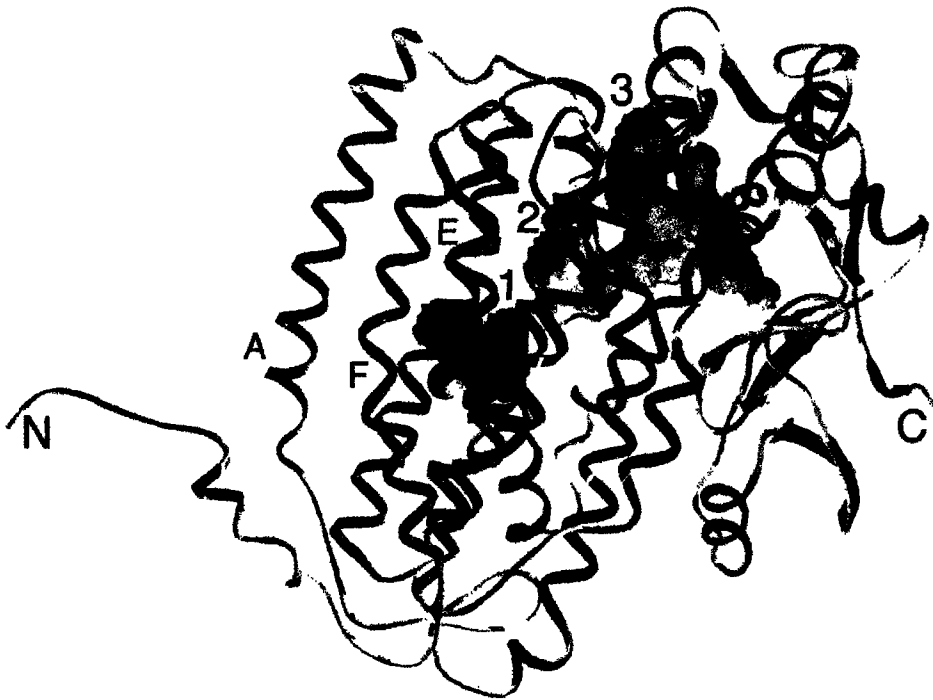


Figure 4.1. The α -subunit of MMOH depicting the hydrophobic cavities. The diiron center is depicted as orange spheres. Cavities 1-3, helices A, E, and F, and the N- and C- termini are labeled.

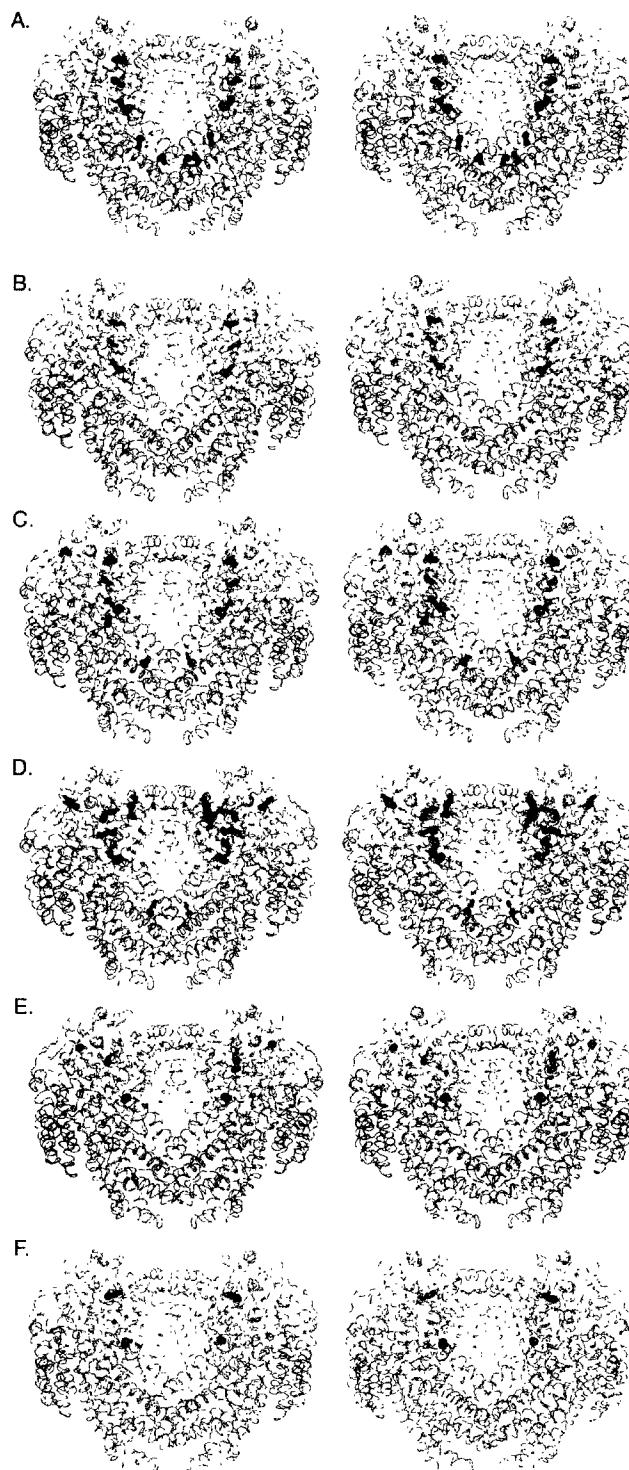


Figure 4.2. Stereoviews of haloalcohol binding sites within MMOH for (A) 2-bromoethan-1-ol (B) 3-chloropropan-1-ol (C) 3-bromo-3-buten-1-ol (D) 6-bromohexan-1-ol (E) 8-bromooctan-1-ol and (F) 4-bromophenol. $|F_o| - |F_c|$ simulated annealing (sa) omit electron density maps contoured to 3σ are depicted for each bound molecule. The α - β - and γ -subunits are depicted in green, gray, and blue, respectively.

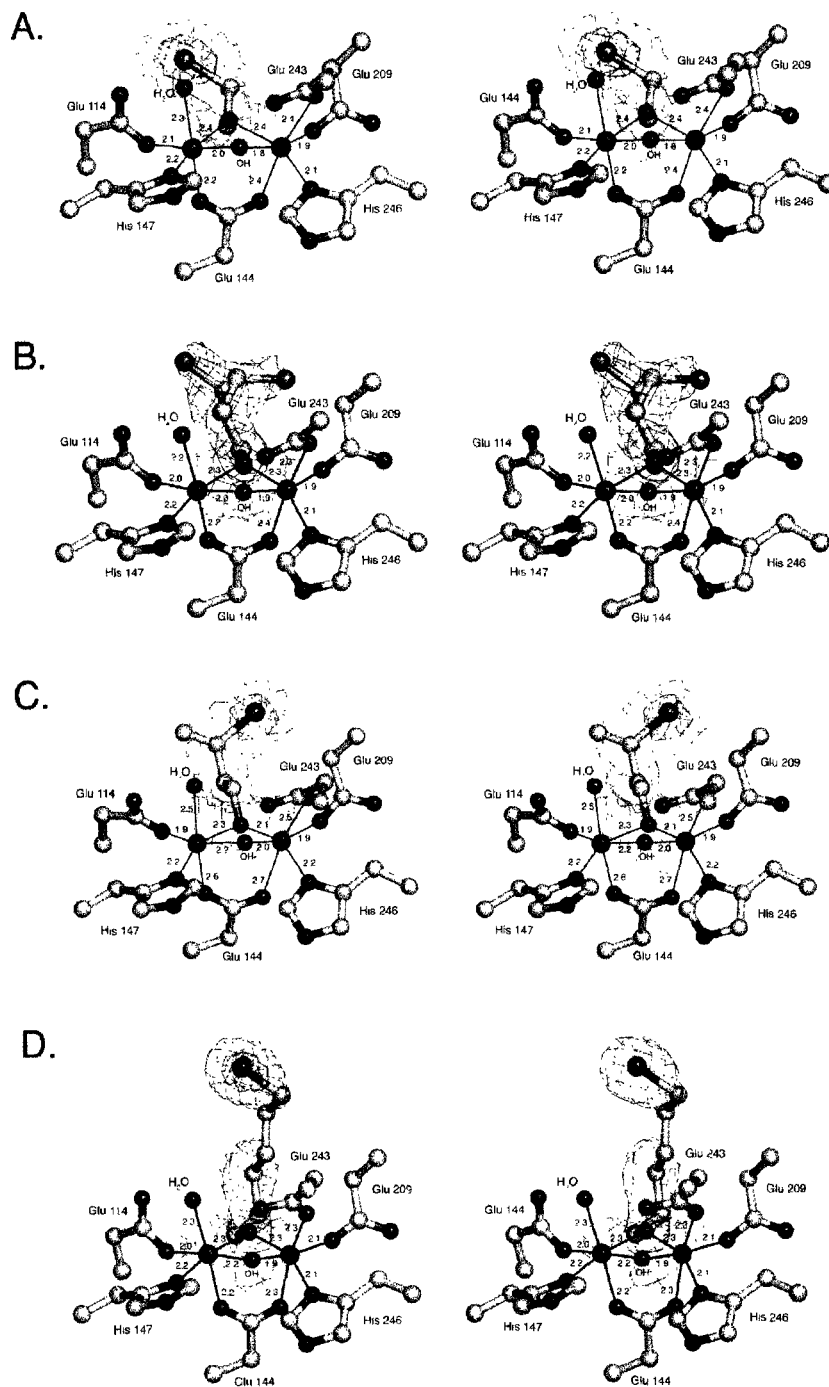


Figure 4.3. MMOH active sites depicting with bound alcohols in stereo. $|F_o| - |F_c|$ σ -omit maps contoured to 3σ (blue/green) and 8σ are shown around the bound (A) 2-bromoethan-1-ol, (B) 3-chloropropan-1-ol, (C) 3-bromo-3-buten-1-ol, and (D) 6-bromohexan-1-ol molecules. The active sites from the second protomer appear similar. The atoms are colored by type where gray is carbon, red is oxygen, blue is nitrogen, orange is iron, green is chlorine, and purple is bromine.

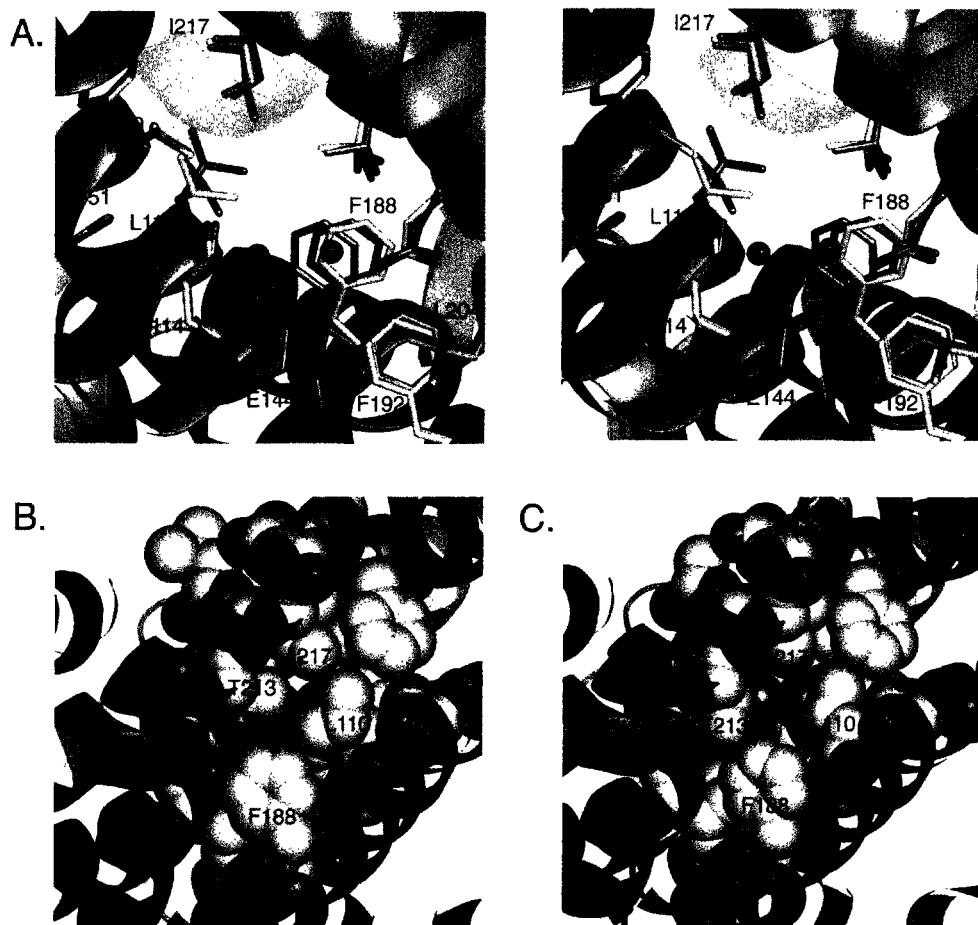


Figure 4.4. (A) Comparison of side chain positions in active site cavities of oxidized form I MMOH (gray), oxidized form II MMOH (blue), and 2-bromoethan-1-ol bound MMOH (green), in stereo. The view is from behind the diiron center looking out at the leucine gate. Also shown are spacefilling representations of the leucine gate as a small molecule may approach the diiron center from cavity 2 in the (B) oxidized form I MMOH and (C) 2-bromoethan-1-ol soaked MMOH structures. Iron atoms are depicted as orange spheres. Carbon, oxygen and nitrogen are colored as described in Figure 4.3. 2-bromoethan-1-ol is not drawn in c.

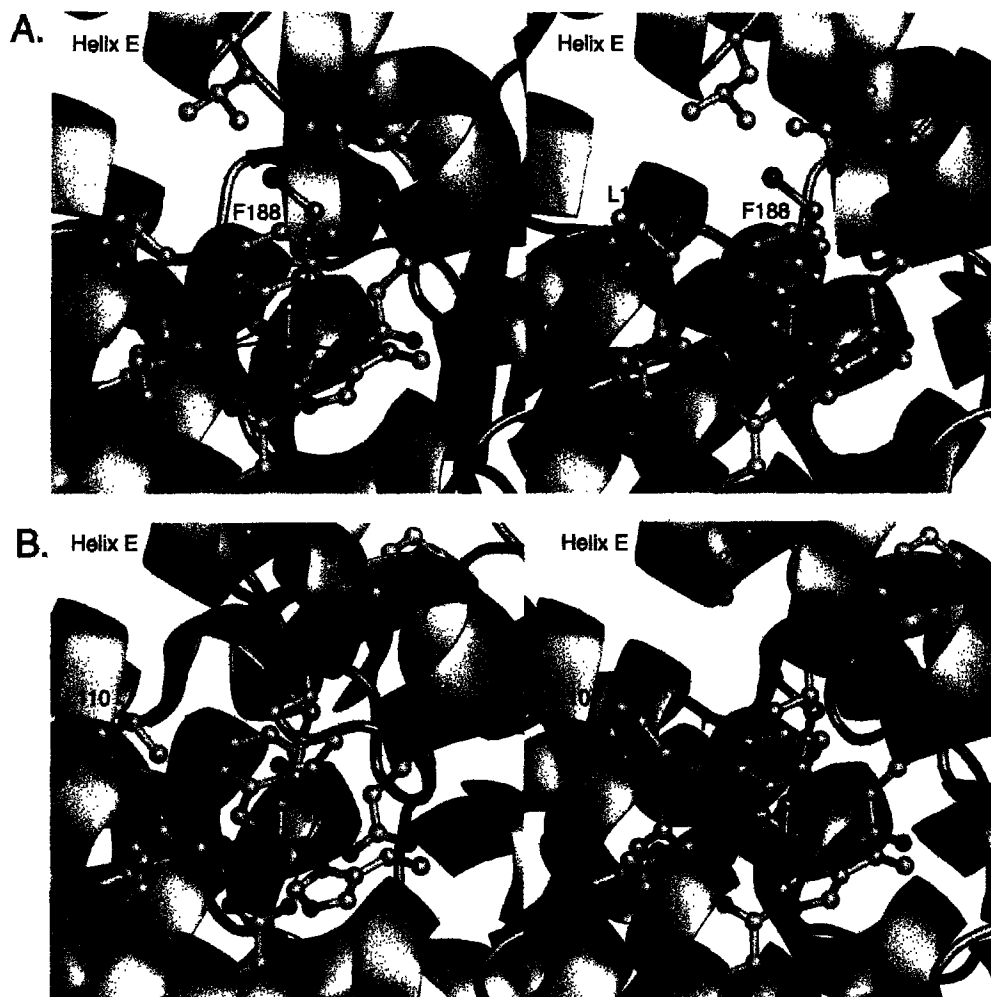


Figure 4.5. Stereoviews comparing the (A) 6-bromohexan-1-ol soaked and (B) oxidized MMOH active site pockets. 6-bromohexan-1-ol is depicted in light blue in both active sites to demonstrate the steric clash between the bromine atom (purple) and Thr-213.

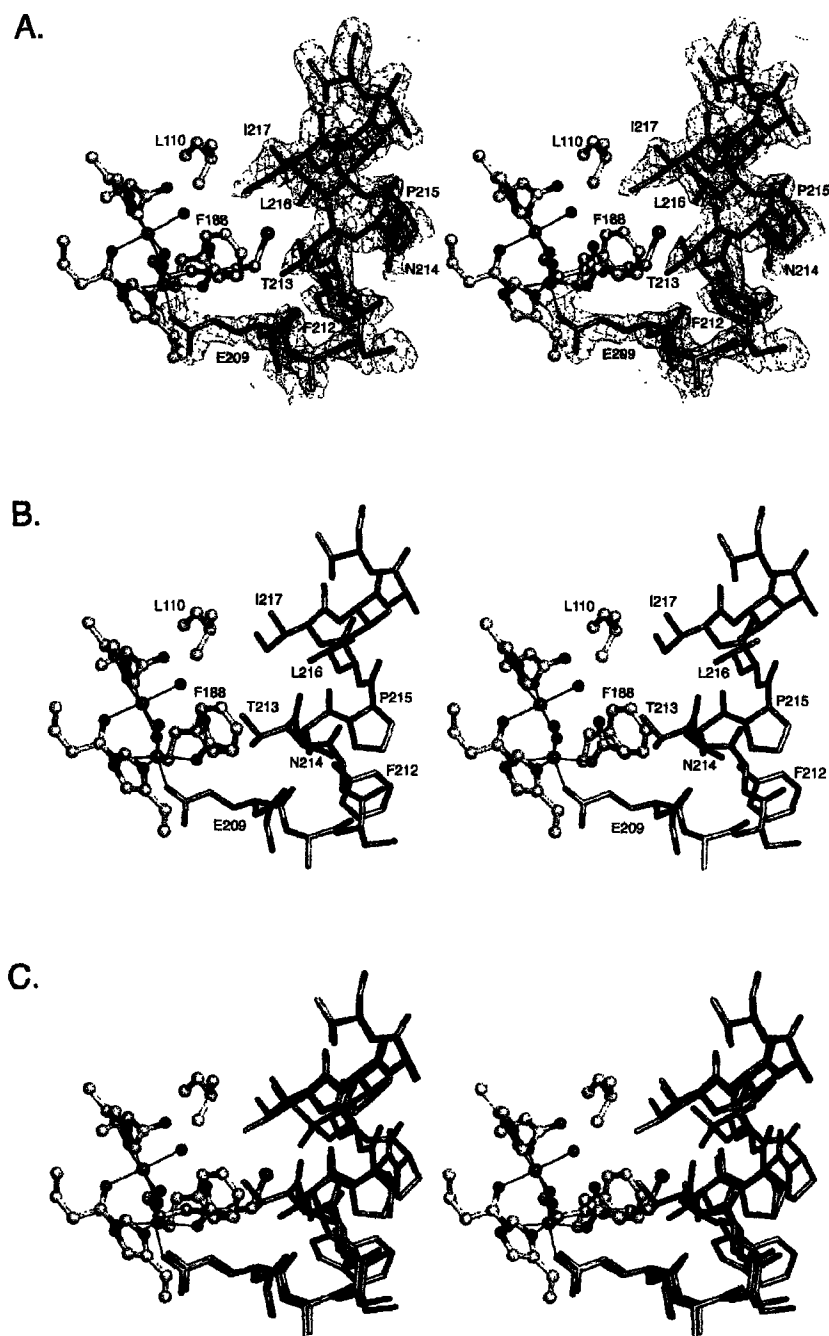


Figure 4.6. Structural changes in helix E of the four-helix bundle. (A) Structure in stereo of helix E near the MMOH active site with bound 6-bromohexan-1-ol (teal). An $|F_o| - |F_c|$ omit map contoured to 3σ is depicted around helix residues 208-220. (B) Structure in stereo of the helix E near the MMOH active site in oxidized MMOH. (C) Direct comparison of helix E from the 6-bromohexan-1-ol soaked (green) and oxidized (salmon) structures. 6-Bromohexan-1-ol is depicted to demonstrate the relative position of the bromine atom (purple) to Thr-213.

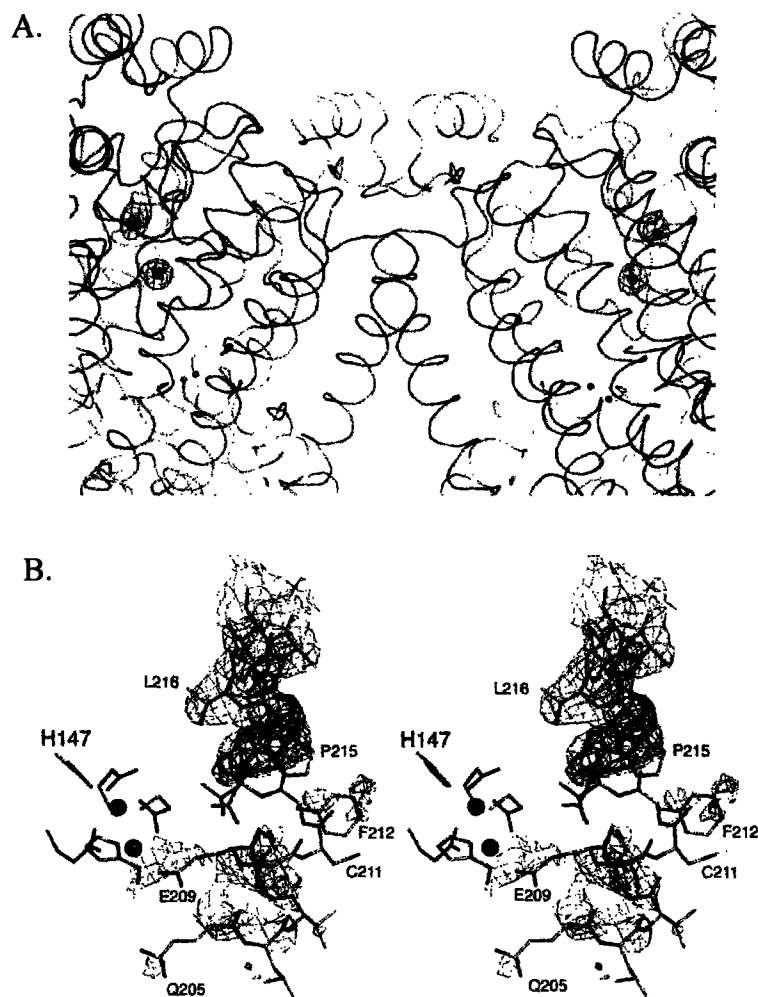


Figure 4.7. Structure of MMOH soaked in 6-bromohexan-1-ol prior to chemical reduction. (A) $|F_o| - |F_c|$ sa-omit electron density map contoured to 3σ (green) and 7σ (red) around the bromine atoms of 6-bromohexan-1-ol bound to cavities 2 and 3 of the MMOH α -subunit (blue). No electron density is observed in cavity 1 for the product analogue. The β -subunit is depicted as yellow ribbons and iron atoms as orange spheres. (B) Residues 205-220 of MMOH α -subunit helix E adjacent to the diiron center in stereo. $2|F_o| - |F_c|$ (green) and $|F_o| - |F_c|$ sa-omit (red) electron density maps depicted around helix E only. The poor electron density within this region, as compared to the rest of the protein, indicates this helix disorders upon reduction.

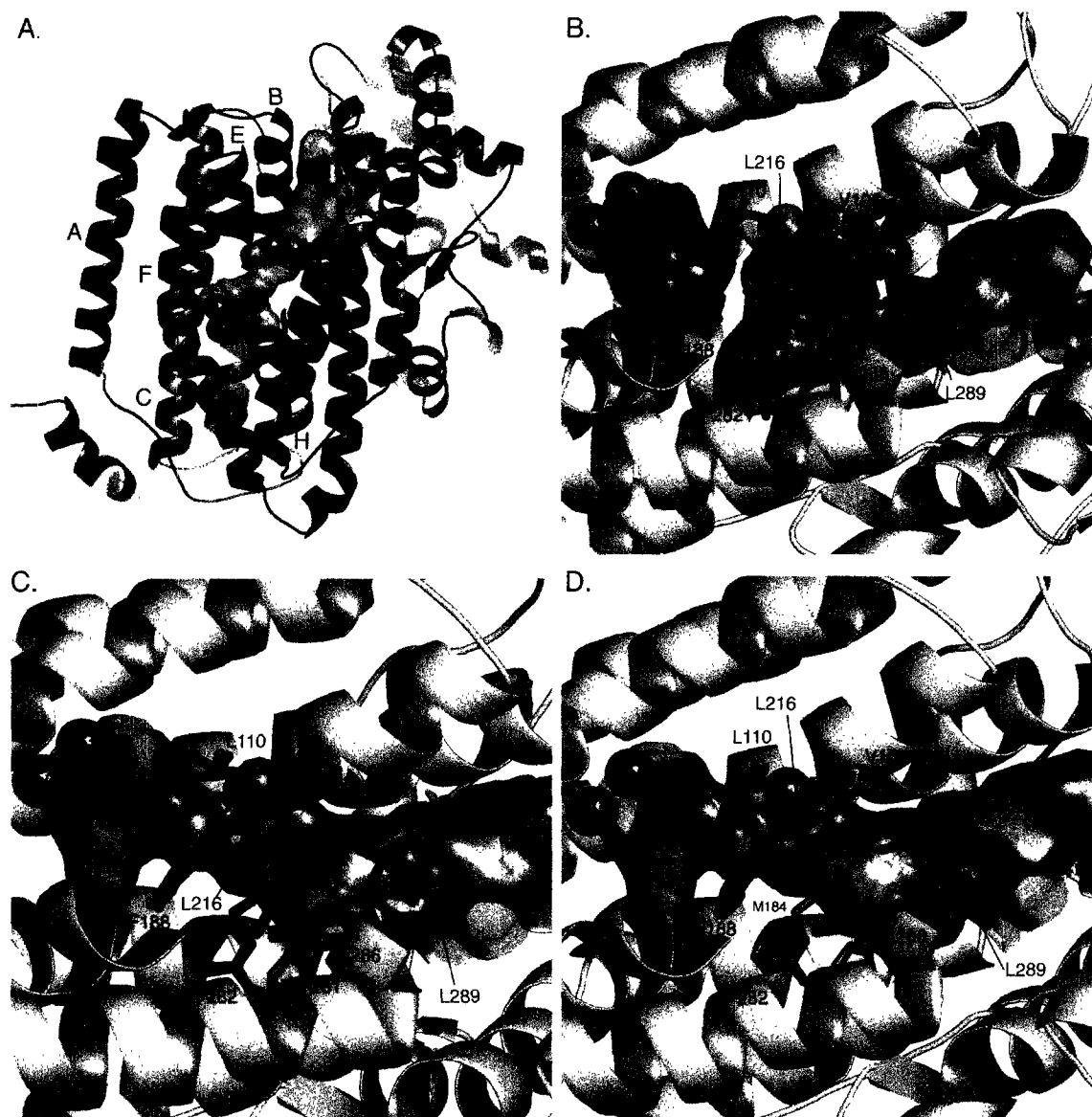


Figure 4.8. (A) Depiction of the channel (gray) formed in the MMOH α -subunit of the 2-bromoethan-1-ol soaked structure. Parts of helices E, B, and H are cut away for better visualization. The molecules of 2-bromoethan-1-ol (red spheres) are bound as depicted in the channel. (B) Three molecules of 6-bromohexan-1-ol (spheres) bound in the α -subunit cavities (light blue). The bromine, carbon, and oxygen atoms are colored purple, yellow, and red, respectively. The positions of the cavity 2 side chains in the oxidized form II (green) and 6-bromohexan-1-ol soaked (red) MMOH structures are represented. (C) and (D) 8-Bromooctan-1-ol bound to the α -subunit channel (light blue) depicting its different positions with respect to the amino acid gate, L289, between cavities 2 and 3 in the two MMOH α -subunits. 8-bromooctan-1-ol is colored as in (B). The cavity 2 side chains for the oxidized form I (blue), oxidized form II (green), and 8-bromooctan-1-ol soaked (red) MMOH structures are identified.

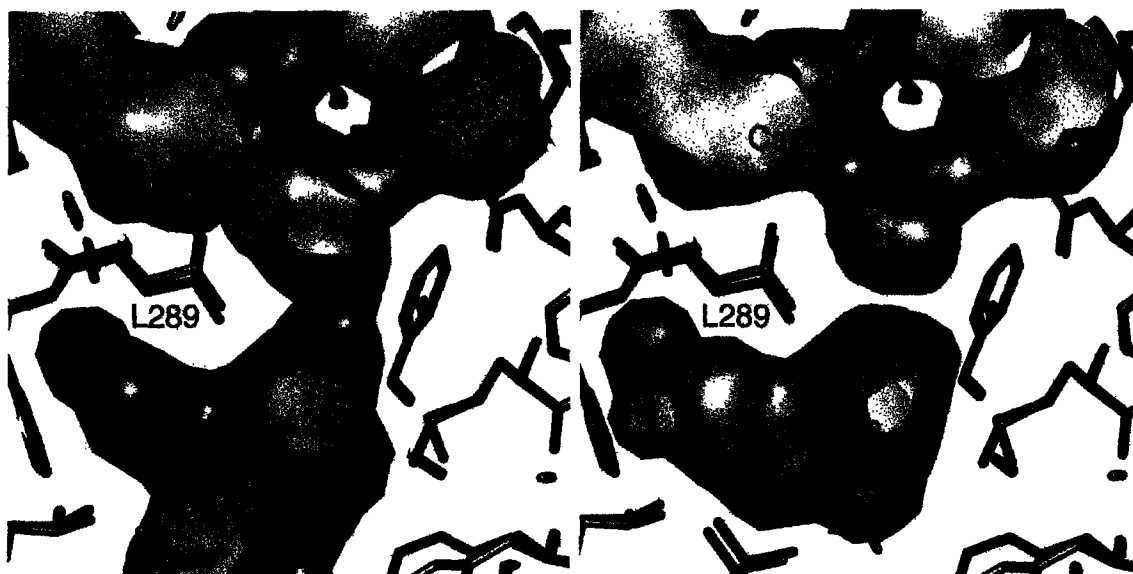


Figure 4.9. Movements in Leu-289 in 2-bromoethan-1-ol soaked (blue) and oxidized form II (green) MMOH influence the connectivity between cavities 2 and 3 (depicted as surfaces). The differences in the position of the Leu-289 side chain may be insignificant with respect to the connectivity between cavities 2 and 3 and may be an arbitrary assignment based on how different programs calculate solvent accessibility.

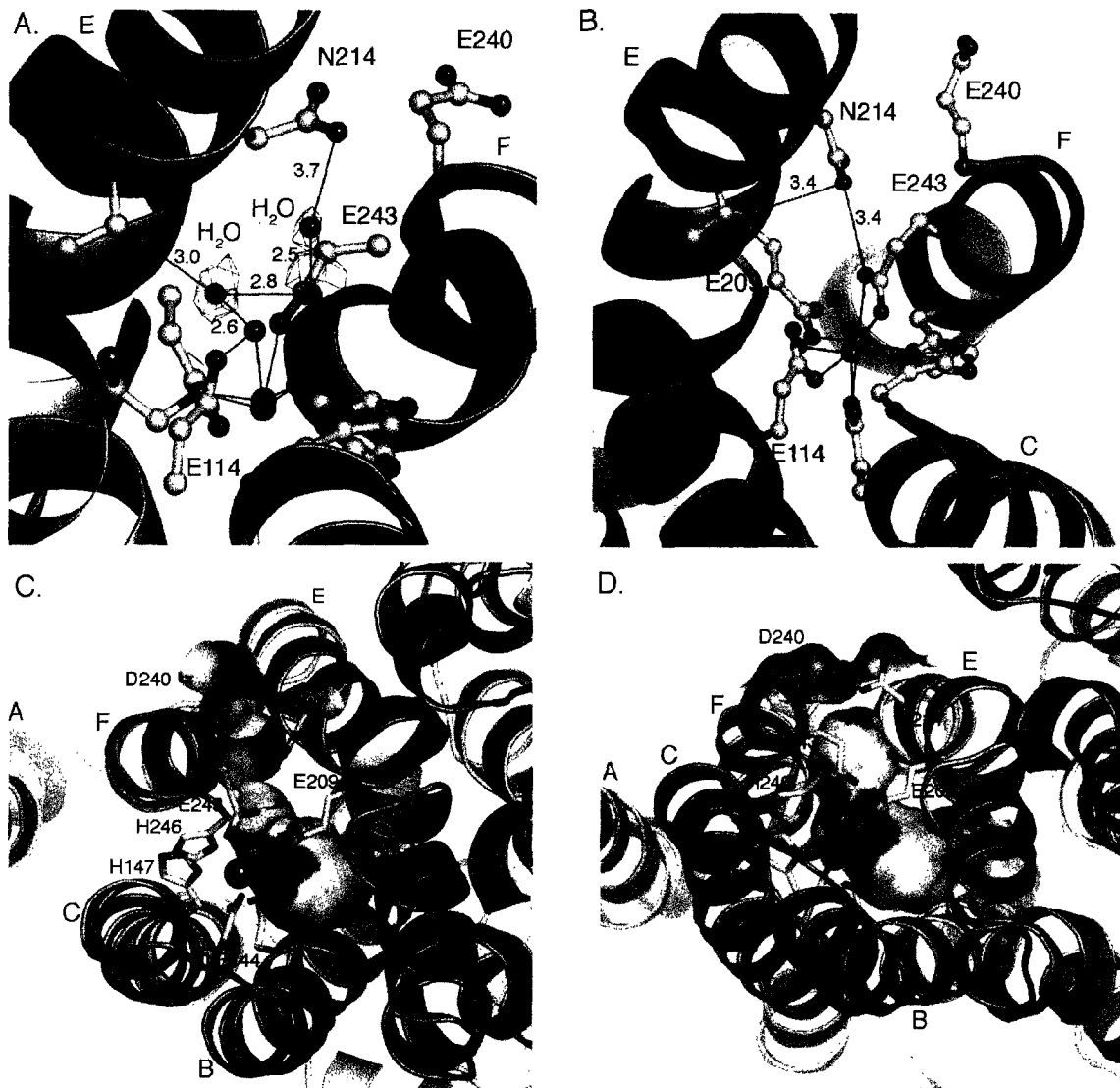


Figure 4.10. The effect of Asn-214 conformation on solvent accessibility to the diiron center. (A) Structure of oxidized MMOH with 2-bromoethan-1-ol bound depicting Asn-214 pointing towards solvent and novel water molecule hydrogen bonding configurations. Each water is surrounded by an $|F_o| - |F_c|$ 2σ omit map contoured to 3σ . (B) Structure of reduced MMOH in which Asn-214 points towards the diiron active site. (C) The formation of pore through the four-helix bundle of reduced MMOH demonstrating enhanced solvent accessibility as compared to (D) oxidized MMOH. All atoms are colored as described in Figure 4.3 and the surfaces are colored by atom type.

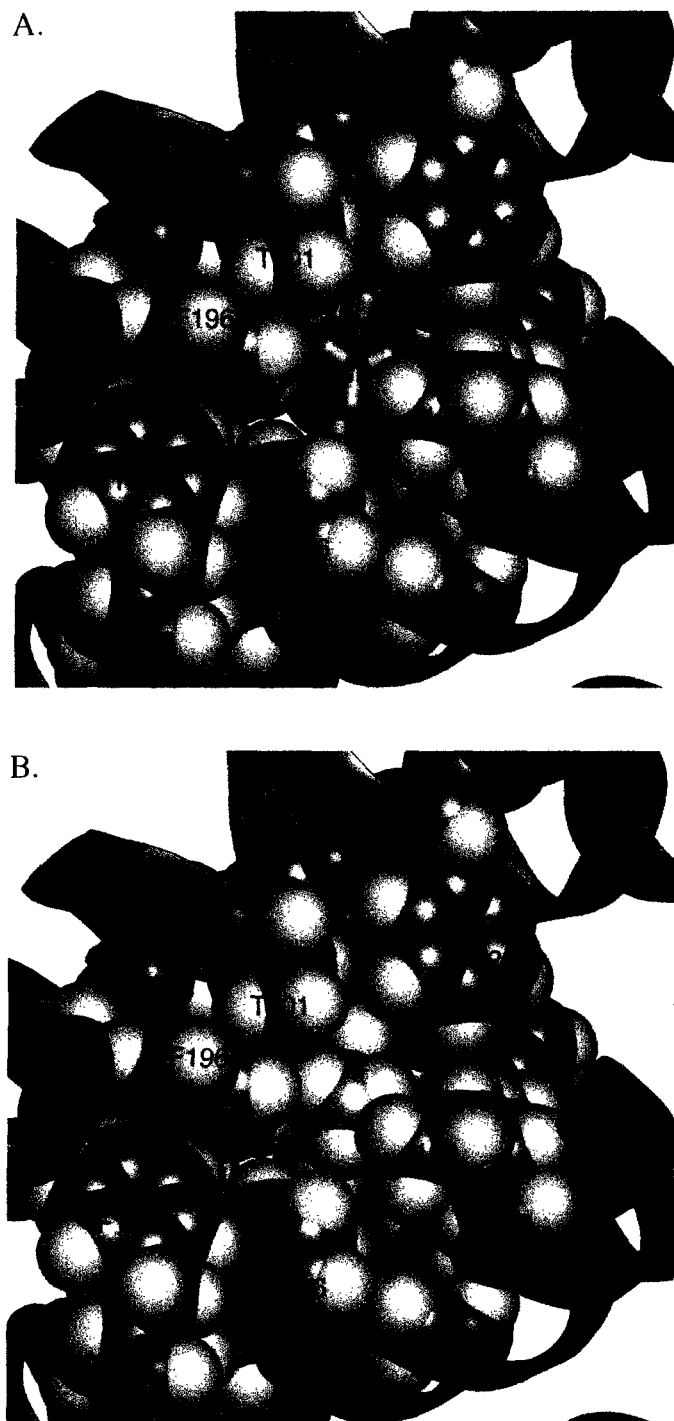


Figure 4.11. Active site of ToMOH as substrate would approach from the channel. *p*-Cresol (green) docked to the diiron center in (A) stick and (B) spacefilling representations. The product was docked by using the program MOE (CCG Inc.).

Appendix 1**Characterization and Crystallization of the MMOH-MMOD Complex from*****Methylococcus capsulatus* (Bath)**

Introduction

Soluble methane monooxygenase (sMMO) is a multicomponent enzyme system that catalyzes the first committed step in the conversion of methane to biomass in methanotrophic bacteria through its ability to hydroxylate methane to methanol at a carboxylate-bridged diiron center housed in the α -subunit of the 251 kDa hydroxylase component, MMOH (eq 1) (1). Also required for this conversion is a cofactorless regulatory protein, MMOB, that couples electron



transfer from an NADH-utilizing ferredoxin- and flavin-containing reductase, MMOR, to the diiron center of MMOH. Although studies carried out on the sMMO systems from both *Methylococcus capsulatus* (Bath) and *Methylosinus trichosporium* (OB3b) have provided many insights into the mechanism of dioxygen activation and substrate oxidation, the inability to express a recombinant form of MMOH in high yield has limited our ability to test hypotheses about sMMO function by site-directed mutagenesis.

A clue to the difficulty in expressing MMOH in recombinant systems may reside in the sMMO operon (Figure A1.1). In addition to the *mmoX*, *mmoY*, *mmoZ*, *mmoB*, and *mmoC* genes that encode for MMOH, MMOB and MMOR, the operon contains three additional genes, *orfY*, *mmoG*, and *mmoR*, the functions of which have yet to be determined (2,3). The *mmoG* and *mmoR* gene products are predicted to be a protein-folding chaperone, similar to GroEL, and a metal-dependent repressor, respectively. The sequence of the 11.9 kDa *orfY* gene product, termed MMOD, has no sequence homology to that of any known protein. In a multicomponent phenol hydroxylase, a small cofactorless protein of

~10.5 kDa (DmpK) is required for assembling the diiron center of the hydroxylase component (4). Based on this finding, MMOD was hypothesized similarly to participate in the assembly of MMOH (5).

MMOD contains 103 amino acids and is monomeric in solution (5). The protein is expressed at ~ 2% the concentration of MMOH in *M. capsulatus* (Bath). It inhibits in vitro hydroxylase activity of sMMO by competing with MMOB for a similar binding site on the α -subunit of MMOH. Chemical cross-linking experiments suggest that MMOD associates with only MMOH and not with any of the other known components. Stopped-flow studies revealed that MMOD may also inhibit sMMO activity by disrupting electron transfer from the reductase to the diiron center (6). The binding of MMOD to MMOH induces a change in the absorption spectrum of the hydroxylase, giving rise to peaks at 352 nm and 500 nm, which are indicative of a (μ -oxo)diiron(III) species. This species, however, represents only 10-25% of the total diiron population present in solution, according to Mössbauer spectroscopy (7). Metal insertion activity for MMOD has yet to be observed.

To help understand the function of MMOD and how a protein component binds MMOH and induces spectroscopic change, it would be of interest to determine the structure of MMOD and the MMOH-MMOD complex. The latter would not only reveal for the first time exactly where a protein component docks onto MMOH, but also provide insight into how this event could affect the structure of the diiron center. By inference, the structure an MMOH-MMOD complex may provide clues as to how the regulatory protein, MMOB, which binds to a similar region of MMOH (5), might function to enhance catalytic activity. If MMOD were indeed a metallochaperone, a structure of both MMOD

and the MMOH-MMOD complex would provide insight into possible mechanisms of iron insertion.

Here we report the crystallization of a MMOH-MMOD complex and biochemical studies to characterize the MMOD structure. The creation of a MMOD Cys67Ser mutant was instrumental in the successful crystallization of the protein complex. These crystals diffract to ~ 4.6 Å and can be indexed in spacegroup $P6_522$ (or $P6_122$) with unit cell dimensions 144.5 Å \times 144.5 Å \times 309 Å. The crystallized MMOD component is a truncated form consisting of residues 15-91, which we term MMOD'. For the purpose of improving crystallization of the MMOD-MMOH complex, we also describe the creation and characterization of the MMOD' and MMOD'C67S proteins.

Experimental

Protein Isolation and Purification

MMOH was isolated from *M. capsulatus* (Bath) cells grown by fermentation in 15 L batches at 45 °C under low copper conditions and purified as described previously (5,8). Protein purity was determined by SDS-PAGE. Purified MMOH was exchanged into a buffer containing 25 mM MOPS, pH 7.0, 100 mM NaCl and 5% (v/v) glycerol and concentrated to > 100 mM by using a Centriprep YM-100 (Amicon) concentrator. The specific activity was determined by using either one of two established methods, either by monitoring the rate of NADH consumption spectroscopically or the production of propylene oxide using gas chromatography (9). NADH assays were performed at 20 °C in a 25 mM MOPS solution, pH 7.0, containing 1 mM DTT, 160 μ M NADH ($A_{340} \sim 1.0$), saturating amounts of furan or propylene, 1.0 μ M MMOH, 2.0 μ M MMOB and

0.5 μM MMOR. The assay was initiated by the addition of NADH, and NADH consumption was measured by UV-vis on an HP 8453 diode array spectrophotometer. Propylene oxide assays were performed by using the same buffer and assay conditions and measuring the product by gas chromatography, as described previously (5). A ferrozine assay was employed to determine the iron content; ~3.6-4.1 iron atoms bound per molecule of MMOH were found.

MMOD and all MMOD mutants were purified by using a His₆-tag and Ni²⁺ binding column as described previously (5). The purity was assayed by SDS-PAGE. After purification, the MMOD proteins were exchanged into 25 mM MOPS, pH 7.0, 100 mM NaCl, and 5% glycerol (v/v) and concentrated to greater than 200 μM .

Construction and Purification of the MMOD Cys67Ser Mutant

Complimentary primers (5'-GTCCAGGAGGGTTCCTCGATCAGCCTGG-AG-3' and 3'-CAGGTCCTCCCAAGGAGGCTAGTCGGACCTC-5') were synthesized on an Applied Biosystems DNA synthesizer leaving the dimethoxytrityl (DMT) protecting group bound. Primers were purified by using the Glen Research Poly Pack II purification cartridges according to the manufacturers protocol. The PCR reaction was performed in an Ericomp thermocycler using a 50 μL reaction mixture containing 125 ng of both the forward and reverse primer, 10 ng of the plasmid pET32orfY, 10 mM dNTPs, and 2.5 U Pfu *Turbo* DNA polymerase (Stratagene) in 1X Pfu *Turbo* DNA polymerase reaction buffer. Reaction mixtures were overlaid with 30 μL of mineral oil before running the PCR. The thermal profile included 25 cycles of 30 s at 95 °C (denaturation), 1 min at 50 °C (reannealing), and 6 min at 72 °C (DNA extension). Following PCR, 10 U of Dpn1 was added to the reaction and allowed to digest

the methylated DNA at 37 °C for 1 hour. The success of the PCR reaction was checked on a 1% agarose gel cast in the presence of 50 ng/mL ethidium bromide. Chemically competent XL1-Blue *E. coli* cells (Stratagene) were transformed by heat shock at 42 °C for 30 s and plated on LB agar plates containing 100 µg/mL ampicillin. Clones containing the C67S mutation were identified by DNA sequencing (MIT Biopolymers Laboratory) using T7 promoter and T7 termination site primers. The success of the site-directed mutagenesis yielded the expression plasmid pET32DC67S, which was transformed into BL21(DE3) *E. coli* cells by heat shock. Cells were grown and protein expression induced according to a previously established protocol (5).

Construction of the MMOD N-Terminal Truncate

The *orfY* gene corresponding to residues 15-103 of MMOD was PCR amplified from the plasmid pCH4 (gift from J. C. Murrell, University of Warwick) using the primers, 5'-GGTATTGAGGGTCGCGAATGGTTCGAGG-AACCACGGCCCC-3' and 5'-AGAGGAGAGTTAGACCTCAATGTTGAAC-TCCGCCGGTCC-3'. The primers were synthesized and purified as described above. The PCR conditions were also similar to those mentioned above, with the exception that the DNA product was allowed to anneal for only 1 min at 72 °C. A 1 % agarose gel containing 50 ng/mL ethidium bromide confirmed the success of the reaction. The PCR product was purified by using the QIAquick PCR Purification Kit (Qiagen) and ligated into a pET32Xa/LIC plasmid (Novagen) according to the manufacturer's protocol. The new vector, pET32DΔ14, was subsequently transformed into NovaBlue Singles Competent Cells (Novagen) and plated on LB containing 100 µg/mL ampicillin. Several colonies were chosen and grown in culture tubes with 5 mL LB and 100 µg/mL ampicillin.

After pelleting the cells, the pET32DA14 plasmid was purified (Qiagen Spin Miniprep Kit), and the gene was sequenced (MIT Biopolymers Lab). The transformation of BL21(DE3) *E. coli* cells and subsequent expression and purification of the MMOD truncate were carried out as described above.

Creation of MMOD' and MMOD'-Cys67Ser

MMOD' (MMOD residues 15-91) was created by mutating the nucleotides corresponding to residue 92 in the full length protein to a stop codon in the plasmid pET32DA14 by using the following forward and reverse primers: 5'-GTTATGACCGAACAACGCTGACCGGCAGAGGAC -3', 3'-CAATACTGGCT-TGTTGCGACTGGCCGTCTCCTG-5'. The final plasmid, pET32D', was created as described above. The MMOD'-C67S construct, pET32D'C67S, was created by using the same primers and methods required for the MMOD C67S mutation as described above.

Proteolytic Digestion of MMOD

MMOD was digested with either endoproteinase Asp-N, trypsin, or endoproteinase Arg-C to identify structural elements in MMOD that are more flexible and to define a stable protein core that could be used improve the quality of MMOH-MMOD crystals (see below). Reactions (50 μ L) using endoproteinase were performed with 20 μ M MMOD, 25 mM MOPS, pH 7.0, 10 mM DTT, and 1 U of protease. The trypsin digest was run in 25 mM Tris-HCl, pH 8.0. Time points were taken at 0.5, 1.5, 2.5, 3.5 and 24 h. Reactions were stopped by the addition of 10 μ L of SDS-PAGE running buffer to a 10 μ L aliquot of the reaction mixture, and the quenched reactions were analyzed by SDS-PAGE. Time points that yielded significant amounts of cleaved MMOD were noted and later used to

make cleaved samples for mass spectrometric analysis. Reactions run for mass spectrometry were stopped by using a specific treatment for each of the proteases: 50 mM EDTA for endoproteinase Asp-N, 50 mM EDTA and 1 mM CoCl_2 for endoproteinase Arg-C, and 1 mM PMSF for trypsin. MMOD Cys67Ser and proteolyzed MMOD proteins were submitted to the MIT Biopolymers Laboratory for LC-MS. All samples contained 50 μM protein in 0.5% propionic acid and 20% isopropanol.

MALDI-MS of MMOD' Cys67Ser

MALDI-MS samples were prepared by using procedures similar to those described (10). The band corresponding to MMOD' was removed from an SDS-PAGE gel with a flame-sterilized razor, cut into small pieces and placed into a sterile microcentrifuge tube. The gel fragments were washed in 250 μL of 100 mM ammonium bicarbonate, pH 8.5, in 50% acetonitrile three times for 20 min and then with 100% acetonitrile for 10 min to remove the Coomassie stain. After drying the gel pieces in a centrifugal evaporator for 15 min, the pieces were resuspended in 50 μL of digestion buffer (50 mM ammonium bicarbonate, pH 8.5, and 12.5 ng/ μL sequencing grade trypsin) on ice for 45 min. A 50- μL digestion buffer solution without gel fragments served as a control. The digests were then incubated overnight (~12 h) at 37 °C. The supernatant was collected and the gel fragments were washed once with 100 μL 20 mM ammonium bicarbonate for 20 min, twice with 100 μL 1% TFA in 50% acetonitrile for 20 min, and once with 100 μL 100% acetonitrile for 20 min. The supernatant and wash solutions were combined, and the extracted peptides dried in a centrifugal evaporator. The dried peptides were submitted to the MIT Biopolymers

Laboratory for MALDI-MS. Peptide fragments were analyzed by using the program PAWS (Genomic Solutions Inc.).

UV-Vis and Circular Dichroism Spectroscopy

UV-Vis absorption spectra were obtained on a Hewlet Packard 8453 diode array spectrophotometer. CD spectra of MMOD, MMOD', MMOD Δ 14 (14 amino acid N-terminal truncate) and MMOD-C67S were measured on an Aviv CD spectrometer (Sauer Lab, MIT). Final solutions contained 1-10 μ M MMOD and 10 mM potassium phosphate buffer, pH 7.0. The spectra, which were a composite of 5 scans, were collected at 25 °C.

Crystallization of the MMOH-MMOD Complex

The MMOH-MMOD complex was crystallized by using the sitting drop and hanging drop vapor diffusion methods. All crystallizations were performed at room temperature by combining equal volumes of protein and well solution. Protein solutions for the crystallization of the MMOH-MMOD complex typically consisted of 40-50 μ M MMOH (apo or holo enzyme) and 100 μ M MMOD (MMOD, MMOD-C67S, MMOD', or MMOD'-C67S) in 25 mM MOPS, pH 7.0, and 5% (v/v) glycerol. Well solutions consisted of either 100 mM sodium cacodylate, pH 6.6-7.4, 1.1-1.2 M sodium sulfate, and 0.03% NaN₃ or 65 mM Tris, pH 8.5, 20 mM NaCl, 4-10% PEG MME 5000, 0-10% glycerol, and 0.03% NaN₃. Since MMOD and MMOD' readily form disulfide bonds, crystallizations using these proteins were performed either anaerobically or in the presence of 1 mM DTT.

Determination of Crystal Content by SDS-PAGE

Crystals were pipetted into a 1.5 mL microcentrifuge tube containing 300 μ L of an appropriate stabilizing solution. Crystallization drops with both

crystals and non-crystalline protein precipitate were avoided. The solution was centrifuged for 5 min at 10,000 rpm. The supernatant containing the non-crystallized protein was removed and replaced with 300 μ L of fresh stabilizing solution to wash the crystals. After vortexing gently for 30 s, the crystal solution was spun again. Washing was repeated three times before all of the supernatant was removed and the crystals were suspended in 30 μ L of doubly distilled water (Millipore). SDS-PAGE samples contained 10 μ L of washed suspended crystal solution and 10 μ L of 2x SDS-PAGE buffer. Protein standards contained both MMOH and MMOD in a 1:2 ratio and ranged from 0.53 - 4.3 mg of total protein. The samples were loaded onto a precast 4-20% Tris-HCl gel (BioRad), run, stained, and destained according to established the manufacturer's protocol.

Data Collection and Refinement

Before mounting, crystals were washed in a stabilizing solution tested for glassing capability at low temperature. Crystals grown in high salt were stable in 100 mM sodium cacodylate, pH 7.2, 1.0 M Na_2SO_4 , and 25% glycerol (v/v). Those grown in the presence of PEG MME 5000 were stable in 65 mM Tris-HCl, pH 8.5, 100 mM NaCl, 15% PEG MME 5000, and 20% glycerol. Each crystal was mounted on a loop and flash frozen at 100 K. Data were collected on beam lines 9-1 and 11-1 at SSRL. The data were indexed and scaled using the HKL program suite (11). Molecular replacement was performed by using both CNS and EPMR (12,13).

Mössbauer spectroscopy

Mössbauer spectroscopy was performed by Dr. Guy Jamison (Huynh Lab, Department of Physics, Emory University) on oxidized samples of ^{57}Fe -MMOH

containing 0.5 mM MMOH in 25 mM MOPS, pH 7.0, and 25% glycerol with and without 1.0 mM MMOB.

Results and Discussion

Prediction of MMOD Structure

Very little is known about the structure of the 11 kDa MMOD. Sequence homology indicates that the core of the protein is highly conserved among different species of methanotroph and contains several amino acid residues that can potentially coordinate to divalent metal ions (Figure A1.2). In contrast, the N- and C-termini of MMOD are the least conserved regions. Secondary structure prediction using NNPRELECT suggests that residues 30-80 of the MMOD core are primarily α -helical while the N- and C-termini are relatively unstructured. Cys-67, which is responsible for disulfide-mediated dimer formation of MMOD (5), lies within a loop region between two predicted helices. The CD spectrum of MMOD reveals a secondary structure comprising of 40% α -helix, 44% random coil, and 16% β -strand (7), an assignment that is consistent with results from NNPRELECT. Preliminary attempts to obtain a reliable HSQC spectrum of ^{15}N -labeled MMOD indicate that the tertiary fold is highly flexible and not amenable to solution structure determination (14). Based on the current knowledge of MMOD secondary structure, a hypothetical model is presented schematically in Figure A1.3.

The Function of Cys-67

A Cys to Ser mutation was created at position 67 to prevent the formation of MMOD dimers, facilitate its co-crystallization with MMOH and test the

function of this highly conserved residue. Activity assays indicate that this mutant does not significantly inhibit sMMO activity (Figure A1.4). Moreover, only a weak (μ -oxo)diiron(III) charge transfer band at 352 nm appears when the mutant is added to MMOH, suggesting that the affinity of MMOD-C67S is weaker than the wild-type protein. These findings indicate that Cys-67 is essential to either the folding of MMOD or its binding to MMOH. Non-reducing SDS-PAGE analysis of the MMOH-MMOD complex indicates that MMOD does not form a disulfide bond with the hydroxylase and that the interaction between the two proteins is non-covalent (7). The pH dependence of MMOD binding to MMOH, followed by monitoring the 352 nm band, suggests that MMOD binds weakly at pH 8.0-8.5 and tightly at pH 6.5-7.5 (7). Below pH 6.0, MMOH and MMOD start to precipitate. Since the pK_a values for Cys and Ser are approximately 8 and 16, respectively, the protonation state of the Cys-67 cannot explain the differences in the affinity of the mutant and wild-type proteins for MMOH. The current data offer no insight into why a single atom mutation in Cys-67 greatly perturbs the properties of MMOD.

MMOB Induces Formation of an Oxo-bridged Diiron(III) Center in MMOH

Optical spectra of oxidized MMOH with and without MMOB were recorded to determine whether or not the effector protein can induce similar spectroscopic changes in MMOH as MMOD. Four distinct absorption bands appeared at a 2:1 MMOB:MMOH ratio in the difference spectra at 336 nm, 366 nm, 480 nm, and 720 nm, with respective extinction coefficients of ~ 1200 , 1700, 320, and $35 \text{ M}^{-1} \text{ cm}^{-1}$ for the MMOH homodimer (Figure A1.5). Addition of > 2 equiv of MMOB per MMOH did not perturb the spectrum, suggesting that a 2:1 complex forms (Figure A1.5, inset). By comparison to $\text{Fe}_2(\text{III})$ proteins and model

compounds, we tentatively assign these optical bands to a (μ -oxo)diiron(III) center (15-20). Because the extinction coefficients are lower than those observed for (μ -oxo)diiron(III) proteins and model compounds, which range from 4,000-10,000 $M^{-1} cm^{-1}$, the μ -oxo species most likely represents only a fraction (~10-25%) of the iron present in the MMOH-MMOB complex. Previous EPR data on a cryo-reduced protein complex revealed a μ -oxo species corresponded to 2-5% of some samples (21). Mössbauer data indicate that the MMOH-MMOB complex comprises 1-10% of a (μ -oxo)diiron(III) species, a finding that is consistent with previous observations (Figure A1.6). Like MMOD, the effect of MMOB binding on the presence of (μ -oxo)diiron(III) species is pH dependent (Figure A1.5b). At high pH, this species is less pronounced whereas, at low pH, the optical signal is more intense. The differences in intensities most likely reflects a pH dependence in MMOB binding to MMOH since oxo-bridged formation is favored at higher pH values.

The presence of a (μ -oxo)diiron(III) species when either MMOD and MMOB are complexed to MMOH suggests that both can exert a similar affect on the diiron center and that this spectral change is not a unique feature of MMOD. The MMOH-MMOB complex from *Methylocystis sp. M* also has a spectral signature consistent with a small percentage of a (μ -oxo)diiron(III) center (data not shown), indicating that this phenomenon is not species-specific. Given that a small percentage of oxo-species forms when either MMOB or MMOD are bound to MMOH, it is possible that this unit arises in only misfolded or damaged protein. Hydroxylase activity, however, does not appear to correlate with the optical signal for the (μ -oxo)diiron(III) center (Table A1.1.)

Proteolysis and Mass Spectrometry of MMOD and MMOD Cys67Ser

An LC-MS analysis of proteolysed MMOD and C67S-MMOD were performed to identify a stable protein core that could be used improve the quality of MMOH-MMOD crystals (see below). The analysis revealed the presence of several cleavage products (Figure A1.7). The major protein species are listed in Table A1.2. The molecular weight 11,927 g/mol corresponds to the value predicted for the MMOD Cys67Ser mutant. Analysis of the smaller molecular weight fragments indicates that MMOD is cleaved at specific regions in the N- and C-terminus, predominantly after Ser 4 (11,481 g/mol) and Gln 90 (10,424 g/mol). The double cleavage product at these positions (9,977 g/mol) is also observed. A minor cleavage site occurs between residues Asp14 and Glu15 (10,424 g/mol). Proteolytic cleavage at both termini suggests that these regions of MMOD are more exposed to bulk solvent and possibly disordered. These findings are consistent with our prediction that the fold of MMOD has unstructured regions at the N- and C-termini and a defined α -helical core in the middle of the protein (Figure A1.2).

To probe further the domain structure of wt-MMOD, proteolytic digestion experiments were performed using trypsin, endoproteinase Asp-N, and endoproteinase Arg-C. Digestion of MMOD with endoproteinase Asp-N appeared limited to the termini (Table A1.2). Native MMOD has a molecular weight of 11,949 g/mol, 6 amu greater than what is predicted by the sequence. For unknown reasons, all of the cleavage products were also 6 amu greater in their expected molecular weights, suggesting that the additional mass may be due to a calibration problem. The major cleavage product was 10,577 g/mol which corresponds to a deletion of residues 1-13. The minor proteolysis

products had molecular weights of 9,725 and 9,997 g/mol, which probably corresponds to residues 14-95 and 5-90. The 14-95 fragment is a predicted proteolysis product of endoproteinase Asp-N treatment, whereas the 5-90 fragment is an additional cleavage product that is also observed in the C67D-MMOD LC-MS sample. The LC-MS of trypsin and endoproteinase Asp-C digested MMOD was less interpretable, since it appeared as if the entire protein were digested. The results of wt-MMOD protease treatment confirm that the termini are relatively disordered and that middle of the protein contains all of the significant structural elements. The similar cleavage patterns in wt-MMOD and MMOD-C67S provide some evidence suggesting that the Cys67Ser mutation does not disrupt the global fold of MMOD.

Characterization of the MMOD Truncates

Biochemical studies were conducted to determine the possible functional significance of the MMOD N- and C-termini. MMOD' (MMOD residues 15-91), like full length MMOD, can induce the formation of a (μ -oxo)diiron(III) species when complexed to MMOH and bind with a 2:1 MMOD':MMOH stoichiometry (Figure A1.8). MMOD' also inhibits sMMO activity (Figure A1.9). These findings suggest that the MMOD N- and C- termini are not required for binding to MMOH.

Crystallization of the MMOH-MMOD Complex

Crystals of the MMOH-MMOD complex were grown initially either in the presence of > 1.0 M sulfate or in solutions containing PEG MME 5000 and glycerol. The absence of either MMOD or MMOH from the crystallization solution did not produce crystals, suggesting that both protein components are in the crystal lattice. Since the morphology of these crystals was that of small

needles, it was hypothesized that the native cysteine of MMOD interferes with crystal growth by participating in the formation of MMOD dimers. It was also speculated that the MMOD dimers limited the amount of monomers available to bind to MMOH and created a heterogeneous protein crystallization solution. The mutation of Cys-67 to Ser dramatically improved the size and quality of the crystals, resulting in cylindrical rods of 1.0 x 0.2 mm under the high salt conditions and hexagonal rods of 1.4 x 0.5 mm under the PEG MME 5000 conditions. These observations support the notion that MMOD dimer formation impedes crystal growth. SDS-PAGE analysis of the MMOH-MMOD-C67S high salt crystals confirmed the presence of both protein components in the crystals; however, a proteolyzed form of MMOD, henceforth termed MMOD', co-crystallized with the hydroxylase (Figure A1.10). The MALDI-MS spectrum of the trypsin digested MMOD' band from the SDS-PAGE gel is presented in Table A1.3. The only contiguous protein fragment that can be assembled from the observed peptide masses are products of the trypsin digest that correspond to residues 15-91 of MMOD. The other observed peptides are not predicted to result from a trypsin cut site and cannot be assembled into a protein of any significant length. Because the results of the MALDI-MS agree with those of the LC-MS, it is likely that MMOD' is a 78 amino acid peptide consisting of residues 15-91 of MMOD.

To improve the crystallization, MMOD' and MMOD' Cys67Ser constructs were created and purified. Crystals of the MMOH-MMOD' Cys67Ser complex grew best under two conditions: 100 mM sodium cacodylate, pH 7.2, 1.1 M Na₂SO₄, 50 mM KBr, 50 mM KI, 10 mM CsCl, 0.03% NaN₃ and 65 mM Tris-HCl, pH 8.5, 50 mM NaCl, 3-6% glycerol, 15% PEG MME 5000, 0.01% NaN₃. Both

conditions resulted in crystals having the shape of hexagonal rods, the largest being 1.5 x 1.0 x 1.0 mm and 1.4 x 0.4 x 0.4 mm from the high salt and PEG 5K conditions, respectively (Figure A1.11).

The MMOH-MMOD' Cys67Ser crystals grown in the presence of high salt diffracted maximally to 4.6 Å and can be indexed in the space group $P6_522$ or $P6_122$ with unit cell parameters $a = b = 144.5$ Å, $c = 309$ Å (Table A1.4). The diffraction pattern reveals that several other reflections are present and indicates the presence of a second lattice (Figure A1.12). All MMOH-MMOD crystals grown under the high salt conditions have this second lattice, which diffracts more weakly than the primary lattice. Attempts to index the second lattice were unsuccessful. Several data sets were collected on three different forms of the MMOH-MMOD' Cys67Ser crystals, holo, apo, and apo + Xe. Attempts to solve the structure of the MMOH-MMOD complex by molecular replacement using either an $\alpha\beta\gamma$ or $(\alpha\beta\gamma)_2$ MMOH model with and without iron in CNS or EPMR were unsuccessful. Typical values for R and R_{free} from the most promising solutions were between 56-60%. A positive hit should yield an R value between 35-45% and an R_{free} within 5% of R. Several possibilities may explain why molecular replacement failed. MMOH may have undergone a conformational change, the reflections from the second lattice in the crystals may be contributing to the intensities of the first, or higher resolution data are required to perform molecular replacement on an all α -helical protein in which most of the helices are aligned in the same direction. Attempts to use the apo and apo + Xe data sets for single isomorphous replacement phasing were unsuccessful.

The large hexagonal crystals grown with the PEG MME 5000 conditions diffract to $\sim 9 \text{ \AA}$. Like the high salt crystals, the PEG MME 5000 crystals index in $P6_522$ or $P6_122$, have unit cell dimension of $a = 145 \text{ \AA}$, $c = 309 \text{ \AA}$. They too are not single crystals. The PEG MME 5000 grown crystals are more sensitive to changes in their solution environment than the high salt grown crystals. It was therefore more difficult to find a good cryo-protectant that does not crack or dehydrate the crystal. The addition of glycerol or PEG 400 or the use of oils caused the crystals to crack. Even the slow transfer of the crystals into stabilizing solutions with increasingly higher glycerol content, which allows for the crystals to equilibrate with its new environment, resulted in crystal cracking and dehydration. Attempts to grow the crystals under cryogenic conditions were unsuccessful. The highest glycerol concentration in which PEG MME 5000 crystals can grow is 10% and the resulting crystals were small and of little use. Data collection at $4 \text{ }^\circ\text{C}$ in capillaries resulted in the fast decay of the crystals over several minutes.

Conclusions

The MMOH-MMOD'-C67S complex was successfully crystallized and diffracts to 4.6 \AA . Attempts to solve the structure have not been successful. MMOD', a truncated form of MMOD consisting of residues 15-91, is present in the crystals. Biochemical analysis of MMOD' suggests the N- and C-termini are not required for the binding of MMOD to MMOH or for the formation of a (μ -oxo)diiron(III) species in the MMOH-MMOD complex. Cys-67, however, is critical to the binding of MMOD to MMOH. It is presently unknown how this single atom mutation decreases the affinity of MMOD for the hydroxylase. Previous NMR data indicate that MMOD by itself is disordered.

Crystallographic data presented here suggest MMOD may order itself when complexed to MMOH. The formation of a (μ -oxo)diiron(III) species induced by MMOB in a small percentage of the MMOH diiron centers indicates that this spectral change is not unique to MMOD binding. The formation of the diiron(III) oxo-bridge when either MMOB or MMOD is complexed to MMOH does suggest, however, that both proteins bind to similar regions of MMOH, a finding that is consistent with previous inhibition and metal reconstitution data (5,22).

Acknowledgments

We thank Dr. Maarten Merkx for characterization of MMOD-C67S as well as Sonya Tang and Michelle Nyein for their work on MMOD' and MMOH-MMOD crystallizations.

References

1. Merkx, M., Kopp, D. A., Sazinsky, M. H., Blazyk, J. L., Müller, J., and Lippard, S. J. (2001) *Angew. Chem. Int. Ed.* **40**, 2783-2807.
2. Stafford, G. P., Scanlan, J., McDonald, I. R., and Murrell, J. C. (2003) *Microbiology* **149**, 1771-1784.
3. Csaki, R., Bodrossy, L., Klem, J., Murrell, J. C., and Kovacs, K. L. (2003) *Microbiology* **149**, 1785-1795.
4. Powlowski, J., Sealy, J., Shingler, V., and Cadieux, E. (1997) *J. Biol. Chem.* **272**, 945-951.
5. Merkx, M., and Lippard, S. J. (2001) *J. Biol. Chem.* **277**, 5858-5865.
6. Blazyk, J., and Lippard, S. J. Unpublished results.
7. Merkx, M., Jamison, G., Huynh, B. H., and Lippard, S. J. Unpublished results.
8. Willems, J.-P., Valentine, A. M., Gurbiel, R., Lippard, S. J., and Hoffman, B. M. (1998) *J. Am. Chem. Soc.* **120**, 9410-9416.
9. Gassner, G. T., and Lippard, S. J. (1999) *Biochemistry* **38**, 12768-12785.
10. Shevchenko, A., Wilm, M., Vorm, O., and M., M. (1996) *Anal. Chem.* **68**, 850-858.
11. Otwinowski, Z., and Minor, W. (1997) *Methods Enzymol.* **276**, 307-326.
12. Brünger, A. T., Adams, P. D., Clore, G. M., Delano, W. L., Gros, P., Grosse-Kunstleve, R. W., Jiang, J.-S., Kuszewski, J., Nilges, N., Pannu, N. S., Read, R. J., Rice, L. M., Simonson, T., and Warren, G. L. (1998) *Acta Cryst. D* **54**, 905-921.
13. Kissinger, C. R., Gehlhaar, D. K., and Fogel, D. B. (1999) *Acta Cryst D* **D55**, 484-491.

14. Müller, J., Merkx, M., and Lippard, S. J. Unpublished results.
15. Kurtz, D. M., Jr. (1990) *Chem. Rev.* **90**, 586-606.
16. Fox, B. G., Shanklin, J., Ai, J., Loehr, T. M., and Sanders-Loehr, J. (1994) *Biochemistry* **33**, 12776-12786.
17. Mann, G. J., Graslund, A., Ochiai, E. I., Ingemarson, R., and Thelander, L. (1991) *Biochemistry* **30**, 1939-1947.
18. Ravi, N., Prickril, B. C., Kurtz, D., C., Jr., and Huynh, B. H. (1993) *Biochemistry* **32**, 8487-8491.
19. Richardson, D. E., Reem, R. C., and Solomon, E. I. (1983) *J. Am. Chem. Soc* **105**, 7780-7781.
20. Cadieux, E., Vrajmasu, V., Achim, C., Powlowski, J., and Münck, E. (2002) *Biochemistry* **41**, 10680-10691.
21. Davydov, R., Valentine, A. M., Komar-Panicucci, S., Hoffman, B. M., and Lippard, S. J. (1999) *Biochemistry* **38**, 4188-4197.
22. Sazinsky, M. H., Merkx, M., Cadieux, E., Tang, S., and Lippard, S. J. Manuscript in preparation.

Table A1.1. Relative Absorbance of the MMOH (μ -Oxo)diiron(III) Species vs. sMMO Activity from Different MMOH Purifications

MMOH Batch	Absorbance at 350 nM	Iron/MMOH	Activity (mU/mg)
1	0.044	3.7	156
2	0.040	3.5	186
3	0.028	3.6	213
4	0.045	3.6	228
5	0.027	3.2	132
6	0.029	3.4	100
7	0.031	3.7	147

Table A1.2. LC-MS of MMOD and MMOD Cys67Ser

Trial	Observed Mass (g/mol)	Change in Expected Mass (g/mol)	Predicted Cleaved Peptide		Proteolyzed MMOD Protein/MW
MMOD Cys67Ser	11927	0	--		--
	11481	- 446	1-4	MVES	5-103 11480.7
	10442	- 1485	1-14	MVESAFQPFSGDAD	15-103 10443.6
	10424	- 1503	91-103	QRAPAEDRTGGVQH	1-90 10422.0
	9977	- 1950	1-4 91-103	MVES QRAPAEDRTGGVQH	5-90 9981.1
	9242	- 2685	1-11 91-103	MVESAFQPFSG QRAPAEDRTGGVQH	12-90 9241.4
	13111	+ 1184	Unknown		Unknown
Endoproteinase Asp-N digest	11949	+6	Native Protein		--
	10577	- 1372	1-13	MVESAFQPFSGDAD	14-103 10569.1
	9725	- 2224	1-13 96-103	MVESAFQPFSGDAD EDRTGGVQH	14-95 9718.7
	9997	- 1952	1-4 91-103	MVES QRAPAEDRTGGVQH	5-90 9981.1
	12160	+ 211	Unknown		Unknown

Table A1.3. MALDI-MS of Trypsin Digested MMOD' from the SDS-PAGE of MMOH-MMOD Crystals

Observed MW (g/mol)	MMOD Peptide Fragment
*672.4	54-58 (673)
937.6	28-35 (938.05)
*982.4	47-53 (984)
*992.4	15-21 (992.05); 78-85 (992.14)
998.4	72-80 (999.09) 95-103 (998.02)
1014.48	52-58 (1014.24)
1026	?
1030.3	38-46
1169.6	47-54 (1168.34)
*1187.57	37-46 (1189)
1423.7	50-59 (1421.6)
1440.7	79-90 (1439.61)
1490	23-35, 24-36, 58-70, 72-84
1497.7	82-94 (1497.69)
1519.7	12-28, 48-58, 75-87
1604.8	62-76
*1713.87	22-36 (1714)
*1767.8	76-90, 77-91, 78-92 (1766.0)
1810	7-21
1851.9	14-28 (1851.9)
1864.9	32-48 (1865) 78-93 (1863.12)
1941.9	86-103 (1940.08)
*2019	59-76 (2021)
2034.8	?
2068.9	?

*Fragments were used to determine the length of MMOD'. Numbers in parentheses indicate calculated mass. The fragments are consistent with trypsin cut sites.

Table A1.4. Data Collection and Processing Statistics of the MMOH-MMOD Crystals

Crystal type	HD-holo1	HD-holo2	HD-apo	HD-apo-Xe	HD-holo3
X-ray source	SSRL (BL9-1)	SSRL (BL9-1)	SSRL (BL9-1)	SSRL(BL9-1)	SSRL(BL11-1)
wavelength (Å)	0.918	0.918	0.918	0.918	1.001
temperature (K)	100 K	100 K	100K	100K	100K
wedge	1°	0.5°	1°	1°	0.3°
exposure time (s)	55	50	55	80	90
no. of images	242	120	242	120	267
space group	<i>P</i> _{6₅,22} / <i>P</i> _{6₁,22}	<i>P</i> _{6₅,22} / <i>P</i> _{6₁,22}	<i>P</i> _{6₅,22} / <i>P</i> _{6₁,22}	<i>P</i> _{6₅,22} / <i>P</i> _{6₁,22}	<i>P</i> _{6₅,22} / <i>P</i> _{6₁,22}
cell dimensions					
<i>a</i> (Å)	145.09	144.82	144.4	143.76	145.16
<i>c</i> (Å)	310.05	309.19	309.78	309.65	309.36
resolution (Å)	40-5.3	40-5.1	40-6.4	40-6.5	40-5.5
total observations	675,319	271,140	201,490	195,337	510,468
unique reflections	7568	15,018	7586	7199	12,267
<i>R</i> _{sym} (%)	11.1 (39.3)	11.6 (39.4)	9.3 (36.3)	9.8 (35.4)	11.2 (38.9)
<i>I</i> / <i>s</i> (<i>I</i>)	11.7 (11.0)	8.5 (3.8)	10.8 (4.5)	11.7 (5.6)	18.9 (4.9)
completeness (%)	100 (100)	99.9 (99.9)	99.9 (100)	99.6 (99.9)	99.2 (99.3)
no. reflections used	199,196	55,980	22,654	44,028	58,853

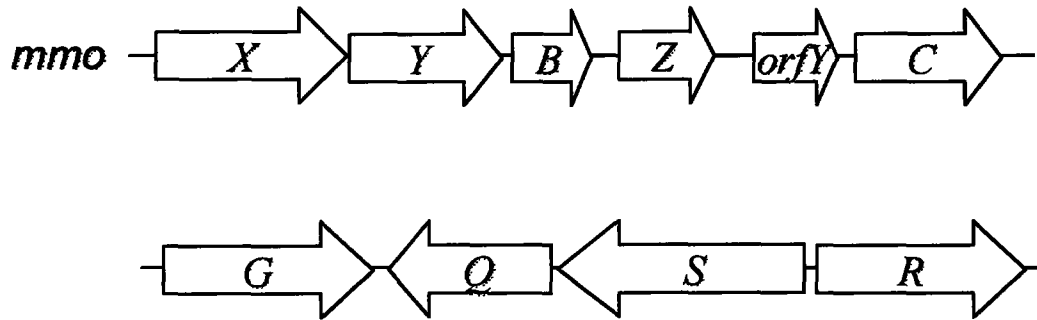


Figure A1.1. sMMO operon from *Methylococcus capsulatus* (Bath). The *mmoXYZ* genes code for MMOH, *mmoB* is the regulatory protein, *mmoC* is the reductase, and *orfY* is MMOD. *mmoG* codes for a putative chaperone similar to GroEL, *mmoR* is proposed to be a metal dependent repressor. The *mmoQ* and *mmoR* genes code for a putative two-component sensor-regulator system.

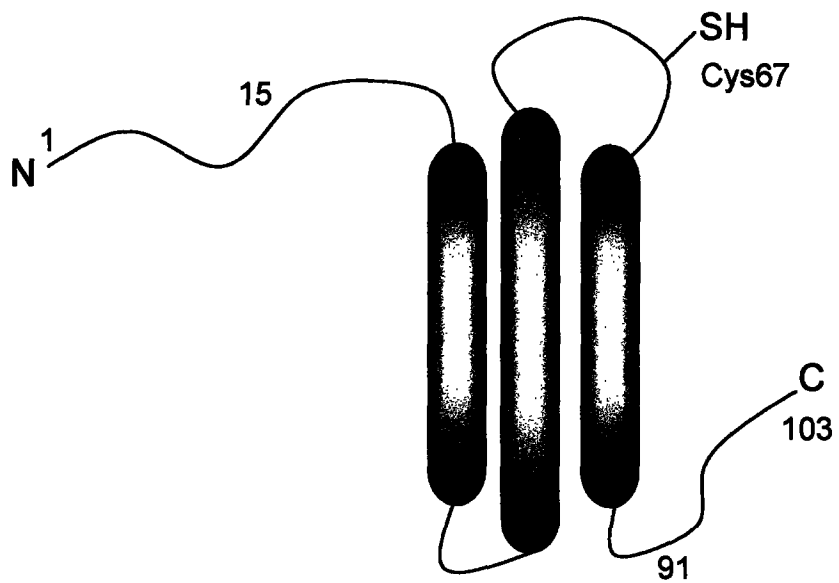


Figure A1.3. Hypothetical 3D-model of MMOD based on sequence alignment, secondary structure prediction, CD spectroscopy, proteolysis studies.

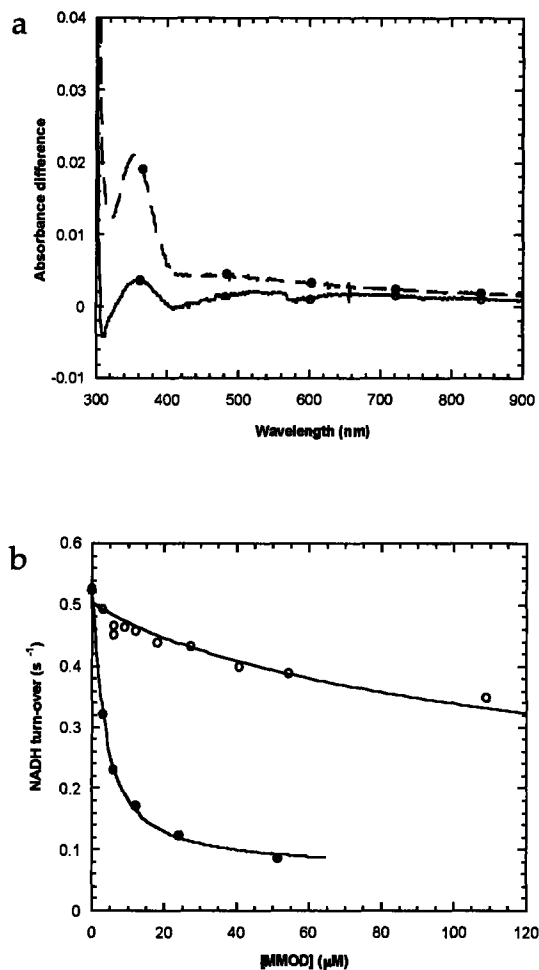


Figure A1.4. (a) Optical difference spectra monitoring the binding of C67S-MMOD (27 μM) to MMOH (9 μM) (solid line) and the subsequent addition of wt-MMOD (32 μM) (dashed line). (b) NADH turn-over rate as a function of wt-MMOD (solid circles) and C67S-MMOD (open circles) concentration for the sMMO-catalyzed epoxidation of propylene at 25 $^{\circ}\text{C}$. Assays contained 1.5 μM MMOH, 3.75 mM MMOB, 0.9 mM MMOR, 1 mM propylene, and 2 mM NADH in 25 mM MOPS, 1 mM DTT, pH 7.0. The solid lines represent the best fits assuming a model in which MMOD binding competes with MMOB binding. The K_d for the MMOH-MMOB complex was 0.2 mM whereas those for the wt-MMOD and C67S-MMOD MMOH complexes were 0.13 mM and 11 mM, respectively.

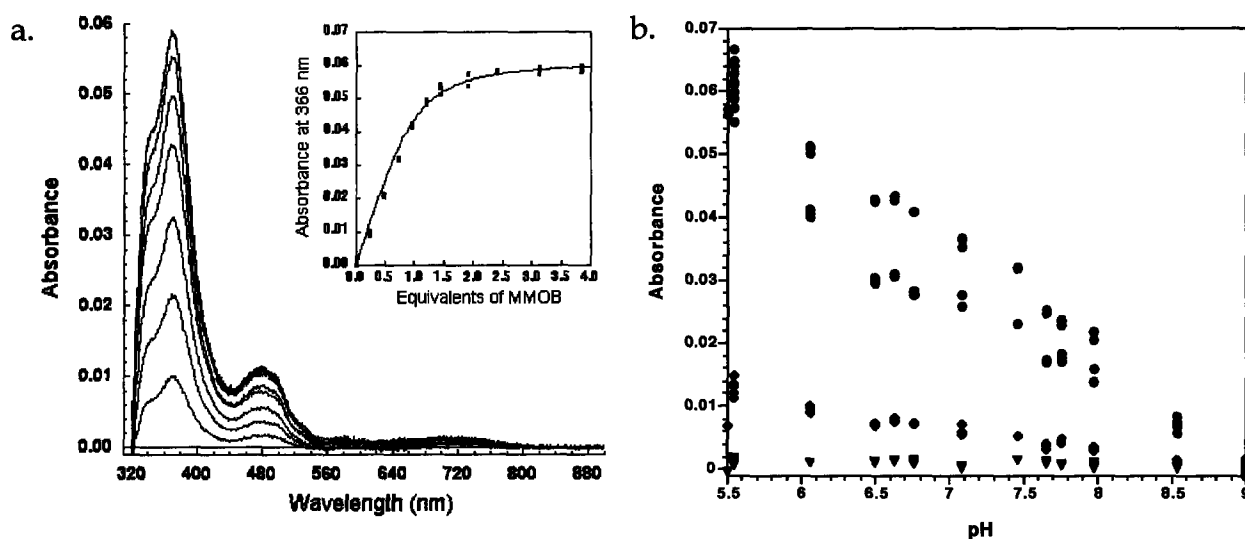


Figure A1.5. (a) Difference optical absorption spectra induced by the formation of the MMOH-MMOB complex at variable MMOB:MMOH ratios. Spectra were recorded at 24 °C in 25 mM MOPS, pH 7.0, 5% glycerol, and 20 mM NaCl. The titration data were normalized to a final MMOH concentration of 28.2 μM . Inset: MMOH-MMOB binding as monitored by absorption at 366 nm. The K_d value from the best fit to the data (solid line) is $3.4 \pm 1.1 \mu\text{M}$. (b) Plot of the absorbance at 336 nm (black), 366 nm (red), 480 nm (blue), and 720 nm (green) from MMOH-MMOB complex formation as a function of pH.

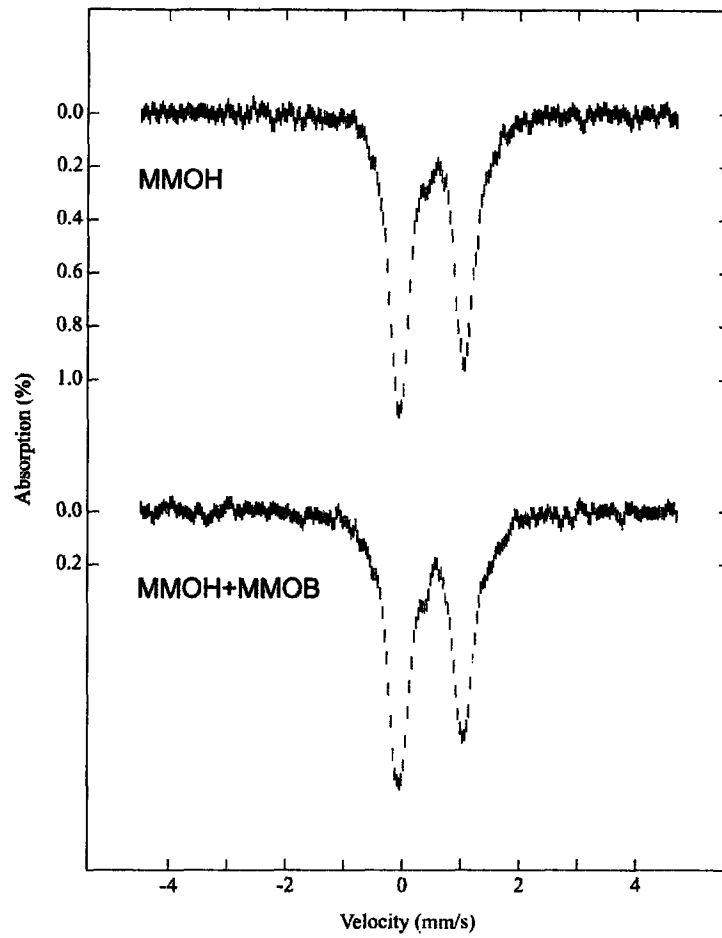
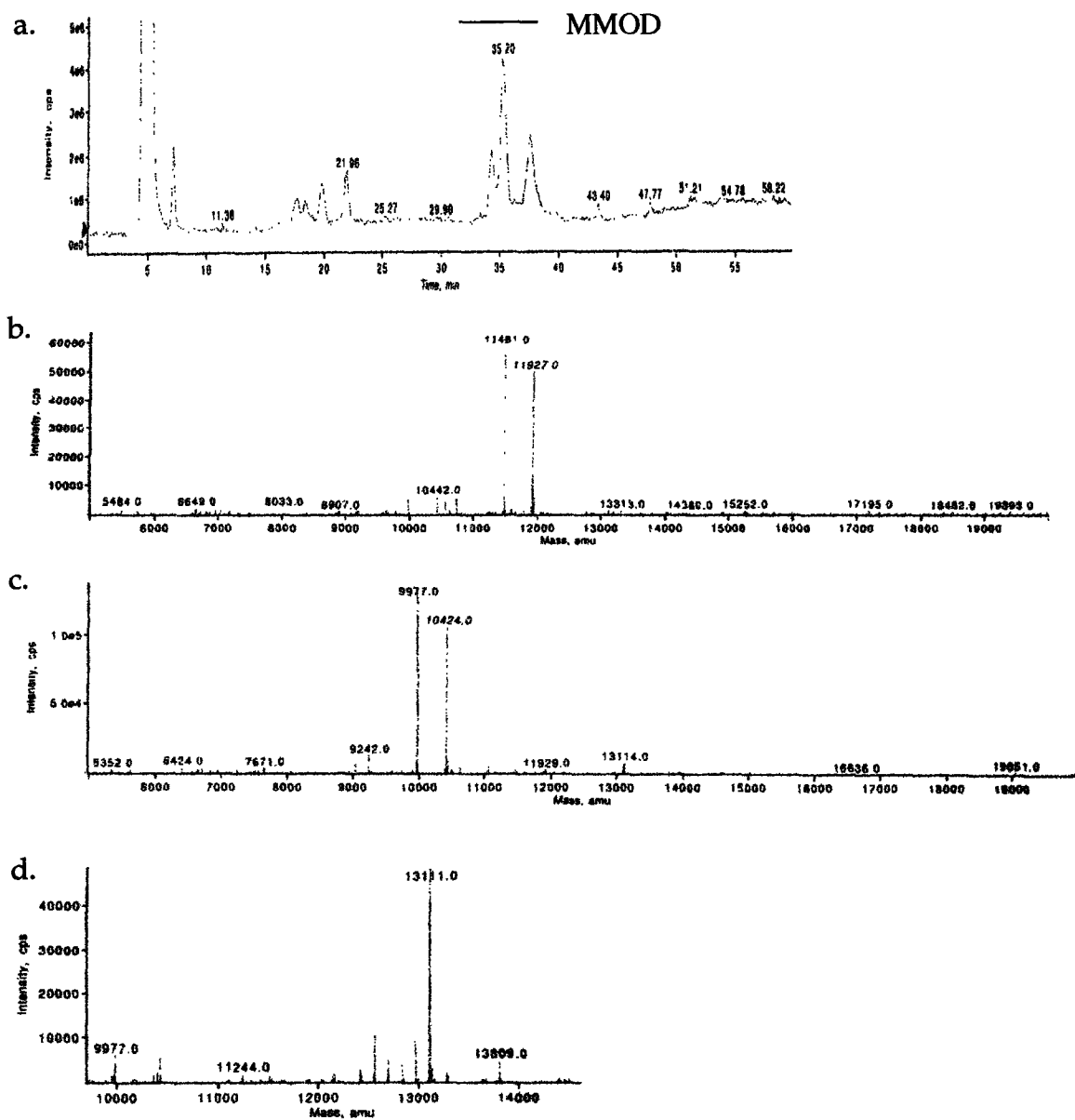


Figure A1.6. Mössbauer spectra of ^{57}Fe -MMOH and ^{57}Fe -MMOH+MMOB. The spectrum is perturbed slightly in the presence of MMOB as evidenced by the shoulders on the right side of each peak. The spectra have yet to be fully analyzed.



4

Figure A1.7. LC-MS of Cys67Ser MMOD. Three peaks resolved in the LC contained MMOD (a). The MS of the resolved peaks are presented in b-d.

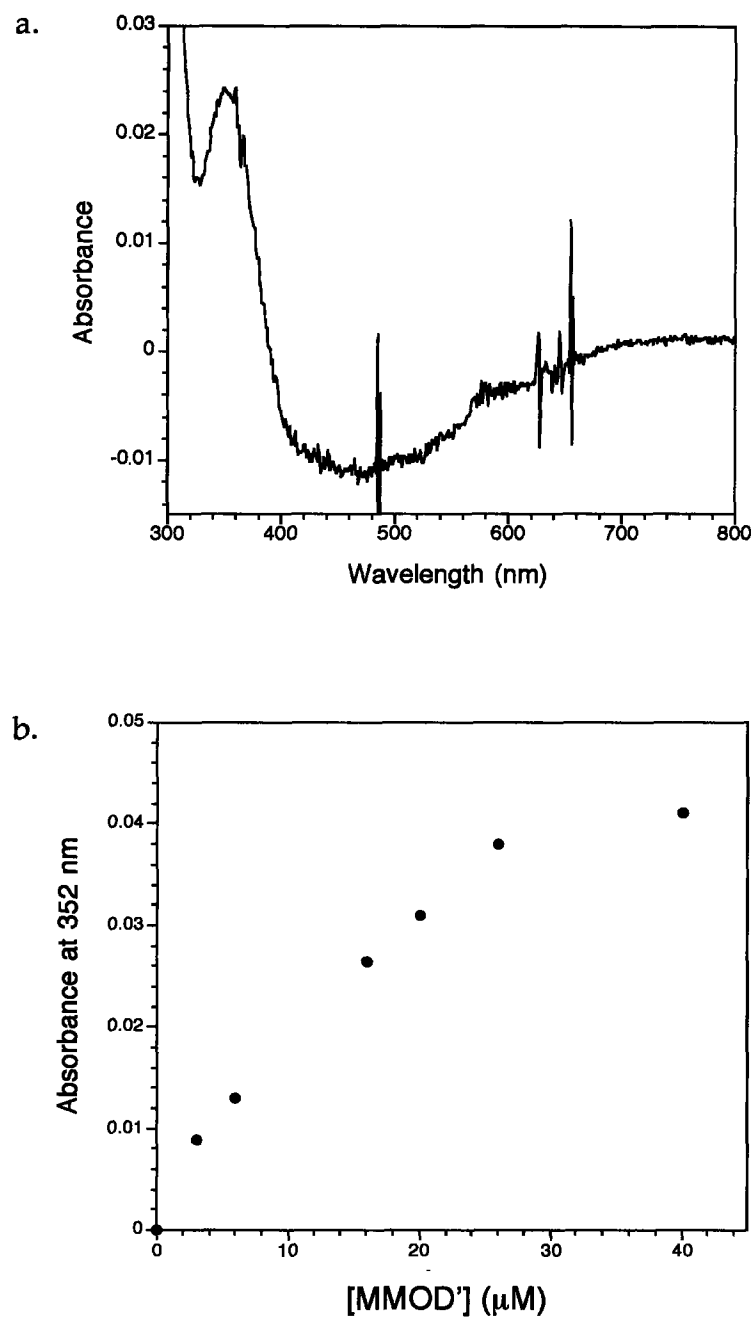


Figure A.1.8. (a) MMOH-MMOD' difference spectrum. Solutions contained 20 μM MMOH and 40 μM MMOD' in 25 mM MOPS at pH 7.0. (b) Titration of MMOD' into a solution containing 20 μM MMOH in 25 mM MOPS at pH 7.0 at 25 $^{\circ}\text{C}$.

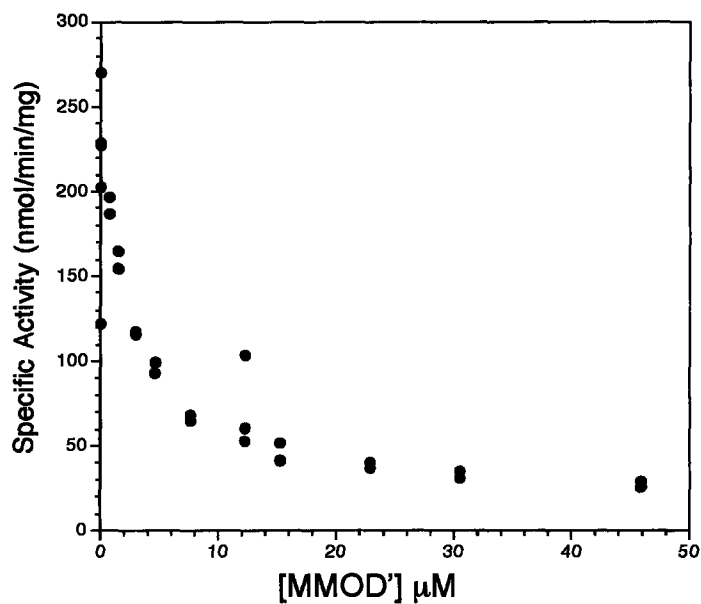


Figure A.1.9. Inhibition of sMMO activity by MMOD'. Assay solutions contained 1 μM MMOH, 2 μM MMOB, 0.5 μM MMOR, variable quantities of MMOD', in 25 mM MOPS pH 7.0, with saturating amounts of furan and 200 μM NADH. NADH consumption was monitored at A_{340} .

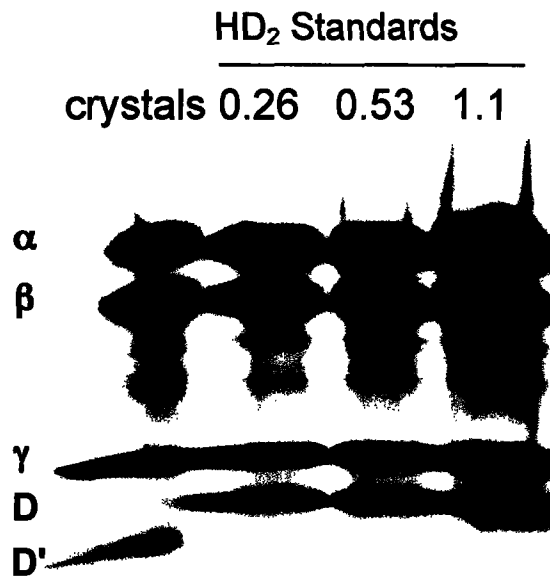
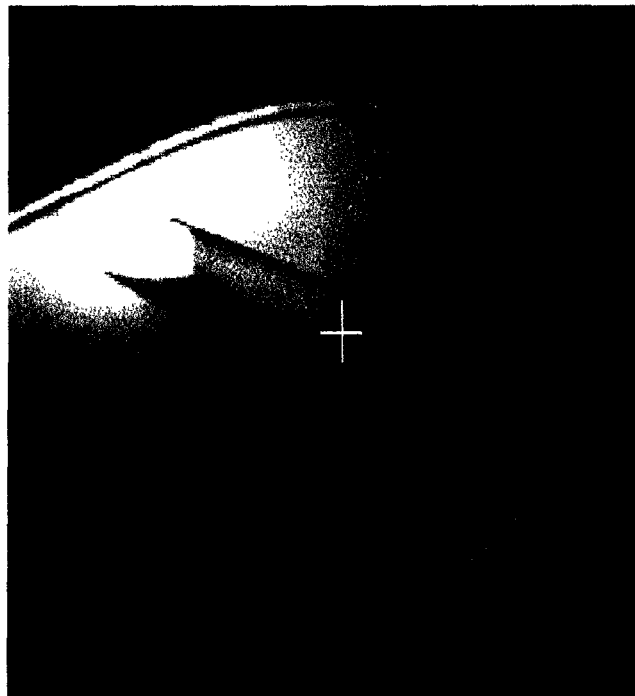


Figure A1.10. SDS-PAGE of the MMOH-MMOD high salt crystals. Lane 1 represents the washed protein crystals. Lanes 2-4 are MMOH-MMOD protein standards at different concentrations in a 1MMOH: 2 MMOD ratio. The bands between the β - and γ -subunit are due to the degradation of α and β .

a.



b.

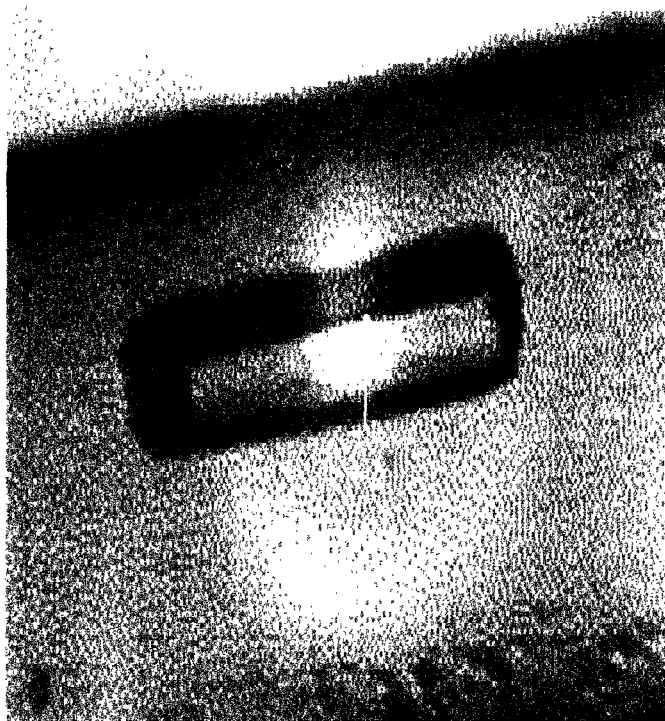


Figure A1.11. Crystals of the MMOH-MMOD' Cys67Ser complex grown under (a) high salt and (b) PEG MME 5000 conditions. Both crystals are hexagonal rods with approximate dimensions of 1.4 x 0.4 x 0.4 mm.

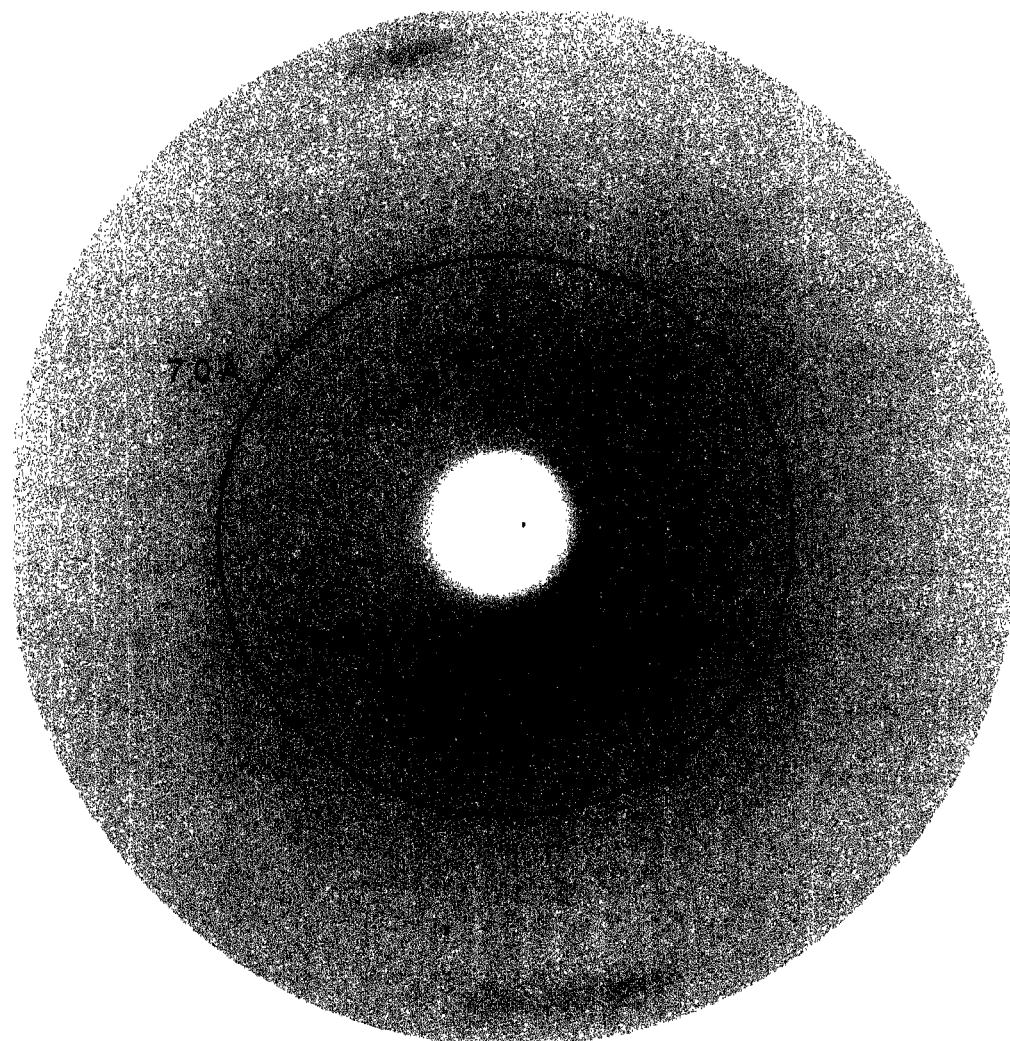


Figure A1.12. Diffraction pattern of the MMOH-MMOD'-C67S crystals to 7.0 Å resolution.

Biographical Note

The author was born in Wynnewood, PA, on November 30, 1976, to David and Barbara Sazinsky. He was raised along with one brother, Stephen, in Cherry Hill, NJ, and attended Cherry Hill High School East, where his interest in chemistry and biology was encouraged by Mr. Paul Siler. After graduating in 1995, he attended Haverford College in Haverford, PA, where he majored in chemistry and did undergraduate research on porphobilinogen synthase under the guidance of Professor Robert C. Scarrow and Dr. Eileen K. Jaffe at Fox Chase Cancer Center in Philadelphia, PA. He graduated in May 1999 with a Bachelor of Science degree in Chemistry with high honors, and began graduate work at MIT in the fall of that year. After the completion of his Ph. D., the author plans to do postdoctoral work in the lab of Professor Amy C. Rosenzweig at Northwestern University.

Matthew Howard Sazinsky

EDUCATION

Ph.D. Biological Chemistry
1999-2004

Massachusetts Institute of Technology, Cambridge, MA.
Advisor: Professor Stephen J. Lippard

B.S., Chemistry
1995-1999

Haverford College, Haverford PA
Advisor: Professor Robert C. Scarrow

PUBLICATIONS

Sazinsky, M. H., Ehrenfeld, J., Jaffe, E. K., Scarrow, R. C. Zinc Ligation in the Active Site of Human and Bovine Porphobilinogen Synthase. *J. Inorg. Biochem.* **1999**, *74*, 287.

Jaffe, E. K., Volin, M., Bronson-Mullins, C. R., Dunbrack, D. L., Kervinen, J., Martins, J., Quinlan, J. F., Sazinsky, M. H., Steinhouse, E. M., Yeung, A. T. An Artificial Gene for Human Porphobilinogen Synthase Allows Comparison of an Allelic Variation Implicated in Susceptibility to Lead Poisoning. *J. Biol. Chem.* **2000**, *275*, 2619-2626.

Whittington, D. A., Sazinsky, M. H., and Lippard, S. J. X-ray Crystal Structure of Alcohol Products Bound at the Active Site of Soluble Methane Monooxygenase Hydroxylase. *J. Am. Chem. Soc.* **2001**, *123*, 1794-1795.

Merkx, M., Kopp, D. A., Sazinsky, M. H., Muller, J., Blazyk, J. B., Lippard, S. J. Dioxygen Activation and Methane Hydroxylation by Soluble Methane Monooxygenase: A Tale of Two Irons and Three Proteins. *Angew Chem. Int. Edit.* **2001**, *40*, 2782-2807.

MacArthur, R., Sazinsky, M. H., Kuhne, H., Whittington, D. A., Lippard, S. J., Brudvig, G. Component B Binding to the Soluble Methane Monooxygenase Hydroxylase by Saturation-Recovery EPR Spectroscopy of Spin-Labeled MMOB. *J. Am. Chem. Soc.* **2002**, *124*, 13392-13393.

Sazinsky, M. H., Bard, J., DiDonato, A., Lippard, S. J. Crystal Structure of the Toluene/ *o*-Xylene Monooxygenase Hydroxylase from *Pseudomonas stutzeri* OX1: Insight into the Substrate Specificity, Substrate Channeling and Active Site Tuning of Multicomponent Monooxygenases *J. Biol. Chem.* **2004**, *279*, 30600-10610.

Jackson-Rudd, D., Sazinsky, M. H., Merkx, M., Lippard, S. J., Hedman, B., Hodgson, K. O. Determination by X-ray Absorption Spectroscopy of the Fe-Fe Separation in the Oxidized Form of the Hydroxylase of Methane Monooxygenase Alone and in the Presence of MMOB (submitted *Inorg. Chem.* **2004**, *43*, 4579-4589.

Jackson-Rudd, D., Sazinsky, M. H., Lippard, S. J., Hedman, B., Hodgson, K. O. X-ray Absorption Spectroscopic Study of the Reduced Hydroxylases of Methane Monooxygenase and Toluene/*o*-Xylene Monooxygenase: Differences in Active Site Structure and Effects of the Coupling Proteins MMOB and ToMOD. manuscript in preparation.

Fishman, A., Tao, Y., Sazinsky, M. H., Lippard, S. J., Wood, T. K. Controlling Regiospecific Oxidation of Aromatics via Active Site Engineering of Toluene para-Monooxygenase of *Ralstonia pickettii* PKO1. Manuscript in preparation.

Sazinsky, M. H., Merkx, M., Tang, S., Lippard, S. J. Preparation and X-ray Structures of Metal-Free, Dicobalt and Dimanganese Forms of Soluble Methane Monooxygenase Hydroxylase from *Methylococcus capsulatus* (Bath). Manuscript in preparation.

Sazinsky, M. H. Lippard, S. J. Product Bound Structures of the Soluble Methane Monooxygenase Hydroxylase from *Methylococcus capsulatus* (Bath): Protein Motion in the α -Subunit. Manuscript in preparation.

Sazinsky, M. H., Zhu, K., Pozharski, E., Lakshmi, K. V., Brudvig, G. A., Lippard, S. J. Protein B and Ferredoxin Domain Binding to the Soluble Methane Monooxygenase Hydroxylase from *Methylococcus capsulatus* (Bath) by EPR Spectroscopy, Site-Directed Spin-labeling, and Molecular Docking. Manuscript in preparation.

PRESENTATIONS

227th National Meeting of the American Chemical Society, Anaheim, CA, Mar. 28 – Apr. 1, 2004, Short talk title: Structural and Mechanistic Insights into Hydrocarbon Oxidizing Non-Heme Diiron Enzymes: Substrate Specificity and Diiron Center Tuning.

Metals in Biology Gordon Research Conference, Ventura, CA, Jan. 18-23, 2004, Poster title: Structure of the Toluene /*o*-Xylene Monooxygenase Hydroxylase from *Pseudomonas stutzeri* OX1.

16th Enzyme Mechanisms Conference, Napa, CA, Jan. 6-10, 1999, Poster title: X-ray Absorption Spectroscopy Studies of Zinc Binding to the Active Site of Mammalian Porphobilinogen Synthase.